Kaon to two-pion decay and pion-pion scattering from lattice QCD

Tianle Wang

Submitted in partial fulfillment of the
requirements for the degree of
Doctor of Philosophy
under the Executive Committee
of the Graduate School of Arts and Sciences

COLUMBIA UNIVERSITY

2021

Abstract

Kaon to Two Pions decay and Pion-Pion scattering from Lattice QCD

Tianle Wang

In this work, we present a lattice QCD calculation of two closely related quantities: 1). The $\pi\pi$ scattering phase shift for both $I = 0$ and $I = 2$ channels at seven energies in total, and 2). The $\Delta I = 1/2$, $K \longrightarrow \pi\pi$ decay amplitude A_0 and ϵ', the measure of direct CP violation. These two results improve our earlier calculation presented in 2015[1]. The calculation is performed on an ensemble of $32^3 \times 64$ lattice with $a^{-1} = 1.3784(68)$GeV. This is a physical calculation, where the chiral symmetry breaking is controlled by the $2 + 1$ flavor Möbius Domain Wall Fermion, and we take the physical value for both kaon and pion. The G-parity boundary condition is used and carefully tuned so that the ground state energy of the $\pi\pi_{I=0}$ state matches the kaon mass. Three sets of $\pi\pi$ interpolating operators are used, including a scalar bilinear "σ" operator and paired single-pion bilinear operators with the constituent pions carrying various relative momenta. Several techniques, including correlated fits and a bootstrap determination of the p-value have been used, and a detailed analysis of all major systematic error is performed. The $\pi\pi$ scattering phase shift results are presented in Fig. 5.10 and Tab. 5.12. For the Kaon decay amplitude, we finally get $\mathrm{Re}(A_0) = 2.99(0.32)(0.59) \times 10^{-7}$GeV, which is consistent with the experimental value of $\mathrm{Re}(A_0) = 3.3201(18) \times 10^{-7}$GeV, and $\mathrm{Im}(A_0) = -6.98(0.62)(1.44) \times 10^{-11}$GeV. Combined with our earlier lattice calculation of A_2[2], we obtained $\mathrm{Re}(\epsilon'/\epsilon) = 21.7(2.6)(6.2)(5.0) \times 10^{-4}$, which agrees well with the experimental value of $\mathrm{Re}(\epsilon'/\epsilon) = 16.6(2.3) \times 10^{-4}$, and $\mathrm{Re}(A_0)/\mathrm{Re}(A_2) = 19.9(2.3)(4.4)$, consistent with the experimental value of

$\mathrm{Re}(A_0)/\mathrm{Re}(A_2) = 22.45(6)$, known as the $\Delta I = 1/2$ rule.

Table of Contents

List of Figures

List of Tables

Acknowledgements

First of all, I would like to thank my advisor, Prof. Norman Christ, for his guidance and encouragement during my research project. The weekly discussion helps me a lot in understanding physics and generating new ideas in research.

I would like to thank Dr. Chris Kelly for his collaboration. He not only teaches me lots of coding skills but generates many new ideas in research. He also helped me double-check all the results I got. Also, I have learned many things during the weekly meeting between Norman and us, and I really enjoy it.

I would like to thank Prof. Robert Mawhinney for many helpful suggestions during the group meeting. I want to thank our collaborators in RBC-UKQCD, including but not limited to, Chris Sachrajda, Tom Blum, Peter Boyle, Armajit Soni, Taku Izubuchi, Xu Feng, Luchang Jin, Masaaki Tomii, and Dan Hoying, for their helpful ideas and refinements on my project.

I would like to thank my roommate and colleague, Bigeng Wang. The frequent discussions between us are constructive, and he helps me a lot in my daily life. I would also like to thank other colleagues and friends, including Ziyuan Bai, Jiqun Tu, Duo Guo, Yidi Zhao, Tuan Nguyen, Zhenghan Gao, and Minghao Cheng, for their help.

Finally, I would like to thank my parents for their support and understanding throughout these years.

Chapter 1: Introduction

There are three most important discrete symmetry operations in particle physics, parity symmetry (P), time-reversal symmetry (T), and charge conjugation symmetry (C). In 1956, Lee and Yang first pointed out that the violation of P-symmetry could be the solution to the $\tau - \theta$ puzzle[3]. This violation was later confirmed by the experimental results from beta decay of ^{60}Co[4]. Later in 1964, the violation of CP-symmetry was found in the neutral kaon decay, where the long-lived kaon could decay to CP-even, two-pion final state. This violation is much weaker than the P-violation. There are two sources of CP violation in this decay process: the first one is indirect CP violation, which comes from the $K - \bar{K}$ mixing and can explain the majority of CP violation in the experimental result. The second one is direct CP violation, where the CP-odd kaon eigenstate decays directly to $\pi\pi$ state. The second one is a much smaller effect ($O(10^{-3})$ compared to the first one), and was first found in the later 1990s[5]. This small effect, which is highly sensitive to the mechanism of CP violation in the Standard Model, is a good place for us to understand the Standard Model. In Chapter 2 we will discuss in more detail the kaon decay, its phenomenology and its relation to CP violation and the Standard Model, and discuss the quantity $\mathrm{Re}(\epsilon'/\epsilon)$, which measures the direct CP violation.

CP violation is also important in helping us to understand the matter–antimatter imbalance in our universe. The amount of CP violation in the Standard Model is believed to be too small to explain for the dominance of matter over antimatter. This suggests possible new physics beyond the Standard Model, and underscores the importance of a direct calculation of CP violation. However, a standard perturbative calculation is hard to perform. This is because the strength of the strong interaction increases at lower energy, which makes the pertubative expansion fail at low energy. Some analytic tools, including chiral perturbation theory and dispersion theory, are invented to overcome this problem, but they can not give us a result from first-principles.

Lattice QCD is currently the only known method which can determine the properties of low-energy QCD from first-principles with controlled systematic errors. In a typical lattice QCD calculation, spacetime is discretized by the lattice spacing a, which serves as a regulator of the theory. In Chapter 3 we will describe the lattice method, how we treat the gauge action and fermion action on the lattice, and how to make a calculation on the lattice. With the lattice method, people are able to calculate various quantities, including the hadron spectrum, decay amplitudes and hadron structure. These calculations can be compared with experimental values to measure parameters of the Standard Model, or find possible physics beyond the Standard Model. Also, with lattice QCD and the finite-volume Lüscher technique [6], we can calculate the $\pi\pi$ scattering phase shifts within the energy region from $2m_\pi$ to approximately $4m_\pi$. Such calculations complement the existing determinations of the scattering lengths obtained using chiral perturbation theory [7] and the dispersive calculations [8, 9, 10, 11] of the energy dependence of the phase shift based on the Roy equations [12] and experimental input.

In this work, we are focusing on two closely related topics: The calculation of the $\pi\pi$ scattering phase shift for both the $I = 0$ and $I = 2$ channels foe energies around the kaon mass, and the decay amplitude A_0 for a single kaon decay to $I = 0$ two-pion state ($K \longrightarrow \pi\pi(I = 0)$), both at physical pion mass. There are two main difficulties in these calculations: 1). The presence of “vacuum diagrams" in both calculations, which gives rise to a much larger statistical error compared with the $K \longrightarrow \pi\pi(I = 2)$ and $\pi\pi(I = 2)$ scattering calculation. 2). The final two-pion state in the decay process is composed of two pions that are carrying momenta, which will be an excited finite-volume state on a lattice with periodic boundary condition. Several techniques are used to overcome these difficulties, including using a lattice with G-parity boundary conditions (GPBC), which will be discussed in Sec. 3.4 and a more detailed discussion can be found in Ref. [13], and using All-to-All propagators (A2A) to construct $\pi\pi$ interpolating operators that overlap better with physical state (See Ref. [14]). With these techniques, in 2015 the RBC/UKQCD collaborations published the first lattice calculation of A_0 using 216 lattice configurations with a $32^3 \times 64$ volume, an inverse lattice spacing of $a^{-1} = 1.3784(68)$ GeV, and with physical kinematics[1]. We found $\mathrm{Re}(\epsilon'/\epsilon) = 1.38(5.15)(4.59) \times 10^{-4}$, which is 2.1σ lower than the experimental value. Meanwhile, for an energy near the kaon mass we obtained a $\pi\pi_{I=0}$ phase shift of $\delta_0(E_{\pi\pi} \approx m_K) = 23.8(4.9)(1.2)^\circ$, which is significantly lower than the dispersive result.

After several attempts to explain the discrepancy between these phase shift results as pure statistical error by including more statistics, or imperfect data analysis by using more sophisticated methods, we concluded that a possible explanation for the discrepancy to be contamination from one or more excited states whose contribution with increasing time is masked by the rather rapid reduction in the signal-to-noise of our data. Therefore we introduced several new operators, including a bilinear σ operator which has the same quantum number as $\pi\pi_{I=0}$ state, as well as other $\pi\pi$ interpolating operators in which the individual pions carry higher relative momenta. We can then use a multi-state multi-operator fit to extract the ground state energy with a smaller excited state contamination error. We also developed a method to obtain a more accurate measure of the quality of the agreement between our data and our theoretical fitting formula. These will be explained in detail in Chapter 4.

In Chapter 5 we present the new calculation on the $\pi\pi$ scattering phase shift. We also extend our calculation beyond a single $\pi\pi$ energy by computing $\pi\pi$ two-point correlation functions with the two pions carrying several values of the total momentum, allowing for an exploration of the scattering phase shift at center-of-mass energies between approximately $2m_\pi$ and the kaon mass, which allows us to directly calculate the LL factor from our lattice QCD data. We show that with additional operators we obtain a significant improvement in statistical precision, and gain better control over the contamination from neglected excited states. We also applied a second approach to the analysis of our multi-operator, multi-state data, the generalized eigenvalue problem (GEVP) method. This new method gave results consistent with those of our traditional fitting approach with similar statistical errors.

In Chapter 6 we present in detail how we calculate A_0 and ϵ'/ϵ on the lattice. Again we use multiple operators to suppress the excited state error. We also include an improved non-perturbative determination of the renormalization factors relating the bare matrix elements to those of operators renormalized in the $\overline{\text{MS}}$ scheme (see Sec. 6.4). This calculation utilizes step-scaling technique to raise the matching scale from 1.53 GeV to 4.01 GeV, significantly reducing the systematic error associated with the perturbative matching between RI-SMOM and $\overline{\text{MS}}$ scheme in which the Wilson coefficients have been computed.

In writing Chapter 4, 5 and 6, the contents are mostly taken from Ref. [15], which I am the principle author of, and Ref. [16], to which I am one of the major contributors.

Chapter 2: Kaon decay and CP violation

The Standard Model is a theoretical model which includes our knowledge of the strong and electroweak interactions. In this chapter, we first discuss the origin of CP violation in the Standard Model. Then we discuss the relation between CP violation and neutral kaon decay in a phenomenological way, introducing two parameters, ϵ and ϵ', which measure the direct and indirect CP violation in this decay. Finally, we discuss the low energy effective theory for this decay, writing down the operators we should include in the calculation and the corresponding Wilson coefficients.

2.1 CKM matrix and CP violation

The CKM matrix describes the flavor mixing of fermions in the charged current. This mixing originates from the difference between the fermion mass eigenstates and flavor eigenstates. There is a free complex phase parameter in the CKM matrix, which leads to the CP violation in the weak interaction. In this section, I will describe the above in more detail.

The Lagrangian L_{HF}, which describes the interaction between fermions and Higgs, can be written as:

$$-L_{\mathrm{HF}} = f_u^{\alpha\beta}\bar{q}'_{L,\alpha}\tilde{\Phi}u'_{R,\beta} + f_d^{\alpha\beta}\bar{q}'_{L,\alpha}\Phi d'_{R,\beta} + f_e^{\alpha\beta}\bar{l}'_{L,\alpha}\Phi e'_{R,\beta} + \text{h.c.}, \tag{2.1}$$

with the following notation:

$$\begin{aligned}
\vec{u}' &= (u', c', t') \\
\vec{d}' &= (d', s', b') \\
\vec{e}' &= (e', \mu', \tau') \\
\vec{q}' &= ((u', d')^T, (c', s')^T, (t', b')^T) \\
\vec{l}' &= ((\nu'_e, e')^T, (\nu'_\mu, \mu')^T, (\nu'_\tau, \tau')^T)
\end{aligned} \tag{2.2}$$

and $\tilde{\Phi}$, Φ are the two-component Higgs field; f_u, f_d and f_e are the 3×3 coupling matrix in the flavor space, which are not necessarily diagonal. The prime suggests that the states here are the flavor eigenstates and are not necessarily the mass eigenstates. After spontaneous symmetry breaking, the vacuum expectation value of the Higgs field gives rise to the mass term:

$$-L_{\text{HF,mass}} = \bar{u}'_L m'_u u'_R + \bar{d}'_L m'_d d'_R + \bar{e}'_L m'_e e'_R + \text{h.c.}, \tag{2.3}$$

We can then diagonalized the mass matrix using the 3×3 unitary matrices $S^\alpha_{L,R}$ ($\alpha = u, d, e$), so that

$$\begin{aligned}
\alpha'_h &= S^\alpha_h \alpha_h \\
m'_\alpha &= S^\alpha_L m_\alpha S^{\alpha\dagger}_R \\
-L_{\text{HF}} &= \bar{u} m_u u + \bar{d} m_d d + \bar{e} m_e e
\end{aligned} \tag{2.4}$$

where $\alpha = u, d, e$ and $h = L, R$. The 3×3 matrices m_α are now diagonal and are the mass matrices, whose three diagonal elements are the masses of the three generations of fermion α. We now look at the quark contribution to the charged weak current (there will not be flavor mixing in the neutral weak current):

$$J^\mu_{\text{ch,quark}} = 2\bar{u}'_L \gamma^\mu d'_L = 2\bar{u}_L \gamma^\mu S^{u\dagger}_L S^d_L d_L = 2\bar{u}_L \gamma^\mu V d_L \tag{2.5}$$

where $V = S^{u\dagger}_L S^d_L$ is a 3×3 unitary matrix called Cabibbo–Kobayashi–Maskawa (CKM) matrix.

This matrix describes quark flavor mixing in the charged current.

$$V = \begin{pmatrix} V_{ud} & V_{us} & V_{ub} \\ V_{cd} & V_{cs} & V_{cb} \\ V_{td} & V_{ts} & V_{tb} \end{pmatrix} \tag{2.6}$$

The CKM matrix is a 3 × 3 unitary matrix, which means it has 9 real parameters, but some of them are not physical since they can be removed by a quark rephasing:

$$\alpha_{L,i} \longrightarrow e^{i\theta_i^\alpha} \alpha_{L,i}, \quad (i = 1, 2, 3; \quad \alpha = u, d), \tag{2.7}$$

Notice an overall rephasing by the same amount will not change the CKM matrix, which means five of the parameters are not free, and we only have four free parameters. Under the KM representation, three of them can be interpreted as mixing angles, and the last one is a complex phase, which makes the CKM matrix complex and leads to CP violation. This can be seen from the Lagrangian $L_{GF,ch,quark}$ which describes the interaction between W-boson and the quark contribution to the charged weak current:

$$L_{\text{GF,ch,quark}} = \frac{e}{\sqrt{2}\sin\theta_W}(W_\mu^+ \bar{u}_L \gamma^\mu V d_L + \text{h.c.}), \tag{2.8}$$

Under the CP transformation, we have:

$$L_{\text{GF,ch,quark}} \xrightarrow{\text{CP}} \frac{e}{\sqrt{2}\sin\theta_W}(W_\mu^+ \bar{u}_L \gamma^\mu V^* d_L + \text{h.c.}), \tag{2.9}$$

which suggests that a complex CKM matrix could lead to CP violation.

2.2 CP Violation in Neutral Kaon Decay

Before we discuss CP violation in neutral kaon decay, it is important to first introduce kaon mixing. There are two neutral kaon states, $\left|K^0\right\rangle$ and $\left|\bar{K}^0\right\rangle$, which are related by CP operation:

$$\mathrm{CP}\left|K^0\right\rangle = (-1)\left|\bar{K}^0\right\rangle, \tag{2.10}$$

These two states can mix with each other due to strangeness non-conservation. The time evolution of the $\left|K^0\right\rangle - \left|\bar{K}^0\right\rangle$ system can be formulated as:

$$i\frac{d}{dt}\left|\phi(t)\right\rangle = \left(M - \frac{i}{2}\Gamma\right)\left|\phi(t)\right\rangle, \tag{2.11}$$

where $|\phi(t)\rangle = (a(t), b(t))^T = a(t)\left|K^0\right\rangle + b(t)\left|\bar{K}^0\right\rangle$, and the mass matrix is given by

$$M_{ij} = m_K^{(0)}\delta_{ij} + \frac{\langle i|H_W|j\rangle}{2m_K} + P\sum_n \frac{\langle i|H_W|n\rangle\langle n|H_W|j\rangle}{m_K - E_n} \tag{2.12}$$

$$\Gamma_{ij} = \frac{1}{2m_K}\sum_n \langle i|H_W|n\rangle\langle n|H_W|j\rangle 2\pi\delta(E_n - m_K) \tag{2.13}$$

which can be parameterized by:

$$M - \frac{i}{2}\Gamma = \begin{pmatrix} A & p^2 \\ q^2 & A^2 \end{pmatrix} \tag{2.14}$$

If CP is an exact symmetry, we have $p = q$, and the CP eigenstates $|K_\pm\rangle = \frac{1}{\sqrt{2}}(\left|K^0\right\rangle \mp \left|\bar{K}^0\right\rangle)$ will also be the mass eigenstate. In the real world where CP is mildly violated, p differs from q by a small amount, and the two mass eigenstates become:

$$|K_{\mathrm{L/S}}\rangle = \frac{1}{\sqrt{|p|^2+|q|^2}}\left(p\left|K^0\right\rangle \pm q\left|\bar{K}^0\right\rangle\right) \tag{2.15}$$

where L/S stands for long/short lived kaon state whose lifetimes differ by a factor of 580. We can rewrite the above equation in terms of the CP eigenstates:

$$
\begin{aligned}
|K_{\mathrm{L/S}}\rangle &= \frac{1}{\sqrt{1+|\bar{\epsilon}|^2}}\left(\left|K^0_{\mp}\right\rangle + \bar{\epsilon}\left|K^0_{\pm}\right\rangle\right) \\
\bar{\epsilon} &= \frac{p-q}{p+q}
\end{aligned}
\tag{2.16}
$$

This means that the long(short) lived kaon state is mostly composed of the CP odd(even) kaon state, but with a small fraction of the other CP even(odd) kaon state. The mixing can be observed from the oscillation of $\left|K^0\right\rangle$ and $\left|\bar{K}^0\right\rangle$ states as a function of time, which reflects the tiny mass difference between $|K_{\mathrm{S}}\rangle$ and $|K_{\mathrm{L}}\rangle$ states.

Notice that the s-wave $\pi\pi$ final state is a CP-even state. If CP is conserved, the $|K_{\mathrm{L}}\rangle$ state will be CP-odd and will not decay to the s-wave $\pi\pi$ final state. This means the $|K_{\mathrm{L}}\rangle \to \pi\pi$ decay mode implies CP violation. There are two sources of CP violation in this decay. The first one, which is called indirect CP violation, comes from the fact that $|K_{\mathrm{L}}\rangle$ has a small component of CP-even state, which could decay to the s-wave $\pi\pi$ final state via CP conserved decay mode. The second one, which is called direct CP violation, originates from the CP-odd component of $|K_{\mathrm{L}}\rangle$ decaying to the s-wave $\pi\pi$ final state via the CP-violating decay mode.

We can introduce two parameters, ϵ and ϵ', to describe the size of indirect and direct CP violation in this decay. These two parameters are defined as:

$$
\begin{aligned}
\frac{\langle\pi^+\pi^-|\, H_W\, |K_L\rangle}{\langle\pi^+\pi^-|\, H_W\, |K_S\rangle} &= \epsilon + \epsilon' \\
\frac{\left\langle\pi^0\pi^0\right|\, H_W\, |K_L\rangle}{\left\langle\pi^0\pi^0\right|\, H_W\, |K_S\rangle} &= \epsilon - 2\epsilon'
\end{aligned}
\tag{2.17}
$$

They are related to the decay amplitudes of $\left|K^0\right\rangle$ to s-wave $\pi\pi$ final states with definite isospin quantum numbers I (I=0/2), defined by:

$$
A(K^0 \to \pi\pi(I)) = A_I e^{i\delta_I} \tag{2.18}
$$

where δ_I is the scattering phase shift in isospin I channel. Applying the CPT symmetry, we also get

$$A(\bar{K}^0 \to \pi\pi(I)) = -A_I^* e^{i\delta_I} \tag{2.19}$$

A complex phase, or the imaginary part of A_I, implies CP violation. After some algebra, we can work out the expression for ϵ and ϵ':

$$\begin{aligned} \epsilon &= \bar{\epsilon} + i\left(\frac{\mathrm{Im}(A_0)}{\mathrm{Re}(A_0)}\right) \\ \epsilon' &= \frac{ie^{\delta_2-\delta_0}}{\sqrt{2}}\left|\frac{A_2}{A_0}\right|\left(\frac{\mathrm{Im}(A_2)}{\mathrm{Re}(A_2)} - \frac{\mathrm{Im}(A_0)}{\mathrm{Re}(A_0)}\right) \end{aligned} \tag{2.20}$$

Notice if direct CP violation is absent, $\mathrm{Im}(A_2) = \mathrm{Im}(A_0) = 0$, which implies $\epsilon' = 0$; if indirect CP violation is absent, $\bar{\epsilon} = 0$, which suggests $\mathrm{Re}(\epsilon) = 0$. This suggests that ϵ and ϵ' describe the size of indirect and direct CP violation, respectively.

Currently the experimental value for ϵ and ϵ' are[17]:

$$\begin{aligned} |\epsilon| &= 0.002228(11), \\ \arg(\epsilon) &= 0.7596 \text{ rad}, \\ \mathrm{Re}(\epsilon'/\epsilon) &= 16.6(2.3) \times 10^{-4}, \end{aligned} \tag{2.21}$$

and the large relative error on $\mathrm{Re}(\epsilon'/\epsilon)$ suggests this is a quantity hard to measure in experiment. One of the main topics of this work is to calculate it using lattice methods and to compare these two results.

There is also an interesting experimental finding in the decay amplitudes A_0 and A_2. The current experimental values for them are:

$$\begin{aligned} \mathrm{Re}(A_0) &= 3.3201(18) \times 10^{-7}\mathrm{GeV}, \\ \mathrm{Re}(A_2) &= 1.479(4) \times 10^{-8}\mathrm{GeV}, \\ \frac{\mathrm{Re}(A_0)}{\mathrm{Re}(A_2)} &= 22.45(6), \end{aligned} \tag{2.22}$$

The large dominance of the $\Delta I = 1/2$ amplitude over the $\Delta I = 3/2$ amplitude is called the $\Delta I = 1/2$ rule, which will be verified in this work.

2.3 Effective Hamiltonian and Wilson Coefficient

In principle, given the full Lagrangian of the Standard Model, we can include both QCD and the weak interaction in a lattice calculation. However, the large mass of gauge boson is incompatible with the much smaller inverse lattice spacing a^{-1}, which typically has an order of $1-3$ GeV. That means if we include the gauge bosons directly in a lattice calculation, we will not be able to see their kinematic effects. In other words, the lattice method is unable to deal directly with such high energy contributions.

One standard way to solve this problem is to introduce an energy scale μ and divide the physics into the high energy contribution ($> \mu$) and low energy contribution ($< \mu$). After that, we can use the lattice method to calculate the low energy contribution. This can be done by the method of operator product expansion, where the effective Lagrangian can be expanded as a set of local operators, with coefficients that are μ dependent. These coefficients, which we call the Wilson coefficients, include the high energy effects and can be evaluated using renormalization group improved perturbation theory. Since the introduction of μ is artificial, the real physics should not depend on μ, which means both Wilson coefficient c_i and operator Q_i should be a function of μ, so that the μ-dependence cancels. In this work, we are using the 3-flavor effective lagrangian H_{eff} defined in Eq. (2.23), where both the heavy gauge boson and the c,b,t quarks are integrated out. The Wilson coefficients are calculated to the next leading order in the $\overline{\text{MS}}$ scheme, and their value with $\mu = 4$GeV, is presented in Tab. 6.16.

$$H_{\text{eff}} = \frac{G_F}{\sqrt{2}} V_{us}^{*} V_{ud} \sum_{i=1}^{10} C_i(\mu) Q_i(\mu) \tag{2.23}$$

where G_F is the Fermi constant, and the ten Q_i operators are defined as:

$$
\begin{aligned}
Q_1 &= (\bar{s}_\alpha d_\alpha)_{V-A}(\bar{u}_\beta u_\beta)_{V-A},\\
Q_2 &= (\bar{s}_\alpha d_\beta)_{V-A}(\bar{u}_\beta u_\alpha)_{V-A},\\
Q_3 &= (\bar{s}_\alpha d_\alpha)_{V-A}\sum_{q=u,d,s}(\bar{q}_\beta q_\beta)_{V-A},\\
Q_4 &= (\bar{s}_\alpha d_\beta)_{V-A}\sum_{q=u,d,s}(\bar{q}_\beta q_\alpha)_{V-A},\\
Q_5 &= (\bar{s}_\alpha d_\alpha)_{V-A}\sum_{q=u,d,s}(\bar{q}_\beta q_\beta)_{V+A},\\
Q_6 &= (\bar{s}_\alpha d_\beta)_{V-A}\sum_{q=u,d,s}(\bar{q}_\beta q_\alpha)_{V+A},\\
Q_7 &= \frac{3}{2}(\bar{s}_\alpha d_\alpha)_{V-A}\sum_{q=u,d,s}e_q(\bar{q}_\beta q_\beta)_{V+A},\\
Q_8 &= \frac{3}{2}(\bar{s}_\alpha d_\beta)_{V-A}\sum_{q=u,d,s}e_q(\bar{q}_\beta q_\alpha)_{V+A},\\
Q_9 &= \frac{3}{2}(\bar{s}_\alpha d_\alpha)_{V-A}\sum_{q=u,d,s}e_q(\bar{q}_\beta q_\beta)_{V-A},\\
Q_{10} &= \frac{3}{2}(\bar{s}_\alpha d_\beta)_{V-A}\sum_{q=u,d,s}e_q(\bar{q}_\beta q_\alpha)_{V-A},
\end{aligned}
\tag{2.24}
$$

Here α and β are color indices, and the spin indices are contracted implicitly. Q_1 and Q_2 are called current-current operators, Q_3, Q_4, Q_5 and Q_6 are called QCD penguin operators, and Q_7, Q_8, Q_9 and Q_{10} are called electroweak penguin operators. Notice all these ten operators are dimension 6 operators. This is because those lower dimension operators (with dimension 4 and 5) which are present will not contribute to the decay process, and the effects from higher dimension operators will be suppressed by at least $O(\mu/M_W)$. Also notice that among the 10 operators, only 7 of them are linearly independent, and we can prove the following three identities:

$$Q_{10} - Q_9 = Q_4 - Q_3 \tag{2.25}$$

$$Q_4 - Q_3 = Q_2 - Q_1 \tag{2.26}$$

$$2Q_9 = 3Q_1 - Q_3. \tag{2.27}$$

One last thing that needs to be mentioned here is that the matrix element of the ten operators are calculated in the lattice scheme, while the Wilson coefficient is evaluated in the $\overline{\text{MS}}$ scheme, so a matching between lattice scheme and $\overline{\text{MS}}$ scheme must be performed. We will discuss this in Sec. 6.4.

Chapter 3: Lattice QCD

Due to the quark confinement, the QCD coupling constant becomes large at low energy, suggesting a non-perturbative treatment is necessary for solving problems involving QCD at low energy. Introducing a lattice is a method that regularizes quantum field theory and defines problems non-perturbatively. This feature suggests that the lattice method could be powerful in solving the low energy part of the $K \to \pi\pi$ problem mentioned in Chapter 2. In this Chapter, we will first briefly introduce the lattice method, including the treatment of the quark field and the gauge field. Then we introduce the boundary conditions we use in this work, the G-parity boundary conditions, which is different from the trivial periodic boundary conditions that most other groups use. We then list the detailed information of the gauge ensemble we use in this work.

3.1 General Idea

In the continuous Quantum Chromodynamics (QCD), the expectation value of an operator $O(A_\mu, \bar{\psi}, \psi)$ can be obtained from the path integral:

$$\langle O \rangle = \frac{1}{Z} \int [D\bar{\psi}][D\psi][DA_\mu] O(A_\mu, \bar{\psi}, \psi) e^{iS_{\text{QCD}}}, \tag{3.1}$$

where

$$\begin{aligned}
Z &= \frac{1}{Z} \int [D\bar{\psi}][D\psi][DA_\mu] e^{iS_{\text{QCD}}}, && (3.2) \\
S_{\text{QCD}} &= \int d^4x \mathcal{L}(x), && (3.3) \\
\mathcal{L}(x) &= \sum_f \bar{\psi}_f (i\not{D} - m_f) \psi_f - \frac{1}{4} F^a_{\mu\nu} F_a^{\mu\nu}, && (3.4) \\
F^a_{\mu\nu} &= \partial_\mu A^a_\nu - \partial_\nu A^a_\mu + g f^{abc} A^b_\mu A^c_\nu, && (3.5)
\end{aligned}$$

Here ψ_f is the spin-$\frac{1}{2}$ fermion field where f is the flavor index. According to Chapter 2, we integrate out the heavier c,t,b quarks, so we are dealing with 3-flavor QCD where $f \in \{u, d, s\}$. The fields A^a_μ are the spin-1 gluon fields while g is the QCD coupling constant, and f^{abc} are the SU(3) structure constants.

To make the numerical calculation accessible, the first step is to get rid of the sign problem which originates from the fast oscillating factor $e^{iS_{\text{QCD}}}$. To do that we perform the Wick rotation, which transforms the above definition from Minkowski space to Euclidean space. This is done by introducing $x_0 \to -ix_4$, which leads to the following modification:

$$\begin{aligned} \langle O \rangle &= \frac{1}{Z}\int [D\bar{\psi}][D\psi][DA_\mu] O(A_\mu, \bar{\psi}, \psi) e^{-S^E_{\text{QCD}}}, & (3.6) \\ \mathcal{L}^E(x) &= \sum_f \bar{\psi}_f (\not{D}^E + m_f)\psi_f + \frac{1}{4} F^a_{\mu\nu} F^{\mu\nu}_a. & (3.7) \end{aligned}$$

Notice that the Dirac matrices in Eq. (3.7) should be the Euclidean gamma matrices. Later in this work, I will neglect all superscript “E" and assume everything is defined in Euclidean space.

The next problem we met is the tremendously large dimension of the integral. Let us think of a lattice with $O(10)$ units on each dimension. The total number of sites of the lattice is $O(10^4)$, even a coarse mesh of 2 points on each dimension of the integral means $O(10^{3000})$ terms to be calculated, which means we can not evaluate the integral in Eq. (3.6) directly. The solution is to approximate this integral using a statistical method. This is usually done by generating a large number of uniformly distributed samples and then calculating the ensemble average of the integrand. This is usually not efficient since most of the samples will have a negligible contribution to the integral due to the small factor of $e^{-S_{\text{QCD}}}$. One way to solve this problem is to do importance sampling, which means instead of generating samples that are evenly distributed in parameter space, we generate samples (labeled by $s_1, s_2, ..., s_N$) so that their probability distribution function is proportional to $e^{-S_{\text{QCD}}}$. With these samples, we can rewrite Eq. (3.6) with the following:

$$\langle O \rangle = \frac{1}{N}\sum_{i=1}^{N} O(s_i), \tag{3.8}$$

where N is the total number of samples we use for the measurement, and $O(s_i)$ is the observable O evaluated on the sample s_i. These samples are obtained from a Markov chain generated from the Rational Hybrid Monte Carlo algorithm (RHMC) in this work.

Unfortunately, we are still unable to perform a numerical calculation with Eq. (3.6) and (3.8) directly. This is because the fermion field, $\bar{\psi}$ and ψ, are Grassman numbers which can not be sampled on a conventional computation directly. One way to solve this problem is to notice that the fermion part of the Lagrangnian is a bilinear function of the fermion field, and that we have the following identity:

$$\int [D\bar{\psi}][D\psi] e^{-\bar{\psi}M\psi} = \det(M). \tag{3.9}$$

We can then “integrate out" the fermion field analytically in Eq. (3.6) with following:

$$\begin{aligned}\langle O\rangle &= \frac{\int [D\bar{\psi}][D\psi][DA_\mu] O(A_\mu,\bar{\psi},\psi) e^{-S_{\text{QCD}}}}{\int [D\bar{\psi}][D\psi][DA_\mu] e^{-S_{\text{QCD}}}} \\ &= \frac{\int [DA_\mu] O_{\text{eff}}(A_\mu) e^{-S_G} \int [D\bar{\psi}][D\psi] e^{-\sum_f \bar{\psi}(\not{D}^E + m_f)\psi}}{\int [DA_\mu] e^{-S_G} \int [D\bar{\psi}][D\psi] e^{-\sum_f \bar{\psi}(\not{D}^E + m_f)\psi}} \\ &= \frac{\int [DA_\mu] O_{\text{eff}}(A_\mu) e^{-S_G - S_F}}{\int [DA_\mu] e^{-S_G - S_F}}\end{aligned} \tag{3.10}$$

where

$$O_{\text{eff}} = \frac{\int [D\bar{\psi}][D\psi] O(A_\mu,\bar{\psi},\psi) e^{-\sum_f \bar{\psi}(\not{D}^E + m_f)\psi}}{\int [D\bar{\psi}][D\psi] e^{-\sum_f \bar{\psi}(\not{D}^E + m_f)\psi}}, \tag{3.11}$$

$$S_F = -\ln(\det(\not{D}^E + m_f)), \tag{3.12}$$

$$S_G = \frac{1}{4}\int d^4x F^a_{\mu\nu} F_a^{\mu\nu} \tag{3.13}$$

and S_F can be reconstructed using a “pseudo-fermion" scalar field that can be represented using complex number.

3.2 Gauge action

Given Eq. (3.10), the next step is to discretize the action on the lattice. In this Section, we discuss the discretization of the gauge action. We first introduce gauge links $U_\mu(x)$, which are SU(3) matrices. They have the physical meaning of connecting the n^{th} site with its neighboring site along the μ^{th} direction. They are related to the gauge field $A_\mu(x)$ via:

$$\begin{aligned} U(x, x + a\hat{\mu}) &= U_\mu(x) = e^{igaA_\mu(x)}, \\ U(x + a\hat{\mu}, x) &= U_\mu^\dagger(x) \end{aligned} \tag{3.14}$$

The link variable is critical in discretizing non-abelian gauge action (e.g., SU(3) gauge action for QCD) where we need to preserves gauge invariance on the lattice. Terms that look like the product of two fermion fields at different sites will show up when we discretize the fermion action on the lattice. These terms break the SU(3) gauge-invariance explicitly. In order to fix that, the gauge links are introduced, which can be understood as parallel transporting two fields onto the same site, by which we preserve the gauge invariance for the fermion action.

Since both the gauge action and the path ordered products of gauge links which forms closed loop are gauge invariant, we would expect the gauge action to be a function of all possible loop product of links. It can be shown that for a sufficiently small box of fixed physical size that perturbation theory can be used, the lattice action

$$S_G^W = \beta \sum_{x, \mu < \nu} \left[1 - \frac{1}{3} P_{\mu\nu}(x) \right] \tag{3.15}$$

will reproduce the conventional continuum field theory, where $\beta = 6/g^2$ and $P_{\mu\nu}(x)$ is the plaquette link product defined by:

$$P_{\mu\nu}(x) = \text{ReTr} \left[U_\mu(x) U_\nu(x + a\hat{\mu}) U_\mu^\dagger(x + a\hat{\nu}) U_\nu^\dagger(x) \right]. \tag{3.16}$$

This is called the Wilson action. An improved version of the gauge action can be written down as:

$$S_G^R = -\frac{\beta}{3}\left[(1-8c_1)\sum_{x,\mu<\nu} P_{\mu\nu}(x) + c_1 \sum_{x,\mu\neq\nu} R_{\mu\nu}(x)\right] + \text{const}, \tag{3.17}$$

where $R_{\mu\nu}(x)$ is the 1×2 rectangle plaquette link product defined as:

$$R_{\mu\nu}(x) = \mathrm{ReTr}\left[U_\mu(x)U_\mu(x+a\hat{\mu})U_\nu(x+2a\mu)U_\mu^\dagger(x+a\hat{\mu}+a\nu)U_\mu^\dagger(x+a\hat{\nu})U_\nu^\dagger(x)\right] \tag{3.18}$$

The choice of c_1 is somewhat arbitrary since all different values of c_1 give the same continuum limit. One choice is to set $c_1 = -0.331$, and this is called the Iwasaki gauge action. In this work we use Iwasaki gauge action.

3.3 Fermion action

The most naive way of discretizing the fermion action can be done by replacing the derivative term by a finite difference with an extra gauge link which preserves the gauge invariance:

$$S_F^{\text{naive}} = a^4 \sum_x \left\{ \sum_\mu \frac{1}{2a}\bar{\psi}(x)\gamma_\mu \left[U_\mu(x)\psi(x+a\hat{\mu}) - U_\mu^\dagger(x-a\mu)\psi(x-a\mu)\right] + m_f\bar{\psi}(x)\psi(x) \right\} \tag{3.19}$$

However, this version of the fermion action describes a theory with 2^d species of fermions with degenerate mass instead of a single species. This is called the fermion doubling problem, where the extra species of fermions are generated due to the exact chiral symmetry in the massless limit. This can be understood by looking at the U(1)-axial anomaly: This anomaly appears in the continuum limit due to the infinite number of degrees of freedom. It disappears on the lattice since the lattice only supports a finite number of degree of freedom. The extra species of fermions are generated to cancel the anomaly on the lattice. This argument suggests that one way of solving the doubling problem is to break the chiral symmetry explicitly. One simple way to do that is to add a Laplacian term into the action:

$$S_F^{\text{Wilson}} = S_F^{\text{naive}} - a^4 \frac{r}{2a} \sum_{x,\mu} \bar{\psi}(x) \left[U_\mu(x)\psi(x + a\hat{\mu}) + U_\mu^\dagger(x - a\hat{\mu})\psi(x - a\hat{\mu}) - 2\psi(x) \right] \tag{3.20}$$

This is called the Wilson action, and it solves the doubling problem by giving the extra species of fermion a divergent mass in the continuum limit. We don't use this action in this work, since the breaking of chiral symmetry makes our result less physical. Also, the chiral symmetry breaking will lead to extra operator mixing, making the calculation more complicated.

The action we use in this work is called the Domain Wall Fermion action. It introduces a fifth dimension with size L_s and can solve the doubling problem with an exponentially suppressed chiral symmetry breaking effect as we increase L_s. This action can be written as:

$$S_F^{\text{DWF}} = - \sum_{x,x',s,s'} \bar{\psi}(x,s) D^{\text{DWF}}(x,s;x',s')\psi(x',s') \tag{3.21}$$

$$D^{\text{DWF}}(x,s;x',s') = \delta_{s,s'} D^{\parallel}_{x,x'} + \delta_{x,x'} D^{\perp}_{s,s'} \tag{3.22}$$

$$D^{\parallel}_{x,x'} = \frac{1}{2} \sum_{\mu} \left[(1-\gamma_\mu) U_\mu(x) \delta_{x+\hat{\mu},x'} + (1+\gamma_\mu) U_\mu^\dagger(x') \delta_{x-\hat{\mu},x'} \right] + (M-4)\delta_{x,x'} \tag{3.23}$$

$$\begin{aligned} D^{\perp}_{s,s'} = & \frac{1}{2} \left[(1-\gamma_5)\delta_{s+1,s'} + (1+\gamma_5)\delta_{s-1,s'} - 2\delta_{s,s'} \right] \\ & - \frac{m_f}{2} \left[(1-\gamma_5)\delta_{s,L_s-1}\delta_{0,s'} + (1+\gamma_5)\delta_{s,0}\delta_{L_s-1,s'} \right] \end{aligned} \tag{3.24}$$

where the coordinate are in lattice units. Notice $D^{\parallel}_{x,x'}$ is actually the Wilson fermion Dirac operator with $r = 1$ and $M = -m_f$. Here M is called the domain wall height and satisfy $0 \le M \le 2$. This action results in a left-hand fermion mode that is bound to the $s = 0$ 4-dimensional boundary and a right-hand fermion mode that is bound to the $s = L_s - 1$ boundary. These two modes will decay exponentially along the fifth dimension, leading to the exponentially suppressed chiral symmetry breaking effect as we increase L_s. Despite the fact that we can not take L_s as infinite in the real calculation, one finds that the choice of $L_s = O(10)$ is large enough to neglect the residual chiral symmetry breaking effects. While suppressing the chiral symmetry breaking effects with the domain wall action, the introduction of the fifth dimension drastically increases the computational cost of the calculation.

3.4 G-parity Boundary Conditions

One more detail we should discuss here is the choice of the boundary conditions for the fermion field (the boundary conditions that the gauge field obeys depends on that for the fermion field). We always choose anti-periodic boundary conditions along the time direction. However, the choice of the boundary conditions along the spatial directions is more flexible and usually depends on the problem. For example, in most cases, we can choose the periodic boundary conditions, which is the simplest. In the previous $K \to \pi\pi_{I=2}$ calculation, we chose the anti-periodic boundary conditions for the down quark (this is called H-parity boundary conditions) to make the calculation easier.

In this work, where we want to measure the matrix elements for the $K \to \pi\pi_{I=0}$ decay, one important challenge is that, if we use periodic boundary conditions, the mass of the initial kaon state and the ground state energy of the final $\pi\pi$ state do not match. This suggests that we need to use multi-exponential fits to isolate an excited $\pi\pi$ state whose energy matches the kaon mass. This is difficult due to the presence of disconnected diagrams, which will introduce substantial statistical noise. The trick of using HPBC also fails here. Because of that, we will use new boundary conditions called G-parity boundary conditions(GPBC).

G-parity is defined as a product of charge conjugation and an isospin rotation by 180 degrees about the y-axis:

$$\hat{G} = \hat{C} e^{-i\pi \hat{I}_y} = e^{-i\pi \hat{I}_y} \hat{C}, \tag{3.25}$$

Notice pions are all G-parity odd, and if we impose GPBC for the quark field, the pions will satisfy anti-periodic boundary conditions. Because of that, their allowed momenta become odd-integer multiples of π/L, which would change the spectrum of the final $\pi\pi$ state, making it possible to tune the lattice parameters so that the ground state energy of the final $\pi\pi$ state matches the kaon mass.

It can be shown that the gauge and translational invariance of the action requires that the gauge field $U_\mu(x)$ satisfy complex conjugate boundary conditions as:

$$U_\mu(x+L) = U_\mu(x)^*. \tag{3.26}$$

In the following discussion we introduce a new notation where the field operators u, d and their conjugates are reorganized into two-component vectors for convenience:

$$\Psi = \begin{pmatrix} d \\ C\bar{u}^T \end{pmatrix} \tag{3.27}$$

$$\bar{\Psi} = (\bar{d}, u^T C), \tag{3.28}$$

where C is the 4×4 charge conjugation matrix. We will refer to the indices of these vectors as flavor indices. It can be shown that this notation makes the application of a G-parity transformation simpler:

$$\Psi(x+L_x) = \hat{G}\Psi(x)\hat{G}^{-1} = i\sigma_2\Psi(x), \tag{3.29}$$

$$\bar{\Psi}(x+L_x) = \hat{G}\bar{\Psi}(x)\hat{G}^{-1} = \bar{\Psi}(x)(-i\sigma_2), \tag{3.30}$$

where σ_2 is the second Pauli matrix. The relation between the new notation and the usual two-component quark field can be written as:

$$q = \begin{pmatrix} u \\ d \end{pmatrix} = F_{12}C\bar{\Psi}^T + F_{21}\Psi, \tag{3.31}$$

$$\bar{q} = \begin{pmatrix} \bar{u} \\ \bar{d} \end{pmatrix} = \Psi^T C F_{21} + \bar{\Psi}F_{12}, \tag{3.32}$$

$$\Psi = F_{12}q + F_{21}C\bar{q}^T, \tag{3.33}$$

$$\bar{\Psi} = \bar{q}F_{21} + q^T C F_{12}, \tag{3.34}$$

where

$$F_{12} = \begin{pmatrix} 0 & 1 \\ 0 & 0 \end{pmatrix} = \frac{1}{2}(\sigma_1 + i\sigma_2) \qquad\qquad F_{21} = \begin{pmatrix} 0 & 0 \\ 1 & 0 \end{pmatrix} = \frac{1}{2}(\sigma_1 - i\sigma_2) \tag{3.35}$$

For later use we also define the following two matrices:

$$F_0 = \begin{pmatrix} 1 & 0 \\ 0 & 0 \end{pmatrix} = \frac{1}{2}(1 + \sigma_3) \qquad\qquad F_1 = \begin{pmatrix} 0 & 0 \\ 0 & 1 \end{pmatrix} = \frac{1}{2}(1 - \sigma_3) \tag{3.36}$$

The strange quark is introduced into the G-parity framework as a member of an isospin doublet that includes a fictional degenerate partner, s'. Note that this fictional s' should be suitably weighted out of the path integral to ensure that we are doing a physical $2 + 1$ flavor calculation instead of an unphysical $2 + 2$ flavor calculation, cf. Ref. [16]. Similar to Eq. (3.27) and (3.28), we define the following two-component vector:

$$\Psi_H = \begin{pmatrix} s \\ C\bar{s}'^T \end{pmatrix} \tag{3.37}$$

$$\bar{\Psi}_H = (\bar{s}, s'^T C) \tag{3.38}$$

With these definitions, we can write down the phase conventions for the meson states we use in our calculation:

$$|\pi^+\rangle = \frac{i}{2}\psi^T(\gamma_5\sigma_1 C)\psi|0\rangle \qquad \langle\pi^+| = \langle 0|\frac{i}{2}\bar{\psi}(\gamma_5\sigma_1 C)\bar{\psi}^T \tag{3.39}$$

$$|\pi^-\rangle = -\frac{i}{2}\bar{\psi}(\gamma_5\sigma_1 C)\bar{\psi}^T|0\rangle \qquad \langle\pi^-| = -\langle 0|\frac{i}{2}\psi^T(\gamma_5\sigma_1 C)\psi \tag{3.40}$$

$$|\pi^0\rangle = -\frac{i}{\sqrt{2}}\bar{\psi}\sigma_3\gamma_5\psi|0\rangle \qquad \langle\pi^0| = -\langle 0|\frac{i}{\sqrt{2}}\bar{\psi}\sigma_3\gamma_5\psi \tag{3.41}$$

$$|K^{0\prime}\rangle = \frac{i}{\sqrt{2}}(\bar{\psi}\gamma_5\psi_H)|0\rangle \qquad \langle K^{0\prime}| = \langle 0|\frac{i}{\sqrt{2}}(\bar{\psi}_H\gamma_5\psi) \tag{3.42}$$

$$\overline{|K^{0\prime}\rangle} = -\frac{i}{\sqrt{2}}(\bar{\psi}_H\gamma_5\psi)|0\rangle \qquad \overline{\langle K^{0\prime}|} = -\langle 0|\frac{i}{\sqrt{2}}(\bar{\psi}\gamma_5\psi_H) \tag{3.43}$$

$$|\sigma\rangle = \frac{1}{\sqrt{2}}\bar{\psi}\psi|0\rangle \qquad \langle\sigma| = \langle 0|\frac{1}{\sqrt{2}}\bar{\psi}\psi \tag{3.44}$$

It is worth mentioning that the kaon states in Eq. (3.42) and (3.43) are different from the usual definition of the kaon due to the inclusion of the fictional s' operator. It is easy to verify that after including the s' operator, the new kaon operator, $K^{0\prime}$, satisfies periodic boundary conditions, suggesting that the ground state kaon is stationary. This is important in our calculation since we want our initial and final states to have zero total momentum. For more details on performing lattice simulations with G-parity boundary conditions including further discussion of the lattice symmetries and the treatment of the strange quark, we refer the reader to Ref. [13]. Also notice that these expressions are not exactly the expression we use to construct the interpolating operators on the lattice. The detailed expression for the interpolating operator will be discussed in Sec. 4.1. For the remainder of this section we will focus specifically on how these boundary conditions affect the measurement of the two-pion system.

Including GPBC introduces some significant differences from a calculation with periodic boundary conditions(PBC). Three significant differences might be identified. First, the $\pi\pi$ states that can be studied with these two types of boundary condition will be different. When non-interacting pions satisfy anti-periodic boundary conditions in all three directions, their allowed momenta become $(2n_1+1, 2n_2+1, 2n_3+1)\frac{\pi}{L}$, where n_i are integers. These are different from those on a volume with PBC, where the allowed momenta are $(2n_1, 2n_2, 2n_3)\frac{\pi}{L}$. However, if we take advantage of moving frames, there is still a correspondence between the states that we can construct on a PBC volume and those present for a volume obeying GPBC. For example, if we wish to work with a $\pi\pi$ state comprising two pions at rest, for a volume with PBC we can do the calculation in the stationary frame, where the two component pion operators are constructed with zero momentum. However, for a GPBC volume the calculation can be performed in a moving frame where both pions have the same momentum, *e.g.* $(\pi/L, \pi/L, \pi/L)$. With this choice, in the center-of-mass frame these two pions are at rest.

Since a moving frame calculation relies on a distorted volume which doesn't have cubic symmetry, there will be lower angular momentum partial waves whose phase shifts will enter the quantization condition that determines the s-wave phase shift, *e.g.* d-waves. In the stationary frame the lowest partial waves that enter beyond the s-wave are those with with $l = 4$. Fortunately in this work the interaction energies involved in our moving frame calculations are relatively small (around the kaon mass), and those higher partial waves that enter will have a negligible effect on the s-wave phase shift.

A second troublesome aspect of G-parity is the breaking of cubic symmetry at the quark level even for a lattice with cubic symmetry. As discussed in Ref. [13] there is a sign convention that can be chosen when G-parity is imposed in one direction that can be changed by changing the relative sign of the up and down quark fields. However, the choice of this sign in the remaining two directions is not conventional and breaks cubic symmetry by identifying one of the four diagonals connecting two corners of the cubic lattice and passing through its center. For a cubic volume in a stationary frame, the symmetry group is broken down from O_h to D_{3d} [18]. Because of confinement, we believe that this breaking of cubic symmetry has only exponentially suppressed effects on the QCD transfer matrix. However, the quark-level operators used to construct the QCD eigenstates are affected and care must be taken when constructing translationally covariant operators to suppress the creation of finite-volume states belonging to unwanted representations of the cubic symmetry group O_h. This will be discussed when we write out the explicit form of these operators in Sec. 4.1 and the remaining cubic-symmetry breaking effects are discussed in Sec. 5.4.

Finally around-the-world effects in a moving frame will be different in a volume with GPBC compared to one with PBC. When we are performing a moving frame calculation in a volume with GPBC with one of the three smallest allowed total momenta (those with $P_{\text{tot}} = (\pm 2, 0, 0)$, $(\pm 2, \pm 2, 0)$ or $(\pm 2, \pm 2, \pm 2)$ in units of π/L), the first-order around-the-world contribution will come from a single pion propagating from one $\pi\pi$ interpolating operator to the second (leg A) and a second single pion propagating from the second, through the time boundary to the first (leg B). This behavior is shown schematically as part of a later more detailed discussion in Figure 5.4.

For GPBC the momentum injected by each $\pi\pi$ interpolating operator can change the direction but not the magnitude of the momentum carried by the pion as it moves from leg A to leg B. Thus, for GPBC this around-the-world pion can carry the same energy on each leg and so that its contribution behaves as a constant when the time separation between the two operators is changed. We refer to this case where the pions in both legs carry momenta of minimum magnitude as the "first-order" around-the-world effect. The case in which the pion propagating in one of the legs carries momentum greater than the minimum is termed "second-order". Both cases are considered when performing the fits described in Section 5.2.2. In contrast, for the three smallest non-zero total momenta in a calculation with periodic boundary conditions all of the around-the-world terms will be time-dependent since the pions in the two legs will have different energies.

3.5 Gauge Ensembles

In this work for both the $\pi\pi$ scattering and $K \longrightarrow \pi\pi$ calculation, we employ a single $32^3 \times 64$ lattice with 2+1 flavors of Möbius DWF with $L_s = 12$ and Möbius parameters $b + c = 32/12$ and $b - c = 1$ and light and strange quark masses of 1×10^{-4} and 0.045, respectively. The Möbius DWF is an improved version of DWF, which decreases L_s while keeping the chiral symmetry breaking effects the same[19]. We take the square root of the 2-flavor version of the heavier quark determinant in Eq. (3.12) to ensure that we are doing the physical 2+1 flavor calculation, and further detail can be found in [13]. We use Iwasaki+DSDR gauge action with $\beta = 1.75$, corresponding to an inverse lattice spacing of $a^{-1} = 1.3784(68)$GeV [20]. The dislocation suppressing determinant ratio

(DSDR) factor reduces the dislocations or tears in the gauge field that enhance chiral symmetry breaking at coarse lattice spacings [21, 22, 23, 24]. It enables us to work with a large, $(4.6\text{ fm})^3$ spatial volume and therefore has good control over finite-volume systematic errors, without a dramatic increase in computational cost, albeit at the cost of increased discretization errors. We use G-parity boundary conditions (GPBC) in all three spatial directions in order to obtain nearly physical kinematics for the $K \to \pi\pi$ decay, where the $\pi\pi_{I=0}$ ground state energy matches the kaon mass. It should be mentioned here that, in principle, GPBC can also be used to do the $K \to \pi\pi_{I=2}$ calculation, but we can not use the same lattice to do both calculations. This is because the interaction between two pions is attractive in $\pi\pi_{I=0}$ ground state, while it is repulsive in $\pi\pi_{I=2}$ ground state, which makes the two energies different. Since we tune the lattice parameter so that the $\pi\pi_{I=0}$ ground state energy matches the kaon mass, the $\pi\pi_{I=2}$ ground state energy is different from the kaon mass. This will be shown in Sec. 5.2.

In order to rapidly improve the statistical precision of our calculation, we generated configurations via seven independent Markov chains, each originating from widely separated configurations in our original thermalized ensemble. To compensate for any residual effects of the random number error, we discarded the first 20 configurations of each stream. Subsequent algorithmic improvements, particularly the introduction of the exact one-flavor algorithm (EOFA) [25, 26] further enhanced our rate of generation such that we have completed over 5000 MD time units to date. In this work, with a measurement separation of 4 molecular dynamics time units (MDTU), the measurement is performed on 741 configurations.

Chapter 4: Measurement

In this section we start by describing the details of the interpolating operators we use in this calculation. The introduction of GPBC suggests that we need to deal with the cubic symmetry breaking carefully. We then discuss the matrix of two-point correlation functions, which is important in understanding the fitting strategies in Chapter 5 and 6. Next we list the contraction diagrams for the $\pi\pi$ scattering calculation. Those diagrams for the $K \to \pi\pi$ calculation will be shown in Chapter 6. In the final section we outline the resampling methods used to determine statistical errors and an improved method to assign a p-value to those fits.

4.1 Interpolating Operators

Here we discuss the structure of the interpolating operators used in this work. There are two different types of two-pion interpolating operators. The first type are denoted as “$\pi\pi(\ldots)$" operators and are constructed as the product of two single-pion interpolating operators and for which the parentheses and the quantity contained within are used both to specify the pion momenta and to distinguish these labels from the general set of $\pi\pi$ interpolating operators which can produce two pions when acting on the vacuum, the set in which all of our operators reside. The second type has the form of a quark-bilinear scalar sigma operator which shares the same quantum number as $I = 0$ $\pi\pi$ state. We start by constructing the single pion and sigma interpolating operators with momentum $\vec{P} = \vec{p} + \vec{q}$, where $\vec{p}$ and $\vec{q}$ are the momenta of the individual quarks:

$$\pi^+(t,\vec{P}) = \sum_{\vec{x},\vec{y}} e^{-i(\vec{p}\cdot\vec{x}+\vec{q}\cdot\vec{y})} h(|\vec{x}-\vec{y}|)\Psi^T(\vec{x},t)\frac{1}{2}(1-e^{in_p\pi}\sigma_2)\frac{i}{2}\gamma^5 C\sigma_1(1+e^{in_q\pi}\sigma_2)\Psi(\vec{y},t) \tag{4.1}$$

$$\pi^-(t,\vec{P}) = \sum_{\vec{x},\vec{y}} e^{-i(\vec{p}\cdot\vec{x}+\vec{q}\cdot\vec{y})} h(|\vec{x}-\vec{y}|)\overline{\Psi}(\vec{x},t)\frac{1}{2}(1-e^{in_p\pi}\sigma_2)\frac{-i}{2}\gamma^5 C\sigma_1(1+e^{in_q\pi}\sigma_2)\overline{\Psi}^T(\vec{y},t) \tag{4.2}$$

$$\pi^0(t,\vec{P}) = \sum_{\vec{x},\vec{y}} e^{-i(\vec{p}\cdot\vec{x}+\vec{q}\cdot\vec{y})} h(|\vec{x}-\vec{y}|)\overline{\Psi}(\vec{x},t)\frac{1}{2}(1-e^{in_p\pi}\sigma_2)\frac{-i}{\sqrt{2}}\gamma^5 \sigma_3(1+e^{in_q\pi}\sigma_2)\Psi(\vec{y},t) \tag{4.3}$$

$$\sigma(t,\vec{P}) = \sum_{\vec{x},\vec{y}} e^{-i(\vec{p}\cdot\vec{x}+\vec{q}\cdot\vec{y})} h(|\vec{x}-\vec{y}|)\overline{\Psi}(\vec{x},t)\frac{1}{2}(1-e^{in_p\pi}\sigma_2)\frac{1}{\sqrt{2}}(1+e^{in_q\pi}\sigma_2)\Psi(\vec{y},t) \tag{4.4}$$

where, using the notation in Sec. 3.4, Ψ and $\overline{\Psi}$ are the quark and anti-quark isospin doublets defined as:

$$\Psi = \begin{pmatrix} d \\ C\bar{u}^T \end{pmatrix} \quad \text{and} \quad \overline{\Psi} = (\bar{d}, u^T C). \tag{4.5}$$

As explained in Ref. [13] the 2×2 flavor projection matrix $(1+e^{in_q\pi}\sigma_2)$ ensures that the quark field $\sum_{\vec{x}}(1+e^{in_q\pi}\sigma_2)e^{-i\vec{q}\cdot\vec{x}}\Psi(x)$ transforms as an eigenstate under translations (including positions which translate through the boundaries) if the integer $n_q = Lq_i/\pi - 1/2$ for all three components $\{q_i\}_{1\le i\le 3}$ of the momentum vector $\vec{q}$. Here C is the 4×4 charge conjugation matrix and $h(|\vec{x}|)$ is the meson smearing function. In this work, we choose all the smearing functions to be the $1s$ hydrogen wave function $h(x) = e^{-x/r}$, with a radius $r = 2$ for both the pion and sigma operators. This smearing function is introduced to increase the overlap between the pion and sigma interpolating operators and the lattice pion and $\pi\pi$ ground states while at the same time reducing the overlap of the $I = 0$ $\pi\pi$ operator with the vacuum state. In earlier studies this smearing was found to give a two-fold reduction in statistical errors [14].

Following Sec. 3.4, a stationary (G-parity even) kaon-like state can be constructed as

$$|\tilde{K}^0\rangle = \frac{1}{\sqrt{2}}\left(|K^0\rangle + |K'^0\rangle\right), \tag{4.6}$$

where K^0 is the physical kaon and K'^0 a degenerate partner with quark content $\bar{s}'u$. This $|\tilde{K}^0\rangle$ state can be created using the following operator

$$O_{\tilde{K}^0}(t) = \frac{i}{\sqrt{2}}\sum_{\vec{x},\vec{y}} e^{i\vec{p}\cdot(\vec{x}-\vec{y})}\overline{\psi}_l(\vec{x},t)\gamma^5 h(|\vec{x}-\vec{y}|)\frac{1}{2}(1+\sigma_2)\psi_h(\vec{y},t) \tag{4.7}$$

where $\vec{p} = (1,1,1)\frac{\pi}{2L}$ is the quark momentum and $h(x)$ is the same meson smearing function defined above.

With the operators constructed above, we use the all-to-all (A2A) propagator technique [27] to perform the measurements. The A2A technique divides the quark propagator into an exact low mode contribution which we can calculate using the Lanczos algorithm and a high mode contribution which can be accessed using stochastic approximation. In our calculation, we choose the number of low mode eigenvectors to be 900 for the up and down quark, and 0 for the strange quark. For the high mode contribution, we perform spin, color, flavor and time dilution (*i.e.* we perform a separate inversion for each of the 24 colors, spins and flavors for each time slice). We use the same spatial field of random numbers for these 24 inversions but a different such field for each time slice [14]. We choose the number of random hits to be 1 (*i.e.* we use only a single random field on each time slice) since increasing it does not reduce the uncertainty [14].

We will work with two groups of pion operators. The first is labeled as $\pi(111)$ with 8 different operators. These operators create pions carrying momenta $(\pm\pi/L, \pm\pi/L, \pm\pi/L)$. The second group is labeled as $\pi(311)$ and contains 24 different operators. For this group one of the momentum components is replaced by $\pm 3\pi/L$.

We then combine two of these single-pion interpolating operators to construct $\pi\pi(\vec{p},\vec{q})$ operators with momenta $\vec{P} = \vec{p} + \vec{q}$, where now $\vec{p}$ and $\vec{q}$ are the momenta of the individual pions:

$$O^{\alpha,\beta}_{\pi\pi}(t,\vec{p},\vec{q}) = \pi^{\alpha}(t+4,\vec{p})\pi^{\beta}(t,\vec{q})\,, \tag{4.8}$$

where α and β are isospin indices. As suggested by this equation, when we construct the $\pi\pi(\vec{p},\vec{q})$ operators, we separate the two single-pion operators in the time direction by 4 units. This suppresses the statistical error from the disconnected diagrams (the V diagram below) by a factor of two in the $I = 0$ channel [28]. For consistency, when we construct the $I = 2$ $\pi\pi(\ldots)$ operators, we also separate the two pion operators by 4 units in the time direction.

4.1.1 Momentum decomposition

The cubic symmetry breaking mentioned in Section 3.4 manifests as differences in the couplings between interpolating operators and meson states whose momenta are related by cubic rotations (the energies themselves are not affected). In order to obtain $\pi\pi$ interpolating operators that respect the cubic symmetry and that can therefore be related to the continuum s-wave states, it is vital that we control this symmetry breaking. In Ref. [13] it was demonstrated that the cubic symmetry breaking in the pion states can be heavily suppressed by averaging over pairs of pion interpolating operators of the same total momenta but with different assignments of quark momenta. We apply this technique for the present work and extend it to include the sigma operator. The two quark and anti-quark momentum pairs for each pion momentum are listed in Appendix A. In Section 5.4 we carefully analyze our data in order to account for any residual cubic symmetry breaking effects as a systematic error.

In evaluating the Wick contractions it is often convenient to utilize the γ^5-hermiticity of the quark propagator $\mathcal{G}$:

$$\gamma^5[\mathcal{G}(x,y)]^\dagger\gamma^5 = \mathcal{G}(y,x)\,, \tag{4.9}$$

where the dagger (†) indicates the hermitian conjugate of the matrix in its spin, color and flavor indices, in order to exchange the source and sink for a particular quark propagator. It is worth mentioning here that γ^5-hermiticity is not an exact symmetry between the A2A approximations to the quark propagators used here because of the asymmetric treatment of the source and sink in the A2A approach. A further implication of our use of γ^5-hermiticity to combine related contractions arises from the effective exchange of the $\bar{q}$ and q operators appearing in a meson field when γ^5-hermiticity is used on both the propagator leaving $\bar{q}$ and that arriving at q. By symmetrizing over the assignments of momenta to the $\bar{q}$ and q factors in each meson field, we insure that this use of γ^5-hermiticity does not result in a different amplitude. This determines the final pion interpolating operator we use: for each pion momentum we average over a total of four quark and anti-quark momentum assignments. For the sigma operator, since it satisfies PBC and has zero momentum we average over the eight different quark momentum assignments that are listed in Appendix A to suppress cubic symmetry breaking. (Note: this symmetrical treatment of the quark and anti-quark components of the meson field implies that the contractions presented in Refs. [14] and [16] for the case of a local pion interpolating operator can be unambiguously extended to the case of a non-local meson field.)

4.1.2 Total momentum

We perform both a stationary-frame calculation where the total two-pion momentum is zero and moving-frame calculations for which the total momentum is non-zero. In the stationary-frame calculation we include the scalar σ operator for the $I = 0$ channel and for both isospin channels two classes of bilinear pair "$\pi\pi(\ldots)$" operators: One class has both pions in the group $\pi(111)$ but with opposite momenta, which we label $\pi\pi(111, 111)$. The second class is made up of pions in the group $\pi(311)$, again with opposite momenta and are labeled $\pi\pi(311, 311)$.

In the moving frame calculation we can also construct a $\pi\pi(111, 311)$ operator for which the constituent pion operators belong to the two different groups described above. For the present work we did not collect data using a sigma operator with non-zero momentum; however the analysis presented in the following sections suggests the inclusion of this operator may be beneficial in future work. In summary, we therefore have three different classes of operators in the moving-frame calculation for each isospin channel, as well as in the stationary frame $I = 0$ channel and only two classes of operators in the stationary-frame, $I = 2$ calculation. (Note: our notation distinguishing the two-pion interpolating operators does not specify the total momentum that they carry which must be determined from the context.)

4.1.3 Angular momentum

After identifying numerous $\pi\pi$ operators with different total momenta, the next step is to project those $\pi\pi$ operators onto angular momentum eigenstates. In this work we are interested in only the s-wave phase shift but we will also use d-wave states to estimate the size of cubic symmetry breaking in Section 5.4. The angular momentum l indexes the irreducible representations of the continuum SO(3) Lie group, but the lattice (assuming we have successfully overcome the cubic symmetry breaking) is symmetric under only a discrete subgroup of SO(3): either the cubic group for the stationary frame or a smaller, related group in the case of the moving frame for which relativistic length contraction alters the shape of the finite volume when viewed from the perspective of the center of mass frame. In order to generate angular momentum eigenstates on the lattice we must therefore establish a mapping from the irreducible representations Γ of the discrete lattice symmetry group G to those of SO(3), from which, given a desired value of l, we can determine an appropriate choice of irreducible representation of G in which to construct our lattice operators. In general this mapping is one-to-many such that to each representation Γ of G there corresponds a set $S(G,\Gamma)$ of values of l to which it corresponds in the SO(3) group. As such there are usually several representations which satisfy this condition, and we want to choose the one that is the simplest and which couples to the fewest other values of l, *i.e.* for which the set $S(G,\Gamma)$ is the smallest. For example, we can always use the maximally symmetric representation (A_1) to obtain the s-wave phase shift. For d-wave states in the stationary frame, we can use the T_2 representation [18].

The second step is to construct an operator in the representation Γ by combining the operators in one of the classes described above using the characters of Γ. The detailed procedure is as follows:

$$O^{\alpha\beta}_{\pi\pi,\Gamma,i}(\vec{P},t) = \sum_{\hat{T}\in G} \chi_\Gamma(\hat{T}) O^{\alpha\beta}_{\pi\pi,i}(t+4,t,\frac{\vec{P}}{2}+\hat{T}[\vec{p}\,],\frac{\vec{P}}{2}-\hat{T}[\vec{p}\,])\,. \tag{4.10}$$

Here $\hat{T}[\vec{p}\,]$ means we apply symmetry operation $\hat{T}$ on momentum $\vec{p}$. We sum over all elements $\hat{T}$ of the finite-volume symmetry group G, $\vec{P}$ is the total momentum, and $\chi(\hat{T})$ is the character of each group element $\hat{T}$ in the representation Γ. We choose $\vec{p}$ so that all the $\pi\pi$ operators appearing in the sum belong to the i^{th} class. After projection, for each total momentum $\vec{P}$, instead of having three or two classes of $\pi\pi$ operators, we will only have three or two $\pi\pi$ operators, each transforming under a specific representation of G and constructed from the operators within that class. Henceforth we will use the labels $\pi\pi(111,111)$, $\pi\pi(111,311)$, $\pi\pi(311,311)$ to refer to those projected operators rather than to the classes from which they were constructed.

In the moving-frame calculations reported here, due to the limited number of classes (two) of single pion operators, we are only able to focus on the three sets of non-zero total momenta $\vec{P}$ with the smallest individual components: $\vec{P} = (\pm 2, 0, 0)\frac{\pi}{L}, (\pm 2, \pm 2, 0)\frac{\pi}{L}$ and $(\pm 2, \pm 2, \pm 2)\frac{\pi}{L}$, so that the number of different classes of $\pi\pi$ operators we construct on the lattice is more than one (three in this work).

4.2 Matrix of two-point correlation functions

We begin a discussion of the correlation functions using a single operator constrained to a single timeslice (recall our $\pi\pi(\ldots)$ operators have the pion bilinears on separate timeslices). For isospin I the two-point $\pi\pi$ correlation function is determined by the Euclidean Green's function

$$C^I(t_{snk}, t_{src}) = \langle O^{I\dagger}_{\pi\pi}(t_{snk}) O^I_{\pi\pi}(t_{src}) \rangle \,, \tag{4.11}$$

where $\langle \ldots \rangle$ indicates the expectation value from a Euclidean-space Feynman path integral, performed in a finite spatial volume of side L and time extent T, obeying periodic boundary conditions for the gauge field but anti-periodic boundary conditions for the fermion fields in the time direction and G-parity boundary conditions in the three spatial directions.

Here and in our two earlier papers [13, 16] the hermitian conjugate which appears on the left-hand operator in Green's functions such as shown in Eq. (4.11) requires some explanation. For the case that the operator involves Euclidean fields evaluated at a single time, the hermitian conjugate represents a combination of path integral field variables which corresponds to the Hermitian conjugate of the indicated operator in the time-independent Schrödinger picture which is subsequently transformed to the time-dependent Heisenberg picture operator whose expectation values are described by a Euclidean path integral. For the case that the operator $O^I_{\pi\pi}$ is itself the product of two such operators evaluated at different times, each operator is to be interpreted in this fashion. In this case the two operators appearing in this pair are always symmetrized to insure that the resulting two-point functions are positive as this notation suggests in spite of the fact that their order is not exchanged by this prescription.

By inserting two complete sets of intermediate states, we can rewrite this two-point function as

$$\begin{aligned} C^I(t_{snk}, t_{src}) = &\langle\pi|O^{I\dagger}_{\pi\pi}|\pi\rangle\langle\pi|O^I_{\pi\pi}|\pi\rangle e^{-tE_{\pi,in}} e^{-(T-t)E_{\pi,out}} \\ &+ \langle 0|O^{I\dagger}_{\pi\pi}|\pi\pi\rangle\langle\pi\pi|O^I_{\pi\pi}|0\rangle e^{-tE_{\pi\pi}} \\ &+ \langle\pi\pi|O^{I\dagger}_{\pi\pi}|0\rangle\langle 0|O^I_{\pi\pi}|\pi\pi\rangle e^{-(T-t)E_{\pi\pi}} \\ &+ \langle 0|O^{I\dagger}_{\pi\pi}|0\rangle\langle 0|O^I_{\pi\pi}|0\rangle\delta_{I,0} \end{aligned} \tag{4.12}$$

in the limit where both $t \equiv t_{snk} - t_{src}$ and $T - t$ are large so that we can neglect the contribution from excited intermediate states. Notice the first term describes the "around-the-world effect", which is exponentially suppressed in T. Here $E_{\pi,in}$ and $E_{\pi,out}$ are the energies of the pions propagating from the source along the positive and negative time directions, respectively. These two energies should be the same in a stationary frame calculation but they may be different for a moving frame. The second and third terms, which can be combined together into a cosh function of the time separation t, describe the ground state $\pi\pi$ scattering, one for the forward propagating $\pi\pi$ along the time direction and the other for the backward propagating case. The last term, which describes the contribution of the vacuum intermediate state, appears only in the $I = 0$ channel and does not describe the physics of $\pi\pi$ scattering. This term is the largest source of statistical error because it is time-independent and therefore results in a decreasing signal-to-noise ratio as we increase the time separation t to suppress excited state contamination.

In practice, due to the rapid reduction in signal-to-noise ratio and the finite temporal extent of the lattice it is necessary to include data in the region where t or $T - t$ is not very large. By including data from smaller time separations our results will be affected by contamination from excited-states. One way to suppress these errors is to expand the sum over intermediate states in Eq. (4.12) to include not only the ground state but also one or more excited states and then to fit using this more complicated expression. However, even if we only include one more state, performing such a multi-state fit may be difficult using a single interpolating operator since we are attempting to determine an increasing number of parameters purely from the time dependence of data with a rapidly falling single-to-noise.

While increasing statistics will ultimately allow the various states to be isolated, a far more powerful technique is to introduce additional interpolating operators which all share the same quantum numbers and therefore project onto the same set of states, albeit with different coefficients. While naively equivalent to increasing statistics, the additional operators actually introduce a wealth of new information that helps constrain the fit. This additional information can also be exploited more directly using the GEVP technique (described in more detail in Section 5.2) whereby the energies of N states can be obtained from Green's functions comprising N operators using only three timeslices. A simpler method which allows for the detection of the presence of excited states using data from only a single timeslice by looking at the "normalized determinant" will be discussed in Section 5.2.

In order to perform a stable fit where both ground and excited states are included, we introduce additional interpolating operators which all share the same quantum numbers so that the number of operators can be larger than or equal to the number of states included in the fit. Thus, we consider the matrix of two-point correlation functions:

$$C^I_{ij}(t_{snk}, t_{src}) = \langle O^{I\dagger}_i(t_{snk}) O^I_j(t_{src})\rangle \,, \tag{4.13}$$

where indices i and j distinguish the operators. We can then expand Eq. (4.13) to include excited-state contributions:

$$\begin{aligned} C^I_{ij}(t_{snk}, t_{src}) = {} & \langle\pi|O^{I\dagger}_i|\pi\rangle\langle\pi|O^I_j|\pi\rangle e^{-tE_{\pi,in}} e^{-(T-t)E_{\pi,out}} \\ & + \sum_{n=0}^{m} \left\{ \langle 0|O^{I\dagger}_i|n\rangle\langle n|O^I_j|0\rangle e^{-tE_n} + \langle n|O^{I\dagger}_i|0\rangle\langle 0|O^I_j|n\rangle e^{-(T-t)E_n} \right\} \\ & + \langle 0|O^{I\dagger}_{\pi\pi}|0\rangle\langle 0|O^I_{\pi\pi}|0\rangle \delta_{I,0} \,. \end{aligned} \tag{4.14}$$

Now the excited state contamination error has been reduced since the lightest state that we neglect is the one with energy E_{m+1}, which is higher than E_1, the energy of the first state that we neglected in Eq. (4.12). For simplicity in the discussion above we have identified a single time $t_{snk/src}$ that is associated with each two-pion operator. However, these operators are constructed from two, single-pion operators evaluated at the times $t_{snk/src}+4$ and $t_{snk/src}$ as shown in Eq. (4.10). In the remainder of this paper we will use the variable $t = t_{snk} - t_{src} - 4$ to describe the separation between the two operators which indicates a minimum distance of propagation needed to connect the two, two-pion operators.

Assuming that the fit is able to reliably obtain the parameters then clearly the larger number of states that are included in the fit, the smaller the resulting excited state contamination. However, given the added computational cost and resulting fit complexity, we should be careful to include only operators which help to distinguish the relevant excited states. An important criterion, discussed later, is the degree to which the operators introduced overlap with the state being studied or a common set of excited states.

4.3 Contraction diagrams for $\pi\pi$ scattering

We are interested in the scattering process for specific isospin channels. The $I = 0$ and $I = 2$ $\pi\pi$ state with $I_z = 2$ can be constructed from π^+, π^-, π^0 states as below:

$$|I=2, I_z=2\rangle = |\pi^+\rangle|\pi^+\rangle \tag{4.15}$$

$$|I=0, I_z=0\rangle = \frac{1}{\sqrt{3}}\left\{|\pi^+\rangle|\pi^-\rangle - |\pi^0\rangle|\pi^0\rangle + |\pi^-\rangle|\pi^+\rangle\right\}\ . \tag{4.16}$$

The matrix of two-point correlation functions for the $\pi\pi$ and σ operators can be obtained from a linear combination of eight different diagrams, labeled as C, D, R, V, $C_{\sigma\pi\pi}$, $V_{\sigma\pi\pi}$, $C_{\sigma\sigma}$ and $V_{\sigma\sigma}$, each corresponding to a particular Wick contraction that is identified in Fig. 4.1. Their definition in terms of quark propagator is given in Appendix C. They can be combined to obtain the two-point

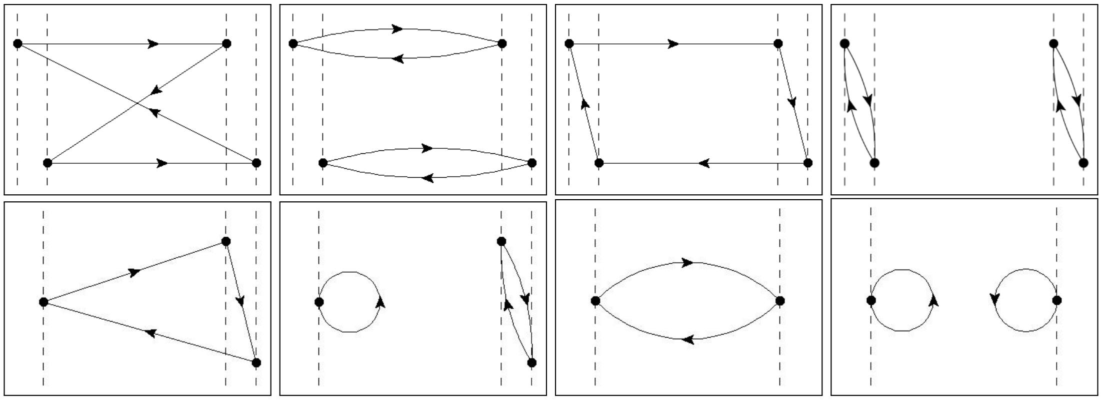

Figure 4.1: Diagrams showing the contractions which contribute to the two-point functions involving the $\pi\pi(\ldots)$ and σ operators. The solid dots indicate the positions of the pion two-quark operators and the dotted vertical lines passing through these points indicate the separate 3-dimensional time slices on which these operators are placed, with the nearby pairs of lines separated by four time units as described in Eq. (4.10). Identical diagrams appear for the σ operator only with a single vertical line at the source and/or sink, with the dots now representing the scalar bilinear. The top 4 diagrams are labeled by C, D, R and V diagrams from left to right, and the lower 4 diagrams are labeled by $C_{\sigma\pi\pi}$, $V_{\sigma\pi\pi}$, $C_{\sigma\sigma}$ and $V_{\sigma\sigma}$ from left to right.

correlation functions as follows:

$$\begin{aligned} \langle \pi\pi(t)\pi\pi(0)\rangle^{I=2} &= 2D - 2C \\ \langle \pi\pi(t)\pi\pi(0)\rangle^{I=0} &= 2D + C - 6R + 3V \end{aligned} \tag{4.17}$$

$$\begin{aligned} \langle \sigma(t)\sigma(0)\rangle &= \frac{1}{2}V_{\sigma\sigma} - \frac{1}{2}C_{\sigma\sigma} \\ \langle \sigma(t)\pi\pi(0)\rangle &= \frac{\sqrt{6}}{4}V_{\sigma\pi\pi} - \frac{\sqrt{6}}{2}C_{\sigma\pi\pi}\,. \end{aligned} \tag{4.18}$$

If we were to perform the contractions for each of the different total momenta by substituting Eq. (4.10) into Eqs. (4.17) and (4.18), the number of different contractions to be evaluated for each gauge configuration would be 7848, which is unnecessarily large. The technique which we employ to reduce the number of momentum combinations takes advantage of three kinds of symmetry in $\pi\pi$ scattering: parity symmetry, which corresponds to changing each momentum from $\vec{p}$ to $-\vec{p}$, axis permutation symmetry, which permutes the three coordinate axes and an “auxiliary-diagram” symmetry, which relies on the combination of γ_5 hermiticity and the “around-the-world” contraction to show that two diagrams whose source and sink momenta satisfy a special relation are identical (For more details about the "auxiliary-diagram" symmetry, we refer readers to Ref. [29]). Using a subset of the gauge configurations in this study, we have found that excluding all but one of the momentum combinations that are related by these three symmetries does not increase the statistical error for the measured $\pi\pi$ energy. This strategy substantially reduces the number of momentum combinations from 7848 to 1037 [29].

4.4 Estimating statistical errors and goodness of fit

In this paper we use multi-state correlated fits to determine the energies of each state and the overlap amplitudes between the different states and operators. The fitting procedure is flexible, e.g. we can perform a fit where the number of operators and states are different and we can perform a "frozen fit" where some of the parameters are held fixed during the fit, which is useful in the excited-state error analysis. An important benefit of our fitting procedure is our ability to calculate a p-value, which is a measure of how well our data matches with our theoretical expectation for the time dependence of the two-point function being analyzed.

However, the determination of statistical errors and the calculation of a p-value are not straightforward. Not only are we performing a correlated fit where the covariance matrix is itself determined by the data and therefore has its own, often substantial uncertainties, but there are autocorrelations between configurations, since the sampling interval between neighboring configurations used in our analysis is comparable to or smaller than the autocorrelation time which separates truly independent samples. While our number of samples, 741, is relatively large compared to many lattice calculations, if we group these samples into bins of two or four and thereby reduce the autocorrelations between these binned samples, the resulting decrease in the effective number of samples loses significant information about the fluctuations which is required for adequate control of the covariance matrix upon which our correlated fits are based.

Fortunately, we have developed methods to solve both of these issues. These methods are based on a combination of the jackknife and the non-overlapping blocked-bootstrap resampling techniques [30]. The bootstrap technique uses uncorrelated, non-overlapping blocks of data for its samples and gives statistical errors unaffected by the autocorrelation between our 741 samples. However, the inner jackknife resampling introduced to calculate the covariance matrix for each outer bootstrap sample is applied to the unbinned data obtained as a union of all of the blocks in a given jackknife sample. In this paper the block size is chosen to be 8 to suppress the effects of autocorrelation. Finally the distribution of bootstrap means about the mean for the entire sample, determines the proper χ^2 distribution that can be used to correctly determine the p-value for the fit. (Recall that the usual standard χ^2 distribution is not accurate when χ^2 is determined using an uncertain covariance matrix in the presence of autocorrelations.) More details of this method can be found in Ref. [30].

Chapter 5: Results for $\pi\pi$ scattering

In this chapter we briefly summarize our previous work on the $\pi\pi$ scattering phase shift calculation[15]. In the first section we discuss the single-pion two point function and the corresponding pion energy on our lattice with GPBC. In the second section we discuss the results for the finite volume $\pi\pi$ energies for isospin $I = 0$ and $I = 2$ channel calculated based on one stationary frame and three moving frames. In the third section we discuss how we use Lüscher's finite-volume quantization method to calculate the physical phase shift. In the last section we discuss the systematic errors in this calculation.

5.1 Single pion two-point function and its result

In order to determine the pion energy and mass, we calculate a two-point function using the neutral pion operator:

$$C(\vec{p}, t_{snk}, t_{src}) = \left\langle \pi^0(t_{snk}, -\vec{p})\pi^0(t_{src}, \vec{p}) \right\rangle \tag{5.1}$$

for all possible values of t_{src} and t_{snk} and then we average over t_{src} while keeping $t = t_{snk} - t_{src}$ fixed. We have in total 32 different pion momenta, 8 from the $\pi(111)$ group of operators and the other 24 from the $\pi(311)$ group. Up to the effects of the cubic symmetry breaking induced by the boundary conditions, which are heavily suppressed by the procedure discussed in Section 3.4 and the residual effects shown to be negligible in Section 5.4, the two point functions within each group are related by cubic rotations hence we average the two-point functions within each group. This leaves us with two correlation functions, $C^i_\pi(t)$, where $i \in \{(111), (311)\}$ represents the momentum of the pion without specifying its direction.

We then perform correlated fits of each correlation function to the form

$$C^i_\pi(t) = A^i_\pi(e^{-E^i_\pi t} + e^{-E^i_\pi(T-t)}) \tag{5.2}$$

using various fit ranges, all of which share the same upper limit $t_{\text{max}} = 29$. Here A^i_π is related to the normalization of the operator O^i_π while E^i_π is the energy of a moving pion state with momentum $(1,1,1)\frac{\pi}{L}$ or $(3,1,1)\frac{\pi}{L}$. The fitted results for E^i_π plotted as a function of t_{min} are shown in Figure 5.1. From both plots we can see a clear plateau starting from $t_{\text{min}} = 14$. For that reason we choose the fit range to be $14 - 29$ and the fit results for that choice are listed in Tab. 5.1. The good p-values for both fits suggest that our data is well described by this single-state model.

Knowledge of the mass of the pion is required for the determination of the $\pi\pi$ phase shifts via the Lüscher procedure. Unfortunately, with GPBC we are unable to measure this mass directly and must instead infer it from the energy of a moving state with a suitable choice of dispersion relation. In Tab. 5.1 we give the results of applying the continuum dispersion relation to the (111) and (311) moving pion energies, which are labeled as $m_{\pi,\text{CD}}$. We can see that the resulting masses are inconsistent, which we interpret as the result of discretization effects on the dispersion relation. We also calculate the pion mass using the dispersion relation obeyed by a free particle on our discrete lattice

$$\cosh(E_\pi) = \cosh(m_\pi) + \sum_{i=1}^{3}(1 - \cos(p_i)), \tag{5.3}$$

where the pion mass is identified as the energy of a pion with zero-momentum. The results are listed in Tab. 5.1 as $m_{\pi,\text{LD}}$ and are consistent between the two momenta.

The large discrepancy between the two pion masses calculated using different dispersion relations suggests that when we calculate the pion mass using the larger-momenta $\pi(311)$ operators the result has not only a statistical error that is 3 times larger than that from the $\pi(111)$ operators, but also a large systematic error. For the remainder of this paper, we will use $m_{\pi,\text{CD}} = 142.3(0.7)$ MeV calculated from the $\pi(111)$ operators using the continuum dispersion relation as the pion mass. This 142.3(0.7) MeV value differs from the physical pion mass of 135 MeV by 7 MeV. This

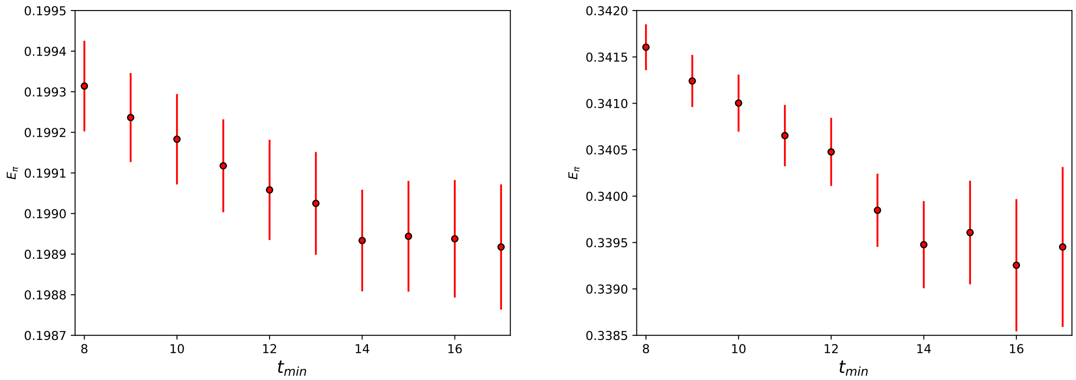

Figure 5.1: The t_{min} dependence of the fitted energy E_π for the $\pi(111)$(left) and $\pi(311)$(right) cases. Here E_π is shown in lattice units with t_{max} fixed to be 29.

State	Fit range	A_π	E_π	p-value	$m_{\pi,\text{CD}}$(MeV)	$m_{\pi,\text{LD}}$(MeV)
$\pi(111)$	14-29	$6.194(11) \times 10^6$	0.19893(13)	0.99	142.3(0.7)	143.3(0.7)
$\pi(311)$	14-29	$3.138(18) \times 10^6$	0.33948(47)	0.64	132.4(2.4)	144.3(2.3)

Table 5.1: Results for the fitted energies for the pion states with momenta in the groups (111) and (311). The right-most two columns show the pion masses calculated from those energies using the continuum ($m_{\pi,\text{CD}}$) and free-particle lattice ($m_{\pi,\text{LD}}$) dispersion relations. We have converted to units of MeV by using the inverse lattice spacing for this ensemble, $1/a = 1.3784(68)$ GeV, where the error on a also has been propagated into the errors on the energies given here.

introduces an “unphysical pion mass” error into our results which will be discussed in Sections 5.3 and 5.4. We will neglect the discretization error that remains in our determination of the pion mass since the 1 MeV discrepancy between the $m_{\pi,\text{CD}}$ and $m_{\pi,\text{LD}}$ in Tab. 5.1 is small compared to the 7 MeV “unphysical pion mass” error identified above.

5.2 Finite-volume $\pi\pi$ energies

In this section we describe our multi-state, multi-operator fitting strategies and the resulting fit parameters for both the stationary frame and the moving frame calculations and for both the $I = 0$ and $I = 2$ channels. Since these four situations are different, we will discuss them separately. At the end of this section we briefly discuss results obtained from another data analysis technique, the GEVP. This both provides alternative results for these quantities and an opportunity to compare these two methods. Because the primary focus of this paper is on the properties of the $\pi\pi$ ground state, this discussion of the GEVP method is limited to the ground state energies which it determines.

5.2.1 Stationary frame

$I = 2$ **Channel**

In the stationary $I = 2$ channel, we have two classes of operators, $\pi\pi(111, 111)$ and $\pi\pi(311, 311)$. We project them onto the trivial A_1 representation of the cubic symmetry group, which is the approximate symmetry group of a finite-volume lattice. (A discussion of possible cubic symmetry breaking effects resulting from our G-parity boundary conditions will be presented in Section 5.4.) This projection results in two different $\pi\pi$ operators, $O_a = \pi\pi_{A_1}(111, 111)$ and $O_b = \pi\pi_{A_1}(311, 311)$. We then calculate the matrix of two-point functions constructed from these two operators by measuring

$$C_{ij}(t_{snk}, t = t_{snk} - t_{src} - \Delta) = \langle O_i^\dagger(t_{snk}) O_j(t_{src}) \rangle, \tag{5.4}$$

where $\Delta = 4$ is the time-separation between two pion fields used to construct each $\pi\pi$ operator. We average over all values of t_{src} while fixing t and then average the data at t with that at $t = T-t-2\Delta$ to improve the statistics. (The individual single-pion operators at the times $t_{snk/src}+\Delta$ and $t_{snk/src}$ that make up each two-pion operator are constructed to be identical so when taking this second average we are combining equivalent physical quantities.) We then try two different fitting strategies:

1) Fit the single two-point function $C_{aa}(t)$ assuming a single intermediate state and an around-the-world constant using the form

$$C_{aa}(t) = A\left(e^{-E_{\pi\pi} t} + e^{-E_{\pi\pi}(T-t-2\Delta)}\right) + B, \tag{5.5}$$

where A describes the normalization of the operator, $E_{\pi\pi}$ is the energy of the finite-volume $\pi\pi$

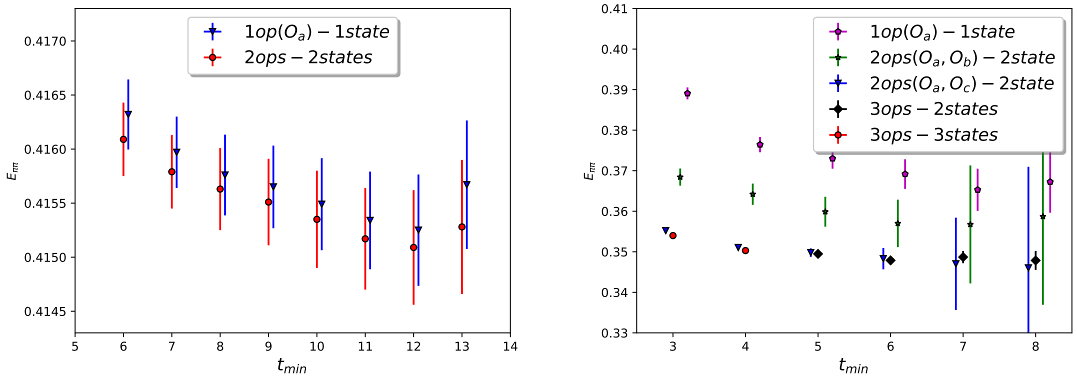

Figure 5.2: The $t_{\min}$ dependence of fitted ground state energy for the stationary $\pi\pi_{I=2}$ channel (left) with $t_{\max} = 25$ and the stationary $\pi\pi_{I=0}$ channel (right) with $t_{\max} = 15$. Left: The circles represent the two-operator, two-state fit and downward pointing triangles the one-operator, one-state fit. Right: The pentagons represent the one-operator, one-state fit. The stars and downward pointing triangles show the results from the two two-operator, two-state fits. Finally the circles show the three-operator, three-state fit for $t_{\min} = 3$ and 4 while the diamonds show the three-operator, two-state fit for $t_{\min} = 5 - 8$. For the $I = 0$ channel, including additional operators (especially the σ) substantially improves the determination of the ground state energy.

ground state and B is the around-the-world constant. Thus, a total of three fit parameters are required. We neglect all data related to the second operator O_b so this is a one-operator, one-state fit.

2) Fit the upper triangular component of the 2×2 matrix of two-point functions C_{ab} using two intermediate states and three different around-the-world constants using the form

$$C_{ij}(t) = \sum_{x=1}^{2} A_{ix} A_{jx} \left(e^{-E_x t} + e^{-E_x (T-t-2\Delta)} \right) + B_{ij}, \tag{5.6}$$

where A_{ix} is the overlap between the i^{th} operator and the x^{th} state; E_x is the energy of the x^{th} state and B_{ij} is the around-the-world constant constructed from operators O_i and O_j for a total of 9 real fit parameters. Note that, as the lower triangular component of the matrix is related to the upper triangular component by the time-translational symmetry, we did not measure these terms in order to reduce the computational cost.

For each case, we perform correlated fits with various choices for $t_{\min}$ and set $t_{\max} = 25$. We plot the resulting ground state energy as a function of t_{min} in the left panel of Figure 5.2. As we can see from the plot, the introduction of the second operator does not noticeably improve the fit result, as the ground state energies given by both fitting strategies are statistically consistent for all t_{min} and the statistical errors are also consistent. As we increase t_{min}, the ground state energy first decreases, which suggests a non-negligible excited state contamination for small t_{min} and then reaches a plateau for $t_{\text{min}} \approx 10$. We adopt the 2-operator, 2-state fit with the fitting range of $10-25$ for our final result. In Tab. 5.2 we list the p-values and the final parameters obtained from that approach. We observe an excellent p-value indicating a strong consistency between the data and our model.

The fact that B_{aa} is 60σ resolved from zero suggests the importance of including these around-the-world constants in our fits. This conclusion can also be reached by performing a similar fit in which the only change is that these constants are excluded. These fits give p-values that are consistent with zero, suggesting that these constants are required.

We also observe that the matrix of overlap amplitudes A_{ix} is nearly diagonal, where the operator O_a predominantly couples to the ground state and the operator O_b couples almost exclusively with the first excited state. The intercoupling between the operators and excited states is essential to exploiting the power of the multi-operator technique; without it one is merely performing several independent fits simultaneously. The fact that the amplitude matrix is near diagonal therefore likely explains the lack of improvement of the fit to the ground state energy when the second operator is introduced. The reason why this matrix is so diagonal can be intuitively explained by the weak strength of the $\pi\pi$ interaction potential in the $I = 2$ channel as indicated by the small phase shifts. Such an interaction is required for the pions to exchange momentum and thus transform into other $\pi\pi$ states.

$I = 0$ Channel

In the stationary $I = 0$ channel, we have three classes of interpolating operator, two of which are constructed from two-pion interpolating operators and the other is the stationary σ operator.

$I = 2$ channel	(2,2,2)	(2,2,0)	(2,0,0)	(0,0,0)
Fit range	10-25	12-25	11-25	10-25
Fit strategy	3op-3state	3op-3state	3op-3state	2op-2state
A_{a0}	0.3941(6)	0.2770(5)	0.1933(3)	0.4214(9)
A_{a1}	0.004684(565)	0.007011(548)	0.009301(455)	0.012(10)
A_{a2}	0.001209(1890)	0.005350(1812)	0.005249(1482)	-
A_{b0}	$-2665(31) \times 10^{-6}$	$-4632(27) \times 10^{-6}$	-0.007711(43)	-0.01164(10)
A_{b1}	0.08800(29)	0.07457(39)	0.07485(34)	0.0696(60)
A_{b2}	0.003506(901)	0.001437(1382)	0.0050(13)	-
A_{c0}	$-9626(124) \times 10^{-7}$	$-1522(11) \times 10^{-6}$	$-2327(14) \times 10^{-6}$	-
A_{c1}	$-3319(114) \times 10^{-6}$	$-3914(162) \times 10^{-6}$	$-4637(145) \times 10^{-6}$	-
A_{c2}	0.04690(66)	0.04592(111)	0.03940(103)	-
E_0	0.3984(3)	0.4001(3)	0.4045(3)	0.41535(45)
E_1	0.5453(7)	0.5480(10)	0.5514(9)	0.713(17)
E_2	0.6902(28)	0.6874(40)	0.6916(48)	-
B_{aa}	$8097(68) \times 10^{-9}$	$4034(35) \times 10^{-9}$	$1979(19) \times 10^{-9}$	$940(16) \times 10^{-8}$
B_{ab}	$-5748(3888) \times 10^{-12}$	$-1388(169) \times 10^{-11}$	$-1865(157) \times 10^{-11}$	$134(350) \times 10^{-11}$
B_{ac}	$-1025(178) \times 10^{-11}$	$-8835(934) \times 10^{-12}$	$-9792(986) \times 10^{-12}$	-
B_{bb}	$1136(154) \times 10^{-11}$	$9200(1074) \times 10^{-12}$	$9798(1111) \times 10^{-12}$	$-101(16) \times 10^{-9}$
B_{bc}	$-2642(4459) \times 10^{-13}$	$206(3020) \times 10^{-13}$	$-2617(3372) \times 10^{-13}$	-
B_{cc}	$2967(3749) \times 10^{-13}$	$1084(2540) \times 10^{-13}$	$2153(2980) \times 10^{-13}$	-
p-value	0.477	0.641	0.293	0.159

Table 5.2: Final fitting results for the $I = 2$, $\pi\pi$ channel. The right-most column lists the parameters obtained from a two-operator, two-state fit to the $\pi\pi$-$\pi\pi$ correlation function in the case of total momentum $(0, 0, 0)$ that is discussed in this subsection. The next three columns from the right show the parameters obtained from three-operator, three-state fits for three non-zero values of the total momentum.

After projecting the $\pi\pi$ operators onto the A_1 representation, we obtain three different operators: $O_a = \pi\pi_{A_1}(111, 111)$, $O_b = \pi\pi_{A_1}(311, 311)$ and $O_c = \sigma$ and calculate the matrix of two-point functions

$$C_{ij}(t_{snk}, t = t_{snk} - t_{src} - \Delta_j) = \langle O_i^\dagger(t_{snk}) O_j(t_{src}) \rangle - \langle 0|O_i(t_{snk})|0\rangle \langle 0|O_j(t_{src})|0\rangle, \tag{5.7}$$

where the second term represents the vacuum subtraction which removes the disconnected piece in Eq. (4.12), since it does not contribute to $\pi\pi$ scattering. We then average over all t_{src} while fixing $t = t_{snk} - t_{src}$ and average the data at t with that at $t = T - t - \Delta_i - \Delta_j$. Here $\Delta_a = \Delta_b = 4$ while $\Delta_c = 0$. We then explore three different fitting strategies:

1) Fit $C_{aa}(t)$ using a single state and the equation

$$C_{aa}(t) = A \left(e^{-E_{\pi\pi} t} + e^{-E_{\pi\pi}(T - t - 2\Delta_a)} \right), \tag{5.8}$$

where A and E have the same physical meaning as in the stationary $I = 2$ fit. This is a one-operator, one-state fit and we have only two fit parameters in total. In contrast with the stationary $I = 2$ fit, here we neglect the around-the-world constant since an estimate of the size of the dominant contribution resulting from a single pion propagating through the temporal boundary gives a value which is approximately ten times smaller than the statistical error on these noisier $I = 0$ channel data. Note, if fit as a free parameter, the result for this around-the-world constant is consistent with zero and gives a ground-state energy consistent with the result obtained when this constant is excluded, but with a statistical error that is 50% larger.

2) Fit the upper triangular components of the 2×2 submatrix spanned by O_a and one of the other two operators using two states and the equation

$$C_{ij}(t) = \sum_{x=1}^{N} A_{ix} A_{jx} \left(e^{-E_x t} + e^{-E_x (T - t - \Delta_i - \Delta_j)} \right), \tag{5.9}$$

where $N = 2$, A_{ix} is the overlap amplitude between the i^{th} operator and the x^{th} state, E_x is the energy of the x^{th} finite-volume state and (i, j) takes values from either $\{a, b\}$ or $\{a, c\}$. Thus, this is a six-parameter fit. An analysis similar to that mentioned in 1) above shows that the three around-the-world constants should be excluded.

3) Fit the upper triangular component of the entire 3×3 matrix of two-point functions using two or three states and the fitting form given in Eq. (5.9) where $N = 2$ or 3 is the number of states we include in the fit. We neglect the around-the-world constants for the same reasons as above, resulting in 12 (N=3) or 8 (N=2) fit parameters in total.

For each fitting strategy, we perform correlated fits with various values of t_{min} and set $t_{\text{max}} = 15$. We do not extend t_{max} to 25 as we did for the $I = 2$ channel since the data for $t > 15$ have larger statistical errors than in the $I = 2$ case, so including them will not benefit our fit. However, adding more fit points will destabilize the correlation matrix inversion procedure because of its increased dimension. We also risk introducing data for which the neglected around-the-world contribution may be a dominant component of the large-time data that has been introduced. This behavior is suggested because although the around-the-world constants remain statistically consistent with zero the p-value does fall as t_{max} is increased. Note that we do not observe any corresponding statistically significant effects on the amplitudes and energies as t_{max} is increased suggesting that our fits remain robust even in the presence of around-the-world contributions. A similar issue is encountered for the moving frame $I = 0$ fits and is discussed in greater detail in Section 5.2.2.

We plot the ground state energies from these fits as a function of t_{min} in the right panel of Fig. 5.2. For the three-operator case, we perform the three-state fit for $t_{\text{min}} \leq 4$ while for $t_{\text{min}} \geq 5$ we use the two-state fit as we observed that the three-state fits with $t_{\text{min}} \geq 5$ were unstable and did not converge for many bootstrap samples, indicating that the third state can no longer be reliably resolved in the data. As we increase the number of operators, the ground state energy at fixed t_{min} becomes significantly lower and the plateau region becomes more clear and begins earlier. We conclude that in contrast with the $I = 2$ channel, the introduction of the two extra operators, especially the σ interpolating operator, substantially reduces not only the statistical error but also the systematic error resulting from excited state contamination.

Since the plateau region for the three-operator fit starts at $t = 6$, we choose the three-operator, two-state fit with a fitting range of $6 - 15$ to determine our final results. In the right-hand column of Tab. 5.3 we list the p-value and final parameters for that fit. We can see that especially for the $\pi\pi(111, 111)$ (a) and σ (c) the overlap amplitudes between a given operator and the two states are of comparable size, which explains the effectiveness of the multiple operators that we included. This strong intercoupling between operators and states is consistent with the fact that the phase shift and hence the $\pi\pi$ interaction strength, is considerably larger than in the $I = 2$ case. Hence the exchange of momentum between the two pions required for the mixing between states is enhanced. For $I = 2$ the two $\pi\pi$ operators assign momenta with different magnitudes to the pions and would each couple to a different $\pi\pi$ energy eigenstate if the pions were non-interacting.

The fact that the overlap between operator O_a and the first excited state is about half of the overlap of that operator with the ground state also provides a strong indication that there is likely to be non-negligible excited-state contamination in a single-operator, single-state fit. This explains the substantial discrepancy between the phase shift at an energy near the kaon mass that we published in Ref. [1] and both the results presented here and those from the earlier dispersive prediction [9]. This can also be seen in the right panel of Fig. 5.2, where the single-operator fit reaches an apparent plateau at around $t = 6$ or 7 with an energy that is consistent with our previously published value but which is substantially larger than the ground-state revealed by the introduction of the additional operators.

5.2.2 Moving frame

$I = 2$ **Channel**

In the moving $I = 2$ channel, we have three classes of operators, $\pi\pi(111, 111)$, $\pi\pi(111, 311)$ and $\pi\pi(311, 311)$. We project them onto the trivial representation of the little group of the cubic symmetry group which leaves the total momentum unchanged. These little groups are C_{4v} for $\vec{P}_{tot} = (\pm 2, 0, 0)\frac{\pi}{L}$, C_{2v} for $\vec{P}_{tot} = (\pm 2, \pm 2, 0)\frac{\pi}{L}$ and C_{3v} for $\vec{P}_{tot} = (\pm 2, \pm 2, \pm 2)\frac{\pi}{L}$. For each choice of $\vec{P}_{tot}$, this gives us three different operators, $O_a = \pi\pi_{A_1}(111, 111)$, $O_b = \pi\pi_{A_1}(111, 311)$ and

$I = 0$ channel	(2,2,2)	(2,2,0)	(2,0,0)	(0,0,0)
Fit range	6-10	8-15	7-15	6-15
Fit strategy	3op-3state	3op-3state	3op-3state	3op-2state
A_{a0}	0.3873(7)	0.2626(31)	0.1772(26)	0.3682(31)
A_{a1}	-0.02647(391)	-0.05371(1262)	-0.05431(776)	-0.1712(91)
A_{a2}	-0.01354(312)	-0.03438(559)	-0.02450(274)	-
A_{b0}	$-1298(439) \times 10^{-6}$	0.002231(1392)	0.005861(1306)	0.0038(3)
A_{b1}	0.08361(100)	0.06894(318)	0.06781(261)	0.0513(27)
A_{b2}	-0.01121(395)	-0.01277(940)	-0.02008(636)	-
A_{c0}	$-8172(1223) \times 10^{-7}$	$-1920(3981) \times 10^{-7}$	$4871(4239) \times 10^{-7}$	-0.000431(4)
A_{c1}	0.000837(1050)	0.001713(2049)	0.003439(1464)	-0.000314(17)
A_{c2}	0.04786(126)	0.04602(456)	0.03735(263)	-
E_0	0.3972(4)	0.3895(17)	0.3774(23)	0.3479(11)
E_1	0.5264(37)	0.5129(100)	0.5032(75)	0.569(13)
E_2	0.6881(93)	0.6758(243)	0.6514(183)	-
p-value	0.094	0.016	0.635	0.314

Table 5.3: Table giving our final fitting results for $I = 0$, $\pi\pi$ channel. The right-most column lists the parameters obtained from a three-operator, two-state fit to the $\pi\pi$-$\pi\pi$ correlation function in the case of total momentum $(0, 0, 0)$ that is discussed in this subsection. The next three columns from the right show the parameters obtained from three-operator, three-state fits for three non-zero values of the total momentum.

$O_c = \pi\pi_{A_1}(311, 311)$. We calculate the matrix of two-point functions constructed from these three operators, $C_{ij}(t_{snk}, t_{src})$ and combine the various values of t_{src} and t_{snk} in the same way as was done for the stationary $I = 2$ calculation, except for an extra step where for each value of $|\vec{P}_{tot}|$, we also average over all of the possible total momentum directions. This leaves us with three correlation matrices, one for each $|\vec{P}_{tot}|$. We then try three different fitting strategies for each $|\vec{P}_{tot}|$:

1) Fit C_{aa} alone with a single state and an around-the-world constant, as we did in the stationary $I = 2$ calculation.

2) Fit the upper triangular component of the 2×2 submatrix spanned by O_a and one of the other two operators using two states and three different around-the-world constants using the equation

$$C_{ij}(t) = \sum_{x=1}^{N} A_{ix}A_{jx}\left(e^{-E_x t} + e^{-E_x(T-t-2\Delta)}\right) + B_{ij}, \tag{5.10}$$

where the definitions of A_{ix}, E_x and B_{ij} are the same as the stationary frame, $N = 2$ and (i, j) takes value from either $\{a, b\}$ or $\{a, c\}$, giving nine fit parameters for either fit.

3) Fit the upper triangular component of the entire 3×3 matrix of two-point functions using three states, six around-the-world constants and Eq. (5.10) with $N = 3$. In this case there are a total of 18 fit parameters.

For each value of $|\vec{P}_{tot}|$ and fitting strategy, we perform correlated fits with $t_{\max} = 25$, vary the value of $t_{\min}$ and plot the fitted ground state energy as a function of $t_{\min}$ in Figure 5.3, as in the stationary $I = 2$ calculation.

Similar to the stationary $I = 2$ calculation, for all three values of $|\vec{P}_{tot}|$, the introduction of the two extra operators has little impact on the ground state energy. As we increase $t_{\min}$, the ground state energy first decreases, suggesting a non-negligible excited state error for small $t_{\min}$ and then reaches the plateau region. This plateau starts at $t_{\min} = 11$ for $P_{tot} = (\pm2, 0, 0)\frac{\pi}{L}$, $t_{\min} = 12$ for $P_{tot} = (\pm2, \pm2, 0)\frac{\pi}{L}$ and $t_{\min} = 10$ for $P_{tot} = (\pm2, \pm2, \pm2)\frac{\pi}{L}$. We choose the three-operator, three-state fit with tmax=25 and tmin fixed to the start of the plateau region identified above.

In Tab. 5.2 we list the p-value and the final parameters for each choice of P_{tot}. With the chosen fit ranges we observe excellent p-values for all values of the total momentum. The fact that for each P_{tot}, B_{aa} is 100σ resolved from zero suggests the importance of including these around-the-world constants in the fitting. The overlap matrices are all nearly diagonal as in the stationary $I = 2$ calculation so that each operator is dominated by a different one of the three states. Thus, as was the case for the stationary frame $I = 2$ calculation, this explains why the introduction of these two additional operators does not improve the determination of the ground state energy.

It is also worth mentioning that the constant terms we include in the fit only describe the lowest-order around-the-world (ATW) effect mentioned in Sec. 3.4, where both the pions on leg A (direct propagation between the two single-pion operators) and leg B (propagation through the temporal boundary) carry a minimum momenta with components $\pm\pi/L$. Here we refer to segments of an around-the-world propagation path identified in Fig. 5.4. In contrast to the stationary case, the higher-order ATW terms in the moving frame need not be described by a constant term in the Green's function. For example, one of the pions on leg A or leg B could be replaced by a pion one of whose components has the larger $\pm 3\pi/L$ value. This possibility still conserves momentum and will show an exponential time dependence.

When compared with the first-order ATW effect, this second-order ATW effect is exponentially suppressed by the energy difference between a pion with three $\pm\pi/L$ momentum components and a pion with one component increased to $\pm 3\pi/L$. However, in our calculation, due to the time separation Δ between the two single-pion operators that make up our $\pi\pi$ operator, this second-order effect can be enhanced in some cases. For example, we can look at the Green's function constructed from two O_b operators. We define the state that propagates between the two temporally-separated pion operators in our $\pi\pi$ operator as the “internal state". Notice we have two internal states here, since we have two $\pi\pi$ operators. For the first-order case, the two internal states cannot both be the vacuum while conserving momentum, but for the second-order effect they can. This is illustrated in Figure 5.4. Thus, in this example the second-order effect is enhanced at least by a factor of $e^{E\Delta} = 4.2$, where E is the lowest energy of the internal state which we approximate by the $I = 0$ $\pi\pi$ energy.

$I = 2$ channel	(2,2,2)	(2,2,0)	(2,0,0)
Fit range	10-25	12-25	11-25
$E_{ATW,2nd}$	0.3985(3)	0.4002(3)	0.4045(3)
δE	$411(1167) \times 10^{-7}$	$867(1981) \times 10^{-7}$	$-731(1700) \times 10^{-7}$

Table 5.4: Fit results used for estimating the size of the second-order ATW effect in the $I = 2$ results given in Sec. 5.2.2. Here $E_{ATW,2nd}$ is the ground state energy when the second order ATW term is included in the fit and δE is the energy difference between $E_{ATW,2nd}$ and E_0 given in Tab. 5.2, which is significantly smaller that the statistical error on E_0 given in Tab. 5.2, in all three cases.

In order to investigate the size of the higher-order ATW terms we perform a fit to the $I = 2$ data. It can be easily shown that third- and higher-order ATW effects are always exponentially suppressed when compared with the first-order and second-order effects. This means we can perform a fit which includes some extra parameters which represent the second-order ATW effect and neglect third- and higher-order effects. Here we fit the matrix of correlation functions with the following fit function:

$$C_{ij}(t) = \sum_{x=1}^{N} A_{ix}A_{jx}\left(e^{-E_x t} + e^{-E_x(T-t-2\Delta)}\right) + B_{ij} + D_{ij}\left(e^{-(E_1^\pi - E_0^\pi)t} + e^{-(E_1^\pi - E_0^\pi)(T-t-2\Delta)}\right). \quad (5.11)$$

Compared with Eq. (5.10), the extra term with coefficient D_{ij} describes the second order ATW effect. Here E_0^π and E_1^π are the energies of moving pions with momenta $(1,1,1)\pi/L$ and $(3,1,1)\pi/L$, respectively. Their values can be obtained from Tab. 5.1. The fitting results for the ground state $\pi\pi$ energy and the sample-by-sample difference between the results with and without the second order ATW effect are shown in Tab. 5.4. Since the difference is negligible and statistically consistent with zero, we conclude that we need not include the second- or higher-order ATW effects in our fits.

$I = 0$ Channel

As in the case of the moving $I = 2$ channel, we have three classes of operators, defined as $O_a = \pi\pi_{A_1}(111,111)$, $O_b = \pi\pi_{A_1}(111,311)$ and $O_c = \pi\pi_{A_1}(311,311)$ which are projected onto the trivial representation of the corresponding little group. We calculate the 3×3 matrix of two-point functions constructed from these operators for each of the three values of $|\vec{P}_{tot}|$ in the same way as was done for the $I = 2$ case. We fit the data using three fitting strategies that are similar to the three used for the moving $I = 2$ case, except that we exclude the around-the-world constants from all the fits. The effect of these constants will be discussed below. We then perform correlated fits with $t_{\max} = 15$, vary $t_{\min}$ and plot the ground state energy as a function of $t_{\min}$ in Figure 5.3.

Figure 5.3 suggests that the introduction of the two extra operators does improve the fit result, since the ground state energy from the one-operator, one-state fit is always 2σ higher than its value from the three-operator, three-state fit, suggestive of remnant excited state contamination in the one state fit. The consistency of the ground state energy between the two-operator (O_a, O_b), two-state fit and the three-operator, three-state fit in the plateau region suggests that operator O_c may not be very useful. This is similar to the stationary $I = 0$ calculation, where the operator constructed from the two $\pi(311)$ operators plays little role in controlling the excited state error.

Another interesting feature is seen in the errors of the fitted parameters when we perform a single-operator, single-state fit using only the $\pi\pi(111, 111)$ operator. Consider how the sizes of either the relative error of the amplitude, or the absolute error of the ground state energy change as we decrease the total momentum from $(2, 2, 2)\frac{2\pi}{L}$ to $(0, 0, 0)\frac{\pi}{L}$, when the fit range is fixed (e.g., $6 - 15$). The pattern is that these errors *increase* as the total momentum decreases, as can be seen in Tab. 5.5! This behavior conflicts with the expectation that these errors would be approximately the same based on the Lepage argument [31]. For our kinematics, the non-zero total momentum is created by reversing some of the momentum components of one of the pions. Thus, if the modest $\pi\pi$ interactions are ignored, the four-pion states with zero total momentum which can contribute to the error will have approximately the same energy as the states which contribute to the signal.

This unexpected phenomenon can be understood by comparing the contributions to the central values of E0 and A0 and the corresponding errors obtained from the I=0 Green's functions.. From Eq. (4.17), there are four types of diagram that contribute to the $I = 0$ scattering. With $\sqrt{s} \le m_K$, the interaction between the pions is small, and the Green's function is dominated by the D-type

P_{tot}	(2,2,2)	(2,2,0)	(2,0,0)	(0,0,0)
E_0	0.39852(36)	0.39439(44)	0.38553(85)	0.36917(364)
A_0	0.15152(50)	0.07300(23)	0.03454(15)	0.01611(26)
$\frac{\delta A_0}{\bar{A}_0}$	0.0033	0.0032	0.0044	0.016

Table 5.5: Single operator (O_a) single state fit result with fit range $6-15$ for the $I = 0$ channel. The absolute error of the ground state energy and relative error of the amplitude are approximately the same when $P_{tot} = (2,2,2)\frac{\pi}{L}$ and $(2,2,0)\frac{\pi}{L}$ and increase as we further decrease the total momentum. This effect can be partially understood by comparing the number of momentum matched D-type diagrams that dominate the central value of the Green's function to the total number of D-type diagrams.

diagrams when $t \leq 10$ because in the non-interacting limit, the D-type diagrams represent products of two separate single-pion Green's functions. The V-type diagrams contain, in the stationary case, a vacuum contribution that is explicitly subtracted and for all four choices of P_{tot} contributions in which gluons propagate between the disconnected components. The error on these diagrams does not decrease with increasing operator separation and becomes dominant when $t \geq 4$. Given that the V-type diagrams are by far the dominant contribution to the error within our fit ranges, the size of the error on our fit results will depend primarily on the relative size of the V-diagram contribution to the overall Green's function, which, due to the dominance of the D-diagrams in the signal, is closely related to the relative size of the V and D-diagram contributions. Assuming that the errors on the amplitudes and the energies are uncorrelated, the pattern of these ratios as the total momentum varies (our four cases) should then be reflected in the errors on the fitted energies and amplitudes.

Notice that according to Eq. (4.10), the $\pi\pi$ operator with definite momentum $\vec{P}$ will contain 1, 2, 4 and 8 terms for the four cases above with total momentum containing three, two, one or zero non-zero components, respectively. Since the number of two-point function contractions that we must evaluate grows like the product of the numbers of terms in its constituent operators, there will be 1, 4, 16 and 64 different contractions needed for each type with total momentum $(2,2,2)\frac{\pi}{L}$, $(2,2,0)\frac{\pi}{L}$, $(2,0,0)\frac{\pi}{L}$ and $(0,0,0)\frac{\pi}{L}$, respectively. All these terms contribute V-type diagrams and hence to the error of the Green's function, with each of approximately the same size.

However, not all of these terms contribute D-type diagrams (and hence to the central value of the Green's function), because of a mismatch between the momenta. This can be understood by looking at the non-interacting limit in which a D-type diagram will only be non-zero when the two independent single-pion Green's functions are non-zero. This happens only when each of the two pions in the source $\pi\pi$ operator has the opposite momentum to that carried by one of the pions in the sink $\pi\pi$ operator, which we call momentum matching. Counting these terms gives the numbers of momentum-matched D-type diagrams for these four possible total momenta: 2, 4, 8 and 16, respectively. After dropping a common factor of two in this counting of D-type diagrams, these estimates suggest that the proportions between the relative errors for these four total momenta become $\frac{1}{1} : \frac{4}{2} : \frac{16}{4} : \frac{64}{8} = 1 : 2 : 4 : 8$. For a cosh fit, if the error of the amplitude and the error of the energy are uncorrelated, we can see that the relative error of the amplitude and the absolute error of the energy should be proportional to the relative error of the Green's function, which partially explains how the size of the errors on the ground state energy and amplitudes shown in Tab. 5.3 changes as we decrease the total momentum. A similar analysis can be applied to the $I = 2$ channel, which suggests that these relative errors should be approximately the same, independent of the total momentum, which is consistent with what is shown in Tab. 5.2.

Similar to the moving $I = 2$ channel, as we increase $t_{\min}$, the ground state energy first decreases, which suggests a non-negligible excited-state contamination for small $t_{\min}$. The ground state energy then reaches a plateau region which starts with $t_{\min} = 7$ for $P_{tot} = (\pm 2, 0, 0)\frac{\pi}{L}$, $t_{\min} = 8$ for $P_{tot} = (\pm 2, \pm 2, 0)\frac{\pi}{L}$ and $t_{\min} = 6$ for $P_{tot} = (\pm 2, \pm 2, \pm 2)\frac{\pi}{L}$. For our final result we choose the three-operator, three-state fit with $t_{\min}$ equal to the beginning of the plateau region identified above. The choice of $t_{\max}$ is more subtle and will be discussed together with the effect of the neglected around-the-world constants below. In Tab. 5.3 we list for each P_{tot} the fit range, fit procedure, as well as the resulting p-value and final parameters. We also observe in this table a trend towards smaller intercoupling between the operators and states, *i.e.* a more diagonal amplitude matrix A_{ix}, as we increase the total momentum and thus decrease the center-of-mass energy. This is again consistent with our understanding of the relation between this intercoupling and the strength of the

$\pi\pi$ interaction, which also decreases as the center-of-mass energy is decreased. This also explains why the additional operators appear to have the largest impact on the ground-state energy for the moving frame, $P_{\text{tot}} = (2, 0, 0)\pi/L$ fits in Figure 5.3.

Next we discuss our treatment of the around-the-world constants in the fit. There are two potential sources of systematic error in our results that must be treated carefully: the excited state contamination and the around-the-world contributions. The first error is expected to be much more significant and is discussed in Section 5.4. To leading exponential order in the time extent of the lattice volume, the around-the-world contributions are time-independent constants even in this moving frame calculation because of our G-parity boundary conditions. We observe that fitting with these around-the-world constants as free parameters results in good p-values for $t_{\text{min}} \geq 6$ but gives results for the constants that are either statistically consistent with 0 ($P_{tot} = (2, 2, 2)$ and $(2, 0, 0)$), or which have an unphysical, negative sign ($P_{tot} = (2, 2, 0)$). For all three cases either their errors when the constants are unresolved or the non-zero fitted values when these constants can be resolved are ten times larger than the expected size, that of the I=2 around-the-world constant.

For the case of $P_{tot} = (2, 2, 2)$ or $(2, 0, 0)$, we can neglect these constants in the fit since there is no statistical inconsistency between the fitted energy with and without these constants and we expect that the effects of the true around-the-world constants will be approximately ten times smaller than these sub-statistical effects. Note that excluding theses constants from the fit gives us an improvement in the statistical error of the ground state energy by a factor of $1.2 - 1.5$. For the second $P_{tot} = (2, 2, 0)$ case, the most likely explanation is that the constants are acting as “nuisance parameters” that help to partially account for the excited state contamination but do not reflect true around-the-world behavior. Rather than leaving the constants as free parameters and using an unphysical model to describe our data we choose to fix the constants to zero and to account for the systematic, excited-state contamination errors separately.

The model with zero around-the-world contributions should be a good description of the data in the window $[t_{\text{min}}, t_{\text{max}}]$ for which t_{min} is large enough that excited state effects are small and t_{max}

small enough that the contribution of these constants is small relative to the size of the data. For $t_{\max} = 15$ we observe very poor p-values even for large $t_{\min} \leq 10$. Reducing $t_{\max}$ from 15 to 10 we observe a significant improvement in the goodness-of-fit, finding acceptable p-values for $t_{\min} \geq 6$. This behavior is consistent with the effects of around-the-world contributions, although the excited state contributions may also play a role. Note however that, despite the dramatic improvement in p-value observed when reducing $t_{\max}$ from 15 to 10, we observe consistency in the ground-state fit parameters and no loss of precision, suggesting that the around-the-world systematic error is negligible and that the fits are under good control. In Figure 5.3 we use $t_{\max} = 15$ to show that reasonable behavior is seen when the around-the-world constants are omitted even for this large value of $t_{\max}$. Further evidence that supports the argument that for $P_{tot} = (2, 2, 0)$ these constants are "nuisance parameters" can be found by including them in the fit, fixing $t_{\max}$ and increasing $t_{\min}$. The resulting around-the-world constants monotonically decrease with increasing $t_{\min}$, which suggests that they likely result from excited state contamination, which is expected to decrease as $t_{\min}$ is increased, rather than representing the effects of single-pion around-the-world propagation. For uniformity, in Tab. 5.3 we choose to list the results for the three smallest total momenta with the same value of $t_{\max} = 15$. This results in the small p-value of 0.016 for the $(2, 2, 0)$ case. However, had we used $t_{\max} = 12$ we would have obtained equivalent results with a p-value of 0.205.

5.2.3 Normalized determinant

It is important to emphasize that the introduction of these additional $\pi\pi(\ldots)$ operators (in all cases) and σ operators (in the stationary $I = 0$ case) offers something more than a simple statistical improvement but gives new information about the underlying energy eigenstates. The two-point Green's functions C_{xy} for $x \neq a$ and/or $y \neq a$ typically have larger statistical uncertainties than C_{aa} at the same t, suggesting that including these additional operators may lead to only a small reduction in the statistical errors of the fitting parameters. However, in some cases including these operators significantly improves the statistical error of the ground state energy, (*e.g.* the stationary $I = 0$ case shown in Figure 5.2). We also observe in several cases a significant reduction in the energy of the apparent plateau as well as an earlier onset of the plateau region, suggesting that the extra operators are dramatically improving our ability to resolve nearby excited states which may be very difficult to distinguish from the ground state when we have only a single operator, even with large statistics.

Some insight into how this improvement comes about can be gained by considering the "normalized determinant" of the $N \times N$ matrix of Green's functions, $\mathcal{N}(t)$, defined as

$$\mathcal{N}(t) = \left| \frac{Det(C(t))}{\prod_{i=1}^{N} C_{ii}(t)} \right| , \tag{5.12}$$

where $C(t)$ is the matrix of Green's functions. We normalize the determinant using the product of the diagonal elements of the matrix so that this quantity does not depend on the scale of the interpolating operators. In fact, it can be shown that $0 \leq \mathcal{N}(t) \leq 1$. If the number of intermediate states that contribute to $C(t)$, N', is smaller than N then $\mathcal{N}(t) = 0$ (since the N', N-component vectors constructed from the matrix elements of the N operators between these N' states and the vacuum, which determine the $N \times N$ matrix C_{ij} do not span the entire N dimensional space on which C_{ij} acts). Thus, if at a given time t we find $\mathcal{N}(t) \neq 0$, then we can be certain that at least N distinct states are contributing to $C(t)$. When $\mathcal{N}(t) \approx 1$, it suggests that these operators create states from the vacuum which are orthogonal to each other.

In Figure 5.5 we plot $\mathcal{N}$ as a function of t for both the 2×2 matrix of stationary $I = 0$ two-point functions comprising $\pi\pi(111, 111)$ and σ operators and the 3×3 matrix of Green's functions constructed from all three operators. For the two-dimensional matrix case we find at $t = t_{\text{min}} = 6$, $\mathcal{N}(t) = 0.31(7)$ giving unambiguous proof that more than one state must be present, while for the three-dimensional matrix case, $\mathcal{N}(t)$ is relatively suppressed and takes value of 0.14(13) at $t = 5$ and consistent with zero at $t \geq 6$. The observation that the third state can no longer be distinguished from the noise for $t \geq 5$ explains why we were unable to perform reliable 3-operator, 3-state fits to the $I = 0$ stationary two-point functions with $t_{\text{min}} \geq 5$ earlier in this section. This is closely related to the discussion of the size of the excited state systematic error, as will be explained in Section 5.4. We emphasize that the determinant is computed from two-point function measurements *at a single time separation* and provides information beyond that which can be obtained from the time dependence of a single operator. The slow decrease of $\mathcal{N}(t)$ as a function of t throughout our fitting range suggests that there are states with similar energies, which can be distinguished even at a single time separation by the multiple operators in our fitting procedure. Note, according to Tab. 5.3 for the $I = 0$ channel these three nearby energies expressed in units of MeV are: $E_0 = 547.5(6)$, $E_1 = 725(5)$ and $E_2 = 948(13)$. While the differences between these energies are sufficient to easily see the time dependence of shown in Figure 5.5, they are insufficient to be resolved in a single-operator fit, even with the statistical precision achieved with 741 configurations.

5.2.4 Comparison of multi-operator multi-state fits with the GEVP method

Multi-parameter fitting is a straightforward method to analyze the correlation functions between pairs of interpolating operators to determine the energies of finite-volume states which these operators create and the overlap amplitudes between these operators and states. A second approach to analyze such data is the generalized eigenvalue problem (GEVP) approach [32, 33]. The GEVP can be viewed as a generalization of the concept of effective mass, from single-operator to multiple-operator Green's functions. In principle, this approach has good control over the systematic error resulting from the excited states that are not included in the analysis. Following the notation of Ref. [33], the N-dimension GEVP can be defined as

$$C(t)v_n(t,t_0) = \lambda_n(t,t_0)C(t_0)v_n(t,t_0) \quad 1 \le n \le N, t_0 \le t\,, \tag{5.13}$$

where $C(t)$ is the N-dimensional matrix of two-point functions, v_n, $1 \le n \le N$ are the eigenvectors and $\lambda_n(t,t_0)$ are the corresponding generalized eigenvalues. (In this section only, we follow the conventions of Ref. [33], and construct the correlation function $C_{ij}(t)$ from the product $O_i(t)O_j(0)^\dagger$.) In the limit where the lattice temporal extent, T, is large, the energy of the n^{th} state is related to λ_n by

$$\begin{aligned} E_n &= \lim_{t\to\infty} E_n^{\text{eff}}(t, t_0) \\ E_n^{\text{eff}}(t, t_0) &= \log(\lambda_n(t, t_0)) - \log(\lambda_n(t+1, t_0))\,. \end{aligned} \tag{5.14}$$

The GEVP approach can also be used to construct an operator $A_n^\dagger$ which creates the normalized lattice energy eigenstate:

$$\begin{aligned} A_n(t, t_0) &= e^{-Ht} Q_n(t, t_0) \\ Q_n(t, t_0) &= R_n(t, t_0) \sum_{i=1}^{N} O_i v_i^{n*}(t, t_0) \\ R_n(t, t_0) &= \left(\sum_{i,j=1}^{N} v_i^{n*}(t, t_0) C_{ij}(t) v_j^n(t, t_0) \right)^{-0.5} \frac{\lambda_n(t_0 + t/2, t_0)}{\lambda(t_0 + t, t_0)}\,. \end{aligned} \tag{5.15}$$

It has been shown that in the region where $t_0 > t/2$, the systematic error in the energy of the i^{th} state resulting from states omitted from the analysis is constrained by [33]

$$\Delta E = O\left(e^{-(E_{N+1} - E_i)t}\right). \tag{5.16}$$

If T is not sufficiently large, we need to consider two complications to the GEVP procedures described above. The first is around-the-world propagation, which introduces time-independent constants into the correlation functions for both isospin channels for each of our four values of total momentum. One way to eliminate this effect is to introduce a “subtracted matrix of two-point functions” $D(t)$ defined as $D(t) = C(t) - C(t + \delta t)$ and use this D matrix in the GEVP calculation [34]. Notice that this step will not affect the formula for the energy, but a modification is needed for the operator A_n which is now given by

$$A_n(t, t_0) = e^{-Ht} Q_n(t, t_0) / \sqrt{1 - e^{-E_n \delta t}}\,. \tag{5.17}$$

The second complication comes from backward propagating states. One way to accommodate this effect is to modify the relation between the eigenvalue and the corresponding energy. For more detail, see Ref. [35]. We will not use this method here but instead work with a smaller time range where the effect of backward propagating states can be neglected.

In this paper we will compare only the ground state energies obtained in our fitting and GEVP analyses. Specifically we compare the energies obtained from our multi-operator simultaneous fits to the GEVP effective energy defined in Eq. (5.14). Our comparison of the fitting and GEVP approaches begins by comparing the fitting results with those obtained from the GEVP at a fixed time t chosen to be the same as the value of $t_{\min}$ used in the fit while the value of the GEVP quantity t_0 is chosen as $\left\lceil \frac{t}{2} \right\rceil$. We find that the GEVP energy is statistically consistent with the fit result but its statistical error is about five times larger. Actually the result of this direct comparison should not be surprising, since much information is lost when the GEVP method is applied to a single (t, t_0) pair.

An improvement to the GEVP method proposed in Ref. [34] is to fit the set of generalized eigenvalues $\lambda_0(t, t_0)$, as a function of t with t_0 fixed and to include in that fit possible correction terms from omitted excited states. This addresses the statistical noise problem identified above by including more of the correlation function data in the GEVP analysis. We adopt a simple version of this fitting approach and perform a correlated fit to the GEVP eigenvalues of the form

$$\lambda_0(t, t_0) = e^{-E_0(t-t_0)}, \tag{5.18}$$

fitting all of the data from $t = t_0 + 1$ to a largest value $t_{\max}$. As shown in Ref. [33], this functional form for $\lambda_0(t, t_0)$ will contain errors from neglected higher energy states which are bounded by

$$\Delta E = O\left(e^{-(E_{N+1}-E_0)t_0}\right). \tag{5.19}$$

By choosing the smallest value of t used in this GEVP fit to be one time unit above t_0 we are minimizing the statistical error in our result for E_0 for a given choice of t_0. We then treat t_0 in the same spirit as $t_{\min}$ in our previous multi-parameter fitting of the matrix of Green's functions (which we will call the "usual fit" in the remainder of this section). Thus, we vary t_0 searching for a plateau region for sufficient large t_0 and then adopt as the result of this GEVP fitting that value obtained for E_0 from the smallest value of t_0 within that plateau region.

While this procedure is similar to what is used in our usual fit, we have not carried out the detailed discussion of the residual systematic errors coming from excited state contamination that is attempted in Section 5.4 for our usual fit. Thus, we are unable to say if choosing a larger value of t than $t_0 + 1$ would have resulted in a sufficiently reduced systematic error to give a reduction in the total error, overcoming the increase in statistical error that would result from increasing $t - t_0$ above one.

In addition to examining the dependence of the GEVP result for E_0 on t_0, we must also make sure that our choice of t_{max} is appropriate: if t_{max} is too large, then neglecting the backward propagating state will introduce an error; if t_{max} is too small, then we will have a small number of input data points which makes our fit less reliable. We will choose t_{max} to be no larger than that used in our usual fit, so that we can use those earlier results to determine how we should treat the around-the-world effects. Thus, based on the results obtained from our usual fit, we neglect the around the world effects for the $I = 0$ channel and work directly with the correlation matrix $C(t)$ of two-point functions. For $I = 2$ these effects were found to be important so in that case we analyze the subtracted matrix $D(t)$ defined above, using $\delta t = 1$. For the $I = 2$ channel, where we perform this matrix subtraction process, t_{max} is taken to be 20, smaller than the $t_{\mathrm{max}} = 25$ in the usual fit, due to the increased noise resulting from the construction of the subtracted matrix of two-point functions $D(t)$. The value of t_{max} in the $I = 0$ channel is chosen to be 15, the largest used in the usual fit. We can then plot the ground state energy from this GEVP fitting as a function of t_0 and look for the beginning of the plateau region and also the p-value in order to determine t_0.

Plots that include both the GEVP fit and the usual fit results are shown in Fig. 5.6. Notice the x-axis represents t_{min} for the usual fit, and t_0 for the GEVP method. This choice for plotting was made to best align both the central values and statistical errors from the two methods. For all but the stationary $I = 0$ case, both the usual fit and the GEVP fit are performed with all operators and

$P_{tot,I}$	sub	t_0	fitting range	E_0 (GEVP)	E_0 (usual fit)	p-value
$(222)_{I=2}$	y	10	11-20	0.39854(27)	0.39842(26)	0.385
$(220)_{I=2}$	y	11	12-20	0.40021(29)	0.40010(32)	0.306
$(200)_{I=2}$	y	11	12-20	0.40447(31)	0.40454(30)	0.294
$(000)_{I=2}$	y	11	12-20	0.41528(46)	0.41535(45)	0.665
$(222)_{I=0}$	n	6	7-15	0.3986(4)	0.3973(4)[17]	0.28
$(220)_{I=0}$	n	8	9-15	0.3907(13)	0.3895(17)[19]	0.622
$(200)_{I=0}$	n	6	7-15	0.3823(18)	0.3774(23)[52]	0.983
$(000)_{I=0}$	n	5	6-15	0.3489(11)	0.3479(11)[10]	0.142

Table 5.6: Comparison between the ground state energy E_0 obtained from the GEVP fit (GEVP) and the direct matrix of two-point functions fit (usual fit) given in Tab.s 5.2 and 5.3, repeated here for convenience. The t_0 used for the GEVP fit is obtained from Fig. 5.6 by recognizing the beginning of the plateau region and the resulting $t_{\text{min}} = t_0 + 1$ is shown in the fitting range above. In the "sub" column we indicate whether (y) or not (n) we are using the subtracted matrix of two-point functions $D(t)$ to perform the GEVP calculation, removing the around-the-world effects. The statistical error for both fits are shown in parenthesis while the systematic errors from excited state contamination for the $I = 0$ channel, estimated in Section 5.4, are shown in square brackets.

the number of states the same as the number of operators. For the stationary $I = 0$ case, the usual fit includes all the operators, and the number of states is 3 when $t_{\text{min}} < 5$ and 2 when $t_{\text{min}} \geq 5$. For the GEVP fit, the statistical error blows up when $t_{\text{min}} > 5$ if we include all operators, so we have used only two operators, O_a and O_c, when $t_{\text{min}} > 5$. It can be seen that for the $I = 2$ channel, the two results are not only consistent with each other, but also show similar time-dependence. For the $I = 0$ channel, the two results are not consistent, but this inconsistency may come from the excited-state error, which will be discussed below.

The final results and the choices of fitting setup are shown in Tab. 5.6. The p-values shown suggest that the quality of all the GEVP fits are relatively good. From the table we can see that for the $I = 0$ channel the GEVP fit results are approximately 2σ larger than the results from the usual fit if we only include the statistical error. However, the two are consistent if the systematic errors arising from excited state contamination in the usual fit are included. These excited-state error estimates were obtained by independent methods as described in Section 5.4 and are also listed in Tab. 5.11 and match surprisingly well the differences between the results obtained from our usual and GEVP fits.

For the $I = 2$ channel the two results are consistent with each other with comparable statistical errors which are much smaller than in the $I = 0$ case. Also notice that in all cases, the GEVP method gives statistical errors that are no larger than the usual fit method, which suggests that the GEVP fitting method is a useful tool for analyzing the matrix of Green's functions for the scattering considered here. We also expect that the usual fits may be less successful than the GEVP method when we increase the number of operators in the fit due to instabilities that will likely result from the larger number of fit parameters. As used here, the GEVP fit is far simpler, being a correlated fit to a single one-parameter function of the time. The multi-operator fits will further suffer from the quadratic increase in the number of elements in the covariance matrix, the inversion of which may become unstable once it becomes too large. In the GEVP case, the size of the covariance matrix depends only on the size of the fit window.

Nevertheless, for the problem at hand, fitting the matrix of two-point functions is more direct than fitting the GEVP eigenvalues and, as we will show in Section 5.4, allows considerable flexibility in estimating the size of the systematic error arising from omitted excited states. In the GEVP method the number of operators and the number of states must be the same, while in the usual fitting approach they can be different. Currently, this is a crucial step in estimating the excited state error as will be seen in Section 5.4 and in identifying a plateau in the stationary $I = 0$ case as can be seen from the lower right panel of Fig. 5.6.

5.3 Determination of the phase shift

In this section we discuss in detail how we determine the $\pi\pi$ phase shifts from the finite-volume $\pi\pi$ energies. We begin with Lüscher's formula generalized to the case of anti-periodic boundary conditions[1] with a general total momentum. Next we discuss the strategy of working with energy differences to reduce discretization errors, especially for the moving frame calculations. We then calculate the $\pi\pi$ scattering phase shifts at various center-of-mass energies for both isospin channels using this technique. We also describe our method for specifying the energy at which these phase

---

[1] In this section we will focus on the case of anti-periodic boundary conditions obeyed by the pions, which result from the G-parity boundary conditions obeyed by the quarks.

shifts have been determined in order to reduce the effects of the slightly unphysical pion mass used in our lattice calculation. Finally we calculate the Lellouch-Lüscher factor [36] that is needed to interpret the finite-volume $K \to \pi\pi$ calculation [16].

5.3.1 Lüscher's quantization condition for non-zero total momentum and anti-periodic boundary conditions

Euclidean-space lattice QCD calculations determine finite-volume $\pi\pi$ energies from which the infinite-volume scattering phase shifts can be obtained using an approach developed by Lüscher [6]. While initially derived for the case of a stationary frame and periodic boundary conditions, this approach was later generalized to non-zero total momentum [37, 38, 39] and it is straightforward to generalize this moving frame result to the case with anti-periodic boundary conditions. In particular, the s-wave phase shift, $\delta(s)$ can be determined from the relation: $\delta(s) + \phi^{\vec{d},\gamma}(s) = n\pi$ where n is an integer and typically allows for more than one solution to this quantization condition, resulting in a series of energy eigenstates in a single volume. The function $\phi^{\vec{d},\gamma}(s)$ is defined by

$$\tan\left(\phi^{\vec{d},\gamma}(s)\right) = \frac{\gamma\pi^{3/2}q}{Z_{00}^{\vec{d},\gamma}(1,q^2)}. \tag{5.20}$$

Here s is the square of the invariant mass of the two-pion system, γ is the Lorentz factor which boosts the laboratory frame to the CM frame and q is related to the magnitude of the momentum k carried by either pion in their center-of-mass frame. Each of these quantities can be determined from the finite-volume $\pi\pi$ energy, $E_{\pi\pi}$ obtained from the lattice calculation:

$$s = E_{\pi\pi}^2 - \vec{P}_{tot}^2, \quad \gamma = \frac{E_{\pi\pi}}{\sqrt{s}}, \quad k^2 = \frac{s}{4} - m_\pi^2, \quad q = k\frac{L}{2\pi}. \tag{5.21}$$

The vector of integers, $\vec{d}$, is related to the total momentum $\vec{P}_{tot}$ by

$$\vec{d} = \frac{L}{2\pi}\vec{P}_{tot} \tag{5.22}$$

and $Z_{00}^{\vec{d},\gamma}(\hat{s}, q^2)$ is the generalized Lüscher's zeta function, which is defined as

$$Z_{00}^{\vec{d},\gamma}(\hat{s}, q^2) = \frac{1}{\sqrt{4\pi}} \sum_{\vec{r} \in \mathcal{N}^{\vec{d},\gamma}} (\vec{r}^{\,2} - q^2)^{-\hat{s}}, \tag{5.23}$$

where the conventional argument s of the zeta function is replaced here by $\hat{s}$ to remove the possible confusion with the square of the center-of-mass energy and the set $\mathcal{N}^{\vec{d},\gamma}$ is defined as

$$\mathcal{N}^{\vec{d},\gamma} = \left\{\vec{r} \,\middle|\, \vec{r} = \hat{\gamma}^{-1}\left(\vec{n} + \vec{d}/2 + \vec{\ell}/2\right), \vec{n} \in \mathbb{Z}^3\right\}. \tag{5.24}$$

Here the vector $\vec{\ell}$ represents the effect of the boundary conditions. If the particle satisfies periodic boundary conditions in the i^{th} direction then $\ell_i = 0$, while with anti-periodic boundary conditions we have $\ell_i = 1$. The quantity $\hat{\gamma}^{-1}$ is a linear transformation on 3-vectors defined as

$$\hat{\gamma}^{-1}(\vec{n}) = \frac{1}{\gamma}\vec{n}_{\|} + \vec{n}_{\perp}, \tag{5.25}$$

using the notation of Ref. [40].

As defined in Eq. (5.23) the generalized zeta function diverges at $\hat{s} = 1$ and needs to be expressed differently to be evaluated at $\hat{s} = 1$. We use a simple generalization of a formula given in Ref. [40] to do this. Combining all of these formulae we can obtain the $\pi\pi$ scattering phase shift at the energy $\sqrt{s}$ from the finite-volume energy eigenvalue $E_{\pi\pi}$ determined from our lattice calculation. Note that in obtaining Eq (5.20) we are implicitly neglecting the contributions to the scattering of partial waves with $l \geq 1$. In the stationary frame, assuming the $\pi\pi$ operators are constructed in the trivial representation of the cubic group, cubic symmetry prevents states with $1 \leq l < 4$ from contributing [6]. The interaction strength in the $l \geq 4$ channels is known to be small and these interactions can be safely neglected [6].

However in the moving frame the relativistic length contraction naturally breaks the cubic symmetry down to a smaller group, the trivial representation of which also allows for contributions from d-wave ($l = 2$) interactions. Previous calculations [41] have shown that the phase shifts in the $l = 2$ channel are small around the kaon mass, which will be further suppressed in the moving frame calculation where $\sqrt{s}$ is smaller than m_K so we can therefore continue to assume s-wave dominance. As described above, the G-parity boundary conditions also break the cubic symmetry but the effects can be suppressed with a careful choice of $\pi\pi$ operator. Any systematic errors arising from this source are discussed further in Section 5.4.1.

5.3.2 Calculation technique

As shown above, the $\pi\pi$ scattering phase shift is related to the energy of a finite-volume $\pi\pi$ state, or more specifically to the "pion momentum" k carried by either pion outside the range of the strong force. However, on a discretized lattice with anti-periodic boundary conditions (*i.e.* a case where the single-pion ground-state has non-zero momentum), the determination of k from the measured $\pi\pi$ energy must be performed carefully. If the $\pi\pi$ interaction is relatively weak then k, which is a measure of that interaction, will be close to its free field value and we must take precautions that the potentially small difference between k and its free field value is nevertheless large when compared with the discretization errors associated with the spatial momenta of the pions in our calculation. However, as can be seen in Eq. (5.21), k is determined from differences of larger quantities and care must be taken to insure that the quantities being subtracted have, to the degree possible, common finite lattice spacing errors so that these errors will largely cancel in the difference. Specifically the quantities being subtracted should be chosen so that their difference will vanish in the limit that the $\pi\pi$ interactions vanish, even when computed at finite lattice spacing.

This cancellation of finite lattice spacing errors can be accomplished by working with two related quantities determined from our calculation: $\Delta E = E_{\pi\pi} - 2E_\pi$, which measures the $\pi\pi$ interaction strength, and E_π, the lowest energy of a moving pion. Using ΔE for example, the effects of the finite lattice spacing upon the pion dispersion relation that enter both $E_{\pi\pi}$ and $2E_\pi$ will largely cancel, leaving only the subtler effects of the discretization upon the two-pion interaction itself. Even for the case of non-zero total momentum $\vec{P}_{tot}$, we will exploit our choice of anti-periodic boundary conditions in all three directions and use for E_π the ground-state, single-pion energy. Each of the three non-zero total momenta that we study can be formed from two pions carrying the minimum allowed momenta $\vec{p} = (\pm1, \pm1, \pm1)\pi/L$ so that $2E_\pi$ will be the minimum energy of two interacting pions in the limit in which that interaction vanishes.

Thus, the quantities ΔE and E_π will be computed on the lattice, and systematic errors estimated to account for the residual effects of the finite lattice spacing. The results are finite-volume predictions for ΔE and E_π in the continuum limit, albeit with an unphysical pion mass, and in Section 5.4 we will estimate and propagate the systematic discretization errors on these quantities. (While it would be better to determine ΔE and E_π by performing calculations at multiple lattice spacings and taking the continuum limit, this is at present beyond our available resources.) Adopting this strategy to account for the discretization effects, we can then apply the generalization of Lüscher's finite-volume quantization condition without ambiguity using the continuum dispersion relation

$$\begin{aligned} k^2 &= (\Delta E + 2E_\pi)^2/4 - E_\pi^2 + 3(\frac{\pi}{L})^2 - \frac{1}{4}\vec{P}_{tot}^2 \\ &= \frac{\Delta E^2}{4} + \Delta E E_\pi + 3(\frac{\pi}{L})^2 - \frac{1}{4}\vec{P}_{tot}^2\,, \end{aligned} \tag{5.26}$$

where we have continued to assume anti-periodic boundary conditions in three directions and note that the last two terms on the right-hand side of Eq. (5.26) are exactly known.

The second line in Eq. (5.26) demonstrates the purpose of this rearrangement: our result for k is proportional to the small quantity ΔE (a measure of the $\pi\pi$ interaction strength) plus other kinematic quantities that are determined without finite lattice spacing error. This guarantees that at finite lattice spacing the phase shift determined in this way from the quantization condition will vanish when $\Delta E \to 0$ so that the fractional finite lattice spacing errors expected in ΔE can be directly propagated to determine the corresponding error in $\delta(s)$.

We thereby obtain a value for the phase shift at an unphysical pion mass, from which a prediction for the physical phase shift can be obtained by assigning suitable systematic errors for discretization effects and the unphysical pion mass as will be discussed in Section 5.4.

5.3.3 Phase shift results (statistical error only)

In this section we tabulate our results for the $\pi\pi$ scattering phase shifts including their statistical errors, computed according to the method described above. For each result we must specify the energy at which the phase shift takes the quoted value and we choose to assign the appropriate $\sqrt{s}$ in such a way as to minimize the error introduced by the unphysical pion mass, 143 MeV, at which our calculation is performed, a value 6% larger than the 135 MeV which we adopt as the physical pion mass in this paper. For values of $\sqrt{s}$ on the order of the kaon mass, the error associated with this unphysical 8 MeV shift in the pion mass is small and is estimated using chiral perturbation theory in Section 5.4. However, since the $I = 0$ and 2 phase shifts vanish when $\sqrt{s} = 2m_\pi$, this unphysical pion mass error can become large as $\sqrt{s}$ approaches $2m_{\pi,\text{unphy}} > 2m_{\pi,\text{phy}}$. This effect can be easily eliminated if we view our computed phase shifts as functions of the pion momentum k rather than $\sqrt{s}$, since a calculation of the phase shifts will give results which vanish at $k = 0$ independent of the pion mass.

Thus, for each computed value of the phase shift we use the measured lattice $\pi\pi$ energy and lattice pion mass to obtain the relative momentum k, and then when presenting our results for the phase shifts assign an energy determined by combining this momentum in the continuum limit with the physical pion mass by applying the dispersion relation

$$s = 4(k^2 + m_{\pi,\text{phy}}^2)\,. \tag{5.27}$$

The effect of the unphysical pion mass on the actual strength of the interaction (*i.e.* upon the phase shift itself) is small and is treated as a systematic error that we estimate using chiral perturbation theory, as discussed in Sec. 5.4.

In Tab. 5.7 we list the phase shifts calculated from 4(3) different momenta of the center of mass for the $I = 2(0)$ channel and calculate the corresponding $\sqrt{s}$ using Eq. (5.27). Here we only include the statistical error. The full error budget will be discussed in Section 5.4. We do not provide a result for the $I = 0$ channel in the case where $P_{tot} = (2, 2, 2)\frac{\pi}{L}$. At this lowest value of $\sqrt{s}$ the

P_{tot}	I	$E_{\pi\pi}$	k	$\sqrt{s}$	δ
$(0,0,0)\frac{\pi}{L}$	0	0.3479(11)	193.0(9)	471.0(1.5)	32.3(1.0)°
$(2,0,0)\frac{\pi}{L}$	0	0.3774(23)	170.6(2.4)	435.1(3.8)	24.0(3.4)°
$(2,2,0)\frac{\pi}{L}$	0	0.3895(17)	123.2(2.6)	365.6(3.4)	18.0(4.5)°
$(0,0,0)\frac{\pi}{L}$	2	0.4153(4)	248.4(3)	565.4(5)	-11.0(2)°
$(2,0,0)\frac{\pi}{L}$	2	0.4045(3)	197.9(2)	479.1(3)	-7.96(23)°
$(2,2,0)\frac{\pi}{L}$	2	0.4001(3)	138.4(3)	386.7(4)	-4.48(40)°
$(2,2,2)\frac{\pi}{L}$	2	0.3984(3)	14.4(2.1)	271.5(4)	-0.32(20)°

Table 5.7: The phase shifts with statistical errors only for 4(3) different total momenta for the $I = 2(0)$ channel and the corresponding $\sqrt{s}$. Here the statistical error of each phase shift is obtained not by simply propagating the statistical error of $E_{\pi\pi}$, but a more elaborate method discussed in Sec. 5.4.6 which removes the uncertainty of the energy at which we quote the phase shift.

attractive interaction between two pions results in a center-of-mass $\pi\pi$ energy that lies below $2m_\pi$, requiring that we determine a scattering length. Unfortunately the statistical error on the amount that this energy is shifted below $2m_\pi$ is so large that the corresponding scattering length is not well determined.

5.3.4 Lellouch-Lüscher factor

In our companion calculation of the $I = 0$ $K \rightarrow \pi\pi$ matrix elements [16], an important ingredient is the Lellouch-Lüscher factor [36], which removes both the difference in normalization between states defined in finite and infinite volume and the leading power-law finite-volume corrections to the finite-volume matrix element. This factor is defined as:

$$F^2 = \frac{4\pi m_K E_{\pi\pi}^2}{k^3}\left(k\frac{\partial \delta_I}{\partial k} + q\frac{\partial \phi^{\vec{d},\gamma}}{\partial q}\right), \tag{5.28}$$

where δ_I is the isospin I, s-wave $\pi\pi$ phase shift an $\phi^{\vec{d},\gamma}$ is defined in Eq. (5.20). This formula should be evaluated at $E_{\pi\pi} = m_K$.

The moving frame calculation enables us to determine the phase shifts at various energies, which allows us to perform an *ab initio* measurement of $\frac{\partial\delta_0}{\partial k}$ using a finite-difference approximation. We now focus on the $I = 0$ case since our calculation has been tuned to give s close to m_K^2 for the $I = 0$, $\pi\pi$ ground state. We approximate the factor F using two different methods. In the first we subtract the values of δ_0 at $P_{tot} = (0,0,0)\frac{\pi}{L}$ and $P_{tot} = (2,0,0)\frac{\pi}{L}$, which gives

$$\frac{\partial \delta_0}{\partial k} = 0.372(153) \tag{5.29}$$

and in the second method we replace the second total momentum with $P_{tot} = (2,2,0)\frac{\pi}{L}$, and obtain

$$\frac{\partial \delta_0}{\partial k} = 0.205(63)\,. \tag{5.30}$$

Both results are consistent with

$$\frac{\partial \delta_0}{\partial k} = 0.276(1)\,, \tag{5.31}$$

which is calculated from the dispersive analysis [9, 16]. Note we have not attempted to account for systematic effects arising from the finite-difference approximation or other effects here. Nevertheless we find good agreement between our lattice results and the dispersive prediction, albeit with large statistical errors. These results are also presented in Ref. [16] where the dispersive result was used for the final analysis. Note that these values differ slightly (within errors) due to different choices of fit range and the finite-difference approximation being applied there to the phase shift is a function of energy rather than a function of k.

5.4 Systematic error analysis

There are several sources of systematic error which affect our results: the breaking of cubic symmetry by our G-parity boundary conditions, the non-zero lattice spacing of our single gauge ensemble, the unphysical value of our pion mass and contamination of our multi-operator, multi-state fits due to the presence of additional excited states, not included in our fit. In this section, we describe our procedure for estimating the size of these errors. The full error budget for the phase shifts we obtain is given at the end of this section and a comparison is made with the dispersive predictions [9].

5.4.1 Cubic symmetry breaking

One distinguishing feature of our calculation is our choice of boundary conditions: we use G-parity instead of the standard periodic boundary conditions commonly used in other $\pi\pi$ scattering calculations. As discussed in Sec. 3.4 and in Ref. [13], G-parity boundary terms in the quark action break the usual cubic symmetry of our lattice action and cubic volume. We will distinguish two possible effects of this breaking of cubic symmetry by the boundary conditions: the effects on the finite-volume eigenstates of the transfer matrix and the limitations on the symmetry properties of interpolating operators constructed from the quark fields.

Since the physical states in our finite volume are pions which obey cubically anti-periodic boundary conditions, we expect that the effects of this quark-level cubic asymmetry will be suppressed exponentially in the linear size of our spatial volume. Local phenomena will not be affected by these boundary terms but only phenomena which span the entire volume. This consideration should apply to the size of the corrections to the standard $\pi\pi$ finite-volume quantization condition, reducing these G-parity cubic symmetry breaking effects to the size of other finite-volume corrections.

Of greater concern is our inability to confidently use cubic symmetry when interpreting the rotational quantum numbers of the states produced by our interpolating operators. The G-parity breaking of cubic symmetry limits the selection of quark momenta that can be introduced when constructing interpolating operators resulting in operators which contain a mixture of representations of the cubic group. The only solution to this problem which we have found is an empirical one: we must carefully construct pion interpolating operators to reduce the mixing of different cubic symmetry representations below the level that we are able to observe.

As described in Ref. [13], a numerical investigation on single-pion correlation functions has been performed on a smaller lattice, which suggests that if we construct these pion interpolating operators with a single choice of quark momentum assignment chosen from the set of allowed quark momenta (for example choice 1 of Appendix A of the present paper), then we observe a clear cubic symmetry breaking effect in the overall normalization of the corresponding two-point functions. In that appendix we also introduce a second choice with the same total momentum but with different assignments of quark momentum. We observe that if we construct our pion interpolating operators by averaging the two momentum choices, then the resulting cubic symmetry breaking becomes sub-statistical. Since this cubic symmetry breaking is purely due to the boundary condition, it will be further suppressed by the larger volume used in the current study, and is therefore negligible in this work. While the normalization of the two single pion operators carrying momenta which are related by cubic symmetry show small differences, the pion energies are always the same providing evidence for the assertion in the preceding paragraph that the spectrum of the transfer matrix shows only exponentially small cubic asymmetry.

We can also calculate the size of the cubic symmetry breaking in our $\pi\pi$ interpolating operators directly by studying the overlap between interpolating operators belonging to different representations of the cubic group. We will focus on the stationary frame since in the moving frame calculation the s and d-waves are coupled to each other even if we have exact cubic symmetry. If we have exact cubic symmetry, we can project all three groups of $\pi\pi$ interpolating operators (they are $\pi\pi(111, 111)$, $\pi\pi(311, 311)$ and σ) onto the A_1 and T_2 representations, which primarily map onto the $l = 0$ and $l = 2$ representations of the continuum rotation group, respectively, and for each group of operators these two representations will be orthogonal. However, if the symmetry group is reduced to the D_{3d} group, both A_1 and T_2 representations are no longer irreducible and contain the same representations of D_{3d} making a nonzero overlap between operators in these two representations possible. The size of this overlap can then serve as a measure of the cubic symmetry breaking.

We start by considering the two projections of the $\pi\pi(111, 111)$ operators and define their overlap as the average

$$C^{I,T_2,A_1}_{a,a}(t) = \frac{1}{T}\sum_{t_{\rm src}}\langle O^{I,T_2}_{\pi\pi(111,111)}(t+\Delta+t_{\rm src})^\dagger O^{I,A_1}_{\pi\pi(111,111)}(t_{\rm src})\rangle\,, \tag{5.32}$$

where $\Delta = 4$, as introduced earlier in Eq. (5.4). Here and below we follow a convention similar to that introduced in Section 5.2 in which the labels a, b and c correspond to $\pi\pi(111, 111)$, $\pi\pi(311, 311)$ and σ respectively. If the cubic symmetry breaking effects are negligible, then $C^{I,T_2,A_1}_{a,a}(t)$ will be consistent with 0.

Since we are interested in the size of these cubic symmetry breaking effects relative to the correlation functions from which we obtain our results, we will present the normalized correlator

$$R^{I,T_2,A_1}_{a,a}(t) = \frac{C^{I,T_2,A_1}_{a,a}(t)}{\sqrt{C^{I,T_2}_{a,a}(t)C^{I,A_1}_{a,a}(t)}} . \tag{5.33}$$

where $C^{I,T_2}_{a,a}(t)$ and $C^{I,A_1}_{a,a}(t)$ are defined by:

$$C^{I,\mathcal{R}}_{a,a}(t) = \frac{1}{T}\sum_{t_{\mathrm{src}}}\langle O^{I,\mathcal{R}}_{\pi\pi(111,111)}(t + \Delta + t_{\mathrm{src}})^{\dagger} O^{I,\mathcal{R}}_{\pi\pi(111,111)}(t_{\mathrm{src}})\rangle , \tag{5.34}$$

where $\mathcal{R} = A_1$ or T_2. The ratio $R^{I,T_2,A_1}_{a,a}(t)$ in Eq. (5.33) provides an estimate of the fractional contamination in the correlation functions which we study that results from cubic symmetry breaking. While we cannot be sure of the quantum numbers of the dominant state which propagates in the mixed correlator given in Eq. (5.32), the ratio given in Eq. (5.33) divides by the time dependence implied by the arithmetic mean of what we expect to be the lowest masses in the A_1 and T_2 channels.

The results are shown in Fig. 5.7, where the left panel shows the normalized overlap amplitude for the $I = 0$ channel, and the right panel shows that for the $I = 2$ channel. Here and in the later graphs shown in Figure 5.8 we choose the time ranges to best present our results. We exclude large times because the statistical errors become very large and would require a highly compressed scale to display. However, in each case sufficiently large times are shown that the signal from the states which we study should be an important contributor to the correlation function, so the small size of $R^{I,T_2,A_1}_{aa}(t)$ for those later times implies at most a fractional percent contamination of our results from cubic symmetry breaking. Of special interest is the size of $R^{I,T_2,A_1}_{a,a}(t)$ for $t = 0$ and 1 where the statistical errors are very small and cubic symmetry breaking is not visible at the tenth of a percent scale.

Having verified the approximate cubic symmetry of the $\pi\pi(111, 111)$ operator, we next calculate the overlap amplitude between the $\pi\pi(111, 111)$ operator in the T_2 representation and the other $(311, 311)$ and σ operators in the A_1 representation by evaluating:

$$C^{I,A_1,T_2}_{b/c,a}(t) = \sum_{t_{\rm src}} \langle O^{I,A_1}_{\pi\pi(311,311)/\sigma}(t + \Delta + t_{\rm src})^\dagger O^{I,T_2}_{\pi\pi(111,111)}(t_{\rm src})\rangle. \tag{5.35}$$

The results are most easily interpreted if we again examine the normalized ratio

$$R^{I,A_1,T_2}_{b/c,a}(t) = \frac{C^{I,A_1,T_2}_{b/c,a}(t)}{\sqrt{C^{I,A_1}_{b/c,b/c}(t) C^{I,T_2}_{a,a}(t)}}\,. \tag{5.36}$$

The results are shown in Fig. 5.8, where the upper panel shows the overlap between the $\pi\pi^{A_1}(311, 311)$ and $\pi\pi^{T_2}(111, 111)$ interpolating operators in the $I = 0$ and $I = 2$ channels, and the lower panel shows the overlap between the $I = 0$, σ and $\pi\pi^{T_2}(111, 111)$ interpolating operators. Similar to Fig. 5.7, all three overlap amplitudes are consistent with 0 at the fractional percent level, which suggests both the $\pi\pi(311, 311)$ and the σ operators obey approximate cubic symmetry.

Based on the above results, we conclude that if we construct the pion interpolating operators by averaging the two sets of quark momentum assignments as described in the appendix, we can achieve accurate cubic symmetry at the meson level, despite the symmetry breaking at the quark level. We therefore do not assign any systematic error arising from cubic symmetry breaking.

5.4.2 Finite lattice spacing

Fundamental to the connection between the scattering phase shifts and the two-particle finite-volume energies is the recognition that it is the interaction between the particles, described by a non-zero scattering phase shift, that causes the two-particle energy in finite volume to be shifted away from the simple spectrum of non-interacting particles in a box. When adopting formulae to determine the scattering phase shifts from the two-particle finite-volume energies in Section 5.3

we were careful to preserve this connection for non-zero lattice spacing.

Specifically Eq. (5.26) determines the relative center of mass momentum k between the two pions in the finite-volume $\pi\pi$ ground state that enters Lüscher's quantization condition as a function of the energy difference ΔE between the finite volume $\pi\pi$ energy and that of two non-interacting pions. This difference would vanish in the absence of interactions, even at non-zero lattice spacing. We then assign a relative systematic error to this measured energy difference that is of the same size as is found for other similar quantities computed on this ensemble for which a continuum limit has been evaluated. Thus, we use

$$\frac{\mathrm{Error}(\Delta \mathrm{E})}{\Delta E} = ca^2, \tag{5.37}$$

where c is chosen from the finite lattice spacing errors reported in Ref. [20]. In detail we use the average ChPTFV value of the magnitudes of c_f^{ID}, $c_{f(K)}^{ID}$, $c_{w_0,a}^{ID}$ and $c_{\sqrt{t_0},a}^{ID}$, given in Tab. XVII in that paper which are the four coefficients which describe the a^2 finite lattice spacing errors for these four different physical quantities computed with the same lattice action and gauge coupling as used here. This gives a relative error of 1.6% for ΔE which we round up to 2%.

Note this relative error is usually a small quantity, and therefore a small absolute error when compared with E_π and $E_{\pi\pi}$ since we are calculating the $\pi\pi$ scattering phase shift at relatively low energies (near the kaon mass). The error determined from Eq. (5.37) is then propagated in the standard way to obtain the $O(a^2)$ error for the scattering phase shift which we use for each of our four values of total momentum.

5.4.3 Finite volume

Finite volume affects the energy of $\pi\pi$ states in two ways. The first effect results in the quantized finite-volume energies, is described by the Lüscher quantization condition and can be viewed for large L as a power law effect. The second effect falls exponentially with the system size and is caused by the interaction radius being a finite fraction of the system size or, equivalently, the effect of off-shell singularities when the Poisson summation formula is used to estimate finite-volume effects. This second effect is usually much smaller than the first and is the source of the systematic error considered here. This exponentially suppressed correction for the $I = 2$ channel for periodic boundary conditions can be formulated as [42]:

$$(k\cot\delta(s))_L = (k\cot\delta(s))_\infty + \Delta_{FV}\,, \tag{5.38}$$

where

$$\Delta_{FV} = -\frac{m_\pi}{\sqrt{2\pi}} \sum_{\vec{n},|\vec{n}|\neq 0} \frac{e^{-|\vec{n}|m_\pi L}}{\sqrt{|\vec{n}|m_\pi L}} \left[1 - \frac{227}{24}\frac{1}{|\vec{n}|m_\pi L} + \ldots\right] \tag{5.39}$$

for the case of near-zero relative momentum. According to Fig. 2 from Ref [42], this correction introduces an approximate 1% relative error in the scattering length for a volume with periodic boundary conditions but the same size and physical parameters as the volume with G-parity boundary conditions studied here.

For our G-parity boundary condition lattice, since the pion satisfies anti-periodic boundary conditions, the formula for Δ_{FV} has to be modified as follows:

$$\Delta_{FV} = -\frac{m_\pi}{\sqrt{2\pi}} \sum_{\vec{n},|\vec{n}|\neq 0} \frac{(-1)^{n_x+n_y+n_z} e^{-|\vec{n}|m_\pi L}}{\sqrt{|\vec{n}|m_\pi L}} \left[1 - \frac{227}{24}\frac{1}{|\vec{n}|m_\pi L} + \ldots\right]. \tag{5.40}$$

This leads to a relative error of approximately 0.6%. We round this number up to 1% and adopt it as an estimate of the finite volume effects for our more general case which includes the $I = 0$ channel, non-zero $\pi\pi$ relative momentum and non-zero total momentum.

5.4.4 Unphysical kinematics

The pion mass which we measured on this ensemble is 142.3 MeV, which is 5% larger than our choice for the physical pion mass (135 MeV) at which we wish to determine the scattering phase shifts. We deal with this pion-mass mismatch in two steps. In the first step we shift the $\pi\pi$ energy at which we quote the phase shift, as has been discussed in Sec. 5.3, by expressing the phase shift as a function of the two-pion relative momentum k in the center-of-mass system and then identifying this value of k with a $\pi\pi$ energy using the physical pion mass. We view this

P_{tot}	I	$\sqrt{s}$	$\delta\phi_{\text{unphy}}$	Method
$(0,0,0)\frac{\pi}{L}$	0	471.0(1.5)	0.833°	Linear extrapolation
$(2,0,0)\frac{\pi}{L}$	0	435.1(3.8)	0.708°	Linear extrapolation
$(2,2,0)\frac{\pi}{L}$	0	365.6(3.4)	0.474°	ChPT
$(0,0,0)\frac{\pi}{L}$	2	565.4(5)	0.181°	ChPT
$(2,0,0)\frac{\pi}{L}$	2	479.1(3)	0.025°	ChPT
$(2,2,0)\frac{\pi}{L}$	2	386.7(4)	0.057°	ChPT
$(2,2,2)\frac{\pi}{L}$	2	271.5(4)	0.020°	ChPT

Table 5.8: The assigned values for the systematic error resulting from our unphysical pion mass and the methods used to determine them.

correction, which will be large for energies near the $\pi\pi$ threshold, as the most important effect of this pion-mass mismatch. In the second step we account for the remaining effects of this pion mass mismatch as a systematic error in our result for the phase shift.

We estimate the remaining pion-mass-mismatch error by using ChPT to calculate the difference between the scattering phase shift evaluated at these two different pion masses but at the same value for k. The NLO ChPT prediction for the scattering amplitude of both the I=0 and I=2 channels for small relative momenta are listed in Appendix B, and the predicted phase shift difference as a function of $\sqrt{s}$ is plotted in Fig. 5.9.

There is a remaining uncertainty in this approach that must be resolved. The ChPT calculation is only valid for small k, a condition not valid for our stationary calculation, which results in the rapid rise of the phase shift difference in the $I = 0$ channel when $\sqrt{s} > 380$ MeV. Similar behavior is seen also in the $I = 2$ channel, although the breakdown appears to occur more slowly as a function of $\sqrt{s}$, suggesting the ChPT result for this channel can be considered sufficiently reliable for energies in our range of interest. We modify our systematic error determination for $\sqrt{s} \approx m_K$ to resolve this issue. Notice that the dispersive prediction, whose range of validity is expected to extend above that of ChPT, shows a relation between the phase shift and $\sqrt{s}$ that is close to linear for a broad range of $\pi\pi$ energy, up to and including the kaon mass [9]. This suggests that the relation between the $\sqrt{s}$-dependence of the difference between the two phase shifts with different pion masses will also be linear.

Thus, we can use ChPT to determine the phase shift difference at relatively small $\pi\pi$ energy and then linearly extrapolate to higher energies. Here we perform a linear fit to the ChPT prediction in the range 290 MeV$\leq \sqrt{s} \leq 360$ MeV. For the $I = 2$ channel the ChPT result remains linear over the range of our data so we simply use the ChPT value to determine this I=2 systematic error. Our assignments of these unphysical-pion-mass errors are listed in Tab. 5.8.

5.4.5 Excited state contamination

In Sec. 5.2 we tried different fit ranges to find a balance between minimizing the excited state contamination error and the statistical error. For the preferred fit ranges shown in Tab. 5.2 and 5.3, there is no obvious evidence that the neglected excited states give a significant contribution to the fitting result, as can be seen in the energy plots in Fig. 5.2 and Fig. 5.3. As discussed in Ref. [41], the presence of an apparent plateau in the fitted energy as a function of the lower limit of the fitting range does not imply that we can neglect excited state contamination since the noisy data may make it difficult to find the "true" plateau before the effects of an omitted excited state are obscured by the noise. An important example is our previous result for the ground state $I = 0$ $\pi\pi$ energy obtained from a portion of the current ensemble [1] where we significantly underestimated this error.

A potentially more robust approach to estimating the error from omitted excited states than examining the dependence of the fitted results on t_{min} is to explicitly include an extra excited state in the fit and to determine the size of the systematic shift in the resulting ground-state energy, an approach we call performing an extra-state fit. Of course, in most cases such an extra-state fit will require some additional assumptions since if this fit could have been easily performed we would have included this extra state in our preferred fit. However, while such extra assumptions may have been inappropriate for the determination of the preferred central value, their introduction may be a reasonable approach to estimate an excited-state systematic error.

The difficulty associated with an extra state fit can be illustrated by the single-operator analysis used in Ref. [1] to determine the energy of the stationary $I = 0$, ground state. Tab. 5.9 lists the results from extra-state fits to the single-operator data presented in that earlier paper. In this case

t_{min}	3	4	5
A_0	0.1589(107)	0.1555(133)	0.1538(48)
A_1	0.05974(7064)	0.02679(2305)	$7822(6959) \times 10^3$
E_0	0.3666(124)	0.3643(133)	0.3606(75)
E_1	1.207(725)	0.8429(4071)	4.835(173)
B	$-753(2366) \times 10^{-7}$	$-784(2362) \times 10^{-7}$	$-793(2223) \times 10^{-7}$

Table 5.9: Single-operator two-state fit results with fit ranges $t_{\text{min}} - 25$ for the stationary, $I = 0$ case. The amplitudes A_0 and A_1 are the couplings between the operator and the ground and first excited state, E_0 and E_1 are their energies while B is the around-the-world constant introduced in an analogous fashion as in Eqs. (5.5) and (5.6). The fit procedure fails when $t_{\text{min}} \geq 6$. The single-state fit with fit range $6 - 25$ gives $E_0 = 0.3606(74)$ which is consistent with the ground state energy in all three extra-state fits.

our preferred single-state fit gave a ground state energy $E_0 = 0.3606(74)$ using the fitting range $6 - 25$. We can see that for $t_{\text{min}} < 6$ adding the extra state does not give a ground state energy that can be resolved from the result of the preferred single-state fit. In addition the couplings between the operator and the first excited state are consistent with 0. We cannot perform the extra-state fit within the same fit range as the one we chose for the preferred single-state fit ($6 - 25$) since the fitting procedure does not converge. We conclude that such (unconstrained) extra-state fits can be misleading for data containing multiple nearby states with limited statistics and/or a rapid loss of signal to noise as a function of time where the available fitting range is insufficiently long to adequately distinguish the energy separations among the multiple nearby states.

One strategy to resolve this problem is to fix one or more of the parameters in the extra-state fit. The first parameter we might fix is the energy of the extra state.

A prediction of this finite-volume energy can be obtained by finding the intersects between Lüscher's formula and a phenomenological model, or a fit to our lattice results, for the scattering phase shift as a function of energy. For simplicity we chose to compute this estimate using the dispersive predictions of Ref. [9]. Unfortunately we found that fixing this extra-state energy alone typically does not solve the problem: sometimes the fitting procedure continues to fail while in those cases where the fit converges, it gives a ground-state energy whose statistical error is several times larger than the statistical error on the result from the preferred fit, which suggests that such an approach may over-estimate the excited state error, conflating it with the statistical error.

Thus, further assumptions are needed to obtain a statistically meaningful estimate of this excited-state contamination error. Because of the very different pattern of operator-eigenstate couplings we will adopt two different strategies, one for the $I = 0$ stationary $\pi\pi$ state and the second for the remaining seven cases: the three $I = 0$ calculations with non-zero total momenta and all four $I = 2$ calculations. The method applied for the latter we will refer to as "method A", and that applied in the special $I = 0$ stationary case as "method B".

For the three moving-frame $I = 0$ and all the $I = 2$ calculations, the operator-eigenstate overlap matrix is close to diagonal and the two-point function of a given operator with itself is well described by one exponential coming from a single energy eigenstate. We call the operator which couples primarily to the ground state the "ground-state operator", and the operator whose two-point function is dominated by the n^{th} excited state the "n^{th} excited operator". We can then make the reasonable assumption, that because of the small value of the couplings between the ground-state operator and those excited states that we include in the preferred fit, the extra-state contribution to these small couplings can be neglected. That means that we can focus on the Green's function constructed from the ground-state operator only where the most important effect of an omitted extra state is to change the two parameters (coupling and energy) associated with the ground-state.

The argument above suggests that we can perform a fit to the two-point function constructed from the ground-state operator in which the number of states included is one more than the number in the preferred fit, and that we can fix the couplings between the ground-state operator and the excited states in that fit to those already determined by the preferred fit. Since these couplings are small, we can also fix the energies of those excited states to their values from the preferred fit. To summarize, if our preferred fit involved n operators and m states, we will fit the single ground-state operator two-point function to an expression which includes $m + 1$ states: the m states which appear in our preferred fit and the new extra state. The choice of whether or not to include an around-the-world constant is the same as the choice made for the preferred fit. In this new fit, we fix the extra-state energy to that given by the dispersive prediction and the parameters that are associated with the first $m-1$ excited state energies and their overlap amplitudes with the ground state to those values determined by the preferred fit.

It should be noticed that since the preferred fit and this extra-state fit are performed on data constructed using the same resampling method, these parameters should be fixed sample-by-sample. Thus, for each bootstrap/jackknife sample, the fixed parameters we used will vary: they are the ones obtained from exactly the same sample used when we perform the preferred fit. That leaves us with three (or four) free parameters to be determined in this extra-state fit: the overlap between the ground-state operator and the ground state, the ground-state energy, the overlap between the ground-state operator and the m^{th} excited state (the extra state) and possibly an around-the-world constant. The results are shown in Tab. 5.10 and Tab. 5.11.

Unfortunately, as described this method gives us a statistical error on the ground-state energy that is still much larger than that given by the preferred fit. This may be the understandable consequence of trying to obtain information about two states from a single operator Green's function, a case where the number of states exceeds the number of operators. Some improvement must be made. One possibility is to fix not only the energy of the extra state, but also its coupling with the ground-state operator. In contrast to the energy of the excited state, we do not have external information that could give us a reasonable theoretical value for this overlap amplitude. However, we can argue that the result from the above fit gives us a reasonable estimate for the size of this coupling.

Thus, in the notation introduced in Eq. (5.6) we view $[A_{am}-\delta_{A_{am}}, A_{am}+\delta_{A_{am}}]$ as a reasonable interval for the overlap amplitude between the operator O_a (using a to label the ground-state operator) and the m^{th} excited state (our extra state). Here $\delta_{A_{am}}$ is the statistical error on the quantity A_{am} found in the fit described above. We then perform three fits, where the only difference between them and the one above is that we fix the coupling between the ground-state operator and the m^{th} excited state using A_{am}, $A_{am}-\delta_{A_{am}}$ and $A_{am}+\delta_{A_{am}}$ (Notice that for each bootstrap/jackknife sample, this coupling will **NOT** vary). We then calculate the difference between these three ground-state energies and the ground-state energy obtained from the preferred fit. The largest difference gives our estimate of the excited-state error. The results are shown in Tab. 5.10 for the $I = 2$ channel and Tab. 5.11 for the $I = 0$ channel. As mentioned above, we refer to this method of estimating the excited-state systematic error, based on the near-diagonal character of the matrix of operator-eigenstate overlap amplitudes, as "method A".

While this method gives a statistically precise result for the excited-state contamination error for the three moving-frame $I = 0$ calculations and all four $I = 2$ calculations, the diagonal pattern of the operator-eigenstate overlap matrix upon which it is based is not found for the stationary $I = 0$ channel, where the couplings between the various normalized operators and eigenstates have similar sizes. Consequently, we cannot apply the method A above in this case. We therefore adopt a different approach, referred to as "method B". While we are unable to perform a convergent extra-state fit (3-operator-3-state fit) with the fit range that we chose for the preferred fit (6-15), we can perform that fit using a fit range with a smaller $t_{\rm min}$, provided the extra-state energy is fixed. For convenience, we again give the extra-state energy the value predicted by the dispersive result for the $I = 0$ phase shift. This fit gives us values for the overlap amplitudes for the extra state and each of the three operators being studied. We then perform a 3-operator-3-state fit with the same fit range as the preferred fit (6-15), while fixing all the information about the extra excited state to that obtained from the fit with the decreased value of $t_{\rm min}$. Note that in this case we did not observe a significant increase in the error on the ground-state energy after applying this procedure, hence it was not necessary to perform a second step holding these couplings fixed to the extrema of their error bars as was the case for method A above.

To summarize, the eight parameters that are allowed to vary in this final fit are the six overlap amplitudes between the three operators and the ground and first excited states, and the energies of these two states. We then calculate the energy difference (for present purposes labeled as ΔE) between the ground-state energy obtained from this extra-state fit and the preferred fit and the statistical error on this difference ($\delta\Delta E$). We then use $\delta E_{\rm exc} = \Delta E + \delta\Delta E$ as our estimate of the systematic error on the ground-state energy resulting from excited-state contamination. The results are listed in the right-most column of Tab. 5.11. This small estimate for the excited state error for the $I = 0$ stationary case is supported by the determinant test result in Sec 5.2 where the normalized determinant of the three dimensional matrix of the Green's function is consistent with zero, suggesting that the 3$^{\text{rd}}$ state is difficult to resolve with a fit range where t_{min} is larger than 5.

I=2 channel	$P_{tot} = (2,2,2)\frac{\pi}{L}$	$P_{tot} = (2,2,0)\frac{\pi}{L}$	$P_{tot} = (2,0,0)\frac{\pi}{L}$	$P_{tot} = (0,0,0)\frac{\pi}{L}$
Fit range	10-25	12-25	11-25	10-25
Fit strategy	1op-4state	1op-4state	1op-4state	1op-3state
A_{a0}	0.3935(10)	0.2768(8)	0.1934(3)	0.4206(13)
A_{a1}	**0.004684(565)**	**0.007011(548)**	**0.009301(455)**	**0.01240(1021)**
A_{a2}	**.001209(1890)**	**0.005350(1812)**	**0.005249(1482)**	**0.1641(1176)**
A_{a3}	**-0.07301(3318)**	**0.03847(3424)**	**-0.00001(3132)**	-
E_0	0.3981(4)	0.4000(4)	0.4045(3)	0.4152(6)
E_1	**0.5453(7)**	**0.5480(10)**	**0.5514(9)**	**0.7128(170)**
E_2	**0.6902(28)**	**0.6874(40)**	**0.6916(48)**	**0.9169(0.0000)**
E_3	**0.6923(0.0000)**	**0.6934(0.0000)**	**0.8047(0.0000)**	-
B_{aa}	$8118(71) \times 10^{-9}$	$4036(35) \times 10^{-9}$	$1981(16) \times 10^{-9}$	$9380(152) \times 10^{-9}$
p-value	0.078	0.157	0.268	0.683
δE_{exc}	0.0007	0.0004	0.0002	0.0006

Table 5.10: Results from the fits used to determine the excited state error for the ground-state energies in the $I = 2$ channel. We use method A described in the text to estimate the error for all four total momenta. As described in the text, these results are obtained in two stages. First all of the quantities in bold font except for the extra-state amplitudes (A_{a3} in columns 2-4 and A_{a2} in column 5) are held fixed for the first stage fits. The results from the first stage fits for these four amplitudes are shown in this table. For the second stage fits these four amplitudes are also held fixed at their central values and at their central values plus and minus the statistical error shown. The largest difference between the resulting ground-state energy and the ground-state energy obtained in the preferred fit is shown in the final row and is our estimate of the excited state error.

5.4.6 Error budget

We will now combine all of the errors detailed in the earlier sections to provide values for the seven $\pi\pi$ phase shifts that we have computed at specific energies and their corresponding errors. We divide these errors into two categories. The first are the measurement errors associated with our lattice calculation of the finite-volume $\pi\pi$ energies, which includes the statistical error and the excited state contamination error. As is discussed below, this category of error requires special attention since when we use Lüscher's finite volume formalism to determine the scattering phase shift, errors in this category lead to correlated errors in both the value for the phase shift and the

I=0 channel	$P_{tot} = (2,2,2)\frac{\pi}{L}$	$P_{tot} = (2,2,0)\frac{\pi}{L}$	$P_{tot} = (2,0,0)\frac{\pi}{L}$	$P_{tot} = (0,0,0)\frac{\pi}{L}$
Fit range	6-12	8-15	7-15	6-15
Fit strategy	1op-4state	1op-4state	1op-4state	3op-3state
A_{a0}	0.3861(25)	0.2633(36)	0.1760(37)	0.3638(50)
A_{a1}	**-0.02647(391)**	**-0.04909(1123)**	**-0.05431(776)**	-0.1958(120)
A_{a2}	**-0.01354(312)**	**-0.03005(552)**	**-0.02450(274)**	**0.01537(2140)**
A_{a3}	-0.06485(3778)	-0.03121(4065)	-0.04877(3298)	-
A_{b0}	-	-	-	0.003244(368)
A_{b1}	-	-	-	0.03248(709)
A_{b2}	-	-	-	**0.05802(618)**
A_{c0}	-	-	-	$-4396(72) \times 10^{-7}$
A_{c1}	-	-	-	$-3644(264) \times 10^{-7}$
A_{c2}	-	-	-	**$9394(5883) \times 10^{-8}$**
E_0	0.3972(12)	0.3898(22)	0.3769(39)	0.3474(13)
E_1	**0.5264(37)**	**0.5148(91)**	**0.5032(75)**	0.5484(208)
E_2	**0.6881(93)**	**0.6788(252)**	**0.6514(183)**	**0.6623(0.0000)**
E_3	**0.6649(0.0000)**	**0.6610(0.0000)**	**0.6851(0.0000)**	-
p-value	0.212	0.545	0.953	0.082
δE_{exc}	0.0017	0.0019	0.0052	0.0010

Table 5.11: Results used to determine the excited state error for the ground-state energies in the $I = 0$ channel. We use method A for the three moving-frame results given in columns 2-4, as described for the $I = 2$ states in the text, so the explanation in the caption to Tab. 5.10 applies. Method B is used for the stationary frame calculation whose results are shown in column 5. In the first stage of this procedure, only the extra-state energy E_2 is held fixed and the other three overlap amplitudes (A_{a2}, A_{b2} and A_{c2}), all four shown in bold font, are determined to have the values shown, using the fit range 4-15. In the second stage, these four quanties are fixed to the values shown in the table and the preferred 3-operator-2-state fit carried out with the data effectively shifted by the fixed extra-state contribution. The difference between the ground-state energies determined from this extra-state fit and the preferred fit gives the excited-state error listed in the final row, as described in the text.

energy at which the phase shift is determined.

We refer to the second category of errors as tuning errors. These include the finite volume error, finite lattice spacing error and the unphysical kinematics error. We assign these errors directly to the seven phase shifts. They represent discrepancies between our physical results as presented and those we actually obtain. For example, we describe our results as phase shifts in the continuum limit, but in reality the number we obtain contains finite lattice spacing errors. Similarly we intend our phase shift results to be for the case where $m_\pi = 135$ MeV. In reality, our calculation was done for a different pion mass and we have made a small correction to the energy at which the phase shift is quoted to compensate for the shifted $\pi\pi$ threshold arising from our incorrect mass and, as was discussed in Section 5.4.4, the remaining errors were estimated using ChPT.

Our first category of errors, the measurement errors, requires special treatment if we are to account for the tight correlation between the way the errors on the measured finite-volume energy shift affect both the implied value of the phase shift and the energy at which that phase shift is quoted. The issue is that we do not know the exact value of the finite volume $\pi\pi$ energy E_{FV}, only that it lies with a certain confidence within the range $\bar{E}_{\mathrm{FV}} \pm \Delta E_{\mathrm{FV}}$, where $\bar{E}_{\mathrm{FV}}$ is the central value of the energy and ΔE_{FV} is the error. As a result, naively propagating the error through the evaluation of the Lüscher function would produce a result for which uncertainties exists on both the phase shift and the energy at which it is evaluated, and for which the errors are completely correlated (through the Lüscher function). This unsatisfactory situation can be remedied by transforming the result such that the phase shift is quoted at a fixed value of the energy and the uncertainty exists only on the phase shift. To achieve this we note that the allowed finite-volume energies E_{FV} mark the intersections of the curve $\delta(E)$, which describes the energy dependence of the phase shift, and the Lüscher curve $W(E)$ relating the energy to the phase shift at a fixed lattice size:

$$\delta(E_{\mathrm{FV}}) = W(E_{\mathrm{FV}}). \tag{5.41}$$

We imagine that the true intersect occurs at some energy E that is close to our measured central value $\overline{E}_{\mathrm{FV}}$ and perform a first-order Taylor expansion in E of both sides of Eq. (5.41) about this central value

$$\delta(\overline{E}_{\mathrm{FV}}) + \frac{d\delta(E)}{dE}\bigg|_{\overline{E}_{\mathrm{FV}}}(E - \overline{E}_{FV}) \approx W(\overline{E}_{\mathrm{FV}}) + \frac{dW(E)}{dE}\bigg|_{\overline{E}_{\mathrm{FV}}}(E - \overline{E}_{FV})\,. \tag{5.42}$$

Rearranging the above we obtain an expression for the phase shift evaluated at our measured finite-volume energy $\overline{E}_{\mathrm{FV}}$

$$\delta(\overline{E}_{\mathrm{FV}}) = W(\overline{E}_{\mathrm{FV}}) + \left\{\frac{dW(E)}{dE} - \frac{d\delta(E)}{dE}\right\}_{\overline{E}_{\mathrm{FV}}}\left(E - \overline{E}_{\mathrm{FV}}\right). \tag{5.43}$$

This approach requires an estimate of the derivative of the phase shift $\delta(E)$ with respect to its energy. While this could be obtained from a fit to our data, we find it simplest to use the result from the dispersive analysis [9] which agrees well with our data as can be seen from the comparisons shown in Figures 5.10 and 5.11.

Thus, the statistical and excited state contamination errors on the measured finite-volume energies are each converted to errors on the phase shift at the fixed energy $E = \overline{E}_{\mathrm{FV}}$ using the following relations:

$$\Delta\delta_{\mathrm{stat/exc}} = \left|\frac{dW(E)}{dE} - \frac{d\delta(E)}{dE}\right|_{\overline{E}_{\mathrm{FV}}}\Delta E_{\mathrm{stat/exc}}\,, \tag{5.44}$$

where ΔE_{stat} and ΔE_{exc} are the statistical and excited state contamination errors that are assigned to the measured finite-volume energy. The three tuning errors $\Delta\delta_{\mathrm{dis}}$, $\Delta\delta_{\mathrm{FV}}$, $\Delta\delta_{\mathrm{unphy}}$ coming from non-zero lattice spacing, finite volume and unphysical pion mass are assigned directly to the phase shifts. All of these errors are listed in Tab. 5.12, where the total systematic error shown in the final column is the combination in quadrature of the systematic errors shown in columns 6 through 9.

P_{tot}	I	$\sqrt{s}$(MeV)	δ	$\Delta\delta_{\text{dis}}$	$\Delta\delta_{\text{FV}}$	$\Delta\delta_{\text{unphy}}$	$\Delta\delta_{\text{exc}}$
$(0,0,0)\frac{\pi}{L}$	0	471.0	32.3(10)(14)	0.64	0.32	0.83	0.90
$(2,0,0)\frac{\pi}{L}$	0	435.1	24.0(34)(76)	0.46	0.23	0.71	7.6
$(2,2,0)\frac{\pi}{L}$	0	365.6	18.0(45)(49)	0.36	0.18	0.47	4.9
$(0,0,0)\frac{\pi}{L}$	2	565.4	-10.98(22)(44)	0.20	0.10	0.18	0.34
$(2,0,0)\frac{\pi}{L}$	2	479.1	-7.96(23)(29)	0.16	0.08	0.03	0.23
$(2,2,0)\frac{\pi}{L}$	2	386.7	-4.48(40)(77)	0.09	0.04	0.06	0.76
$(2,2,2)\frac{\pi}{L}$	2	271.5	-0.32(20)(63)	0.01	0.00	0.02	0.63

Table 5.12: The final error budget for each of the seven $\pi\pi$ scattering phase shifts determined in this paper. Here each of the energies ($\sqrt{s}$) is the center-of-mass energy at which the phase shift δ has been determined, adjusted to correct for the unphysical pion mass according to the procedure described in Section 5.3. The right-most four columns are explained in the text. All of the angles appearing in this table are expressed in degrees. Two errors are shown with the phase shift results in the fourth column. The first is statistical and is given in Tab. 5.7. The second is systematic and is the average in quadrature of the individual errors shown in columns 5-8.

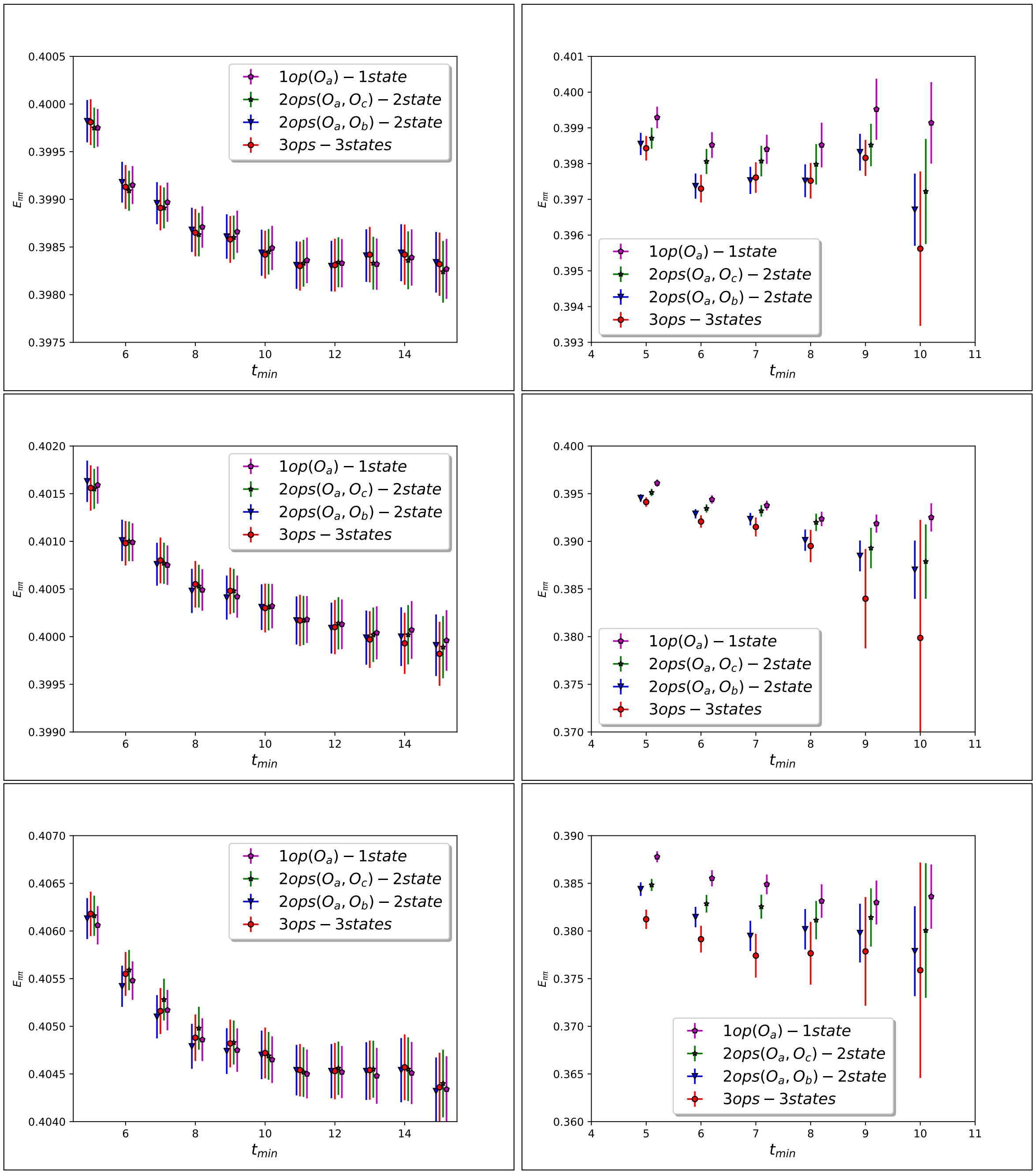

Figure 5.3: The $t_{\min}$ dependence of the fitted ground state energy for the moving $\pi\pi_{I=2}$ channel (left) and moving $\pi\pi_{I=0}$ channel (right) with $t_{\max} = 25$ ($I = 2$) and 15 ($I = 0$). The upper, middle and lower panels are for total momenta $(2, 2, 2)\frac{\pi}{L}$, $(2, 2, 0)\frac{\pi}{L}$ and $(2, 0, 0)\frac{\pi}{L}$, respectively. Our final results were obtained from three-operator, three-state fits. Reading from top to bottom the values of $t_{\min}$ for these results were for $I = 2$ $t_{\min} = 10, 12, 11$ and for $I = 0$ $t_{\min} = 6, 8$ and 7.

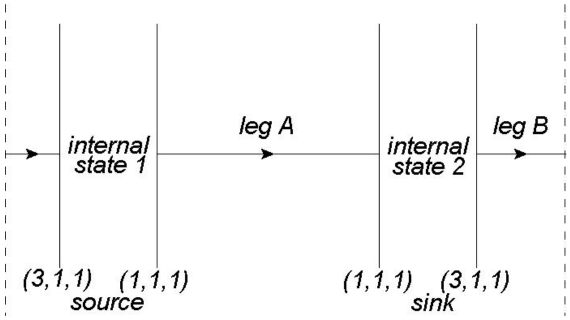

Figure 5.4: A typical diagram for the decomposition of the ATW effect when the Green's function is constructed from two O_b operators. For the first-order ATW effect, both legs are pions with momentum $(1,1,1)\pi/L$, which means if one of the internal states is the vacuum, e.g., internal state 1, then the other internal state cannot be the vacuum. For the second order ATW effect, we can choose leg A to be $(1,1,1)\pi/L$ and leg B to be $(3,1,1)\pi/L$, while keeping both internal states to be the vacuum state.

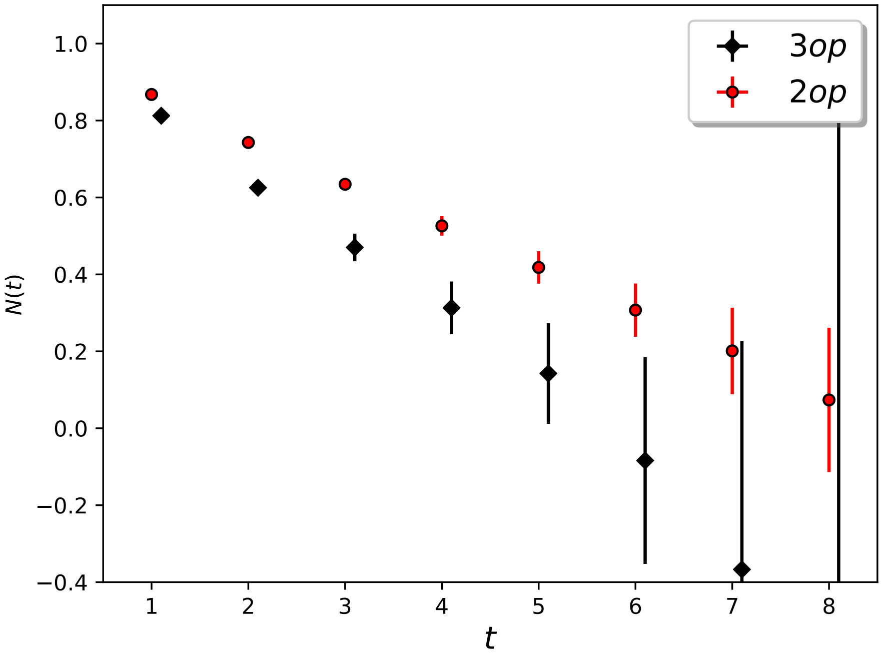

Figure 5.5: The t dependence of $\mathcal{N}(t)$, defined in Eq. (5.12) for the three dimensional (black, which include all operators) and two dimensional (red, only include O_a and O_c operator) matrix of Green's functions for the stationary $I = 0$ case.

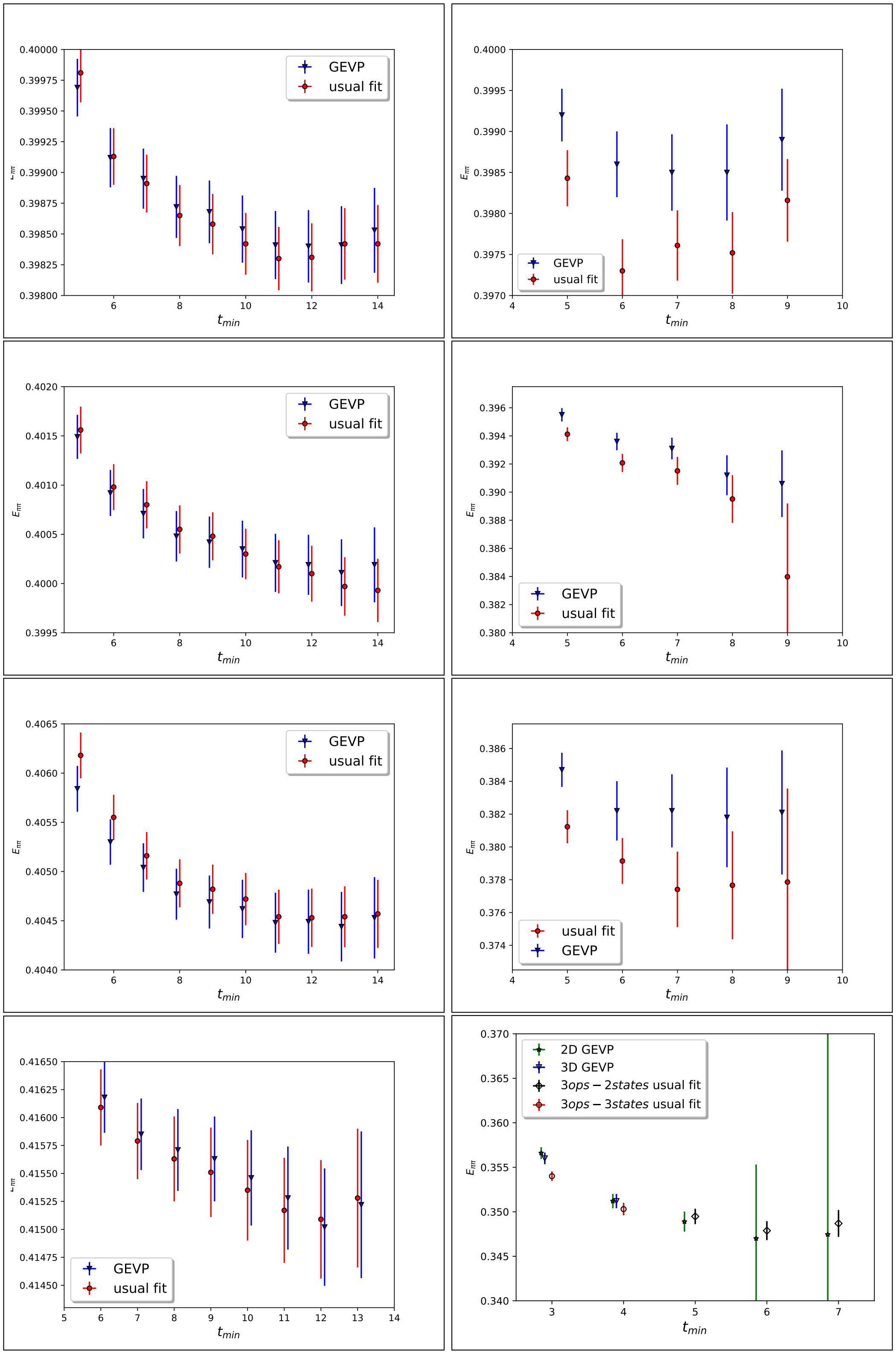

Figure 5.6: The t_{min} or t_0 dependence of the fitted ground state energy from the GEVP and the usual fit for the $\pi\pi_{I=2}$ (left) and $\pi\pi_{I=0}$ (right) channel with $t_{\text{max}} = 20$ ($I = 2$) and 15 ($I = 0$). The total momenta from the top down are $(2,2,2)\frac{\pi}{L}$, $(2,2,0)\frac{\pi}{L}$, $(2,0,0)\frac{\pi}{L}$ and 0. Here the x-axis represents t_{min} for the usual fit, and t_0 for the GEVP fit. In the legend of the lower right panel, 2D and 3D indicate a 2×2 and 3×3 GEVP matrix.

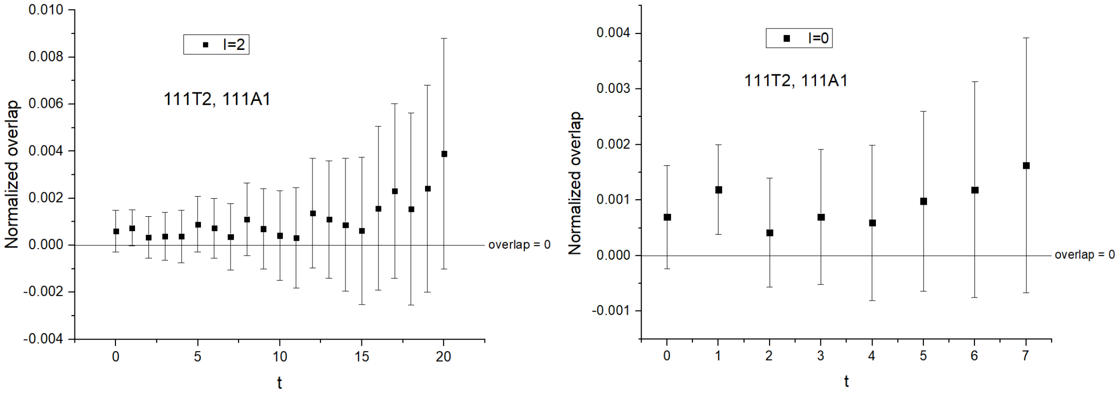

Figure 5.7: The overlap amplitudes between the $\pi\pi^{A_1}(111, 111)$ and $\pi\pi^{T_2}(111, 111)$ operators in the isospin $I = 2$ (left) and $I = 0$ (right) channels. The overlaps amplitudes are consistent with zero at all time separations which implies negligible cubic symmetry breaking for the $\pi\pi(111, 111)$ interpolating operators.

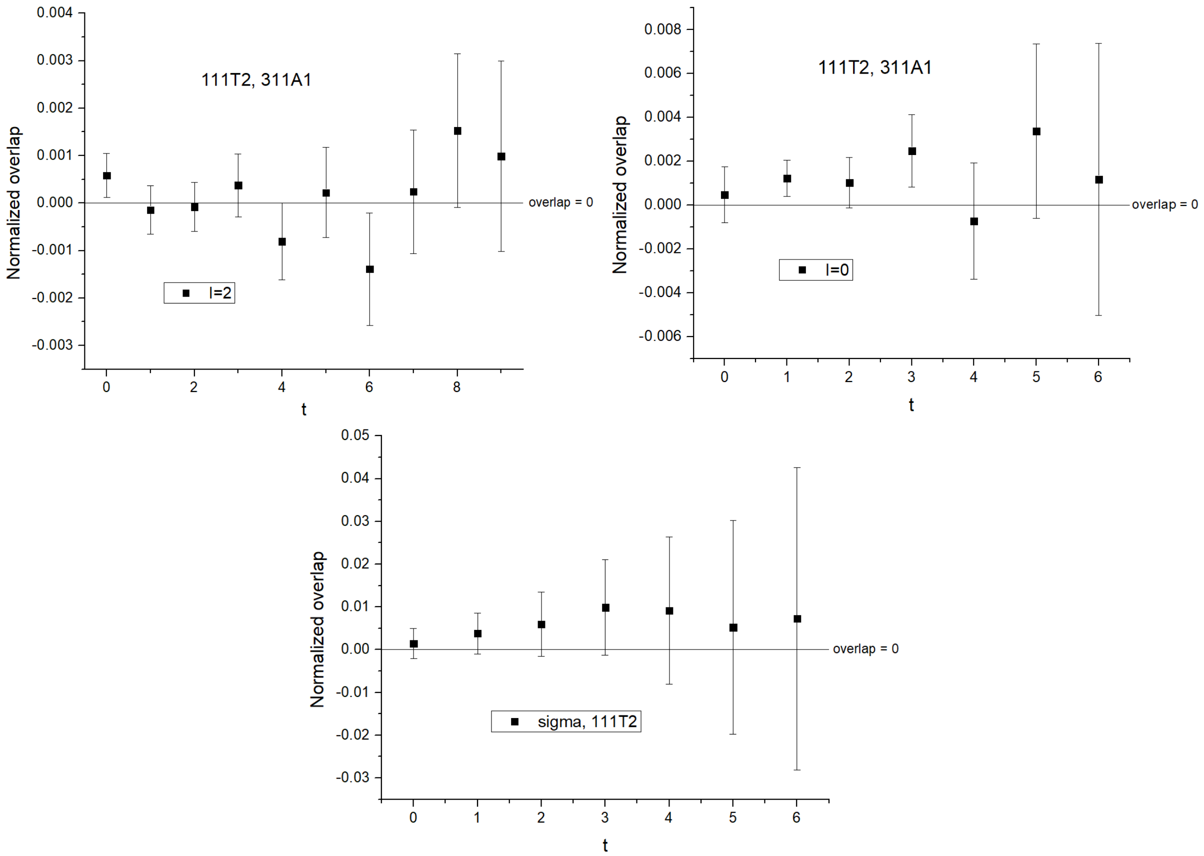

Figure 5.8: Upper: the overlap amplitudes between the normalized $\pi\pi^{T_2}(111, 111)$ operator and the normalized $\pi\pi^{A_1}(311, 311)$ operator in the isospin $I = 2$ (left) and $I = 0$ (right) channels. Lower: the overlap amplitude between the normalized σ operator and the normalized $\pi\pi^{T_2}(111, 111)$ operator. All overlap amplitudes are consistent with zero with errors more than two orders of magnitude smaller than one which implies a negligible cubic symmetry breaking for these $\pi\pi(311, 311)$ and σ interpolating operators.

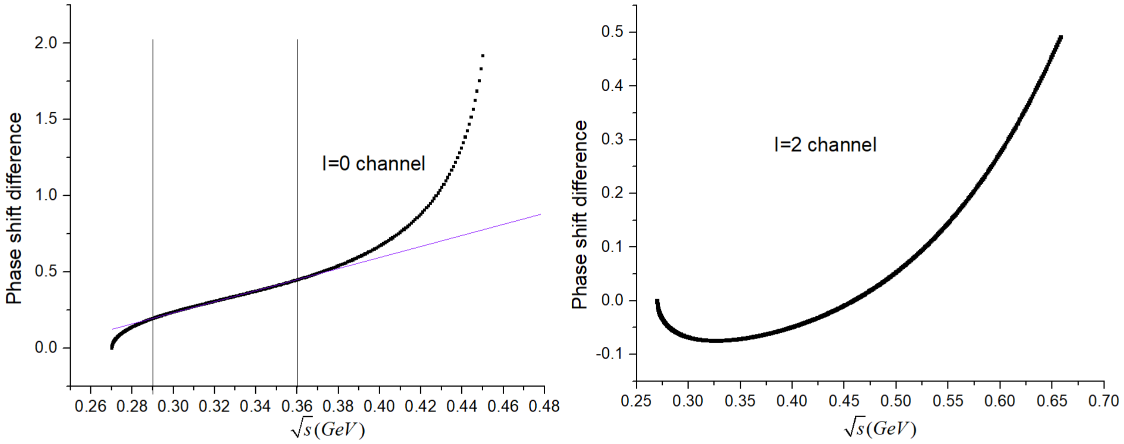

Figure 5.9: A ChPT calculation of the difference between the scattering phase shift evaluated at the physical pion mass and the pion mass calculated for our ensemble, $\delta_I(m_\pi = 142\text{ MeV}) - \delta_I(m_\pi = 135\text{ MeV})$, as a function of $\sqrt{s}$ defined in Eq. (5.27) and shown in degrees. For the $I = 0$ channel, at large $\sqrt{s}$, the ChPT calculation begins to break down while at lower $\sqrt{s}$, the relation is approximately linear, which is consistent with the dispersive prediction. The straight line is a linear fit to the ChPT result in the region $290\,\text{MeV} \leq \sqrt{s} \leq 360\,\text{MeV}$.

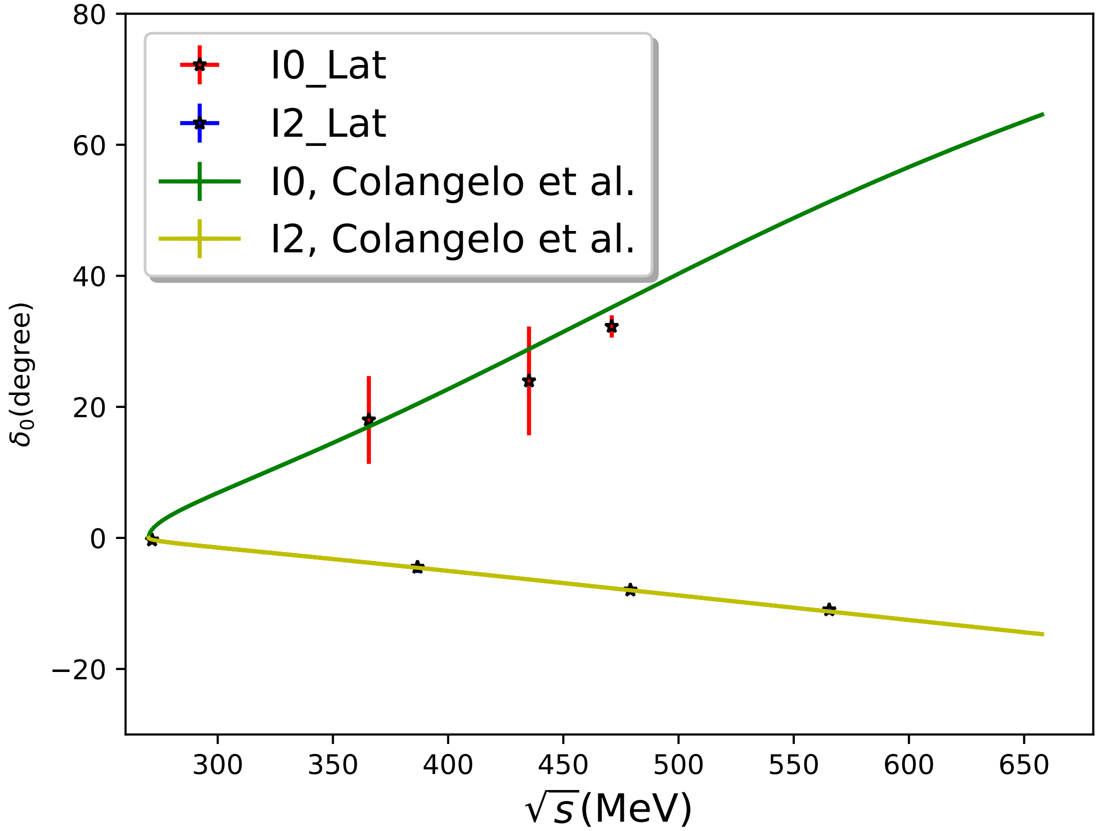

Figure 5.10: A graph of our results for the seven phase shifts for $I = 0$ and $I = 2$ as a function of energy. Shown also on the plot are the corresponding dispersive results [9]. Note: the errors are not shown for the dispersive results.

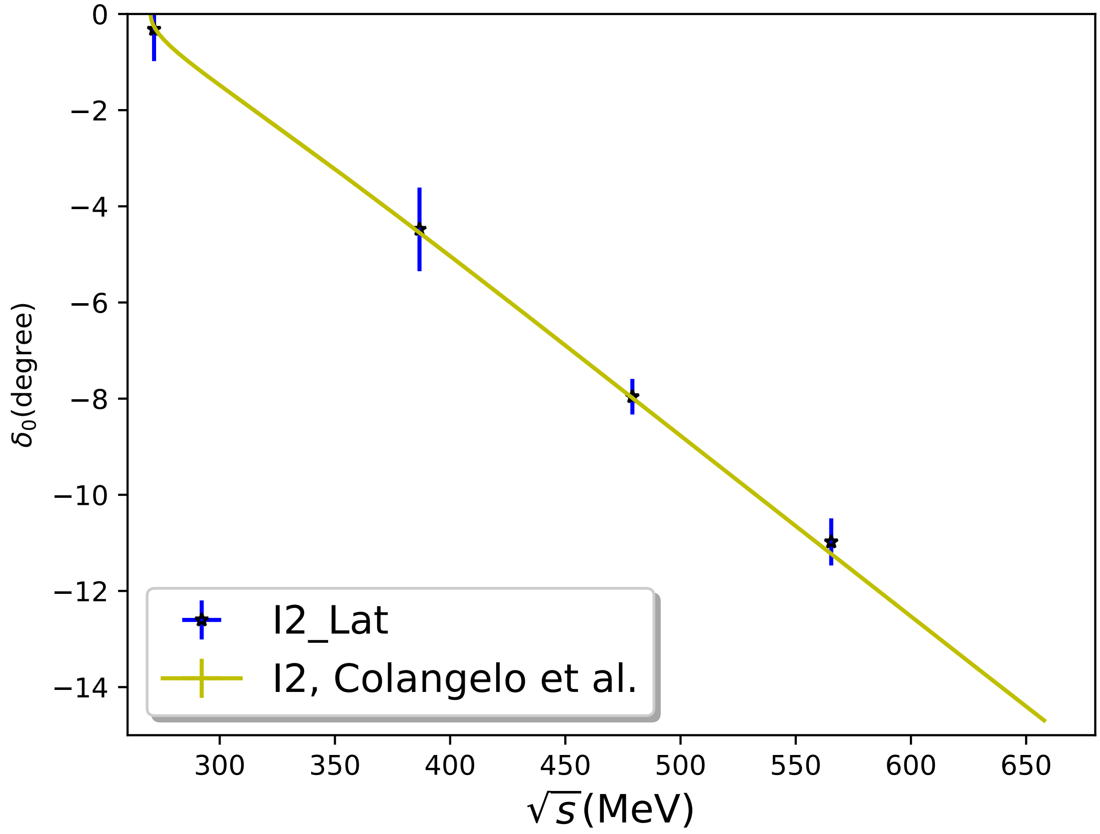

Figure 5.11: The results for the $I = 2$ phase shifts together with the corresponding dispersive results [9] that are shown in Fig. 5.10, but here with an expanded scale.

Chapter 6: Results for the $K \to \pi\pi$ decay amplitude

In this chapter we summarize our previous work on the $K \to \pi\pi$ decay amplitude calculation[16]. In the first section we discuss the result for the kaon two point function. In the second section we discuss how we obtain the optimal $\pi\pi$ operator that maximally projects onto the $\pi\pi$ ground state. In the third section we discuss the results for the finite volume $K \to \pi\pi$ matrix element. In the fourth section we discuss the non-perturbative renormalization procedure and its result. In the last section we summarize the procedure to determine A_0 and ϵ' and present the result.

6.1 Kaon two-point function and its result

In order to compute the $K \to \pi\pi$ matrix elements it is necessary to measure the energies and amplitudes of the pion, kaon and $\pi\pi$ two-point Green's functions. In this section we present results for the kaon two-point function. The results of the pion and $\pi\pi$ two-point functions can be found in Chapter. 5.

The two-point function

$$C_K(t_1, t_2) = \langle 0|O^{\dagger}_{\tilde{K}^0}(t_1) O_{\tilde{K}^0}(t_2)|0\rangle \tag{6.1}$$

is measured for all t_1 and t_2, and subsequently averaged over t_2 at fixed $t = t_1 - t_2$. The data are folded in t, *i.e.* data with $t = t_1 - t_2$ are averaged with those with $t = L_T - (t_1 - t_2)$, where L_T is the lattice temporal extent, to improve statistics. We perform correlated fits to the following function,

$$C_K(t) = A_K \left(e^{-m_K t} + e^{-m_K(L_T - t)}\right) , \tag{6.2}$$

where the second term accounts for the state propagating backwards in time through the lattice temporal boundary. The chosen fit range, p-value and the results of the fit are given in Tab. 6.1, where the results for pion are the same as those given in Tab. 5.1. In physical units our kaon mass is 490.5(2.4) MeV, which is within 2% of the physical neutral kaon mass.

State	Fit Range	A	E	p-value
Kaon	10-29	$4.5964(48) \times 10^6$	0.35587(10)	0.88
Pion	14-29	$6.194(11) \times 10^6$	0.19893(13)	0.99

Table 6.1: Fit results in lattice units, fit ranges and p-values for the pion and kaon states. Here E is the energy of the state in question, which for the kaon is equal to the kaon mass, m_K.

6.2 Optimal $\pi\pi$ operator

For later use in this work, we define here an optimal operator that maximally projects onto the $\pi\pi$ ground state relative to the first-excited state.

Under the excellent assumption that the backwards-propagating component of the time dependence is small in the fit window, the two-point functions can be described as a sum of exponentials:

$$C^{\pi\pi}_{\alpha\beta}(t) = \sum_i A^i_\alpha A^i_\beta e^{-E_i t}\,, \tag{6.3}$$

where again Greek indices denote operators and Roman indices states. We wish to define an optimized operator that projects onto the ground state:

$$O_{\rm opt} = \sum_\alpha O_\alpha r_\alpha\,, \tag{6.4}$$

for which

$$\begin{aligned} C^{\pi\pi}_{\rm opt}(t) &= \langle 0|O^\dagger_{\rm opt}(t)O_{\rm opt}(0)|0\rangle \\ &\approx [A^0_{\rm opt}]^2 e^{-E_0 t}\,, \end{aligned} \tag{6.5}$$

where the approximate equality indicates that additional exponential terms resulting from excited-state contamination, although suppressed, still exist for an optimal operator composed of a finite number of $\pi\pi$ operators. Expanding the Green's function,

$$\begin{aligned} \langle 0|O^\dagger_{\rm opt}(t)O_{\rm opt}(0)|0\rangle &= \sum_{\alpha\beta} r_\alpha \langle 0|O^\dagger_\alpha(t)O_\beta(0)|0\rangle r_\beta \\ = \sum_i \sum_{\alpha\beta} r_\alpha A^i_\alpha A^i_\beta r_\beta e^{-E_i t} &= \sum_i \left[\sum_\alpha A^i_\alpha r_\alpha\right]^2 e^{-E_i t}\,. \end{aligned} \tag{6.6}$$

Without loss of generality we can fix $A^0_{\rm opt} = 1$, which alongside Eq. (6.5) is sufficient to define r_i:

$$\sum_\alpha A^i_\alpha r_\alpha = \delta_{i,0}\,. \tag{6.7}$$

If the number of states is equal to the number of operators this can be interpreted as a matrix equation,

$$\mathbf{A}\vec{r} = \hat{0}\,, \tag{6.8}$$

where the row index of $\mathbf{A}$ is the state index i and the column index the operator index α. Here $\hat{0}$ is a unit vector in the 0-direction, and as such

$$\vec{r} = \mathbf{A}^{-1}\hat{0}\,. \tag{6.9}$$

which gives

$$r_\alpha = [\mathbf{A}^{-1}]_{\alpha,0} \tag{6.10}$$

i.e. $\vec{r}$ is the first column of the inverse matrix.

As our $\pi\pi$ fits include only two states, we drop the noisier $\pi\pi(311)$ operator in order to form a square matrix of correlation functions. We then obtain

$$\vec{r}^{\,T} = (5.24(18)\times 10^{-7}, -2.86(17)\times 10^{-4}) \tag{6.11}$$

where the elements are the coefficients of the $\pi\pi(111)$ and σ operators, respectively. In Fig. 6.1 we compare the effective energy obtained with the optimal operator to that of the $\pi\pi(111)$ and σ operators alone. We observe a marked reduction in the ground-state energy and a noticeable improvement in the length of the plateau region resulting from the removal of excited-state contamination, as well as a significant improvement in the statistical error. This optimal operator will also be used in our matrix element fits in the following section.

6.3 Results from three-point correlation functions for $\Delta I = 1/2$, $K \to \pi\pi$ decays

In this section we detail the measurement and fitting of the $K \to \pi\pi$ three-point Green's functions, from which the unrenormalized matrix elements $\langle(\pi\pi)_{I=0}|Q_i|K^0\rangle$ are obtained.

6.3.1 Overview of measurements

On the lattice we measure the following three-point functions,

$$C_i(t, t_{\rm sep}^{K\to{\rm snk}}) = \langle 0|O_{\rm snk}^\dagger(t_{\rm sep}^{K\to{\rm snk}})Q_i(t)O_{\bar{K}^0}(0)|0\rangle\,, \tag{6.12}$$

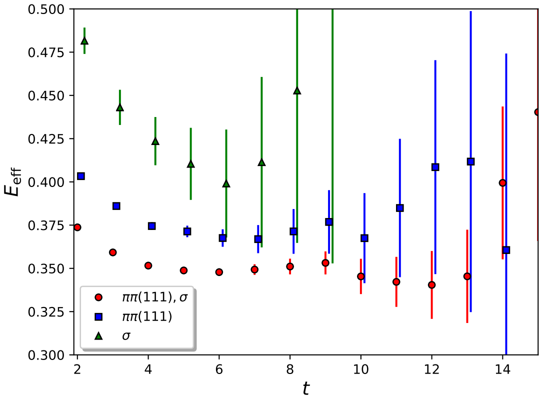

Figure 6.1: A comparison of the effective ground-state energy obtained from the optimal operator (*i.e.* the optimal combination of the σ and $\pi\pi(111)$ operators, and labeled "$\pi\pi(111)$, σ" here) with the energies obtained from the σ and $\pi\pi(111)$ operators separately.

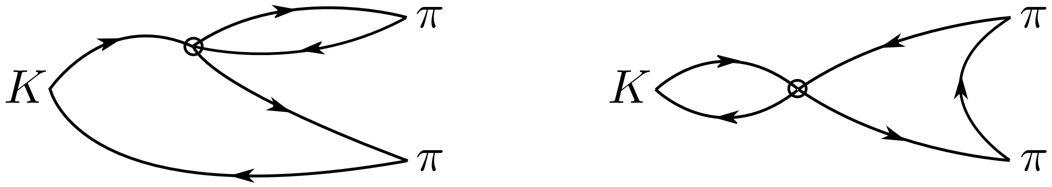

(a) *type1*

(b) *type2*

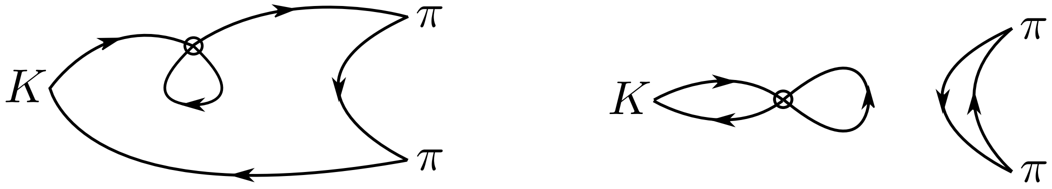

(c) *type3*

(d) *type4*

Figure 6.2: The four classes of $K \to \pi\pi$ Wick contractions.

where t denotes the time separation between the kaon and four-quark operators, and $t_{\text{sep}}^{K\to\text{snk}}$ the time separation between the kaon and the $\pi\pi$ "sink" operator, O_{snk}. As described in Ref. [43], the Wick contractions of these functions fall into four categories based on their topology, as illustrated in Fig. 6.2.

Note that here and below we take care to differentiate between the G-parity kaon state $\tilde{K}^0$, which is a G-parity even eigenstate of the finite-volume Hamiltonian, and the physical kaon K^0 that is not an eigenstate of the system. The matrix elements of the physical kaon are related to those of the G-parity kaon by a constant multiplicative factor of $\sqrt{2}$ that serves as the analogue of the Lellouch-Lüscher finite-volume correction as described in Sec. VI.B. of Ref. [13].

In order to maximize statistics we translate the three-point function over multiple kaon timeslices and average the resulting measurements. As the statistical error is dominated by the *type3* and *type4* diagrams these are measured with kaon sources on every timeslice, $0 \leq t_K < L_T$. The far more precise *type1* and *type2* contributions are measured every eighth timeslice in order to reduce the computational cost. For the remainder of this section we will assume all correlation functions to have been averaged over the kaon timeslice where appropriate.

We compute each diagram with 5 different time separations between the kaon and the $\pi\pi$ sink operators, $t_{\rm sep}^{K\to{\rm snk}} \in \{10, 12, 14, 16, 18\}$, with the $\Delta S = 1$ four-quark operator inserted on all intervening timeslices. Note these five time separations specify the time between the kaon operator and the closest single-pion factor in the $\pi\pi$ operator for those cases when the $\pi\pi$ operator is a product of single-pion operators evaluated on different time slices. (This convention of specifying the minimum time separation from those $\pi\pi$ operators which are non-local in the time is followed throughout this chapter.) As these $\pi\pi$ operators comprise back-to-back moving pions with zero total momentum, we must measure each diagram for all possible orientations of the pion momenta in order to project onto the rotationally symmetric state.

The *type3* and *type4* diagrams both contain a light or strange quark loop beginning and ending at the operator insertion point that results in a quadratic divergence regulated by the lattice cutoff. This divergence is removed by defining the subtracted operators [43, 44],

$$Q_i \to Q_i - \alpha_i \bar{s}\gamma^5 d\,. \tag{6.13}$$

We will henceforth denote the unsubtracted operator with a hat notation, $\hat{Q}_i$. The coefficients α_i in Eq. (6.13) are defined by imposing the condition,

$$\langle 0|\Big\{\hat{Q}_i(t) - \alpha_i(t)[\bar{s}\gamma^5 d](t)\Big\}O_{\bar{K}^0}(0)|0\rangle = 0\,, \tag{6.14}$$

where we have allowed α_i to vary with time as this was found to offer a minor statistical improvement. Although the matrix element of this pseudoscalar operator vanishes by the equations of motion for energy-conserving kinematics and is therefore not absolutely necessary for our calculation, the subtraction reduces the systematic error resulting from the small difference between our

$\pi\pi$ and kaon energies while simultaneously reducing the statistical error and suppressing excited-state contamination.

Due to having vacuum quantum numbers, the $I = 0$ $\pi\pi$ operators project also onto the vacuum state and this off-shell matrix element dominates the signal unless an explicit vacuum subtraction is performed,

$$C_i(t, t_{\rm sep}^{K\to{\rm snk}}) \to C_i(t, t_{\rm sep}^{K\to{\rm snk}}) - \langle 0|O^\dagger_{\rm snk}(t_{\rm sep}^{K\to{\rm snk}})|0\rangle\langle 0|Q_i(t)O_{\bar{K}^0}(0)|0\rangle\,. \tag{6.15}$$

However, due to our definition of the subtraction coefficient α_i in Eq. (6.14), the vacuum matrix elements appearing in the right-hand side vanish making this subtraction unnecessary. In practice this cancellation is not exact in our numerical analysis for the following reason: While the $\pi\pi$ "bubble" $\langle 0|O^\dagger_{\rm snk}|0\rangle$ is formally time-translationally invariant we observed a minor statistical advantage in evaluating this quantity with the $\pi\pi$ operator on the same timeslice as it appears in the full disconnected Green's function that is being subtracted, such that it is maximally correlated. Therefore, for the right-most term in Eq. (6.15) we compute

$$\frac{1}{n_{t_K}}\sum_{t_K\,\in\{t_K\}}\langle 0|O^\dagger_{\rm snk}(t_K + t_{\rm sep}^{K\to{\rm snk}})|0\rangle\langle 0|\left\{\hat{Q}_i(t+t_K) - \alpha_i(t)[\bar{s}\gamma^5 d](t+t_K)\right\}O_{\bar{K}^0}(t_K)|0\rangle\,, \tag{6.16}$$

where t_K is the kaon timeslice and $\{t_K\}$ the set of timeslices upon which measurements were performed, i.e. with the product of the K →vacuum matrix element and the $\pi\pi$ bubble performed under the average over the kaon source timeslice rather than after. As suggested by the above, the coefficients $\alpha_i(t)$ are computed separately from the t_K-averaged matrix elements and therefore the cancellation between the two terms in brackets is exact only up to the degree to which the time translation symmetry is realized at finite statistics. Due to our large statistics we found the difference in the fitted Q_6 matrix element obtained with and without the vacuum subtraction to be at the 0.1% level.

We perform measurements with all three two-pion operators described in Sec. 4.1. For the $K \to \pi\pi$ matrix elements of the four-quark operators, the full set of Wick contractions for the $\pi\pi(111)$ and $\pi\pi(311)$ sink operators can be found in Appendix B.1 and B.2 of Ref. [14], and those of the σ operator in Appendix D of this document. The Wick contractions for the $K \to \pi\pi$ matrix

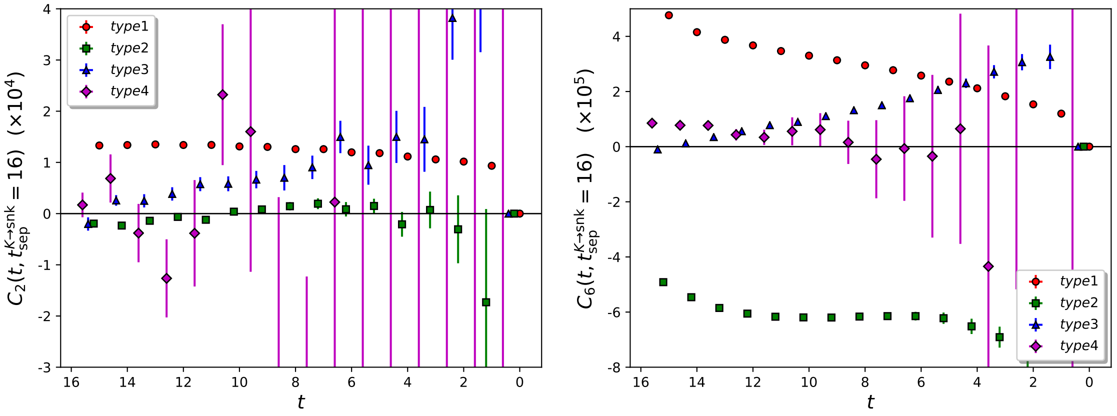

Figure 6.3: The contributions of the four Wick contraction topologies *type1*-*type4* to the C_2 (left) and C_6 (right) three-point functions with the $\pi\pi(111)$ sink operator, plotted as a function of the time separation between the kaon and the four-quark operator, t, at fixed $t_{\rm sep}^{K\to{\rm snk}} = 16$. For clarity we plot with an inverted x-axis such that the $\pi\pi$ sink operator is on the left-hand side. These correlation functions include the subtraction of the pseudoscalar operator.

elements of the pseudoscalar operator (with all three sink operators) as well as the K →vacuum matrix elements of this and the four-quark operators are provided in Appendix E of this document.

In Fig. 6.3 we plot the contributions of the four classes of Wick contraction illustrated in Fig. 6.2 to the three-point functions of the (subtracted) Q_2 and Q_6 operators with the $\pi\pi(111)$ sink operator. As the individual topologies are not separately interpretable as Green's functions of the QCD path integral, their time dependence is not necessarily described by the propagation of physical eigenstates of the QCD Hamiltonian. As such we cannot combine our data sets with different $t_{\rm sep}^{K\to{\rm snk}}$ when generating such plots, and instead plot with a single, fixed $t_{\rm sep}^{K\to{\rm snk}} = 16$. Despite the inability to interpret the time dependence physically, we can look at the relative contributions of each topology within the central region of the plot in which the behavior of the combined data is dominated by the kaon and $\pi\pi$ ground-states, i.e. the region in which we perform our fits below. Our final choices of cut incorporate data from this set in the range $6 \leq t \leq 11$ (cf. Sec. 6.3.5). In this window we observe that for both the C_2 and C_6 correlation functions, the contribution of the noisy, *type4* disconnected diagrams is largely consistent with zero, albeit with much larger errors for the former. C_2 appears dominated by the *type1* and *type3* diagrams, which both contribute with the same sign, with a negligible contribution from the *type2* diagrams. The contribution of the *type1* and *type3* diagrams appears to behave similarly for the C_6 three-point function, however here we observe a strong cancellation between those and the *type2* diagrams.

6.3.2 Determination of α_i

The subtraction coefficients α_i are computed via Eq. (6.14) as the following ratio of two-point functions,

$$\alpha_i(t) = \frac{\langle 0|\hat{Q}_i(t)O_{\bar{K}^0}(0)|0\rangle}{\langle 0|[\bar{s}\gamma^5 d](t)O_{\bar{K}^0}(0)|0\rangle}\,, \tag{6.17}$$

where the average of the correlation functions over the kaon source timeslice is implicit as above.

The Wick contractions for the $\langle 0|\hat{Q}_i(t)O_{\bar{K}^0}(0)|0\rangle$ two-point functions are identical to the components of the *type4* $K \to \pi\pi$ diagrams that are connected to the kaon. While these connected components are formally independent of the sink two-pion operator, in practice these quantities were computed using code that was organized differently for the $\pi\pi$ and σ operators. As described in Appendix E of this work and Appendix B.2 of Ref. [14], the factors entering the *type4* diagrams that determine the α_i were constructed from two separate bases of functions of the quark propagators, one for the σ and the other for the $\pi\pi(\ldots)$ operators, where for each basis γ^5 hermiticity was used in a different way. While γ^5 hermiticity is an exact relation, the fact that we are using a stochastic approximation for the high modes of the all-to-all propagator allows small differences to arise between the values of the α_i computed in these two bases. We therefore have separate results for the α_i from the $\pi\pi$ and σ three-point functions calculations.

In Fig. 6.4 we plot the time dependence of the α_i for all ten operators. We observe excellent agreement between the results obtained from the two different bases of contractions as expected. For a number of operators we find statistically significant but relatively small excited-state contamination for small t that in all cases appears to die away by $t = 6$. While the effects of this contamination are unlikely to significantly affect our final results, the cuts that we later apply to our fits nevertheless exclude data with $t < 6$.

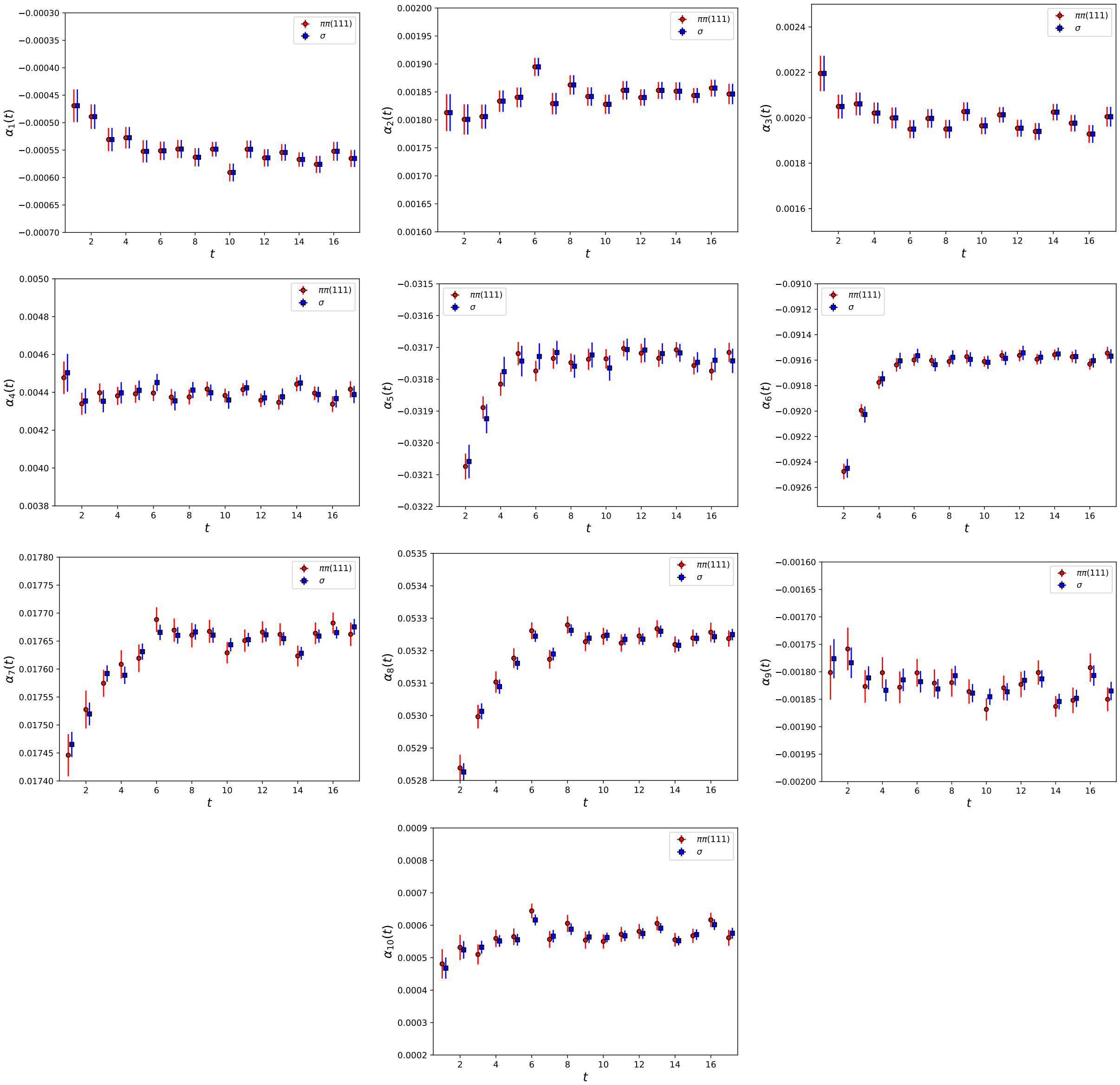

Figure 6.4: The pseudoscalar subtraction coefficient α_i as a function of time for each of the ten operators in the following order: $\hat{Q}_1$-$\hat{Q}_3$ on the first line, $\hat{Q}_4$-$\hat{Q}_6$ on the second, $\hat{Q}_7$-$\hat{Q}_9$ on the third and $\hat{Q}_{10}$ on the fourth. Red circles denote data obtained in the basis of correlation functions used for the $\pi\pi(111)$ operator, and blue squares for the σ sink operator.

6.3.3 $\langle\pi\pi|\bar{s}\gamma^5 d|\tilde{K}^0\rangle$ matrix elements

The $K \to \pi\pi$ matrix elements of the pseudoscalar operator $\bar{s}\gamma^5 d$ are required to perform the subtraction of the divergent loop contribution. In this section we independently analyze these matrix elements in order to understand their time dependence and the corresponding effect of the subtraction on the amount of excited state contamination in the final $K \to \pi\pi$ result.

In the limit of large time separation between the source/sink operators and the four-quark operator, only the lowest-energy $\pi\pi$ and kaon states are present. Since the pseudoscalar matrix elements vanish by the equations of motion when the decay conserves energy and the kaon and $\pi\pi$ ground-state energies in our calculation differ by only 2%, we expect the subtraction to result in only a negligible shift in the central value but a marked improvement in the statistical errors in this limit. However at finite time separations, the contributions of the excited states may take a long time to die away due to the increasing magnitude of the corresponding matrix elements between initial and final states of different energies. It is this concern that prompts us to study this system more carefully.

The lattice three-point function

$$C_P(t, t_{\rm sep}^{K\to{\rm snk}}) = \langle 0|O^\dagger_{\rm snk}(t_{\rm sep}^{K\to{\rm snk}})\ [\bar{s}\gamma^5 d](t)\ O_{\tilde{K}^0}(0)|0\rangle \tag{6.18}$$

for a generic sink $\pi\pi$ operator, $O_{\rm snk}$, has the following time dependence:

$$C_P(t, t_{\rm sep}^{K\to{\rm snk}}) = \sum_{ij} A^i_{\rm in} A^j_{\rm out} M_P^{ij} \exp\left(-E^i_{\rm in} t\right) \exp\left(-E^j_{\rm out}(t_{\rm sep}^{K\to{\rm snk}} - t)\right)\,, \tag{6.19}$$

where the subscript 'in' refers to the incoming kaonic state, 'out' to the outgoing two-pion state, and M_P^{ij} is the matrix element for the term involving in and out states i and j, respectively. It is convenient to define an "effective matrix element" by dividing out the ground-state time dependence and operator amplitudes,

$$M_P^{\rm eff,snk}(t', t_{\rm sep}^{K\to{\rm snk}}) = M_P^{00} + \sum_{i,j\neq 0} A'^{i}_{\rm in} A'^{j}_{\rm out} M_P^{ij} \exp\left(-\Delta E^i_{\rm in}(t_{\rm sep}^{K\to{\rm snk}} - t')\right) \exp\left(-\Delta E^j_{\rm out} t'\right)\,, \tag{6.20}$$

where

$$t' = t_{\rm sep}^{K\to{\rm snk}} - t \tag{6.21}$$

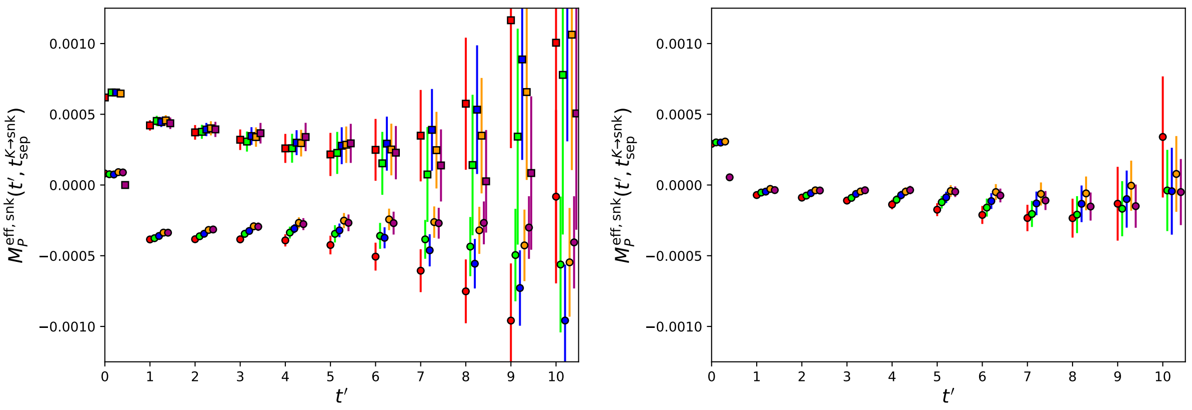

Figure 6.5: The effective pseudoscalar matrix element $M_P^{\rm eff,snk}$ as a function of the time separation between the four-quark operator and the sink, t'. In the left pane we show the data for the $\pi\pi(111)$ operator (circles) and the σ operator (squares) separately, and in the right pane we show the same for the optimal operator. Colored data correspond to the different $t_{\rm sep}^{K\to{\rm snk}}$ as follows: red (10), green (12), blue (14), orange (16) and mauve (18). The data for each of these different separations are staggered in order such that $t_{\rm sep}^{K\to{\rm snk}} = 10$ is the left-most point of each cluster and $t_{\rm sep}^{K\to{\rm snk}} = 18$ the right-most.

is the separation between the four-quark operator and the sink and

$$A'^{i}_{\rm in/out} = A^{i}_{\rm in/out}/A^{0}_{\rm in/out}\,, \tag{6.22a}$$

$$\Delta E^{i}_{\rm in/out} = E^{i}_{\rm in/out} - E^{0}_{\rm in/out}\,. \tag{6.22b}$$

Note that $M_P^{\rm eff,snk}$ is dependent on the sink operator through the terms involving the excited states, in which a ratio of ground and excited state amplitudes appears.

We measure the correlation function Eq. (6.18) for each of our three two-pion operators. Note that a vacuum subtraction is also required here and is performed in the same way as for the four-quark operators. In Fig. 6.5 we plot $M_P^{\rm eff,snk}$ for the $\pi\pi(111)$ and σ operators for each of the five values of $t_{\rm sep}^{K\to{\rm snk}}$. The corresponding data for the $\pi\pi(311)$ operator is much noisier and has therefore been excluded. The form of this plot can be explained as follows: As $E^0_{\rm in} \approx E^0_{\rm out}$ we expect M_P^{00} to be small. If we then assume that the dominant excited state contributions come from the term involving the excited kaon state and ground $\pi\pi$ state ($i = 1, j = 0$) and the term with the ground kaon state and the first excited $\pi\pi$ state ($i = 0, j = 1$), then we expect the data to behave as

$$M_P^{\rm eff,snk}(t', t_{\rm sep}^{K\to{\rm snk}}) \approx A'^{1}_{\rm in} M_P^{10} \exp\left(-\Delta E^1_{\rm in} t_{\rm sep}^{K\to{\rm snk}}\right) \exp\left(+\Delta E^1_{\rm in} t'\right) + A'^{1}_{\rm out} M_P^{01} \exp\left(-\Delta E^1_{\rm out} t'\right)\,. \tag{6.23}$$

This ansatz then implies an exponentially falling contribution from the excited pion state and an exponentially growing piece from the excited kaon state, giving rise to a bowl-like shape assuming that $A'^{1}_{\rm in}$ and $A'^{1}_{\rm out}$ have the same sign, which appears to be the case here. Furthermore, the exponentially-growing piece in t' is expected to be larger for smaller $t_{\rm sep}^{K\to{\rm snk}}$, and indeed we observe that the turnover point at which the exponentially-growing term begins to dominate occurs sooner for smaller $t_{\rm sep}^{K\to{\rm snk}}$.

While the effective matrix elements of both sink operators initially trend towards zero, for the more precise $\pi\pi(111)$ data it seems that none of the five data sets are statistically consistent with zero at their maxima, suggesting we do not reach the limit of ground-state dominance. This is not necessarily an issue for our calculation given that the subtraction will heavily suppress these contributions in our final result, and furthermore the inclusion of multiple sink operators will improve our ability to extract the $\pi\pi$ ground-state matrix element. In order to disentangle these two effects it is convenient to examine the three-point function for the optimized sink operator discussed in Sec. 6.2. The time dependence of $M_P^{\rm eff,snk}$ for this operator is also shown in Fig. 6.5. By definition this operator heavily suppresses $A'^{j}_{\rm out}$ for $j > 0$, and indeed we find the data to be much flatter in the low-t' region and also considerably closer to zero. The exponential growth and $t_{\rm sep}^{K\to{\rm snk}}$ dependence that enters due to the excited kaon term is expected to be largely unaffected by this transformation, however it seems that in several cases the plateaus extend much further into the large-t' region than previously. It is likely that is due to an accidental cancellation owing to the fact that $A'^{1}_{\rm out}$ is positive for the $\pi\pi(111)$ operator and negative for the σ operator (cf. Tab. 6.3) and hence the exponentially-growing terms for these operators have opposite signs.

We conclude by discussing the expected size of the excited-state contamination in the matrix elements of the subtracted four-quark operators arising from the pseudoscalar operator. In the $K \to \pi\pi$ calculation, this dimension-3 operator is introduced to remove what in the continuum limit would be a quadratic divergence resulting from the self-contraction between two of the four quark operators appearing in those operators $\hat{Q}_i$ with a component transforming in the $(8,1)$ or $(8,8)$ representations of $SU(3)_L \times SU(3)_R$. In our lattice calculation these terms behave as $1/a^2$

when expressed in physical units. To leading order in a this $1/a^2$ coefficient does not depend on the external states and is therefore removed from our $\langle 0|(\pi\pi)\hat{Q}_i\tilde{K}^0|0\rangle$ amplitude by the subtraction defined above, even though the coefficients α_i are determined from the $\langle 0|\hat{Q}_i\tilde{K}^0|0\rangle$ matrix element in Eq. (6.17). Because of the chiral structure of the $(8,1)$ and $(8,8)$ operators, these coefficients have the structure: $\alpha_i \sim \frac{m_s-m_d}{a^2} + \ldots$ [45], where the ellipsis represents terms which are not power-divergent.

Thus, the $\bar{s}\gamma^5 d$ subtraction removes the leading $1/a^2$ term in the matrix element of $\hat{Q}_i$, leaving behind a finite piece of size $\sim(m_s - m_d)\Lambda^2_{\mathrm{QCD}}\bar{s}\gamma^5 d$. This remainder is not physical and depends on the condition chosen to define the α_i. However, it will contribute to our final result if $E_{\pi\pi} \neq m_K$. For the ground-state component ($i = 0, j = 0$) this term is thus heavily suppressed by the factor $(E^0_{\pi\pi} - m_K)$. However for the excited states we expect this piece to be on the order of the physical contribution from the dimension-6 four-quark operator. As such it may result in a modest enhancement of the excited state matrix elements. Providing we are able to demonstrate that we have the excited $\pi\pi$ and kaon states under control through appropriate cuts on our fitting ranges, this should pose no obstacle to our calculation.

6.3.4 Description of fitting strategy

For a lattice of sufficiently large time extent that around-the-world terms in which states propagate through the lattice temporal boundary can be neglected, and assuming that the four-quark operator is sufficiently separated from the kaon source that the kaon ground state is dominant, the three-point Green's functions C_i of the weak effective operators defined in Eq. (6.12) have the general form,

$$C_i(t, t_{\mathrm{sep}}^{K\to\mathrm{snk}}) = \sum_j \frac{1}{\sqrt{2}} A_K A^j_{\mathrm{snk}} e^{-m_K t} M^j_i e^{-E_j(t_{\mathrm{sep}}^{K\to\mathrm{snk}} - t)}\,, \tag{6.24}$$

where $M^j_i = \langle(\pi\pi)^j|Q_i|K^0\rangle$ is the matrix element of the four-quark operator Q_i with the $\pi\pi$ state j, with M^0_i corresponding to the physical $K \to \pi\pi$ matrix elements required to compute A_0. The factor of $1/\sqrt{2}$ relates the matrix element involving the kaon G-parity eigenstate to that of the physical kaon [13]. Here A_K is the amplitude of the G-parity kaon operator, A^j_{snk} are the amplitudes of the sink operator with the state j, and E_j is the energy of that state. These parameters are fixed to those obtained from the two-point function fits in earlier sections: A_K and m_K to the results given in Tab. 6.1, and $A^j_{\rm snk}$ and E_j to the results obtained from the three-operator, two-state $\pi\pi$ fits given in the last column of Tab. 5.3.

We perform simultaneous correlated fits over multiple sink operators to the form Eq. (6.24) in order to determine the matrix elements M^j_i, allowing for one or more states j. Independent one-state fits are also performed to the optimized sink operator defined in Sec. 6.2. The fits are performed to each weak effective operator separately, in the 10-operator basis (the relationship between these 10 linearly-dependent operators serves as a useful cross-check of the fit results) using the strategy outlined in Sec. 4.4. We apply a cut $t_{\rm min}$ on the separation t between the kaon and the four-quark operator in order to isolate the ground-state kaon, and also a cut $t'_{\rm min}$ on the separation $t' = t^{K\to{\rm snk}}_{\rm sep} - t$ between the four-quark and sink operators. These cuts, the number of sink operators, and the number of excited $\pi\pi$ states included in the fit are varied in order to study systematic effects.

For use below we again define an "effective matrix element" in which the ground-state $\pi\pi$ and kaon amplitudes and time dependence are multiplied out,

$$\begin{aligned} M^{\rm eff,snk}_i(t') &= C_i(t, t^{K\to{\rm snk}}_{\rm sep}) \left(\frac{1}{\sqrt{2}} A_K A^0_{\rm snk} e^{-m_K t} e^{-E_0(t^{K\to{\rm snk}}_{\rm sep} - t)} \right)^{-1} \\ &= M^0_i + \sum_j \frac{A^j_{\rm snk}}{A^0_{\rm snk}} M^j_i e^{-(E_j - E_0)t'} \,. \end{aligned} \tag{6.25}$$

These effective matrix elements converge exponentially to the ground-state matrix element at large t'. Note that, unlike in Sec. 6.3.3, we are assuming that a cut, $t'_{\rm min}$, on the separation betwen the kaon and four-quark operators has been applied that is sufficient to isolate the contribution of the kaon ground state. As a result, these effective matrix elements can be assumed to be independent of $t^{K\to{\rm snk}}_{\rm sep}$ and a weighted average of our five datasets of different $t^{K\to{\rm snk}}_{\rm sep}$ can be applied to improve the statistical resolution of the data presented in our plots.

6.3.5 Fit results

In this section we examine the results of fitting various subsets of our data, with the goal of finding an optimal fit window in which systematic errors arising from both excited $\pi\pi$ and kaon states are minimized.

In Figs. 6.6 and 6.7 we plot the fitted ground-state matrix elements M_i^0 as a function of $t'_{\rm min}$ for various choices of $t_{\rm min}$, the number of sink operators and the number of states. The three-operator fits are performed using the $\pi\pi(311)$, $\pi\pi(111)$ and σ sink operators; for the two-operator fits we drop the noisier $\pi\pi(311)$ data; and for the one-operator fits we further drop the σ data. The one-operator, one-state fits are equivalent to those performed in our 2015 work, albeit with more statistics and more reliable $\pi\pi$ energies and amplitudes.

The discussion below will be focused on these figures. We will first discuss general features addressing the quality of the data and the reliability of the fits, and will then concentrate on searching for evidence of systematic effects (or lack thereof) arising from kaon and $\pi\pi$ excited states. Based on those conclusions we will then present our final fit results.

Discussion of data and fit reliability

We will first comment on the fits to the optimal operator, labeled "opt." in the figures. This approach is outwardly advantageous in that the fits are performed to a single state and the covariance matrix is considerably smaller. In Fig. 6.8 we compare the t' dependence of the $M_2^{\rm eff,snk}$ and $M_6^{\rm eff,snk}$ effective matrix elements of this optimal operator to that of the $\pi\pi(111)$ and σ operators alone, where we note a marked improvement in the quality of the plateau. This behavior, which is also accounted for implicitly in the multi-state fits, demonstrates the power of the multi-operator technique for isolating the ground state. In Figs. 6.6 and 6.7 we observe that the fit results for the optimal operator agree very well with the multi-state fit results in all cases. While this approach does not appear to offer any statistical advantage, the strong agreement suggests that our complex multi-state correlated fits are under good control.

In Figs. 6.6 and 6.7 we observe for several ground-state matrix elements a trend in the fit results

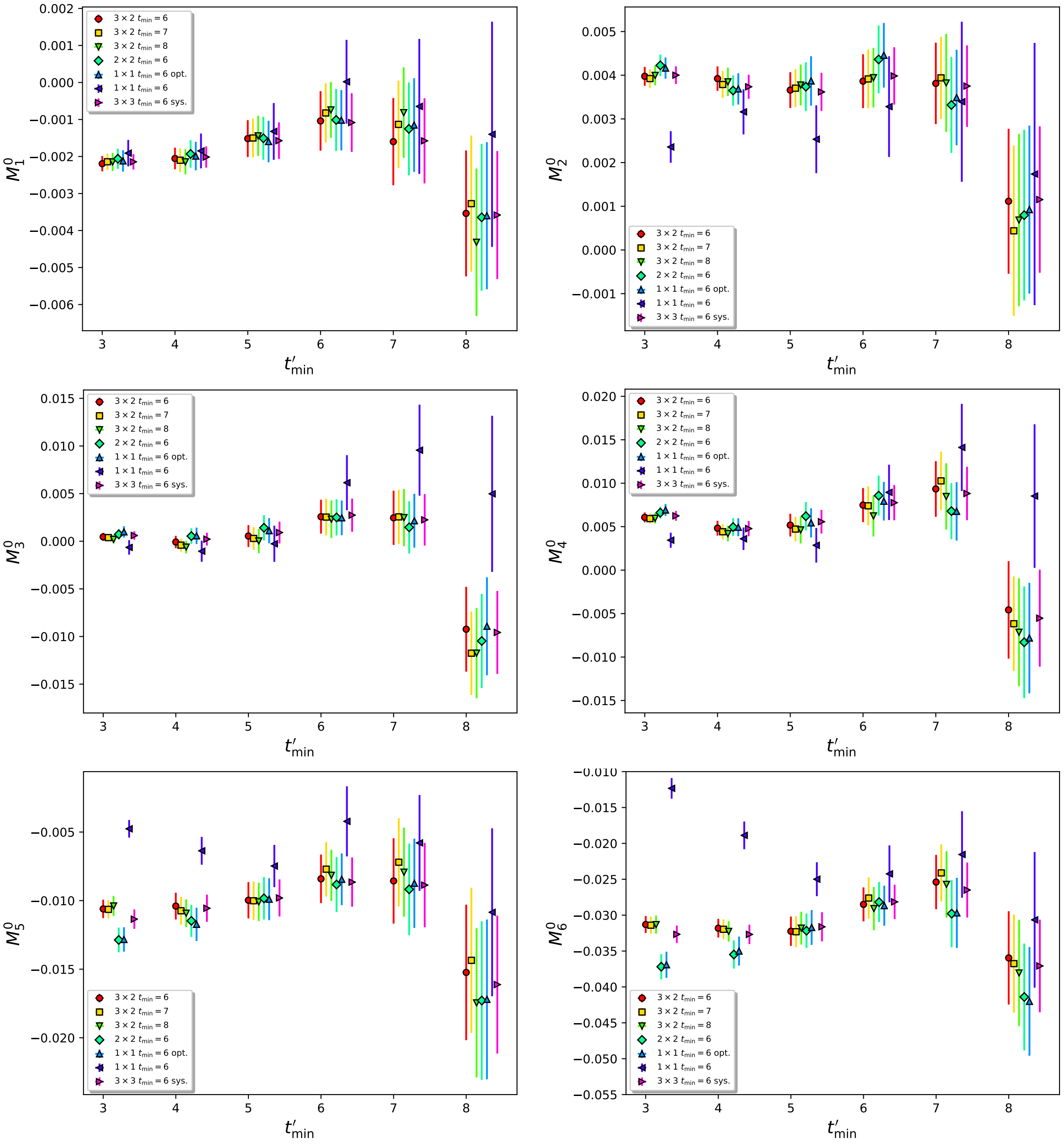

Figure 6.6: Fit results in lattice units for the $K \longrightarrow \pi\pi$ ground-state matrix elements $M_1^0 - M_6^0$ as a function of $t'_{\rm min}$, the minimum time separation between the four-quark and sink operators that is included in the fit. The results have been shifted along the x-axis for clarity in order of their appearance in the legend. The legends are given in the format #ops × #states followed by the cut $t_{\rm min}$ on the time separation between the kaon and the four-quark operators. Here “opt.” is the fit to the optimal operator and “sys.” is used to estimate the systematic error resulting from a third state.

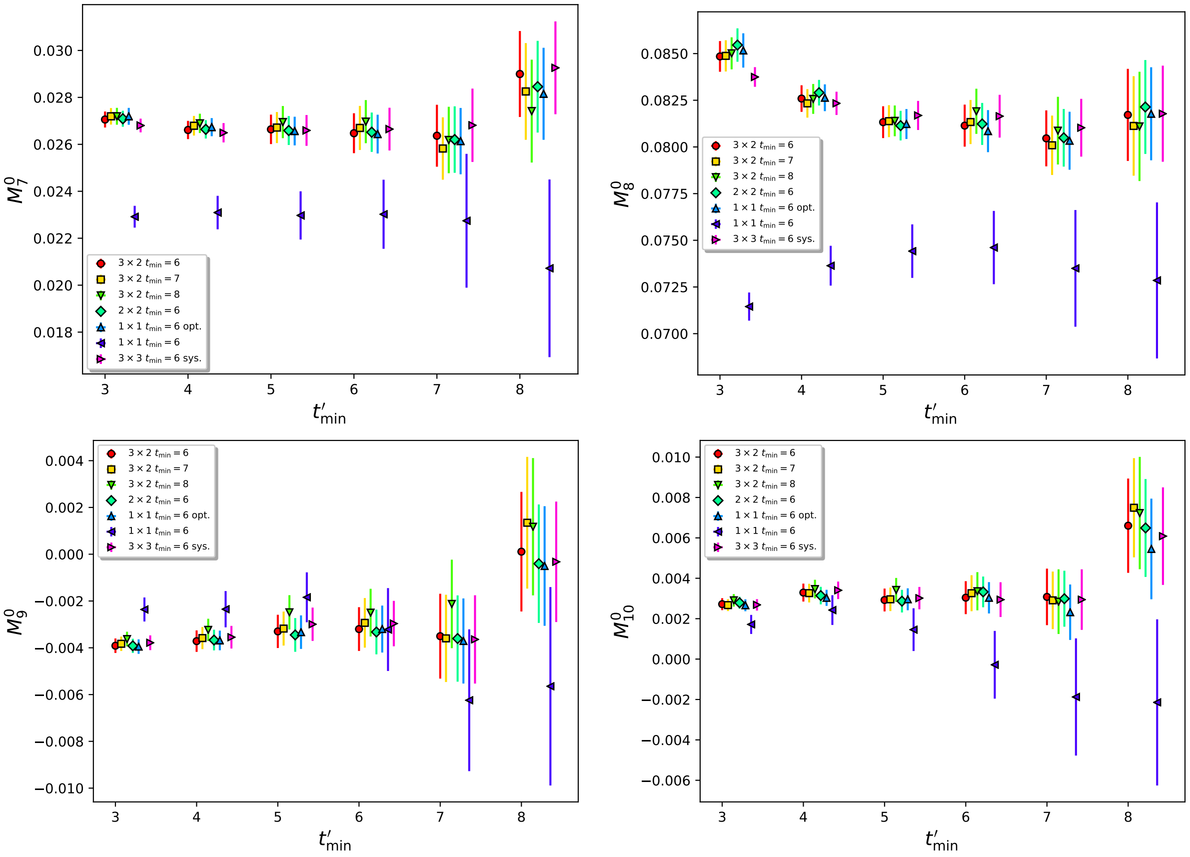

Figure 6.7: The extension of Fig. 6.6 to the ground-state matrix elements $M_7^0 - M_{10}^0$.

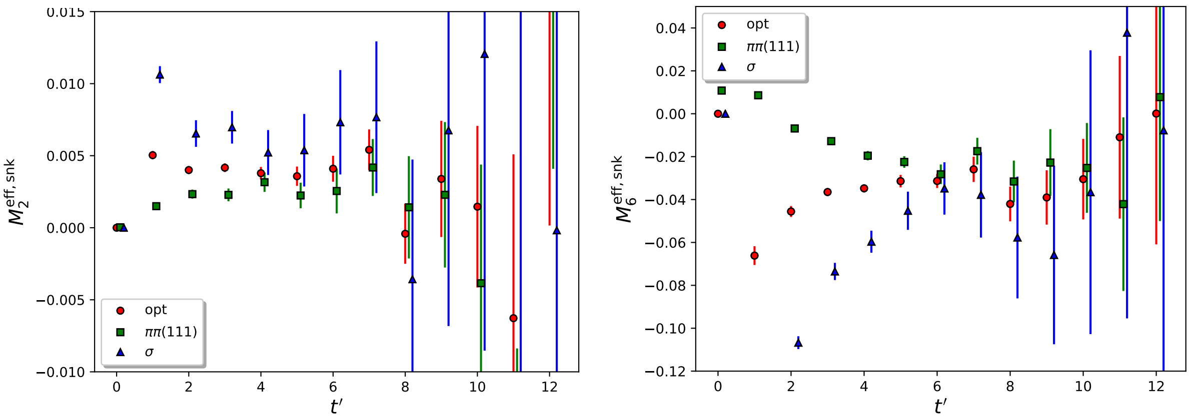

Figure 6.8: The effective matrix elements $M_2^{\text{eff,snk}}$ (left) and $M_6^{\text{eff,snk}}$ (right) for the $\pi\pi(111)$ and σ sink operators and the two-operator two-state optimal sink operator (labeled “opt.” here), plotted as a function of t'. The error-weighted average has been applied to the five different $K \longrightarrow$ sink separations subject to a cut of $t_{\text{min}} = 6$.

i	P-value	i	P-value
1	0.314	6	0.446
2	0.737	7	0.843
3	0.02	8	0.88
4	0.123	9	0.581
5	0.421	10	0.545

Table 6.2: The p-values assessing how well the data with $t' \geq 7$ is described by the model for the C_i correlation functions obtained by fitting to 3 operators and 2 states with $t'_{\text{min}} = 5$ and $t_{\text{min}} = 6$.

up to an extremum at $t'_{\text{min}} = 7$, followed by a statistically significant correction at the level of 1-2σ for the fits with $t'_{\text{min}} = 8$. In this and Sec. 6.6.1 we present substantial evidence that the systematic errors resulting from excited kaon and $\pi\pi$ states are minimal, which makes it unlikely that this rise is associated with excited state contamination. Certainly if it were due to excited $\pi\pi$ states we would expect an improvement as more sink operators are added, but there is little evidence of such, and likewise if excited kaon states were the cause we would expect an improvement as we increase the t_{min} cut, whereas no significant change is observed. The most likely explanation is a statistical fluctuation in our correlated data set, and indeed in Fig. 6.8 we see evidence of such a fluctation peaking at $t' = 7$ which is likely driving this phenomenon.

Given the above, an interesting question we can ask is whether the models we obtain from our fits with $t'_{\text{min}} = 5$, which in all cases lie within the plateau region before this rise, are a good

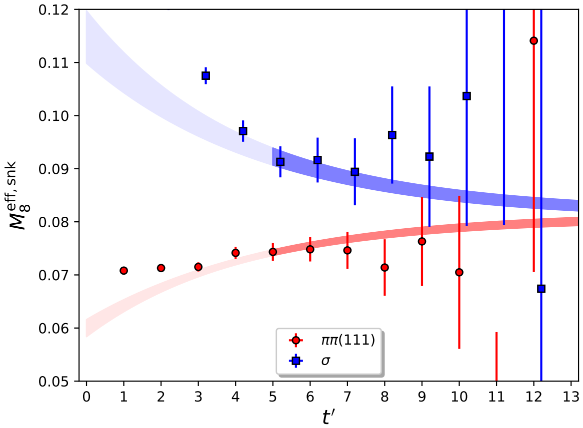

Figure 6.9: The $M_8^{\rm eff,snk}$ effective matrix element for the $\pi\pi(111)$ (red circles) and σ (blue squares) sink operators overlaid by curves showing the function $M_8^{\rm eff,snk}(t')$ predicted using the parameters obtained by fitting the data with $t_{\rm min} = 6$ and $t'_{\rm min} = 5$. The lighter part of the band is the portion of the curve outside of the fit region. An error-weighted average over $t_{\rm sep}^{K\to{\rm snk}}$ has been performed to the data. Recall that the effective matrix elements are defined (Eq. 6.25) such that the result converges to the ground-state matrix element at large t'.

description of the subset of data with $t' \geq 7$, or in other words how likely it is that these data are consistent with this model allowing only for statistical fluctuations. In Tab. 6.2 we list the p-values for these data using the model obtained by fitting to 3 sink operators and 2 states with $t'_{\rm min} = 5$ and $t_{\rm min} = 6$, computed using the technique discussed in Sec. 4.4 (with no free parameters). We observe excellent p-values in all cases bar M_3^0, and to a lesser extent M_4^0. The lower p-values for these operators are common for all of the multi-operator fits and are likely associated with the statistical fluctuations described above which are more apparent for these matrix elements (cf. Fig. 6.6). We expect that such unusual statistical fluctuations will be found when so many different operators and fitting ranges are examined. Of most importance in a calculation of Im(A_0) is M_6^0, for which we find that the model obtained with $t'_{\rm min} = 5$ is an excellent description of the data with $t' \geq 7$. The p-value is in fact little different from the value $p = 0.525$ obtained by fitting to these data directly, suggesting that the models are equally good descriptions despite the tension in the ground-state matrix elements.

For M_7^0 and M_8^0 (and to a lesser extent, M_{10}^0) we observe a discrepancy between the one-operator and multi-operator results at the 1-2σ level that persists even to large $t'_{\rm min}$. Given the

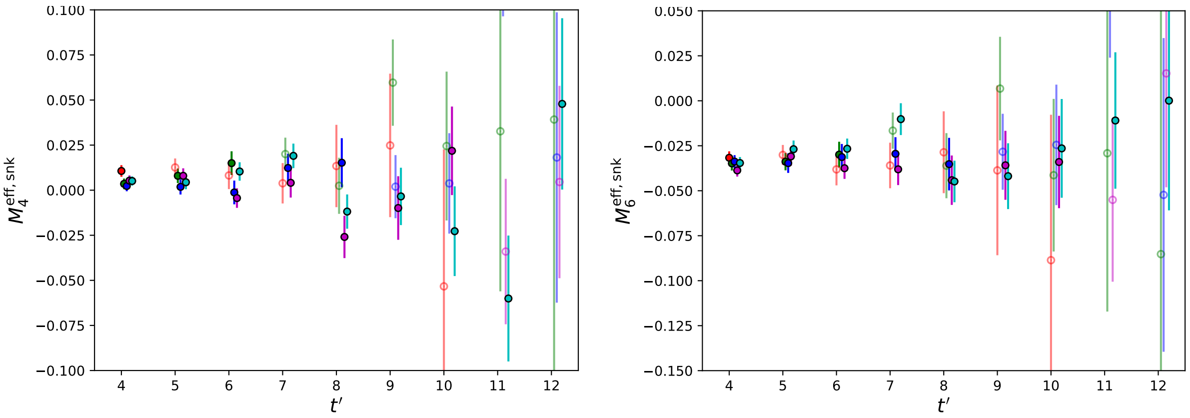

Figure 6.10: The t' dependence of the $M_4^{\mathrm{eff,snk}}$ (left) and $M_6^{\mathrm{eff,snk}}$ (right) effective matrix elements with the optimal sink operator. Each cluster of points, separated for clarity, shows the data for the five different $K \longrightarrow$ snk separations: 10,12,14, 16, and 18, from left to right in that order. The darker, filled points are those that lie within our cut of $t_{\mathrm{min}} = 6$, and the lighter, hollow points are those excluded.

very clear plateaus in the multi-state fit results, this disagreement is likely due again to statistical effects in these correlated data. This is evidenced for example in Fig. 6.9 in which we overlay the $M_8^{\mathrm{eff,snk}}$ effective matrix element for the $\pi\pi(111)$ and σ sink operators by the multi-operator fit curve. We observe that the fit curve for the $\pi\pi(111)$ operator is completely compatible with the data but favors a value that is consistently within the upper half of the error bar, suggesting that the apparent flatness of the $\pi\pi(111)$ effective matrix element represents a false plateau, and the fact that the multi-operator method is capable of resolving the behavior is a testament to its power.

Excited kaon state effects

We now address excited kaon state effects. Because the data rapidly becomes noisier as we move the four-quark operator closer to the kaon operator and thus further away from the $\pi\pi$ operator, such effects are not expected to be significant. The simplest test is to vary the cut on the time separation between the kaon operator and the four-quark operator, t_{min}. The first three points from the left of each cluster in Figs. 6.6 and 6.7 show the result of varying t_{min} between 6 and 8 at fixed t'_{min}. As expected we observe no statistically significant dependence on this cut.

We can also test for excited kaon effects by examining the data near the kaon operator in more detail, alongside looking for trends in the five different $K \rightarrow$ sink separations at fixed t'. The optimal operator proves convenient for examining this behavior as it neatly combines the two dominant sink operators and should be flat within the fit window. In Fig. 6.10 we plot the data for the $M_4^{\text{eff,snk}}$ and $M_6^{\text{eff,snk}}$ effective matrix elements with a distinction drawn between data included and excluded by a cut on the kaon to four-quark operator time separation of $t_{\text{min}} = 6$. We find no apparent evidence of excited kaon state contamination even for data excluded by the cut, nor do we observe any trends of the data in the $K \rightarrow$ sink separation.

We therefore conclude that excited kaon effects in our results are negligible.

Excited $\pi\pi$ state effects

The dominant fit systematic error is expected to be due to excited $\pi\pi$ states. Fortunately, given that we can change both the number of operators and the number of states alongside varying the fit window within a region where our data is most precise, there are a number of tests we can perform to probe this source of error.

We begin by comparing the multi-operator fits to the one-operator ($\pi\pi(111)$) fit, the latter being equivalent to the procedure used for our 2015 work. In the majority of cases we see little evidence of excited state contamination in the one-operator data, as evidenced by its agreement with the multi-operator fits as well as the strong consistency between the fits as we vary the fit window. However for the M_5^0 and M_6^0 matrix elements we observe strong evidence of excited-state contamination in these fits at smaller t'_{min}. Fig. 6.6 clearly demonstrates how these effects are suppressed as we add more operators: Initially the one-operator results converge with the 3-operator results at $t'_{\text{min}} = 5$ and 6, respectively, at which point the excited states appear to be sufficiently suppressed. Introducing a second operator and state we eliminate part of this contamination and the convergence appears earlier, at $t'_{\text{min}} = 4$ and 5, respectively. Finally, in adding the third operator we find results that are essentially flat from $t'_{\text{min}} = 3$. This suggests that the 5% excited-state systematic error on our 2015 result which used $t'_{\text{min}} = 4$ was significantly underestimated for these matrix elements.

Parameter	Value	
	2-state fit	3-state fit
Fit range	6-15	4-15
$A^0_{\pi\pi(111)}$	0.3682(31)	0.3718(22)
$A^0_{\pi\pi(311)}$	0.0038(3)	0.00333(27)
A^0_{σ}	−0.000431(4)	−0.0004318(42)
E_0	0.3479(11)	0.35030(70)
$A^1_{\pi\pi(111)}$	−0.1712(91)	0.1748(67)
$A^1_{\pi\pi(311)}$	0.0513(27)	−0.0528(30)
A^1_{σ}	−0.000314(17)	0.000358(13)
E_1	0.569(13)	0.5879(65)
$A^2_{\pi\pi(111)}$	—	0.116(29)
$A^2_{\pi\pi(311)}$	—	0.063(10)
A^2_{σ}	—	0.000377(94)
E_2	—	0.94(10)
p-value	0.314	0.092

Table 6.3: Fit parameters in lattice units and the p-values for multi-operator fits to the $I = 0$ $\pi\pi$ two-point functions. Here E_i are the energies of the states and A^i_α represents the matrix element of the operator α between the state i and the vacuum. The second column copies the parameters for our usual fit which uses two-states and three operators from Tab. 5.3. The third column shows a fit with the same three operators and one additional state that is used to probe the systematic effects of this third state on the $K \to \pi\pi$ matrix element fits.

In general we observe excellent agreement between two and three-operator fits with two-states. Unfortunately, as mentioned above, the $\pi\pi(311)$ data are considerably noisier than those of the other operators, and the associated $\pi\pi$ energy and amplitudes are less-well known, and as such these data contribute relatively little to the fit. Nevertheless we do observe that for the M^0_5 and M^0_6 matrix elements, the introduction of the third operator results in values that for low t'_{min} (3 or 4) are in considerably better agreement with the results for larger t'_{min}, suggesting that in the regime in which these data are less noisy (i.e. closer to the $\pi\pi$ operator) the third operator is acting to remove some residual excited-state contamination. We conclude that it is beneficial to include the third operator.

In order to study the possibility of residual contamination from a third state we perform three-operator, three-state fits to the matrix elements.Before that we first need to perform three-operator, three-state fits to the $\pi\pi$ three-point function. As mentioned in Sec. 5.2.1, this fit should be done

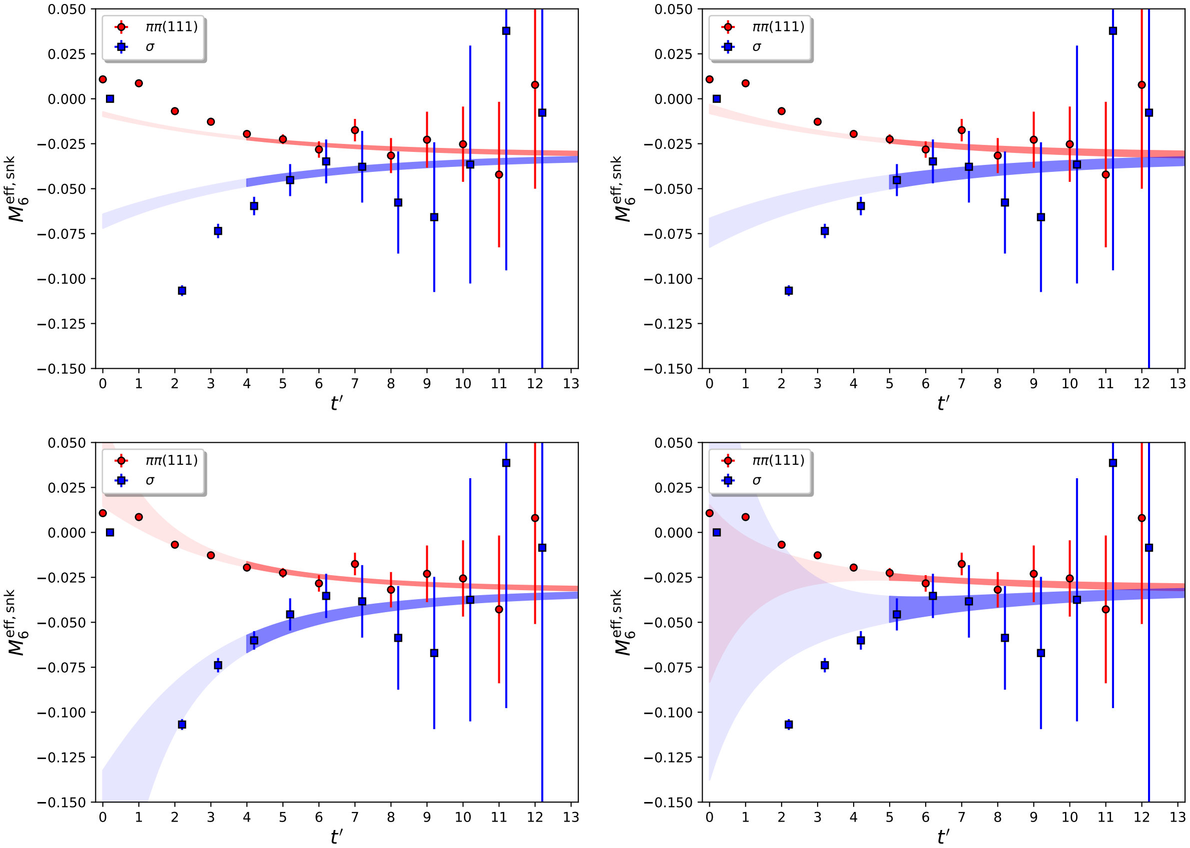

Figure 6.11: The effective matrix element $M_6^{\rm eff,snk}$ for the $\pi\pi(111)$ (red circles) and σ (blue squares) sink operators, overlaid by the fit curves. The lighter part of the band is the portion of the curve outside of the fit region. The upper panels are for the 2-state fits and the lower panels are for the 3-state fits. In each case the left panel is for $t'_{\rm min} = 4$ and the right panel $t'_{\rm min} = 5$. All fits are performed with 3 operators and use $t_{\rm min} = 6$.

with t_min < 5 in order to obtain results that are resolvable from zero. We decide to choose t_min = 4 to suppress the contribution from additional excited states beyond those of the third state whose effects we are trying to estimate. The results are summarized in Tab. 6.3, together with the results from the optimal fit in Sec. 5.2.1. Using the results in the third column of this Table and the same fit ranges for t and t' used in the three-operator, two-state fits. The results for the ground-state matrix elements are also included in Figs. 6.6 and 6.7 with the label “sys.”. We find that including this third state has very little impact and the results agree very well with the three-operator, two-state fits. This again suggests that we have the $\pi\pi$ excited-state systematic error under control.

A further test for excited-state contamination is to study the agreement of the fit curves with the data outside of the fit region. To this end in Fig. 6.11 we plot the $\pi\pi(111)$ and σ operator data for the $M_6^{\rm eff,snk}$ effective matrix element overlaid by the fit curves for the 3-operator, 2-state fits, and for the 3-operator, 3-state fits described above, using $t'_{\rm min} = 4$ and 5. The fitted ground-state matrix elements in these cases are all in complete agreement to within a fraction of their statistical errors. We observe that the 3-operator, 2-state fit curve with $t'_{\rm min} = 5$ describes well the $\pi\pi(111)$ data at $t' = 4$ but shows a tension for the σ data at this timeslice. Fitting with $t'_{\rm min} = 4$ does not resolve this tension, suggesting the effects of a third state are visible in the σ operator data at $t' = 4$. This is consistent with the pattern of couplings of the operators to the states in Tab. 6.3 which show a significant reduction in the couplings to higher states for the $\pi\pi(111)$ operator but almost equal-sized couplings of the σ operator to all three states. The 3-operator, 3-state fit with $t'_{\rm min} = 5$ does not appear to well resolve the contribution of the third state, which is consistent with our observation that this state is no longer visible in the $\pi\pi$ two-point data from this timeslice. However with $t'_{\rm min} = 4$ we are able to resolve the effect of this state, and observe excellent agreement of the model with the data even down to very low times. It should be noted however that the third-state energy of $E_2 = 0.94(10)$ (in lattice units) obtained by our fits is somewhat larger than the value of $E_2 = 0.692$ predicted by dispersion theory suggesting that the effects of even higher excited states may be playing a role here. Nevertheless the strong agreement between the ground-state matrix elements for all of these fits suggest that the residual effects of the higher excited states on the 3-operator, 2-state fits are negligible.

For our final result we choose to focus upon the three-operator, two-state fits. While the majority of the corresponding curves in Figs. 6.6 and 6.7 are essentially flat from $t'_{\rm min} = 3$, we opt for a conservative and uniform cut of $t'_{\rm min} = 5$ at which we can strongly claim an absence of significant excited-state effects. In the Sec. 6.6.1 we will consider means by which we can assign a systematic error to this result.

Param	Value	Param	Value
M_1^0	−0.00152(50)	M_2^0	0.00366(41)
M_1^1	0.0015(22)	M_2^1	−0.0050(21)
p-value	0.488	p-value	0.743
M_3^0	0.0005(11)	M_4^0	0.0052(13)
M_3^1	0.0018(52)	M_4^1	−0.0045(59)
p-value	0.036	p-value	0.139
M_5^0	−0.0100(13)	M_6^0	−0.0322(20)
M_5^1	0.0182(49)	M_6^1	0.0563(81)
p-value	0.458	p-value	0.159
M_7^0	0.02664(63)	M_8^0	0.08133(85)
M_7^1	−0.0158(26)	M_8^1	−0.0464(45)
p-value	0.913	p-value	0.676
M_9^0	−0.00330(71)	M_{10}^0	0.00292(57)
M_9^1	0.0051(30)	M_{10}^1	−0.0048(27)
p-value	0.327	p-value	0.56

Table 6.4: Final $K \longrightarrow \pi\pi$ matrix element results in lattice units obtained from a three-operator, two-state fit with $t_{\rm min} = 6$ and $t'_{\rm min} = 5$. Here M_i^j refers to the matrix element of the Q_i operator with $\pi\pi$ state j.

Final fit results

As discussed above we choose the 3-operator, 2-state fit with $t'_{\rm min} = 5$ for our final result. As we observe no significant dependence on the cut on the separation between the kaon and four-quark operators we will choose $t_{\rm min} = 6$. In Tab. 6.4 we present the full set of p-values and parameters for these fits. We obtain acceptable p-values in the majority of cases, with the notable exception of the Q_3 four-quark operator for which $p = 4\%$. We find that this p-value is not improved by increasing $t'_{\rm min}$, and also that the p-value of the one-operator, one-state fit with the same fit range – with which our chosen value is in excellent agreement – has a p-value of 15%. The low probability is therefore unlikely to be associated with any systematic effect and can be attributed to low-probability statistical effects.

We conclude this section with a comparison of the statistical errors of the matrix elements M_2^0

and M_6^0 to those determined in our 2015 analysis. Previously we obtained

$$\begin{aligned} M_2^0 &= 0.00424(116) \\ M_6^0 &= -0.0189(47)\,. \end{aligned} \tag{6.26}$$

Comparing these values to those in Tab. 6.4 we find that the errors have reduced by factors of 2.8 and 2.4 for M_2^0 and M_6^0, respectively. Comparing the 3-operator, 2-state fits to the 1-operator, 1-state fits in Fig. 6.6 we observe that the larger improvement for M_2^0 can be explained by the additional operators, however for M_6^0 these two approaches have similar errors. The fact that the error on M_6^0 has improved considerably more than the factor of 1.9 expected by the increase in statistics can therefore be attributed to the improved precision of the $\pi\pi$ two-point function fits.

6.4 Non-perturbative renormalization of lattice matrix elements

The Wilson coefficients are conventionally computed in the $\overline{\text{MS}}$ (NDR) renormalization scheme, and therefore we are required to renormalize our lattice matrix elements also in this scheme. This is achieved by performing an intermediate conversion to a non-perturbative *regularization invariant momentum scheme with symmetric kinematics* (RI-SMOM). As the name suggests, these schemes can be treated both non-perturbatively on the lattice (provided the renormalization scale is sufficiently small compared to the Nyquist frequency π/a) and in continuum perturbation theory (providing the renormalization scale is sufficiently high that perturbation theory is approximately valid at the order to which we are working). Thus, we can use continuum perturbation theory to match our RI-SMOM matrix elements to $\overline{\text{MS}}$, avoiding the need for lattice perturbation theory. The matching factors have been computed to one-loop in Ref. [46].

In our 2015 calculation we computed the renormalization matrix at a somewhat low renormalization scale of $\mu = 1.529$ GeV in order to avoid large cutoff effects on our coarse, $a^{-1} = 1.38$ GeV ensemble. Due to this low scale, the systematic error associated with the perturbative RI to $\overline{\text{MS}}$ matching was our dominant error, with an estimated size of 15%. In this work we utilize the step-scaling procedure [47, 48] (summarized below) in order to circumvent the limit imposed by the lattice cutoff and increase the renormalization scale to 4.0 GeV at which the error arising from the use of one-loop perturbation theory is expected to be significantly smaller. A separate step-scaling calculation to 2.29 GeV was performed in Ref. [49] and we will utilize those results to study the scale dependence of the perturbative and discretization errors in our operator normalization.

6.4.1 Summary of approach

Due to operator mixing, the renormalization factors take the form of a matrix. This is most conveniently expressed in the seven-operator chiral basis in which the operators are linearly independent and transform in specific representations of the $SU(3)_L \otimes SU(3)_R$ chiral symmetry group, an accurate symmetry of our DWF formulation even at short distances. In this basis the renormalization matrix is block diagonal, with a 1×1 matrix associated with the Q'_1 operator that transforms in the $(27, 1)$ representation, a 4×4 matrix for the $(8, 1)$ operators Q'_2, Q'_3, Q'_5 and Q'_6 , and a 2×2 matrix for the $(8, 8)$ operators Q'_7 and Q'_8.

In the RI-SMOM scheme the renormalized operators are generally defined thus,

$$O_i^{\rm RI} = Z_{ij}^{\rm RI\leftarrow lat} O_j^{\rm lat} \tag{6.27}$$

where Einstein's summation conventions are implied and the label "RI" is used as short-hand for the RI-SMOM scheme. The renormalization factors are defined via

$$Z_q^{-2}[P_m]^{\beta\alpha\delta\gamma}[\Gamma_{im}^{\rm RI}]^{\alpha\beta\gamma\delta}(p_1, p_2) = F_{im}\,, \tag{6.28}$$

where the index m is not summed over. Here $\alpha - \delta$ are combined spin and color indices, Z_q is the quark field renormalization, q is a four-momentum that defines the renormalization scale and P_m are "projection matrices" described below. The quantities F_{im} on the right-hand side are found by evaluating the left-hand side of the equation at tree level. $\Gamma_{im}^{\rm RI}$ are computed as

$$[\Gamma_{im}^{\rm RI}]^{\alpha\beta\gamma\delta}(p_1, p_2) = \left\langle E_m \sum_x e^{2iqx} O_i^{\rm RI}(x) \right\rangle_{\rm amp.}^{\alpha\beta\gamma\delta} \tag{6.29}$$

where the sum is performed over the full four-dimensional lattice volume and $q = p_1 - p_2$. Here E_m are a set of seven four-quark operators that each create the four quark lines that connect to the weak effective operator,

$$\begin{aligned} E_1 = E_2 = E_4 = E_5 &= s(-p_1)\bar{d}(p_2)u(-p_1)\bar{u}(p_2) \\ E_3 = E_6 = E_7 &= s(-p_1)\bar{d}(p_2) \sum_{q=u,d,s} q(-p_1)\bar{q}(p_2)\,, \end{aligned} \tag{6.30}$$

where the momentum arguments indicate the incoming momenta and the quark momenta satisfy *symmetric kinematics*: $p_1^2 = p_2^2 = (p_1 - p_2)^2 = q^2 \equiv \mu^2$. The subscript "amp." in Eq. (6.29) implies that the external propagators are amputated by applying the ensemble-averaged inverse propagator, such that the resulting Green's function has a rank-4 tensor structure in the spin-color indices.

These Green's functions are not gauge-invariant, hence the procedure must be performed using gauge-fixed configurations, for which we employ Landau gauge-fixing. The use of momentum-space Green's functions introduces contact terms that prevent the use of the equations of motion so that additional operators, beyond those needed to determine on-shell matrix elements, must be introduced if all possible operator mixings are to be included, as is required if the RI-SMOM scheme is to have a continuum limit. These are discussed below.

Note that the Wick contractions of Eq. (6.29) result in disconnected penguin-like diagrams that interact only by gluon exchange; these diagrams are evaluated using stochastic all-to-all propagators and are typically noisy, requiring multiple random hits and hundreds of configurations. The presence of disconnected diagrams also precludes the use of partially-twisted boundary conditions and therefore limits our choices of the renormalization momentum scale to the allowed lattice momenta.

The quark field renormalization Z_q is also computed in the RI-SMOM scheme via the amputated vertex function of the local vector current operator, $\bar{q}\gamma^\mu q$, from which we compute Z_V/Z_q where Z_V is the corresponding renormalization factor for the local vector current. The factor Z_V is not unity as the local vector current is not conserved, however it can be computed independently from the ratio of hadronic matrix elements containing the local and conserved (five-dimensional) vector current allowing Z_q to be obtained from the above. Alternatively, Z_q can also be computed from the local axial-vector current operator $\bar{q}\gamma^\mu\gamma^5 q$. Again the ratio Z_A/Z_q is determined from a three-point function evaluated in momentum space and, providing non-exceptional kinematics are used, is equivalent up to negligible systematic effects at large momentum [50]. The quantity Z_A is then determined by comparing the pion-to-vacuum matrix elements of the local and approximately conserved (five-dimensional) axial current.

The independent projection matrices P_m contract the external spin and color indices, and are chosen with a tensor structure that reflects that of the operator with the same index. For the weak effective operators, we can choose both parity-even and parity-odd projectors, which project onto the parity-even and parity-odd components of the amputated Green's function, respectively, and which should both provide the same result due to chiral symmetry. In practice however we have found that the parity-odd choices are better protected against residual chiral symmetry breaking effects that induce non-zero mixings between the different $SU(3)_L \otimes SU(3)_R$ representations (cf. Sec. 4.5 of Ref. [28]), and so we will use the parity-odd projectors exclusively. We consider two different projection schemes: the "γ^μ scheme", for which the parity-odd projectors have the spin structure,

$$P_m^{\gamma^\mu} = \pm\gamma_\mu \otimes (\gamma^5\gamma^\mu) - (\gamma^5\gamma_\mu) \otimes \gamma_\mu \,, \tag{6.31}$$

and the "$\not{q}$ scheme" with spin structure

$$P_m^{\not{q}} = \pm\not{q} \otimes (\gamma^5\not{q}) - (\gamma^5\not{q}) \otimes \not{q} \,. \tag{6.32}$$

For the full set of parity-odd and parity-even projectors we refer the reader to Sec. 3.3.2 of Ref. [14].

Similar choices of γ^μ and $\not{q}$ projector exist also for the quark field renormalization. We will follow the convention of describing our RI-SMOM schemes with a label of the form SMOM(A, B) where the quantities A and B in parentheses describe the choices of projector for the four-quark operator and Z_q, respectively. In this work we consider only the SMOM(γ^μ, γ^μ) and SMOM$(\not{q}, \not{q})$ schemes as previous studies of the renormalization of the neutral kaon mixing parameter B_K indicate that the non-perturbative running is better described by perturbation theory for these two choices than for the two mixed schemes [51]. We will compare our final results obtained using both intermediate schemes in order to estimate the systematic perturbative and discretization errors in computing the RI to $\overline{\mathrm{MS}}$ matching.

6.4.2 Operator mixing

The seven weak effective operators mix with several dimension-3 and dimension-4 bilinear operators. For the parity-odd components these are $S_1 = \bar{s}\gamma^5 d$, $S_2 = \bar{s}\overrightarrow{\not{D}}\gamma^5 d$ and $S_3 = \bar{s}\overleftarrow{\not{D}}\gamma^5 d$, where the arrow indicates the direction of the discrete covariant derivative. These are accounted for by performing the renormalization with subtracted operators,

$$Q_i^{\prime\text{sub,lat}} = Q_i' + \sum_{j=1}^{3} b_j S_j^{\text{lat}} . \tag{6.33}$$

The subtraction coefficients b_j are obtained by applying the following conditions,

$$P_j^{\beta\alpha} \left\langle s(-p_1)\bar{d}(p_2)O_i^{\text{sub,lat}}(q)\right\rangle_{\text{amp.}}^{\alpha\beta} = 0 \tag{6.34}$$

with symmetric kinematics at the scale q^2. The projection operators can be found in Sec. 7.2.6 of Ref. [49]. In practice we find that the subtraction coefficients are small due to the suppression of the mixing by a factor of the quark mass as a result of chiral symmetry, and also the observation that the amputated vertex function Eq. (6.29) with a four-quark external state and a two-quark operator necessarily involves only disconnected diagrams that are small at large momentum scales due to the running of the QCD coupling.

Mixing also occurs with the dimension-5 chromomagnetic penguin operator and a similar electric dipole operator, conventionally labeled Q_{11} and Q_{12}, respectively [52]. These operators do not vanish by the equations of motion and therefore contribute also to the on-shell matrix elements, but break chiral symmetry and as such are expected to be heavily suppressed [52, 53]. It is therefore conventional to neglect their effects in, for example, the determination of the Wilson coefficients [54]. In our DWF calculation the dimension-1 mixing coefficients of these dimension-5 operators will be of order the input quark masses used in our RI-SMOM calculations or the DWF residual mass — effects, when combined with the required gluon exchange, should be at or below the percent level. Thus, in this work we neglect these operators.

In addition to the lower-dimension operators there is also mixing with both gauge-invariant and gauge-noninvariant dimension-6 two-quark operators. These operators enter at next-to-leading order and above, and are therefore naturally small provided we perform our renormalization at large energy scales.

The gauge-noninvariant dimension-6 operators vanish due to gauge symmetry and in many cases also by the equations of motion, and therefore do not contribute to on-shell matrix elements [55]. These operators enter the renormalization only at the two-loop level [45] and above, and given that the RI→ $\overline{\mathrm{MS}}$ matching factors are at present only available to one loop, the systematic effect of disregarding these operators is likely to be much smaller than our dominant systematic errors. Nevertheless we are presently investigating position-space renormalization [56] which does not require gauge fixing and therefore does not suffer from such mixing, and as such we may be able to remove this systematic error in future work.

Of the gauge-invariant dimension-6 operators,

$$G_1 = \bar{s}\left[D_\mu\left[D^\mu, D_\nu\right]\right]\gamma^\nu(1-\gamma^5)d \tag{6.35}$$

is the only operator that mixes at one loop [57], with all others entering at two-loops and above. In Ref. [49] we have investigated the impact of including the G_1 operator in our RI-SMOM renormalization and have computed the subsequent effect on the $K \to \pi\pi$ amplitudes. This can be achieved without the need for measuring matrix elements of G_1 between kaon and $\pi\pi$ states by taking advantage of the equations of motion to rewrite those matrix elements for on-shell kinematics in terms of the matrix elements of the conventional four-quark operators, such that the entire effect of this operator is captured by changes in the values of the $(8,1)$ elements of the renormalization matrix. Note that at present the results including the G_1 operator have been computed only at the 2.29 GeV renormalization scale and not the 4.0 GeV scale used for our final result. However, as demonstrated in Ref. [49] and also in Sec. 6.6.6, the effects of including G_1 are at the few percent level as expected, implying that the resulting systematic error is small compared to our other errors.

6.4.3 Step-scaling

Step-scaling [48] allows for the circumvention of the upper limit on the renormalization scale imposed by the lattice spacing through independently computing the non-perturbative running of the renormalization matrix to a higher scale using a finer lattice. The multiplicative factor relating the RI-SMOM operators renormalized at two different scales can be obtained from the ratio

$$\Lambda^{\mathrm{RI}}(\mu_2,\mu_1) = Z^{\mathrm{RI}\leftarrow\mathrm{lat}}(\mu_2)(Z^{\mathrm{RI}\leftarrow\mathrm{lat}}(\mu_1))^{-1}\,, \tag{6.36}$$

where μ_1 is a renormalization scale that lies below the cutoff on the original coarser lattice while μ_2 is a higher scale, likely inaccessible on the coarser lattice. The quantity $\Lambda^{\mathrm{RI}}(\mu_2,\mu_1)$ is computed on finer lattices for which μ_2 also lies below the cutoff and can be applied thus,

$$Z^{\mathrm{RI}\leftarrow\mathrm{lat}}(\mu_2) = \Lambda^{\mathrm{RI}}(\mu_2,\mu_1)Z^{\mathrm{RI}\leftarrow\mathrm{lat}}(\mu_1) \tag{6.37}$$

in order to raise the renormalization scale to μ_2, giving the renormalization matrix $Z^{\mathrm{RI}\leftarrow\mathrm{lat}}(\mu_2)$ which non-perturbatively converts our course-lattice operators into an RI scheme defined at a scale μ_2 potentially much larger that the inverse of our coarse lattice spacing. We will take advantage of this technique to avoid having to match perturbatively to $\overline{\mathrm{MS}}$ directly at the lower energy scales allowed by our coarse, $a^{-1} = 1.38$ GeV lattice.

6.4.4 Details and results of lattice calculation

We use the step-scaling procedure to obtain the renormalization matrix at a scale of $\mu_2 = 4.006$ GeV by matching between our $\beta = 1.75$, $a^{-1} = 1.378(7)$ GeV (32ID) ensemble and a second, finer ensemble with $\beta = 2.37$ and $a^{-1} = 3.148(17)$ whose properties are described in Ref. [20] under the label “32Ifine”. These ensembles have periodic spatial boundary conditions rather than G-parity boundary conditions, but as previously mentioned, boundary effects can be neglected for these high-energy Green’s functions. Such quantities are also constructed to be insensitive to the quark mass scale, and therefore we can disregard the unphysically heavy 170 MeV and 370 MeV pion masses on the 32ID and 32Ifine ensembles, respectively. Note also that, although we do not take the continuum limit of the step-scaling matrix computed on the 32Ifine ensemble, the fine lattice spacing and the typically small size of discretization effects on such quantities [58] suggest the induced error is also negligible compared to our other errors. We remind the reader that these calculations do not include the G_1 operator, and its absence in our calculation is treated as a source of systematic error in Sec. 6.6.

Due to the presence of disconnected diagrams in our calculation, the choices of quark momenta are restricted to the discrete values allowed by the finite-volume. The closest match between allowed momenta on the 32ID and 32Ifine ensembles that can be chosen as an intermediate scale is $\mu_1^{\text{32ID}} = 1.531$ GeV and $\mu_1^{\text{32Ifine}} = 1.514$ GeV, respectively. The fact that these scales differ by 1.1% introduces a systematic error that, given the slow evolution of the QCD β-function, can be treated as negligible.

We obtain the quark field renormalization for the 32Ifine ensemble via the vector current operator as described in Sec. 6.4.1. For the 32ID ensemble we use the axial-vector operator as the corresponding renormalization factor, Z_A has been measured to much higher precision than Z_V (0.05% versus 1.2%, respectively) [59]. The measurements of Z_A and Z_V are treated as statistically independent from those of the amputated vertex functions and are incorporated into the calculation using the superjackknife technique.

On the 32ID ensemble we extend the calculation at $\mu_1^{\text{32ID}} = 1.531$ GeV performed in our previous work and documented in Ref. [14] from 100 to 234 configurations, where for each configuration we have increased the number of stochastic sources used in the evaluation of the disconnected diagrams from 1 to 20, improving the statistical errors substantially. We measure the amputated Green's function Eq. (6.29) with quark momentum choices

$$\begin{aligned} p_1 &= (0,4,4,0)\frac{2\pi}{L}\,, \\ p_2 &= (4,4,0,0)\frac{2\pi}{L}\,, \end{aligned} \tag{6.38}$$

that satisfy symmetric kinematics $p_1^2 = p_2^2 = (p_1 - p_2)^2 = (\mu_1^{\text{32ID}})^2$. Combined with the following measurements of the quark field renormalization coefficient in the γ^μ and $\not{q}$ schemes at μ_1^{32ID},

$$\begin{aligned} Z_q^{\gamma^\mu}(\mu_1^{\text{32ID}}) &= 0.7304(4)\,, \\ Z_q^{\not{q}}(\mu_1^{\text{32ID}}) &= 0.8017(4)\,, \end{aligned} \tag{6.39}$$

we obtain the renormalization matrices $Z_{ij}^{\text{RI}\leftarrow\text{lat}}$ for the SMOM(γ^μ, γ^μ) and SMOM$(\not{q}, \not{q})$ schemes given in Tab. 6.5.

For the measurement of the step-scaling matrix on the 32Ifine ensemble we likewise use

$$\begin{aligned} p_1 &= (1, 1, 2, 0)\frac{2\pi}{L}\,, \\ p_2 &= (0, 1, 1, 4)\frac{2\pi}{L}\,, \end{aligned} \tag{6.40}$$

at the low scale $\mu_1^{\text{32Ifine}} = 1.514$ GeV and

$$\begin{aligned} p_1 &= (4, 4, 3, 2)\frac{2\pi}{L}\,, \\ p_2 &= (0, 1, 4, 10)\frac{2\pi}{L}\,, \end{aligned} \tag{6.41}$$

at the high scale $\mu_2 = 4.006$ GeV. The corresponding values of Z_q are

$$\begin{aligned} Z_q^{\gamma^\mu}(\mu_1^{\text{32Ifine}}) &= 0.8082(2)\,, \\ Z_q^{\not{q}}(\mu_1^{\text{32Ifine}}) &= 0.8884(5)\,, \end{aligned} \tag{6.42}$$

at $\mu_1^{\text{32Ifine}} = 1.514$ GeV and

$$\begin{aligned} Z_q^{\gamma^\mu}(\mu_2^{\text{32Ifine}}) &= 0.80235(9)\,, \\ Z_q^{\not{q}}(\mu_2^{\text{32Ifine}}) &= 0.83196(10)\,, \end{aligned} \tag{6.43}$$

at $\mu_2 = 4.006$ GeV.

The results for the step-scaling matrix $\Lambda(4.006\text{ GeV}, 1.514\text{ GeV})_{ij}$ in both schemes are given in Tab. 6.6. In Tab. 6.7 we combine these step-scaling results with the 32ID $Z^{\text{RI}\leftarrow\text{lat}}$ results to produce

0.43216(43)	0	0	0	0	0	0
0	0.4904(62)	−0.0398(60)	−0.0009(22)	−0.0011(13)	0	0
0	−0.0375(24)	0.4937(25)	−0.00242(93)	0.00637(68)	0	0
0	−0.011(19)	−0.017(17)	0.5138(63)	−0.0968(38)	0	0
0	0.0106(77)	0.0304(80)	−0.0328(28)	0.3305(23)	0	0
0	0	0	0	0	0.49839(49)	−0.092841(93)
0	0	0	0	0	−0.027045(31)	0.30819(31)

0.46763(46)	0	0	0	0	0	0
0	0.3670(66)	−0.2593(71)	−0.0025(25)	−0.0005(15)	0	0
0	0.1575(98)	0.835(10)	0.0019(38)	−0.0006(23)	0	0
0	−0.032(32)	−0.016(30)	0.519(11)	−0.0952(63)	0	0
0	−0.048(14)	−0.077(17)	−0.0578(46)	0.3866(36)	0	0
0	0	0	0	0	0.50244(50)	−0.094095(95)
0	0	0	0	0	−0.060488(73)	0.37992(39)

Table 6.5: The elements of the 7 × 7 SMOM(γ^μ, γ^μ) (upper) and SMOM($\not{q}, \not{q}$) (lower) renormalization matrices $Z(1.531\text{GeV})_{ij}^{\text{RI}\leftarrow\text{lat}}$ with renormalization scale $\mu = 1.531$ GeV computed on the 32ID ensemble.

the final renormalization matrices at 4.0 GeV, where the errors on the two independent ensembles have been propagated using the super-jackknife procedure.

As mentioned previously, we will also utilize step-scaled renormalization matrices computed at $\mu_2 = 2.29$ GeV both with and without the G_1 operator included. This calculation used an intermediate scale of $\mu = 1.33$ GeV to match between the coarse and fine ensemble. Details of this calculation can be found in Ref. [49]. In that work the statistical errors on Z_V and Z_A were not included in the results, and Z_V was used rather than Z_A in the determination of Z_q on the 32ID ensemble. In order to match the procedure outlined above we have reanalyzed the data from that work, the results of which are presented in Tab. 6.8 for $\mu = 1.33$ GeV and Tab. 6.9 for $\mu = 2.29$ GeV. Note, at present only results in the SMOM(γ^μ, γ^μ) scheme are available with G_1 included.

6.5 Results for A_0 and ϵ'

In this section we combine our lattice measurements with experimental inputs to obtain Re(ϵ'/ϵ). The set of Standard Model parameters and other experimental values used for these calculations are listed in Tab. 6.10 and their uncertainties are accounted for as a systematic error in the follow-

0.94514(24)	0	0	0	0	0	0
0	0.976(49)	−0.155(41)	−0.022(19)	0.023(15)	0	0
0	−0.105(20)	1.055(19)	−0.0130(69)	−0.0062(64)	0	0
0	−0.10(15)	−0.13(12)	0.855(56)	0.243(47)	0	0
0	0.0010(750)	−0.058(70)	−0.031(27)	1.728(24)	0	0
0	0	0	0	0	0.96601(25)	0.23304(65)
0	0	0	0	0	0.00911(46)	1.8170(26)

0.89837(24)	0	0	0	0	0	0
0	1.110(77)	0.099(62)	−0.002(24)	0.023(17)	0	0
0	−0.486(49)	0.532(41)	−0.026(16)	0.009(10)	0	0
0	−0.19(28)	−0.20(22)	0.844(82)	0.242(58)	0	0
0	0.09(12)	0.09(10)	−0.027(40)	1.597(33)	0	0
0	0	0	0	0	0.97195(23)	0.18510(61)
0	0	0	0	0	0.07468(83)	1.6056(32)

Table 6.6: The elements of the 7×7 SMOM(γ^μ, γ^μ) (upper) and SMOM($\not{q}, \not{q}$) (lower) step-scaling matrices $\Lambda(4.006\text{GeV}, 1.514\text{GeV})_{ij}$ between renormalization scales $\mu_1 = 1.514$ and $\mu_2 = 4.006$ GeV computed on the 32Ifine ensemble.

ing section. In this table the value of Re(A_2) was obtained from the experimental measurement of $K^+ \to \pi^+\pi^0$ decays, and the value of Re(A_0) from $K_S \to \pi^+\pi^-$ and $K_S \to \pi^0\pi^0$ decays. The relationship between the isospin amplitudes and the experimental branching fractions and decay widths is described in detail in Secs. III.A and III.B of Ref. [60].

As previous mentioned, the Wilson Coefficients that incorporate the short distance physics “integrated out” from the Standard Model are known in perturbation theory in the 10-operator basis to NLO in the $\overline{\text{MS}}$ scheme. Partial calculations at NNLO are available in the literature [61, 62, 63, 64, 65], together with a preliminary study on a direct lattice determination [66]; in this manuscript we utilize the complete NLO results of Ref. [54] in the $\overline{\text{MS}}$-NDR scheme for our central values, and the LO predictions to assign a systematic error due to the truncation of the perturbative series.

For consistency with the NLO determination of the Wilson coefficients we follow Ref. [54] in utilizing the 2-loop determination of α_s given in Ref. [54] (and the 1-loop determination for the LO Wilson coefficients used to estimate the systematic error) despite the fact that a 4-loop calculation is available [67]. In order to fix the parameters of the 2-loop (1-loop) calculation, a value of α_s at

0.40845(42)	0	0	0	0	0	0
0	0.485(23)	−0.114(20)	−0.012(10)	0.0077(63)	0	0
0	−0.0908(93)	0.5248(89)	−0.0089(37)	0.0061(26)	0	0
0	−0.051(70)	−0.067(58)	0.432(30)	−0.003(19)	0	0
0	0.021(37)	0.025(35)	−0.073(15)	0.574(10)	0	0
0	0	0	0	0	0.47514(49)	−0.01786(21)
0	0	0	0	0	−0.04460(26)	0.55914(99)

0.42011(43)	0	0	0	0	0	0
0	0.422(38)	−0.207(36)	−0.005(13)	0.0084(77)	0	0
0	−0.094(24)	0.570(24)	−0.0120(83)	0.0059(47)	0	0
0	−0.14(14)	−0.15(12)	0.424(44)	0.013(26)	0	0
0	−0.030(63)	−0.073(66)	−0.106(23)	0.620(15)	0	0
0	0	0	0	0	0.47715(49)	−0.02113(24)
0	0	0	0	0	−0.05960(55)	0.6030(14)

Table 6.7: The elements of the 7×7 SMOM(γ^μ, γ^μ) (upper) and SMOM($\not{q}, \not{q}$) (lower) renormalization matrices $Z(4.006\mathrm{GeV})_{ij}^{\mathrm{RI}\leftarrow\mathrm{lat}}$ with renormalization scale $\mu = 4.006$ GeV computed by applying the step-scaling matrices in Tab. 6.6 with the renormalization matrices in Tab. 6.5. This matrix converts the lattice matrix elements computed in this work to the appropriate RI scheme at $\mu = 4.006$ GeV

a reference scale is required, and to minimize the perturbative truncation error it is desirable that this scale be close to the typical scale of the physical problem, in our case $O(2\ \mathrm{GeV})$. We therefore utilize the 4-loop calculation of α_s to run the value of $\alpha_s^{N_f=5}(M_Z)$ given in Tab. 6.10 down to 1.7 GeV in the 4-flavor theory, and use the result,

$$\alpha_s^{N_f\ =4}(1.7\ \mathrm{GeV}) = 0.32733 \tag{6.44}$$

as input to our 2-loop (1-loop) calculation. (The reason for choosing this scale will be discussed in Sec. 6.6.9.)

6.5.1 Lellouch-Lüscher factor

The Lellouch-Lüscher factor F [36] removes the leading power-law finite-volume corrections to the lattice matrix element. It is defined as

$$F^2 = \frac{4\pi m_K E_{\pi\pi}^2}{k^3}\left(k\frac{d\delta_0}{dk} + q\frac{d\phi}{dq}\right), \tag{6.45}$$

0.43432(44)	0	0	0	0	0	0
0	0.487(14)	−0.033(14)	−0.0013(47)	−0.0044(35)	0	0
0	−0.0197(63)	0.4949(79)	−0.0029(26)	0.0082(22)	0	0
0	−0.006(43)	−0.008(42)	0.526(14)	−0.111(10)	0	0
0	0.024(19)	0.043(22)	−0.0350(73)	0.2907(63)	0	0
0	0	0	0	0	0.49785(50)	−0.10138(10)
0	0	0	0	0	−0.024002(34)	0.27024(28)

0.43432(44)	0	0	0	0	0	0
0	0.488(13)	−0.030(12)	−0.0018(46)	−0.0032(28)	0	0
0	−0.0221(59)	0.4874(61)	−0.0015(25)	0.0060(16)	0	0
0	−0.005(42)	−0.008(36)	0.526(14)	−0.1110(81)	0	0
0	0.019(18)	0.027(19)	−0.0336(69)	0.2872(48)	0	0
0	0	0	0	0	0.49785(50)	−0.10138(10)
0	0	0	0	0	−0.024002(34)	0.27024(28)

Table 6.8: The elements of the 7 × 7 SMOM(γ^μ, γ^μ) renormalization matrix $Z(1.33\text{GeV})_{ij}^{\text{RI}\leftarrow\text{lat}}$ with (upper) and without (lower) the effects of the G_1 operator included. This matrix converts the lattice matrix elements computed in this work to the SMOM(γ^μ, γ^μ) scheme at $\mu = 1.33$ GeV

where δ_0 is the $I = 0$ $\pi\pi$ scattering phase shift and ϕ is a known function [6] of $q = \frac{Lk}{2\pi}$, appropriately modified for our antiperiodic pion boundary conditions [40], with k the interacting pion momentum defined via

$$k^2 = \left(\frac{E_{\pi\pi}}{2}\right)^2 - m_\pi^2 \,. \tag{6.46}$$

Note that Eq. (6.45) differs by a factor of two from the corresponding equation in Ref. [36] due to our different conventions on the decay amplitude (cf. Ref. [43]).

The calculation of the Lellouch-Lüscher factor requires the derivative of the phase shift with respect to interacting pion momentum, or correspondingly the $\pi\pi$ energy, evaluated at the kaon mass. This derivative can be obtained from a phenomenological interpolating ansatz or direct lattice calculation. In Sec. 5.3.3, we obtain the phase-shift at two values of the rest-frame energy that are lower than the kaon mass. These results are also close to their corresponding dispersive predictions, albeit with somewhat larger excited-state systematic errors. Using these results we can directly measure the derivative of the phase-shift with respect to the energy using a finite-difference approximation, for which we obtain

$$\frac{\mathrm{d}\delta_0}{\mathrm{d}q} = 1.76(74)\ \text{rad} \tag{6.47}$$

0.41588(42)	0	0	0	0	0	0
0	0.500(23)	−0.058(43)	−0.0006(82)	0.00000(1300)	0	0
0	−0.055(13)	0.507(26)	−0.0055(48)	0.0115(79)	0	0
0	0.020(68)	−0.01(13)	0.496(22)	−0.071(37)	0	0
0	0.010(46)	−0.059(93)	−0.032(18)	0.392(28)	0	0
0	0	0	0	0	0.48386(49)	−0.063985(81)
0	0	0	0	0	−0.035289(72)	0.40653(45)

0.41588(42)	0	0	0	0	0	0
0	0.498(15)	−0.063(14)	0.0003(53)	−0.0011(33)	0	0
0	−0.0570(72)	0.5009(76)	−0.0042(28)	0.0088(19)	0	0
0	0.024(45)	−0.0010(400)	0.494(16)	−0.0672(94)	0	0
0	0.051(30)	0.040(30)	−0.052(11)	0.4245(79)	0	0
0	0	0	0	0	0.48386(49)	−0.063985(81)
0	0	0	0	0	−0.035289(72)	0.40653(45)

Table 6.9: The elements of the 7 × 7 SMOM(γ^μ, γ^μ) renormalization matrix $Z(2.29\text{GeV})_{ij}^{\text{RI}\leftarrow\text{lat}}$ with (upper) and without (lower) the effects of the G_1 operator included. This matrix converts the lattice matrix elements computed in this work to the SMOM(γ^μ, γ^μ) scheme at $\mu = 2.29$ GeV

from the difference with the nearest energy to the kaon mass, and

$$\frac{\mathrm{d}\delta_0}{\mathrm{d}q} = 1.33(17)\ \text{rad} \tag{6.48}$$

from the next-to-nearest.

We can also obtain the derivative from the dispersive prediction of Colangelo *et al* [9]. The derivative with respect to $s = E_{\pi\pi}^2$, computed at our lattice $\pi\pi$ energy using Eqs. 17.1-17.3 of Ref. [9] with $m_\pi = 135$ MeV, is found to be

$$\frac{\mathrm{d}\delta_0}{\mathrm{d}s} = 3.36(3) \times 10^{-6}\ \text{rad MeV}^{-2}\,, \tag{6.49}$$

where the error is the statistical error arising from the uncertainty in the lattice spacing and measured lattice $\pi\pi$ energy. Note that this result is obtained at the physical pion mass, which is 5% smaller than our lattice value. In order to estimate the impact of the difference in pion masses on this derivative we use NLO chiral perturbation theory [69, 9] (ChPT) to estimate the derivative with respect to energy at $k = 0.1$ GeV, at which ChPT is expected to be reliable. Assuming that the slope with respect to $\sqrt{s}$ is roughly constant (which is well motivated by the dispersion theory result, cf. Fig. 7 of Ref. [9]) we estimate the change in $\frac{\mathrm{d}\delta_0}{\mathrm{d}s}$ evaluated at our lattice $\pi\pi$ energy

Quantity	Value	
G_F	$1.16638{\times}10^{-5}$ GeV^{-2}	
V_{ud}	0.97420	
V_{us}	0.2243	
ϕ_ϵ	0.7596 rad	
τ	0.001558(65) -0.000663(33)i	(*)
$\lvert\epsilon\rvert$	0.002228(11)	(†)
ω	0.04454(12)	(†)
$\mathrm{Re}(A_0)_{\mathrm{expt}}$	$3.3201(18) \times 10^{-7}$ GeV	(†)
$\mathrm{Re}(A_2)_{\mathrm{expt}}$	$1.479(4) \times 10^{-8}$ GeV	(†)
$m_c(m_c)$	1.27(2) GeV	(*)
$m_b(m_b)$	4.18(3) GeV	(*)
$m_W(m_W)$	80.379(12) GeV	(*)
$m_Z(m_Z)$	91.1876(21) GeV	(*)
$m_t(m_t)$	160.0(4.8) GeV	(*)
$\alpha_s^{N_f=5}(m_Z)$	0.1181	
α	1/127.955(10)	(*)
$\sin^2(\theta_W)$	0.23122(3)	(*)

Table 6.10: Standard Model and other experimental inputs required to determine A_0 and $\mathrm{Re}(\epsilon'/\epsilon)$ from the lattice matrix elements. The parameters given in this table were obtained from the PDG Review of Particle Physics [68], apart from those of $\mathrm{Re}(A_0)$, $\mathrm{Re}(A_2)$ and their ratio, ω, which were taken from Ref. [1]. Here ϕ_ϵ is the phase of the indirect CP-violation parameter ϵ. The CKM ratio $\tau = -V_{ts}^*V_{td}/V_{us}^*V_{ud}$ is obtained using the Wolfenstein parameterization expanded to eighth order, with parameters taken from the aforementioned review. The impact upon our result of the errors on those quantities marked with a $(*)$ is incorporated as a systematic error in Sec. 6.6.8. The errors on those quantities marked with (†) are included within the quoted statistical errors on our results. The errors on the remaining quantities are neglected as their contributions to our final error are small in comparison to our statistical error.

as 1.2%. This value is small relative to the final systematic error we assign to the derivative in Sec. 6.6.4 and can therefore be neglected here. Finally, applying $\mathrm{d}s/\mathrm{d}q = 4.18(5) \times 10^5$ MeV^2, where again the errors are statistical, we obtain

$$\frac{\mathrm{d}\delta_0}{\mathrm{d}q} = 1.405(5)\ \mathrm{rad}\,. \tag{6.50}$$

The near-linearity of the dispersive prediction suggests that a linear ansatz,

$$\frac{\mathrm{d}\delta_0}{\mathrm{d}E_{\pi\pi}} \approx \frac{\delta_0}{E_{\pi\pi} - 2m_\pi} \tag{6.51}$$

may also be appropriate. With this ansatz we find

$$\frac{\mathrm{d}\delta_0}{\mathrm{d}q} = 1.259(36)\ \mathrm{rad}\,. \tag{6.52}$$

Given that the derivative of the phase shift is a subleading contribution and that the above values are all in reasonable agreement, we expect that the Lellouch-Lüscher factor can be obtained reliably.

In our 2015 work [1] we also considered a linear ansatz in q,

$$\frac{\mathrm{d}\delta_0}{\mathrm{d}q} \approx \frac{\delta_0}{q} \tag{6.53}$$

for which we obtain

$$\frac{\mathrm{d}\delta_0}{\mathrm{d}q} = 0.790(22)\ \mathrm{rad}\,. \tag{6.54}$$

This value is not as well motivated as the ansatz in Eq. (6.52) and is in disagreement with all four of the above results. Given the good agreement between our measured phase-shifts and the above estimates of the derivative with the dispersive predictions, we will not include this result in our systematic error estimate.

Given the good agreement between our phase shifts and the dispersive predictions [15] we will use the dispersive result given in Eq. (6.50). The variation in the results will be incorporated as a systematic error in Sec. 6.6.4.

We find

$$F = 26.696(52)\,, \tag{6.55}$$

where the error arises primarily from the uncertainty in measured $\pi\pi$ energy and its small size results from the small contribution of the $\pi\pi$ scattering phase shift relative to that of the known function ϕ in Eq. (6.45).

6.5.2 Renormalized physical matrix elements

The infinite-volume matrix elements of the seven chiral-basis operators Q'^{R}_{j} in a scheme R at the scale μ can be expressed without ambiguity in terms of the matrix elements $M'^{\text{lat}}_{j} = \langle \pi\pi | Q'^{\text{lat}}_{j} | K \rangle$ of the corresponding lattice operators:

$$M'^{R}(\mu) = Z^{R \leftarrow \text{lat}}(\mu) \left(a^{-3} F M'^{\text{lat}} \right) , \tag{6.56}$$

where a is the lattice spacing, $Z^{R \leftarrow \text{lat}}(\mu)$ a 7×7 renormalization matrix and F the Lellouch-Lüscher factor obtained in Eq. (6.55).

The ten conventional, linearly-dependent operators Q_i are defined in terms of the seven independent operators Q'_j as follows:

$$Q_i = \sum_i T_{ij} Q'_j, \tag{6.57}$$

where $1 \leq i \leq 10$, j runs over the set $\{1, 2, 3, 5, 6, 7, 8\}$ and the matrix T is given by

$$T = \begin{pmatrix} 1/5 & 1 & 0 & 0 & 0 & 0 & 0 \\ 1/5 & 0 & 1 & 0 & 0 & 0 & 0 \\ 0 & 3 & 2 & 0 & 0 & 0 & 0 \\ 0 & 2 & 3 & 0 & 0 & 0 & 0 \\ 0 & 0 & 0 & 1 & 0 & 0 & 0 \\ 0 & 0 & 0 & 0 & 1 & 0 & 0 \\ 0 & 0 & 0 & 0 & 0 & 1 & 0 \\ 0 & 0 & 0 & 0 & 0 & 0 & 1 \\ 3/10 & 0 & -1 & 0 & 0 & 0 & 0 \\ 3/10 & -1 & 0 & 0 & 0 & 0 & 0 \end{pmatrix} \tag{6.58}$$

which can be found as Eqs. (58) and (59) of Ref. [46]. This relationship applies both to RI scheme and bare lattice operators.

In our lattice calculation we have evaluated the matrix elements of all ten linearly-dependent operators Q_i as given in Tab. 6.4. This gives us a consistency test of the three Fierz identities: these identities are obeyed to within statistical errors and with an absolute size at the 1% level, validating

0.001217	0.0001759	0.001208	0.0006908	0.001206	0.0001964	0.0004749	7.289×10^{-5}	0.0005008	-2.695×10^{-5}
0.0001759	0.0008377	0.0003157	0.001220	0.0004747	0.0008078	0.0004188	0.0009140	5.226×10^{-5}	0.0003670
0.001208	0.0003157	0.006443	0.003560	0.003463	0.003764	-0.0001617	-0.0007452	-0.0009426	-0.001024
0.0006908	0.001220	0.003560	0.008397	0.002873	0.006152	6.055×10^{-6}	-0.0002789	-0.0003660	-0.001078
0.001206	0.0004747	0.003463	0.002873	0.008692	0.004380	-0.0006516	-0.001387	-0.0008054	-0.0003295
0.0001964	0.0008078	0.003764	0.006152	0.004380	0.02195	-0.001279	-0.006099	-0.0003987	-0.001377
0.0004749	0.0004188	-0.0001617	6.055×10^{-6}	-0.0006516	-0.001279	0.002804	0.003961	0.001241	0.0006063
7.289×10^{-5}	0.0009140	-0.0007452	-0.0002789	-0.001387	-0.006099	0.003961	0.01150	0.0004234	0.001589
0.0005008	5.226×10^{-5}	-0.0009426	-0.0003660	-0.0008054	-0.0003987	0.001241	0.0004238	0.002475	0.0003710
-2.695×10^{-5}	0.0003670	-0.001024	-0.001078	-0.0003295	-0.001377	0.0006063	0.001589	0.0003710	0.001571

Table 6.11: The 10×10 covariance matrix C_{ij} between the unrenormalized, infinite-volume lattice operators in the conventional basis and physical units of GeV^3.

our code. We do not expect the Fierz relations to be obeyed to floating point accuracy since our use of all-to-all propagators introduces a stochastic element into the inversion of the Dirac operator and our use of γ^5 hermiticity differs between the ten operators introducing statistical noise in different ways into each evaluation.

Since the Fierz identities are not obeyed exactly by the data in Tab. 6.4, we have a choice as to how the ten linearly-dependent matrix elements M_i^{lat} in that table are to be combined to give the seven independent matrix elements $M_i'^{\,\text{lat}}$ needed on the right-hand side of Eq. (6.56). To this end we choose to treat $M_i'^{\,\text{lat}}$ as fit parameters whose best fit values are obtained by minimizing the correlated χ^2:

$$\chi^2 = \sum_{ij=1}^{10} \left(M_i^{\text{lat}} - \sum_{k=1}^{7} T_{ik} M_k'^{\,\text{lat}} \right) (C^{-1})_{ij} \left(M_j^{\text{lat}} - \sum_{\ell=1}^{7} T_{j\ell} M_\ell'^{\,\text{lat}} \right) . \tag{6.59}$$

The result is an optimal combination that provably minimizes the statistical error on the resulting $M_i'^{\,\text{lat}}$. The 10×10 covariance matrix C_{ij} is estimated by studying the variation of the bootstrap means of the matrix elements, and is given in Tab. 6.11. Note that we use the same covariance matrix for the fit to each bootstrap sample (a frozen fit) and therefore do not take into account in our errors the fluctuations in the covariance matrix over bootstrap samples. However such effects are expected to be minimal due to our large number of configurations. The results for the bare matrix elements obtained by this procedure, along with those obtained by applying Eq. (6.57) to convert those results back into the 10-basis, are given in Tab. 6.12. These results are quoted in physical units and incorporate the Lellouch-Lüscher finite-volume correction.

The results for the seven operators converted to the SMOM(γ^μ, γ^μ) and SMOM($\not{q}, \not{q}$) schemes

i	Q'_i (GeV^3)	Q_i (GeV^3)
1	0.143(93)	−0.119(32)
2	−0.147(24)	0.261(27)
3	0.233(23)	0.023(74)
4	-	0.403(72)
5	−0.723(91)	−0.723(91)
6	−2.211(144)	−2.211(144)
7	1.876(52)	1.876(52)
8	5.679(107)	5.679(107)
9	-	−0.190(39)
10	-	0.190(35)

Table 6.12: The bare lattice matrix elements in the 7-operator chiral basis (second column) that minimize the correlated χ^2 Eq. (6.59), and those results converted back into the 10-operator basis by applying Eq. (6.57) (third column). These results are quoted in physical units and incorporate the Lellouch-Lüscher finite-volume correction. The errors are statistical, only.

i	SMOM($\not{q}, \not{q}$) (GeV^3)	SMOM(γ^μ, γ^μ) (GeV^3)	$\overline{\text{MS}}$ via SMOM($\not{q}, \not{q}$) (GeV^3)	$\overline{\text{MS}}$ via SMOM(γ^μ, γ^μ) (GeV^3)
1	0.060(39)	0.059(38)	−0.107(22)	−0.093(18)
2	−0.125(19)	−0.106(16)	0.147(15)	0.143(14)
3	0.142(17)	0.128(14)	−0.086(61)	−0.053(44)
4	-	-	0.185(53)	0.200(40)
5	−0.351(62)	−0.313(48)	−0.348(62)	−0.311(48)
6	−1.306(90)	−1.214(82)	−1.308(90)	−1.272(86)
7	0.775(23)	0.790(23)	0.769(23)	0.784(23)
8	3.312(63)	3.092(58)	3.389(64)	3.308(63)
9	-	-	−0.117(20)	−0.114(19)
10	-	-	0.137(22)	0.123(19)

Table 6.13: Physical, infinite-volume matrix elements in the SMOM($\not{q}, \not{q}$) and SMOM(γ^μ, γ^μ) schemes at $\mu = 4.006$ GeV given in the 7-operator chiral basis, as well as those converted perturbatively into the $\overline{\text{MS}}$ scheme at the same scale in the 10-operator basis. The errors are statistical only.

are given in the left two columns of Tab. 6.13. The right two columns of that table show the matrix elements of the ten conventional operators in the $\overline{\text{MS}}$ scheme obtained from the left two columns by an application of Eqs. (6.57) and (6.58). For the convenience of the reader in utilizing these results we also provide the covariance matrices for the SMOM($\not{q}, \not{q}$) scheme matrix elements, which we will use as our central values in Sec. 6.7, and also the $\overline{\text{MS}}$ matrix elements derived from them, in Tabs. 6.14 and 6.15, respectively.

0.001516	5.385×10^{-5}	-9.167×10^{-5}	0.0001252	−0.0003965	0.0004930	0.0007192
5.385×10^{-5}	0.0003563	-4.099×10^{-5}	0.0007596	0.0002981	2.914×10^{-5}	−0.0002118
-9.167×10^{-5}	-4.099×10^{-5}	0.0002808	0.0003784	0.0004679	-4.656×10^{-5}	0.0001516
0.0001252	0.0007596	0.0003784	0.003904	0.001679	-8.000×10^{-5}	−0.0004013
−0.0003965	0.0002981	0.0004679	0.001679	0.008188	−0.0003817	−0.002110
0.0004930	2.914×10^{-5}	-4.656×10^{-5}	-8.000×10^{-5}	−0.0003817	0.0005395	0.0009460
0.0007192	−0.0002118	0.0001516	−0.0004013	−0.002110	0.0009460	0.003937

Table 6.14: The 7×7 covariance matrix between the renormalized, infinite-volume matrix elements in the SMOM($\not{q}, \not{q}$) scheme in the chiral basis.

0.0004628	8.315×10^{-6}	0.001058	0.0005998	0.0008504	0.0002622	0.0001246	-6.882×10^{-5}	0.0001651	−0.0002894
8.315×10^{-6}	0.0002367	0.0002796	0.0004981	0.0002866	0.0002532	5.669×10^{-5}	0.0003026	−0.0001273	0.0001010
0.001058	0.0002796	0.003749	0.002929	0.002999	0.001681	-7.629×10^{-7}	−0.0003280	−0.0002872	−0.001066
0.0005998	0.0004981	0.002929	0.002784	0.002406	0.001524	-6.156×10^{-5}	7.545×10^{-5}	−0.0005649	−0.0006666
0.0008504	0.0002866	0.002999	0.002406	0.003902	0.001607	-7.840×10^{-5}	−0.0004062	−0.0002240	−0.0007878
0.0002622	0.0002532	0.001681	0.001524	0.001607	0.008059	−0.0003739	−0.002158	−0.0004472	−0.0004561
0.0001246	5.669×10^{-5}	-7.629×10^{-7}	-6.156×10^{-5}	-7.840×10^{-5}	−0.0003739	0.0005361	0.0009564	0.0001873	0.0001194
-6.882×10^{-5}	0.0003026	−0.0003280	7.545×10^{-5}	−0.0004062	−0.002158	0.0009564	0.004120	6.076×10^{-5}	0.0004322
0.0001651	−0.0001273	−0.0002872	−0.0005649	−0.0002240	−0.0004472	0.0001873	6.076×10^{-5}	0.0003912	9.882×10^{-5}
−0.0002894	0.0001010	−0.001066	−0.0006666	−0.0007878	−0.0004561	0.0001194	0.0004322	9.882×10^{-5}	0.0004892

Table 6.15: The 10×10 covariance matrix between the renormalized, infinite-volume matrix elements in the $\overline{\text{MS}}$ scheme in the chiral basis obtained using the SMOM($\not{q}, \not{q}$) intermediate scheme.

6.5.3 Results for A_0

We can now obtain A_0 from our lattice calculation as follows:

$$A_0 = \frac{G_F}{\sqrt{2}} V_{us}^* V_{ud} \sum_{i=1}^{10} \left(z_i^{\overline{\text{MS}}}(\mu) + \tau y_i^{\overline{\text{MS}}}(\mu) \right) M_i^{\overline{\text{MS}}}(\mu) \, . \tag{6.60}$$

The Wilson coefficients have been computed to next-to-leading order in QCD and electroweak perturbation theory in the $\overline{\text{MS}}$ scheme [54], and at $\mu = 4.006$ GeV take the values given in Tab. 6.16. For the CKM matrix element ratio τ we use the value given in Tab. 6.10. Combining these with the $\overline{\text{MS}}$-renormalized matrix elements obtained in Tab. 6.13 we obtain the following for the SMOM($\not{q}, \not{q}$) intermediate scheme,

$$\text{Re}(A_0) = 2.99(32) \times 10^{-7} \text{ GeV} \, , \tag{6.61a}$$
$$\text{Im}(A_0) = -7.15(66) \times 10^{-11} \text{ GeV} \, . \tag{6.61b}$$

and for the SMOM(γ^μ, γ^μ) intermediate scheme,

$$\text{Re}(A_0) = 2.86(31) \times 10^{-7} \text{ GeV} \, , \tag{6.62a}$$
$$\text{Im}(A_0) = -6.93(64) \times 10^{-11} \text{ GeV} \, . \tag{6.62b}$$

i	y_i	z_i
1	0	-0.199111
2	0	1.08976
3	0.0190166	-0.00525073
4	-0.0560629	0.0244698
5	0.0132642	-0.00607434
6	-0.0562033	0.0174607
7	-0.000271245	0.000134906
8	0.000521236	-0.000119628
9	-0.00946862	5.60698e-05
10	0.00186152	9.34113e-05

Table 6.16: The $\overline{\mathrm{MS}}$ Wilson coefficients $\vec{y}$ and $\vec{z}$ at $\mu = 4.006$ GeV computed via NLO QCD+EW perturbation theory.

The values of $\mathrm{Re}(A_0)$ agree to 4.1(4.2)% between the two schemes, and those of $\mathrm{Im}(A_0)$ to 3.1(3.8)%. This excellent agreement suggests that the systematic errors resulting from discretization effects and the truncation of the perturbative series in the non-perturbative renormalization are minimal at our high 4 GeV scale. In the following section a more detailed discussion of these systematic errors is presented.

The contributions of each of the ten operators to the real and imaginary parts of A_0 are given in Tab. 6.17. The result for $\mathrm{Im}(A_0)$ is dominated by the Q_6 matrix element with a 14(4)% cancelation from Q_4, where the errors are statistical only and the value is obtained using the $\mathrm{SMOM}(\slashed{q},\slashed{q})$ intermediate scheme to match the scheme used for the previous work. This is in contrast to the 51(29)%-level cancelation observed in Ref. [1] and is largely due to a 5.5σ increase in the Q_6 contribution from $-3.57(91)\times 10^{-11}$ GeV to $-8.78(60)\times 10^{-11}$ GeV (again using the $\mathrm{SMOM}(\slashed{q},\slashed{q})$ intermediate scheme). This change appears to largely result from excited-state contamination in our previous result, as we can see in Fig. 6.6 comparing the (larger-statistics) single-operator result at the value of $t'_{\mathrm{min}} = 4$ used for our previous work to our favored three-operator, two-state result with $t'_{\mathrm{min}} = 5$. This suggests that the 5% systematic error we formerly associated with excited-state contamination was significantly underestimated.

	Re(A_0)		Im(A_0)	
i	($\not{q}, \not{q}$) ($\times 10^{-7}$ GeV)	(γ^μ, γ^μ) ($\times 10^{-7}$ GeV)	($\not{q}, \not{q}$) ($\times 10^{-11}$ GeV)	(γ^μ, γ^μ) ($\times 10^{-11}$ GeV)
1	0.383(77)	0.335(64)	0	0
2	2.89(30)	2.81(28)	0	0
3	0.0081(58)	0.0050(42)	0.20(14)	0.12(10)
4	0.081(23)	0.088(17)	1.24(35)	1.34(27)
5	0.0380(68)	0.0339(53)	0.552(99)	0.492(77)
6	−0.410(28)	−0.398(27)	−8.78(60)	−8.54(57)
7	0.001863(56)	0.001900(56)	0.02491(75)	0.02540(75)
8	−0.00726(14)	−0.00708(13)	−0.2111(40)	−0.2060(39)
9	$-8.7(1.5) \times 10^{-5}$	$-8.5(1.4) \times 10^{-5}$	−0.133(22)	−0.128(21)
10	$2.37(38) \times 10^{-4}$	$2.13(32) \times 10^{-4}$	−0.0304(49)	−0.0273(41)
Total	2.99(32)	2.86(31)	−7.15(66)	−6.93(64)

Table 6.17: The contributions of each of the ten four-quark operators to Re(A_0) and Im(A_0) for the two different RI-SMOM intermediate schemes. The scheme and units are listed in the column headers. The errors are statistical, only.

6.5.4 Incorporating experimental results to improve the determination of Im(A_0)

The real and imaginary parts of A_0 comprise different linear combinations of the same basis of real lattice matrix elements. As the real part of the amplitude is precisely known from experiment and is not expected to receive significant contributions from new physics, we can use this quantity to replace part of the lattice input and thereby improve the precision of the imaginary part. The appropriate procedure is discussed in Refs. [70, 71] in the context of the conventional basis of 10 non-independent operators, where the latter authors use it to eliminate the Q_2 matrix element. For our purpose it is more convenient to express the method in terms of the unrenormalized matrix elements in the 7-operator basis. We write

$$\mathrm{Re}(A_0) = \frac{G_F}{\sqrt{2}} V_{us}^* V_{ud} \sum_{k=1}^{7} \mathrm{Re}(w_k^{\overline{\mathrm{MS}}\leftarrow\mathrm{lat}}) M_k'^{\mathrm{lat}} \tag{6.63}$$

$$\mathrm{Im}(A_0) = \frac{G_F}{\sqrt{2}} V_{us}^* V_{ud} \sum_{k=1}^{7} \mathrm{Im}(w_k^{\overline{\mathrm{MS}}\leftarrow\mathrm{lat}}) M_k'^{\mathrm{lat}} \tag{6.64}$$

where the $M'^{\text{lat}}_j = \langle \pi\pi | Q'_k | K \rangle$ are the matrix elements of the unrenormalized lattice operators in the 7-basis in infinite-volume and physical units, and

$$\begin{aligned}
\mathrm{Re}(w_k^{\overline{\mathrm{MS}}\leftarrow\mathrm{lat}}) &= \sum_{i=1}^{10}\sum_{j=1}^{7}\left(z_i^{\overline{\mathrm{MS}}} + \mathrm{Re}(\tau) y_i^{\overline{\mathrm{MS}}}\right) T_{ij} Z_{jk}^{\overline{\mathrm{MS}}\leftarrow\mathrm{lat}} && (6.65)\\
\mathrm{Im}(w_k^{\overline{\mathrm{MS}}\leftarrow\mathrm{lat}}) &= \sum_{i=1}^{10}\sum_{j=1}^{7}\left(\mathrm{Im}(\tau) y_i^{\overline{\mathrm{MS}}}\right) T_{ij} Z_{jk}^{\overline{\mathrm{MS}}\leftarrow\mathrm{lat}} && (6.66)
\end{aligned}$$

are the "lattice Wilson coefficients". Here T_{ij} is the 10×7 matrix expressing the 10 linearly-dependent operators in terms of the seven independent operators in the chiral basis, given in Eq. (6.58). The matrix $Z^{\overline{\mathrm{MS}}\leftarrow\mathrm{lat}}$ is the product of the 7×7 perburbative matrix expressing the seven $\overline{\mathrm{MS}}$ operators in terms of the seven RI operators and the non-perturbative 7×7 matrix which determines the RI operators in terms of the lattice operators.

We can then use Eq. (6.63) to remove the matrix element of the operator Q'_ℓ from $\mathrm{Im}(A_0)$ if we write

$$\begin{aligned}
\mathrm{Im}(A_0) &= \frac{G_F}{\sqrt{2}} V_{us}^* V_{ud} \sum_{k=1}^{7} \mathrm{Im}(w_k^{\overline{\mathrm{MS}}\leftarrow\mathrm{lat}}) M'^{\text{lat}}_k \\
&\qquad + \lambda \left[\mathrm{Re}(A_0) - \frac{G_F}{\sqrt{2}} V_{us}^* V_{ud} \sum_{k=1}^{7} \mathrm{Re}(w_k^{\overline{\mathrm{MS}}\leftarrow\mathrm{lat}}) M'^{\text{lat}}_k \right] && (6.67)
\end{aligned}$$

and choose

$$\lambda = \frac{\mathrm{Im}(w_\ell^{\overline{\mathrm{MS}}\leftarrow\mathrm{lat}})}{\mathrm{Re}(w_\ell^{\overline{\mathrm{MS}}\leftarrow\mathrm{lat}})} \tag{6.68}$$

In Tab. 6.18 we present values for $\mathrm{Im}(A_0)$ obtained through using this procedure to replace successive lattice matrix elements. The most significant gain in statistical error is achieved by replacing the matrix element M'^{lat}_3, for which we obtain the following for the SMOM($\not{q}, \not{q}$) intermediate scheme,

$$\mathrm{Im}(A_0) = -6.98(62) \times 10^{-11}\ \mathrm{GeV} \tag{6.69}$$

and for the SMOM(γ^μ, γ^μ) intermediate scheme,

$$\mathrm{Im}(A_0) = -6.65(58) \times 10^{-11}\ \mathrm{GeV} \tag{6.70}$$

i	SMOM($\not{q}, \not{q}$) ($\times 10^{-11}$ GeV)	SMOM(γ^μ, γ^μ) ($\times 10^{-11}$ GeV)
1	−7.12(65)	−6.89(63)
2	−7.26(72)	−7.23(75)
3	−6.98(62)	−6.65(58)
5	−5.05(1.98)	−3.72(2.09)
6	−0.23(6.16)	0.81(4.92)
7	−2.09(4.67)	−0.11(4.40)
8	2.39(9.00)	6.07(8.58)

Table 6.18: Values of $\mathrm{Im}(A_0)$ obtained for each of the two intermediate schemes by eliminating lattice data for the matrix element of operator Q'_ℓ in favor of experimental value for $\mathrm{Re}(A_0)$.

which have 6% smaller statistical errors.

We could instead choose the parameter λ to give that result for $\mathrm{Im}(A_0)$ with the smallest statistical error. Since the value obtained for λ from this procedure is extremely close to that needed to remove the matrix element $M_3'^{\mathrm{lat}}$, we adopt the simpler procedure of eliminating $M_3'^{\mathrm{lat}}$ and the results given in Eqs. (6.69) and (6.70).

6.5.5 Determination of ϵ'

$\mathrm{Re}(\epsilon'/\epsilon)$ can now be obtained via Eq. (2.20). We use the lattice values for the $I = 0$ and $I = 2$ $\pi\pi$ scattering phase-shifts: δ_0 is given in Tab. 5.12 with

$$\delta_0 = 32.3(1.0)(1.4)^\circ\,, \tag{6.71}$$

and for δ_2 we use

$$\delta_2 = -11.6(2.5)(1.2)^\circ\,, \tag{6.72}$$

obtained from our continuum result [2]. Here the parentheses list the statistical error and an estimate of the excited-state systematic error, respectively.

Writing $\epsilon = |\epsilon| e^{i\phi_\epsilon}$, where both $|\epsilon|$ and its phase ϕ_ϵ can be found in Tab. 6.10, the overall complex phase of ϵ'/ϵ is

$$i e^{i(\delta_2 - \delta_0)} e^{-i\phi_\epsilon} = e^{i(\delta_2 - \delta_0 + \pi/2 - \phi_\epsilon)}\,. \tag{6.73}$$

The resulting real part of the complex phase,

$$\cos(\delta_2 - \delta_0 + \pi/2 - \phi_\epsilon) = 0.999(2)\,, \tag{6.74}$$

is in complete agreement with the value of 0.9998(2) obtained by combining PDG inputs [68] and the dispersive values for the phase shifts [9].

For our primary result we use the more precise experimental values of $\mathrm{Re}(A_0)$ and $\mathrm{Re}(A_2)$, and use the results for $\mathrm{Im}(A_0)$ given in Eqs. (6.69) and (6.70) that incorporate the experimental value of $\mathrm{Re}(A_0)$. The continuum, lattice value for $\mathrm{Im}(A_2)$ is given in Eq. 64 of Ref. [2] and must be corrected for the 20% change of $\mathrm{Im}(\tau) = -0.0005558$ used in that work to the value given in Tab. 6.6.8. We obtain,

$$\mathrm{Im}(A_2) = -8.34(1.03) \times 10^{-13}\ \mathrm{GeV} \tag{6.75}$$

For the SMOM($\not{q}, \not{q}$) intermediate scheme we find

$$\mathrm{Re}(\epsilon'/\epsilon) = 0.00217(26) \tag{6.76}$$

and for the SMOM(γ^μ, γ^μ) intermediate scheme,

$$\mathrm{Re}(\epsilon'/\epsilon) = 0.00203(25)\,, \tag{6.77}$$

where the error is statistical only.

It is illustrative to break the value of $\mathrm{Re}(\epsilon'/\epsilon)$ into the so-called “QCD penguin”

$$\mathrm{Re}\left(\frac{\varepsilon'}{\varepsilon}\right)_{\mathrm{QCDP}} = -\frac{\omega\cos(\delta_2 - \delta_0 + \pi/2 - \phi_\epsilon)}{\sqrt{2}|\varepsilon|}\frac{\mathrm{Im}A_0}{\mathrm{ReA_0}} \tag{6.78}$$

and “electroweak penguin”

$$\mathrm{Re}\left(\frac{\varepsilon'}{\varepsilon}\right)_{\mathrm{EWP}} = \frac{\omega\cos(\delta_2 - \delta_0 + \pi/2 - \phi_\epsilon)}{\sqrt{2}|\varepsilon|}\frac{\mathrm{Im}A_2}{\mathrm{ReA_2}} \tag{6.79}$$

contributions, the sum of which is equal to $\mathrm{Re}(\epsilon'/\epsilon)$. These terms have opposite sign such that the sum involves an important cancellation. For the electroweak penguin contribution we find

$$\mathrm{Re}\left(\frac{\varepsilon'}{\varepsilon}\right)_{\mathrm{EWP}} = -7.96(98) \times 10^{-4}\,. \tag{6.80}$$

Using the results for $\mathrm{Im}(A_0)$ obtained using the SMOM($\not{q}, \not{q}$) intermediate scheme we find

$$\mathrm{Re}\left(\frac{\varepsilon'}{\varepsilon}\right)_{\mathrm{QCDP}} = 0.00297(26)\,, \tag{6.81}$$

and likewise for the SMOM(γ^μ, γ^μ) intermediate scheme,

$$\mathrm{Re}\left(\frac{\varepsilon'}{\varepsilon}\right)_{\mathrm{QCDP}} = 0.00283(25)\,. \tag{6.82}$$

We observe that the two terms cancel at the 27(4)% and 28(4)% level relative to the QCDP contribution for the SMOM($\not{q}, \not{q}$) and SMOM(γ^μ, γ^μ) results, respectively. This degree of cancellation is considerably less than the 71(36)% observed in our 2015 analysis. Here the errors are statistical only.

We can also compute a purely lattice value of $\mathrm{Re}(\varepsilon'/\varepsilon)$ using $\mathrm{Re}(A_0)$ from Eqs. (6.61a) and (6.62a), $\mathrm{Im}(A_0)$ from Eqs. (6.61b) and (6.62b), and both $\mathrm{Re}(A_2)$ and $\mathrm{Im}(A_2)$ from Eq. 64 of Ref. [2]. Note we do not correct $\mathrm{Re}(A_2)$ for the change in $\mathrm{Re}(\tau)$ as its contribution is much smaller than that of the Wilson coefficients z_i. For the SMOM($\not{q}, \not{q}$) intermediate scheme we obtain

$$\mathrm{Re}(\epsilon'/\epsilon) = 0.00293(104) \tag{6.83}$$

and for the SMOM(γ^μ, γ^μ) intermediate scheme,

$$\mathrm{Re}(\epsilon'/\epsilon) = 0.00309(112)\,, \tag{6.84}$$

where the errors are again statistical. Unfortunately these pure-lattice results have considerably larger statistical errors, which suggests that there is little statistical correlation between the results for $\mathrm{Im}(A_0)$ and $\mathrm{Re}(A_0)$ which would be needed to reduce the error in their ratio. Thus, we will use the results given in Eqs. (6.76) and (6.77) for our final results.

6.5.6 Origin of the change in ϵ' compared to our 2015 calculation

In this section we provide further insight into the origin of the significant change between our 2015 result of $\mathrm{Re}(\epsilon'/\epsilon) = 1.38(5.15)(4.59) \times 10^{-4}$ and our results above. Several factors may contribute to this effect:

1. The increase in the minimum time separation between the four-quark operator and the sink $\pi\pi$ operator from 4 to 5 in the $K \to \pi\pi$ matrix element fitting.
2. The change in the procedure for determining the derivative with respect to energy of $\pi\pi$ scattering phase-shift that enters the Lellouch-Lüscher factor.

3. The increase in statistics from 216 to 741 configurations.

4. The addition of the $\pi\pi(311)$ and σ sink operators.

5. The use of step-scaling to raise the renormalization scale from 1.53 GeV to 4.01 GeV.

6. The change in the value of the experimental inputs, notably that of the CKM ratio τ from $0.001543 - 0.000635i$ to $0.001558 - 0.000663i$.

We first note that repeating the $\pi\pi$ two-point function analysis for our larger data set but with a one-state fit to a single operator ($\pi\pi(111)$), and a fit range 6-25 to match that of the 2015 analysis, yields a result (in lattice units),

$$\begin{aligned} A^0_{\pi\pi(111)} &= 0.4028(32) \\ E_0 &= 0.3712(36) \end{aligned} \tag{6.85}$$

that is consistent with the results of our 2015 analysis,

$$\begin{aligned} A^0_{\pi\pi(111)} &= 0.3923(60) \\ E_0 &= 0.3606(74) \end{aligned} \tag{6.86}$$

to 1.5σ and 1.3σ for the amplitude and energy, respectively. Furthermore, the p-value of this fit is 0.451 indicating an excellent fit to the one-state model. The ground-state energy is, however, significantly larger than the value of $E_0 = 0.3479(11)$ found using three operators and two states in Sec. 5.2.1.

We next repeat the analysis of the $K \to \pi\pi$ matrix elements but with only the $\pi\pi(111)$ operator and a one-state fit with $t'_{\rm min} = 4$ to match the 2015 analysis, utilizing the $\pi\pi$ fit parameters from Eq. (6.85) above. Recall $t'_{\rm min}$ is the minimum time separation between the four-quark operator and the $\pi\pi$ sink for data included in the fit. We use the same input experimental parameters and other analysis strategies as in the original work, including the approach to obtaining the Lellouch-Lüscher parameter and the same SMOM($\not{q}, \not{q}$) non-perturbative renormalization factors with $\mu =$ 1.529 GeV. We find,

$$\mathrm{Re}(\epsilon'/\epsilon) = 2.52(2.12) \times 10^{-4}\,, \tag{6.87}$$

where the errors are statistical only. This result is completely consistent with our 2015 result,

$$\mathrm{Re}(\epsilon'/\epsilon) = 1.38(5.15) \times 10^{-4}\,, \tag{6.88}$$

indicating that a 3.4× increase in statistics is not sufficient to account for the difference.

Repeating the above but with the $K \to \pi\pi$ analysis and input parameters updated to match that of the present work gives,

$$\mathrm{Re}(\epsilon'/\epsilon) = 4.20(1.96) \times 10^{-4}\,, \tag{6.89}$$

which is slightly larger but still considerably smaller than the results in the previous section. With the step-scaled renormalization factors with $\mu = 4.01$ GeV we find,

$$\mathrm{Re}(\epsilon'/\epsilon) = 6.50(2.10) \times 10^{-4}\,. \tag{6.90}$$

Again we observe a small increase but insufficient to account for the difference.

The result in Eq. (6.90) differs now from our primary result only in the $\pi\pi$ and $K \to \pi\pi$ fitting strategies. Adopting the final fit ranges determined for the $\pi\pi$ and $K \to \pi\pi$ fits in Secs. 5.2.1 and 6.3, such that the analysis now differs only in the number of $\pi\pi$ operators, gives

$$\mathrm{Re}(\epsilon'/\epsilon) = 12.76(2.71) \times 10^{-4}\,. \tag{6.91}$$

This result is now much closer to our final result. The behavior we observe here is consistent with that displayed in Fig. 6.6 where we plot the dependence of the fitted matrix elements on the cut t'_{min} and the number of $\pi\pi$ operators included in the fits to the matrix elements (the $\pi\pi$ two-point function fits remain unchanged between the results displayed in this figure). This figure shows a significant discrepancy between the Q_6 matrix element obtained from a one-operator, one-state fit with $t'_{\mathrm{min}} = 4$ and the plateau observed when further operators are included. With increased statistics the onset of the apparent plateau for the one-operator, one-state fit does not occur until $t'_{\mathrm{min}} = 5$ (equal to the $t'_{\mathrm{min}} = 5$ used to obtain the result in Eq. (6.91)) but the resulting value for the Q_6 matrix element is still several standard deviations larger than the strong plateau observed in the multi-operator fits.

We therefore conclude that the difference in $\mathrm{Re}(\epsilon'/\epsilon)$ between our present and 2015 analysis results can be attributed primarily to unexpectedly large excited-state contamination in our previous

i	Rel. diff
1	−0.04(16)
2	0.012(39)
3	−0.7(6.8)
4	−0.08(11)
5	0.017(38)
6	0.019(23)
7	0.0017(95)
8	−0.0044(45)
9	0.093(64)
10	−0.032(58)

Table 6.19: Relative differences between the ground-state elements obtained by fitting to 3 operators and 3 states with $t'_{\rm min} = 4$ and those of our primary fit with 3 operators and 2 states with $t'_{\rm min} = 4$.

analysis masked by the rapid reduction in the signal to noise ratio, and that multiple operators are essential to isolate the ground-state matrix element even with large statistics.

6.6 Systematic errors

In this section we describe the procedure used to estimate the systematic errors on our results. We will quote the values as representative percentage errors on either the matrix elements or on A_0 as appropriate. A discussion of the systematic errors in the $\Delta I = 3/2$ calculation can be found in Ref. [2].

6.6.1 Excited state contamination

In Sec. 6.3.5 we devoted considerable effort to finding an optimal fit window in which excited state effects are minimal. We were unable to find evidence of such effects arising from excited kaon states, which is to be expected given both the large relative energy of such states and also the fact that the rapid growth of statistical noise as the four-quark insertion is moved away from the $\pi\pi$ operator implies that the data furthest from the kaon operator dominates the fit results. As such we do not assign a systematic error to possible contamination from excited kaon states.

As for the contribution of excited $\pi\pi$ states, we found little evidence for such effects even within the single operator fits to the $\pi\pi(111)$ data, except for the Q_5 and Q_6 matrix elements where the single-operator fits showed statistically significant deviations from the common plateau region that did not die away until $t' = 6$. We observed that by adding further sink operators and allowing for more $\pi\pi$ states substantially reduced the excited-state contamination such that the fits were highly consistent even if we include data at times as low as $t' = 3$. Despite this we chose a conservative uniform cut of $t'_{\rm min} = 5$ for our fits.

In order to assign a numerical error to the contamination from excited $\pi\pi$ states, we consider the comparison of the 3-operator, 3-state fit with $t'_{\rm min} = 4$ and the 3-operator, 2-state fit with $t'_{\rm min} = 5$, the latter being our chosen best fit. The former includes a third state and with $t'_{\rm min} = 4$ appears capable of describing the data well outside of the fit range, as we observed in Fig. 6.11 (lower-left panel). We compute relative differences under the bootstrap between the values of the ground-state matrix elements, the results of which are shown in Tab. 6.19. The only statistically resolvable difference, at 1.5σ, is for the Q_9 matrix element, which has only a negligible contribution to $\mathrm{Im}(A_0)$. For the dominant Q_4 and Q_6 matrix elements the differences cannot be resolved within our errors. We therefore conclude that the excited state systematic error is likely to be much smaller than our dominant systematic errors and can be neglected.

6.6.2 Unphysical kinematics

As our values of $E_{\pi\pi}$ and m_K differ by 2.2(3)%, the $K \to \pi\pi$ matrix elements are not precisely on shell. As discussed in Sec. 6.3, the primary result of these unphysical kinematics is the rise of a divergent contribution from the pseudoscalar operator $\bar{s}\gamma^5 d$ that vanishes when on shell by the equations of motion. In order to suppress this error we perform an explicit subtraction of the pseudoscalar operator that leaves behind a finite, regulator-independent term that represents the dominant remaining systematic error from the unequal kaon and $\pi\pi$ energies. As we are close to being on shell we can reasonably assume a linear ansatz for the dependence of our result on the energy difference $E_{\pi\pi} - m_K$. We estimate the associated systematic error by observing the change in the Q_2 matrix element as the kaon mass is increased by 4.5%. The measurement was performed

i	Rel. diff
1	−0.0054(51)
2	−0.0086(19)
3	−0.06(73)
4	−0.0144(75)
5	−0.054(12)
6	−0.0521(75)
7	−0.0053(25)
8	−0.0072(21)
9	−0.0055(21)
10	−0.00234(85)

Table 6.20: Relative differences in the unrenormalized lattice matrix elements of Q_i as the pseudoscalar subtraction coefficients α_i are uniformly increased by 5%

using 69 configurations of our original ensemble [1], with 3 different $K \longrightarrow \pi$ time separations (10, 12, and 14), and we observed a 6.9% increase in the matrix element. We scale this increase by the relative difference between our kaon and $\pi\pi$ energies, giving 3%.

Another means of estimating this systematic error is to vary the subtraction coefficients α_i by an amount consistent with the expected size of the residual contribution of the pseudoscalar operator. Given that the operator is dimension-3, its coefficient is originally $O(m_s/a^2)$ where the strange quark mass is in physical units. After the subtraction is performed, the residual term is expected to be of size $O(m_s\Lambda^2_{\text{QCD}})$, which has a relative size of $\sim a^2\Lambda^2_{\text{QCD}}$, or ~5%, of the original contribution, for $\Lambda_{QCD} = 300$ MeV. Increasing the subtraction coefficients α_i by this amount gives rise to the differences in the unrenormalized lattice matrix elements given in Tab. 6.20. The observed variations are generally consistent with the above, but to be conservative we assign a relative systematic error of 5% on the matrix elements resulting from the off-shell difference $E_{\pi\pi} \neq m_K$.

6.6.3 Finite lattice spacing

We use the value provided in Ref. [1] as an estimate of the finite lattice spacing systematic error. This was obtained by comparing the values of the $\Delta I = 3/2$ matrix elements between the continuum limit [2] and the calculation [60] performed on our $32^3 \times 64$, $\beta = 1.75$ (32ID) lattice. The parameters of the latter ensemble are identical to those used in this work to compute

Operator	32ID	continuum	rel. diff
$(27,1)$	0.0461(14)	0.0502(13)	8.7(4.1)%
$(8,8)$	0.874(49)	0.993(22)	13.6(6.1)%
$(8,8)_{\text{mix}}$	3.96(23)	4.54(12)	14.8(6.6)%

Table 6.21: The three $\Delta I = 3/2$ matrix elements in the $\overline{\text{MS}}$ scheme at $\mu = 3.0$ GeV and in units of GeV^3 that contribute to A_2, calculated on the 32ID ensemble (Ref. [60], Eq. (31)) and in the continuum limit (Ref [2], Tab. XIV) along with their relative difference. Only statistical errors are shown.

A_0, albeit without G-parity boundary conditions and with a larger-than-physical light quark mass giving a unitary pion mass of 170 MeV. The $\overline{\text{MS}}$ values for the three continuum matrix elements that contribute to A_2 are obtained by combining the continuum values of those matrix elements in the SMOM($\not{q}, \not{q}$) scheme (Tab. XIV of Ref. [2]) with the RI→ $\overline{\text{MS}}$ renormalization matrix computed on the 32ID lattice (Eq. 66 of Ref. [2]). As such this estimate addresses only the discretization errors on the matrix elements and not to those on the renormalization factors (which are expected to be small). We find the values given in Tab. 6.21. Averaging the three relative errors we arrive at an estimate of 12% discretization errors on the matrix elements.

6.6.4 Lellouch-Lüscher factor

As described in Sec. 6.5.1, the calculation of the Lellouch-Lüscher factor, F, that accounts for the power-law finite-volume corrections to the matrix element, requires an ansatz for the derivative of the $\pi\pi$ phase shift with respect to energy. There we present values for this derivative obtained from three methods:

- The Schenk parameterization [72] of the dispersive energy dependence obtained in Ref. [9]
- A linear approximation in the $\pi\pi$ energy above threshold, $\frac{d\delta_0}{dE_{\pi\pi}} = \frac{\delta_0}{E_{\pi\pi}-2m_\pi}$, which is inspired by the dispersive low-energy dependence found in Ref. [9] and can be related to $d\delta_0/dq$ via Eq. (6.46).
- A direct lattice calculation of the phase shift at energies close to and including the kaon mass.

i	Relative difference
1	−0.038(36)
2	−0.022(12)
3	0.070(576)
4	−0.018(31)
5	0.003(41)
6	0.006(6)
7	0(0)
8	0(0)
9	−0.031(17)
10	−0.023(21)

Table 6.22: The relative difference in $\overline{MS}$ matrix elements at $\mu = 1.33$ GeV obtained through the SMOM(γ^μ, γ^μ) intermediate scheme due to including the G_1 operator.

Ignoring the noisier of the two lattice determinations, the results varied between $\frac{d\delta_0}{dq} = 1.26$ and 1.41, a 12% spread. The resulting values of F differ by 1.5% since the dominant contribution arises from the derivative of the analytic function ϕ. We therefore assign a 1.5% systematic error to the matrix elements from this source.

6.6.5 Exponentially-suppressed finite volume corrections

We expect the remaining finite volume corrections to our matrix elements to be dominated by the (exponentially-suppressed) interactions between the final state pions that are not accounted for by the Lüscher and Lellouch-Lüscher prescriptions. In Refs. [2, 60] we performed an in-depth analysis of the finite-volume errors on the matrix elements that comprise A_2 using SU(3) chiral perturbation theory, in which the mesonic loop integrals are replaced by discrete sums over the allowed momenta. We do not expect these effects to depend strongly on the form of the four-quark operator, and indeed comparable $O(6-6.5\%)$ corrections were estimated for both classes of operator that enter the calculation of A_2. We therefore assign a representative 7% systematic error to the matrix elements.

6.6.6 Neglecting the contribution of the G_1 operator

In the calculation of our step-scaled non-perturbative renormalization factors with scale μ = 4.01 GeV we have not incorporated the effects of the G_1 operator. A previous lattice study [49], performed in the SMOM(γ^μ, γ^μ) scheme and utilizing step-scaling from a low-scale of μ = 1.33 GeV on our 32ID ensemble to a high scale of 2.29 GeV on a finer lattice, revealed the effects on A_0 of including this operator to be on the order of a few percent when combined with the matrix elements measured in our 2015 work [1]. Unfortunately the statistical errors on the differences in the renormalized matrix elements at μ = 2.29 GeV with and without G_1 included were found to be too large to resolve the effect with any precision, and we find that this also applies to the matrix elements obtained in the present work. (The renormalization matrices with and without G_1 at μ = 2.29 GeV can be found in Tab. 6.9.)

As discussed in Ref. [49], the increase in the relative error on the bootstrap differences is associated largely with the step-scaling matrix Λ^{RI} that describes the running between the low and high energy scales. However it is reasonable to expect that the largest effects of neglecting G_1 appear at the low energy scale in the step-scaling where the QCD coupling is larger. We therefore compare the matrix elements renormalized at the low scale in the $\overline{\mathrm{MS}}$ scheme in order to estimate the size of this systematic error with greater precision. We perform this comparison using the SMOM(γ^μ, γ^μ) intermediate scheme with μ = 1.33 GeV, the renormalization matrices of which are given in Tab. 6.8. The relative differences of the resulting $\overline{\mathrm{MS}}$ matrix elements are given in Tab. 6.22. While the observed differences are still poorly resolved, the typical size of the effect appears to be $O(3\%)$, and we therefore assign a 3% systematic error to the effect of neglecting G_1. (This estimate is quite conservative given the tiny difference in the dominant, Q_6 operator observed in the table.)

6.6.7 Sytematic errors in $\overline{\mathrm{MS}}$ operator renormalization

The most important systematic errors in determining the renormalization matrix $Z^{\overline{\mathrm{MS}}\leftarrow\mathrm{lat}}$ arise from three sources: i) The omission of dimension-6, quark bilinear operators which vanish on shell such as G_1 discussed above. ii) Finite lattice spacing errors that result from our large choice of RI renormalization scale μ. iii) The perturbative truncation error introduced when one-loop QCD perturbation theory is used to relate the RI-SMOM and $\overline{\text{MS}}$ schemes. In order to estimate these systematic errors, we examine the difference between the results in the $\overline{\text{MS}}$ scheme obtained from our two different intermediate RI-SMOM schemes. Rather than examining the matrix elements themselves, which can be statistically noisy and vary significantly in size and importance, it is convenient to study instead the differences between the elements of the 7×7 lattice→ $\overline{\text{MS}}$ renormalization matrix

$$R^{\overline{\text{MS}}\leftarrow\text{RI}\leftarrow\text{lat}}_{\text{1-loop}\,j\ell}(\mu) = H^{\overline{\text{MS}}\leftarrow\text{RI}}_{\text{1-loop}\,jk}(\mu) R^{\text{RI}\leftarrow\text{lat}}_{k\ell}(\mu)\,, \tag{6.92}$$

where H is the perturbative matching matrix. In the absence of systematic errors the matrix $R^{\overline{\text{MS}}\leftarrow RI\leftarrow\text{lat}}$ is independent of the intermediate RI scheme. We can then study this systematic error by examining the matrix

$$\Xi \equiv \left| \mathbb{I} - \left[R^{\overline{\text{MS}}\leftarrow\text{SMOM}(\not{q},\not{q})\leftarrow\text{lat}}_{\text{1-loop}} \right]^{-1} R^{\overline{\text{MS}}\leftarrow\text{SMOM}(\gamma^\mu,\gamma^\mu)\leftarrow\text{lat}}_{\text{1-loop}} \right|\,, \tag{6.93}$$

where $\mathbb{I}$ is the 7×7 unit matrix and $|.|$ implies that the absolute value of each element is taken. The ratio of R-matrices in this equation converts from the lattice scheme to $\overline{\text{MS}}$ through one intermediate scheme, and converts back to the lattice scheme via the other scheme, and hence becomes the unit matrix if no systematic errors exist. The difference from the unit matrix is therefore a measure of the size of the systematic error: Under the reasonable assumption that the systematic errors in the two schemes are comparable in size, we expect the elements of Ξ to vary between zero and approximately twice the size of the systematic error present in each. We therefore assign a percentage systematic error that is one half of the largest observed element of Ξ at a scale μ.

In Tab. 6.23 we tabulate the non-zero elements of Ξ for various $\overline{\text{MS}}$ scales and step-scaling procedures. Once again we observe that the effects of including or discounting the G_1 operator, while harder to statistically resolve after passing through the step-scaling procedure, are at the

Element (i, j)	1.33 GeV	1.53 GeV	2.29 GeV	4.01 GeV
(1,1)	0.07406(36)	0.062571(56)	0.04936(42)	0.01686(36)
(2,2)	0.182(34)	0.173(15)	0.044(54)	0.128(83)
(2,3)	0.313(38)	0.282(16)	0.132(58)	0.135(83)
(2,5)	0.006(11)	0.0036(50)	0.013(16)	0.009(31)
(2,6)	0.0005(95)	0.0030(42)	0.0099(100)	0.005(13)
(3,2)	0.276(33)	0.256(14)	0.119(33)	0.058(42)
(3,3)	0.417(38)	0.399(16)	0.197(37)	0.047(43)
(3,5)	0.006(10)	0.0076(47)	0.0084(94)	0.005(13)
(3,6)	0.0420(96)	0.0212(40)	0.0315(68)	0.0020(59)
(5,2)	0.00(14)	0.042(59)	0.18(18)	0.22(27)
(5,3)	0.04(15)	0.001(60)	0.20(19)	0.21(26)
(5,5)	0.004(39)	0.012(18)	0.034(50)	0.022(97)
(5,6)	0.037(34)	0.007(15)	0.044(31)	0.032(38)
(6,2)	0.139(65)	0.173(27)	0.010(110)	0.16(13)
(6,3)	0.321(74)	0.291(33)	0.14(12)	0.23(14)
(6,5)	0.027(20)	0.0104(75)	0.024(34)	0.055(46)
(6,6)	0.110(22)	0.0752(89)	0.052(26)	0.031(24)
(7,7)	0.01424(34)	0.008152(35)	0.01096(40)	0.00360(25)
(7,8)	0.003429(46)	0.002120(29)	0.002029(51)	0.00548(19)
(8,7)	0.026523(94)	0.024917(63)	0.02364(24)	0.00710(92)
(8,8)	0.14784(44)	0.12752(14)	0.09866(58)	0.0263(10)

Table 6.23: The non-zero elements of the matrix Ξ computed using the renormalization matrices obtained at μ = 1.33 GeV and 1.53 GeV on the 32ID ensemble, as well as the step-scaled renormalization matrices with μ = 2.29 GeV and 4.01 GeV. We do not include the G_1 operator here, and its absence is treated as a separate systematic error in Sec. 6.6.6.

percent scale.

As expected there is a general trend towards smaller values as we increase the scale that appears consistent with the factor of three decrease in α_s^2 between 1.33 GeV and 4.01 GeV that is expected to describe the scaling of the missing NNLO terms. Unfortunately the statistical errors on the results at 4.01 GeV are too large to resolve the residual systematic effects. Nevertheless, considering the results of this table and also the 3-4% differences observed in ReA_0 and ImA_0 between the schemes in Sec. 6.5.3, we assign a 4% systematic error to the non-perturbative renormalization factors.

6.6.8 Parametric errors

We propagate the parametric uncertainties shown in Tab. 6.10 to ReA_0 and ImA_0. For ReA_0 the largest such uncertainty is the charm-mass dependence, which, however, is only a 0.3% effect. For ImA_0, the largest uncertainty is 5% from the τ parameter, 3% from α_s, and less than 1% from the charm and top quark masses. The other uncertainties have been estimated but are negligible compared to those quoted. We therefore estimate a total parametric uncertainty of 6% for ImA_0 and 0.3% for ReA_0.

6.6.9 Wilson coefficients

As mentioned previously we compare the NLO and LO determinations of the Wilson coefficients in order to estimate the systematic error arising due to missing higher-order terms. More specifically, we compare Im(A_0) obtained from LO and NLO Wilson coefficients, computed using the 1-loop and 2-loop determinations of α_s, respectively, while keeping fixed the renormalized matrix elements in the $\overline{\text{MS}}$ scheme at 4.01 GeV obtained using the SMOM$(\not{q}, \not{q})$ intermediate scheme, given in Tab. 6.13, together with the various input parameters, such as the quark masses and the QCD coupling constant. For the latter we use the solution of the 4-loop β function [67] to compute $\alpha_s^{N_f=4}(\hat{\mu})$ in the 4-flavor theory, starting from the value of $\alpha_s(m_Z)$ in Tab. 6.10, and we study the dependence of the LO prediction of Im(A_0) as a function of $\hat{\mu}$, relative to the NLO result. (As expected, the NLO shows a mild dependence simply due to the mismatch between the running of α_s from the Z pole (4 loops) and the running used in the calculation of the Wilson Coefficients (2 loops).) Starting at 8% at $\hat{\mu} \approx m_c$, it increases up to 16% at $\hat{\mu} \approx m_b$; hence for our systematic error estimate on the Wilson coefficients, we choose the intermediate point $\hat{\mu} = 1.7$ GeV for which the NLO and LO difference is 12%. We have verified that fixing the value of $\Lambda^{N_f=4}$ leads to similar conclusions.

Additionally we consider the same difference of LO vs NLO predictions for Im(A_0), as a function of the RI intermediate schemes and the scale of the RI to $\overline{\text{MS}}$ conversion, while keeping fixed all parameters, $\alpha_s^{N_f=4}(\hat{\mu})$ included. We find that, despite varying the renormalization scale by almost a factor of two and the use of different intermediate RI schemes, the differences in the values of Im(A_0) are quite consistent, in the range 11-15%. This suggests that the bulk of the observed difference arises from the perturbative 3-to-4 flavor matching and running above the charm threshold, which is common to all of these determinations, and that improved theory input for the 3-to-4 flavor matching could significantly reduce it. (Note that in our calculation we take the matching scale across a flavor threshold equal to the corresponding quark mass in order to avoid large logarithms. Additional insights could be gained by studying the dependence on this matching scale as in Ref. [65].)

In conclusion we assign a 12% systematic error on both ReA_0 and ImA_0 associated with the NLO determination of the Wilson coefficients.

6.6.10 Error budget

We divide the systematic errors into those that affect the calculation of the matrix elements of the $\overline{\text{MS}}$ weak operators Q'_j and those that enter when these matrix elements are combined to produce the complex, physical decay amplitude A_0. The former are collected in Tab. 6.24. In order to obtain the final systematic error on Im(A_0) arising from these matrix elements we note that the result is dominated by the Q_6 operator with only a 20% cancellation from Q_4. In this circumstance it is reasonable simply to apply the same flat percentage error to Im(A_0) as to Q_6.

Error source	Value
Excited state	-
Unphysical kinematics	5%
Finite lattice spacing	12%
Lellouch-Lüscher factor	1.5%
Finite-volume corrections	7%
Missing G_1 operator	3%
Renormalization	4%
Total	15.7%

Table 6.24: Relative systematic errors on the infinite-volume matrix elements of the $\overline{\text{MS}}$-renormalized four-quark operators Q'_j.

Error source	Value	
	Re(A_0)	Im(A_0)
Matrix elements	15.7%	15.7%
Parametric errors	0.3%	6%
Wilson coefficients	12%	12%
Total	19.8%	20.7%

Table 6.25: Relative systematic errors on Re(A_0) and Im(A_0).

Since Re(A_0) is similarly dominated by Q_2, we apply the same strategy. For A_0 we then arrive at the error budget given in Tab. 6.25 which includes this error arising from the uncertainties in the matrix elements as well as those arising from the use of perturbation theory when computing the $\overline{\text{MS}}$ Wilson coefficients and the values of the needed Standard Model input parameters.

6.7 Final results and discussion

In this section we collect our final results including systematic errors and discuss the implications of our results. For consistency with our previous work we will use the SMOM($\not{q}, \not{q}$) intermediate scheme for our central value.

6.7.1 Matrix elements

The renormalized, infinite-volume matrix elements in the RI and $\overline{\text{MS}}$ schemes are given in Tab. 6.13, where the errors are statistical only. The corresponding relative systematic errors can

i	SMOM($\not{q},\not{q}$) (GeV^3)
1	0.060(39)(9)
2	−0.125(19)(20)
3	0.142(17)(22)
5	−0.351(62)(55)
6	−1.306(90)(205)
7	0.775(23)(122)
8	3.312(63)(520)

Table 6.26: Physical, infinite-volume matrix elements in the SMOM($\not{q},\not{q}$) scheme at $\mu = 4.006$ GeV given in the 7-operator chiral basis. The errors are statistical and systematic respectively. Note that our 4% estimate of the renormalization systematic error includes both lattice systematic errors and those associated with the truncation of the perturbative series in the RI→ $\overline{\text{MS}}$ matching. While the latter are inappropriate to apply to matrix elements in the non-perturbative schemes, due to our estimation procedure we are at present unable to isolate these two effects and as such apply the full 4% systematic error also to these RI matrix elements.

be found in Tab. 6.24. For the convenience of the reader we have reproduced the matrix elements in the SMOM($\not{q},\not{q}$) scheme including their systematic errors in Tab. 6.26. In order to allow the reader to compute derivative quantities from these matrix elements, the covariance matrices for the renormalized matrix elements in the SMOM($\not{q},\not{q}$) and $\overline{\text{MS}}$ schemes at 4.01 GeV can be found in Tabs. 6.14 and 6.15, respectively.

6.7.2 Decay amplitude

For the real part of the decay amplitude we take the value from Eq. (6.61a) and apply the systematic errors given in Tab. 6.25 to obtain

$$\text{Re}(A_0) = 2.99(0.32)(0.59) \times 10^{-7}\ \text{GeV}\,, \tag{6.94}$$

where the errors are statistical and systematic, respectively. The imaginary part is obtained likewise from Eq. (6.69), giving

$$\text{Im}(A_0) = -6.98(0.62)(1.44) \times 10^{-11}\ \text{GeV}\,. \tag{6.95}$$

The breakdown of the contributions of each of the 10 operators to these amplitudes can be found in Tab. 6.17. We observe that, at the scale at which we are working, the dominant contribution to Re(A_0) (97%) originates from the tree operator Q_2, while Q_1 has a contribution of about 13% that is largely cancelled by that of the penguin operator [73, 74] Q_6. Likewise, the dominant contribution to $\mathrm{Im}(A_0)$ is from the QCD penguin [73, 74] operator, Q_6, with a 14% cancellation from Q_4.

6.7.3 A comment on the $\Delta I = 1/2$ rule

The "$\Delta I = 1/2$ rule" refers to the enhancement by almost a factor of 450 of the $I = 0$ $K \to \pi\pi$ decay rate relative to that of the $I = 2$ decay, corresponding to the experimentally-determined ratio $\mathrm{Re}(A_0)/\mathrm{Re}(A_2) = 22.45(6)$. A factor of two contribution to this ratio arises from the perturbative Wilson coefficients [75, 76, 77]. While the remaining factor of ten has been viewed for some time as a consequence of the strong dynamics of QCD, the origin of this large factor has remained something of a mystery with no widely-accepted dynamical explanation.

In the past [78, 79, 60], and most recently in Ref. [2], when simulating with physical pion masses we have observed a sizeable cancellation between the two Wick contractions of the dominant $(27, 1)$ operator contributing to the $\Delta I = 3/2$ decay amplitude, leading to a significant suppression of $\mathrm{Re}\,(A_2)$. In these calculations we reproduced the experimental value of $\mathrm{Re}\,(A_2)$ and concluded that this cancellation was likely to be a very significant element in the $\Delta I = 1/2$ rule. We stress that the cancellation between the two leading contributions to $\mathrm{Re}\,(A_2)$ depends sensitively on the light quark mass and becomes much less significant as the light quark mass is increased above its physical value. Note also that such a cancellation is not consistent with naïve factorization, which predicts that both contributions have the same sign and differ in size by a factor of three due to color suppression.

In order to obtain a quantitative, first-principles result for $\mathrm{Re}\,(A_0)/\mathrm{Re}\,(A_2)$, we also require knowledge of $\mathrm{Re}\,(A_0)$ which we provide in Eq. (6.94) of this work. Combining this with our earlier result for A_2 [2], we obtain

$$\frac{\mathrm{Re}(A_0)}{\mathrm{Re}(A_2)} = 19.9\,(2.3)\,(4.4)\,, \tag{6.96}$$

where the errors are statistical and systematic respectively. The value in Eq. (6.96) agrees very well with the experimental result, demonstrating quantitatively that, within the uncertainties, the $\Delta I = 1/2$ rule is indeed a consequence of QCD and thus providing an answer to an important long-standing puzzle.

For earlier theoretical papers on the $\Delta I = 1/2$ rule and the real parts of the individual amplitudes A_0 and A_2, as well as some recent work, see Refs. [80, 81, 82, 83, 84, 85].

6.7.4 Result for $\mathrm{Re}(\varepsilon'/\varepsilon)$

For ε'/ε we use Eq. (2.20), combining the lattice values for the imaginary parts of the decay amplitudes with the experimental measurements of the real parts. The systematic error for $\mathrm{Im}(A_0)$ is taken from Tab. 6.25 and that of $\mathrm{Im}(A_2)$ from Eq. 64 of Ref. [2]. The statistical and systematic errors on $\mathrm{Im}(A_0)$ and $\mathrm{Im}(A_2)$ are combined in quadrature and are therefore enhanced by the cancellation between the two terms in Eq. (2.20). However, one further important systematic error should be addressed: that arising from the effects of electromagnetism and the isospin-breaking difference, $m_d - m_u$, between the down and up quark masses.

While for most quantities these corrections enter at the 1% level or below, for ϵ' this familiar situation does not hold. As can be seen from the formula used to compute ϵ' in the Standard Model given in Eq. (2.20), the $I = 0$ and $I = 2$ amplitudes A_0 and A_2 enter with equal weight. However, as is summarized by the $\Delta I = 1/2$ rule, the amplitude A_2 is 22.5 times smaller than A_0. Thus, a 1% correction to A_0 can introduce an $O(20\%)$ correction to A_2 and a potential correction to ϵ' of 20% or more.

The effects on ϵ' of electromagnetism and $m_d - m_u$ have been the subject of active research for some time [86, 87, 88]. The most recent results are those of Cirigliano *et al.* [88]. They provide a correction that is appropriate for our calculation in which the contribution of the electro-weak penguin operators Q_7 and Q_8 has been included. Their result is parametrized by $\hat{\Omega}_{\mathrm{eff}}$ which is introduced into a version of Eq. (2.20) which incorporates these effects:

$$\frac{\varepsilon'}{\varepsilon} = \frac{i\omega_+ e^{i(\delta_2-\delta_0)}}{\sqrt{2}\varepsilon}\left[\frac{\mathrm{Im}(A_2^{\mathrm{emp}})}{\mathrm{Re}(A_2^{(0)})} - \frac{\mathrm{Im}(A_0^{(0)})}{\mathrm{Re}(A_0^{(0)})}\left(1-\hat{\Omega}_{\mathrm{eff}}\right)\right]. \tag{6.97}$$

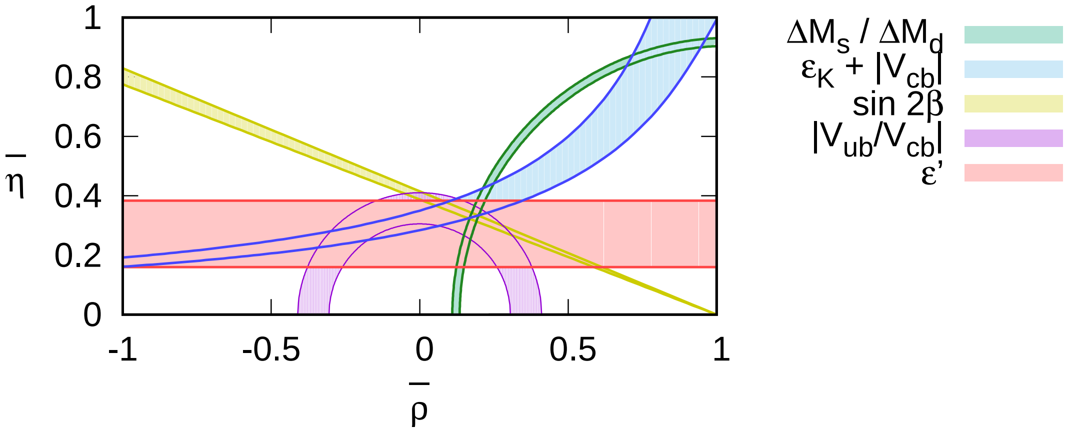

Figure 6.12: The horizontal-band constraint on the CKM matrix unitarity triangle in the $\bar{\rho} - \bar{\eta}$ plane obtained from our calculation of ϵ', along with constraints obtained from other inputs [17, 68, 90]. The error bands represent the statistical and systematic errors combined in quadrature. Note that the band labeled ϵ' is historically (e.g. in Ref. [91]) labeled as ϵ'/ϵ, where ϵ is taken from experiment.

and find $\hat{\Omega}_{\rm eff} = (17.0^{+9.1}_{-9.0}) \times 10^{-2}$. Here we are reproducing Eqs. (54) and (60) from Ref. [88], where $\mathrm{Re}(A^{(0)}_{0,2})$ refer to the real amplitudes in the absence of isospin breaking, $\mathrm{Im}(A^{\rm emp}_2)$ represents the dominant contribution to $\mathrm{Im}(A_2)$ and arises from the electroweak penguin operators $Q_{7,8}$, and $\mathrm{Im}(A^{(0)}_0)$ additionally includes the effects of QCD penguin operators. At the present level of accuracy, our use of the experimental rates for the real amplitudes, together with small differences from the definition of the isosymmetric limit in Ref. [88], do not affect the applicability of Eq. (6.97) to our calculation. (For a review of earlier work on this topic see Ref. [89].) Note also that $\omega_+ = \mathrm{Re}(A^+_2)/\mathrm{Re}(A_0)$, where the plus (+) indicates the amplitude obtained from charged kaon decay, is equal to the value of ω used to represent the isospin-symmetric ratio in this work and given in Tab. 6.10.

Since a careful discussion of these corrections is beyond the scope of this work we choose to treat these effects of isospin breaking as a systematic error whose size is given by the effect of including $\hat{\Omega}_{\rm eff}$ in Eq. (6.97). We find

$$\mathrm{Re}(\epsilon'/\epsilon) = 0.00217(26)(62)(50)\,, \tag{6.98}$$

where the errors are statistical and systematic, with the systematic error separated as isospin-conserving and isospin-breaking, respectively. We note that if we were to apply this negative correction directly to our result for Re(ϵ'/ϵ), the central value obtained, 0.00167, would nearly coincide with the experimental value, albeit with appreciable errors.

Our first-principles calculation of ϵ'/ϵ also allows us to place a new, horizontal-band constraint on the CKM matrix unitarity triangle in the $\bar{\rho}-\bar{\eta}$ plane. In Fig. 6.12 we overlay this band with constraints arising from other sources. We find that our result is consistent with the other constraints and does not at present suggest any violation of the CKM paradigm. For more information on how this band was obtained, as well as the corresponding plot obtained using our 2015 results, we refer the reader to Ref. [91].

Conclusion

In this paper we have presented in detail two related lattice calculations: The calculation of $\pi\pi$ scattering phase shifts for both the $I = 0$ and $I = 2$ channels, and the calculation of $K \to \pi\pi_{I=0}$ decay amplitude and ϵ'. These two calculations substantially enhance the results of our 2015 lattice calculation [1]. Both the 2015 and the current calculation were performed on a single, $32^3 \times 64$ Möbius domain wall ensemble with the Iwasaki+DSDR gauge action, with an inverse lattice spacing of 1.378(7) GeV and physical pion masses. G-parity boundary conditions are used in the three spatial directions which induces non-zero momentum for the ground-state pions so that the energy of the lightest two-pion state matches the kaon mass to around 2%, thereby ensuring a physical, energy-conserving decay.

These two new calculations are based on an increase by a factor of 3.4 in the number of Monte Carlo samples and include two additional $\pi\pi$ interpolating operators, one of which is a four-quark operator constructed from single-pion interpolating operators which each carry larger-than-minimum momentum, while the other is a scalar two-quark operator (the sigma operator). With these improvements we obtain an $I = 0$ $\pi\pi$ scattering phase shift at 471 MeV of $32.3°(1.0)(1.4)$[1]. Comparing this result with the one presented five years ago [1], we have the following improvements: i) The statistical error is improved by a factor of 5. ii) We are able to provide a more reliable and detailed systematic error analysis. iii) We have been able to resolve the 3σ discrepancy between our earlier result for this phase shift and that predicted by a dispersive analysis [9] so that

---

[1] Note this number is slightly different from the number given in Ref. [16]. This is because we have now included an estimate of the error due to the unphysical pion mass, resulting in a correction to the $\pi\pi$ energy and we have refined our excited state error estimation.

our current results agree well with the dispersive prediction (cf. Fig. 5.10). The discrepancy is now understood to have resulted from excited $\pi\pi$ state contamination, which was underestimated in Ref. [1] and is now under much greater control. These improvements also result in a significant, 70% (2.6σ if σ is determined from only the statistical error) relative increase in the size of the unrenormalized lattice value of Q_6, suggesting that our excited-state systematic error in the $K \to \pi\pi$ calculation was previously underestimated. Our final results for the $\pi\pi$ scattering phase shift calculation are presented in Tab. 5.12 and illustrated in Figures 5.10 and 5.11, and a detailed comparison of our old and new result of $K \to \pi\pi$ calculation can be found in Sec. 6.5.6.

In order to obtain a better estimation of the excited-state systematic error in the $\pi\pi$ scattering calculation, we have employed a concrete procedure for estimating the error resulting from a nearby excited state that was not included in our fit. As discussed in Sec. 5.4.5, we introduce one additional state into our fit but with an energy fixed to that given by the dispersive calculation [9] and with couplings to our operators carefully estimated, so as to avoid introducing instability in the fits or inflating the statistical error. The resulting shift in the ground-state energy then provides a meaningful indicator of the size of the corresponding systematic error.

In addition to computing the $I = 0$ phase shift for two pions with zero total momentum, we also perform a moving-frame calculation with three different total momenta. The observation [30] that three types of lattice symmetry can be used to significantly reduce the number of contractions was exploited to reduce the contraction time by a factor of seven. The resulting values of the $\pi\pi$ phase shifts at lower energies not only allow us to perform a comparison with dispersive and chiral perturbation theory predictions but also give us an independent evaluation of the Lellouch-Lüscher correction needed to obtain the $K \to \pi\pi$ decay amplitude from a finite-volume lattice QCD calculation. Because of the critical role played by the sigma interpolating operator in the stationary frame calculation, we will include a sigma operator with non-zero total momentum in future work. This operator might be expected to strongly couple to more states in the fit, in contrast to the $\pi\pi(311, 311)$ operator, and may significantly reduce the errors as it did for the stationary case.

In this work, we have used a combination of bootstrap and jackknife methods [29] together with correlated fits to determine the ground-state energies, the operator-state overlap amplitudes, the bare matrix elements, and the analysis of the excited-state error. This method allows us to estimate the goodness-of-fit, which provides better guidance in our choice of fitting ranges and multi-state fitting functions. In the $\pi\pi$ scattering calculation, we also compared our multi-state fitting with the GEVP method and found that our fitting procedure gave consistent statistical errors for the $I = 0$ case with our implementation of the GEVP method. We did not attempt to estimate the systematic errors resulting from the GEVP approach. The GEVP method may well excel when more states and operators are included.

In the $K \longrightarrow \pi\pi$ calculation, we have also included in this new calculation an improved renormalization technique. As discussed in Sec. 6.4, the lattice matrix operators must be renormalized in the $\overline{\text{MS}}$ scheme in which the Wilson coefficients that parameterize the high-energy weak interactions have been evaluated. This is accomplished by performing an intermediate non-perturbative conversion into two RI-SMOM schemes, each of which can be matched perturbatively to $\overline{\text{MS}}$ at some high energy scale. As we use a somewhat coarse, $a^{-1} = 1.38$ GeV ensemble, our renormalization scale was formerly limited by this cutoff and $\mu = 1.53$ GeV was chosen as the momemtum scale at which our RI-SMOM schemes were converted to $\overline{\text{MS}}$. In the new calculation reported here we have applied the step-scaling procedure to bypass the limitation imposed by the lattice cutoff and raise our renormalization scale to 4.006 GeV, thereby improving our control over the systematic error resulting from the perturbative matching to $\overline{\text{MS}}$. This improved method results in a reduced discrepancy between the results obtained from the two different RI-SMOM intermediate schemes and a reduction in the renormalization systematic error. In the future we expect to improve this systematic error by further raising the renormalization scale.

We estimate the finite lattice spacing effects to be a significant source of error in both the $\pi\pi$ scattering and A_0 calculations. Since we have results from only a single, somewhat coarse lattice spacing our estimate of this error is necessarily indirect and uncertain. In the future we intend to follow the procedure used in our A_2 calculation [2] to compute A_0 at two different lattice spacings, allowing us to perform a full continuum limit. This is hampered by the need to generate new ensembles with GPBC, which alongside the high computational cost of the measurements and the need for large statistics requires significantly more computing power than is presently available.

A second important systematic error, which we plan to reduce in future work, comes from the effects of electromagnetic and light quark mass isospin breaking. As discussed in Sec. 6.7.4, the small size of the amplitude A_2 relative to A_0 gives a potential twenty times enhancement of such effects which are normally at the 1% level. The effects of electromagnetism and the quark mass difference $m_d - m_u$ have been studied in considerable detail using chiral perturbation theory and large N_c arguments, most recently in Ref. [88]. We take the size of their correction as an important systematic error for our present result and are exploring possible methods to also use lattice techniques to determine these effects [92, 93].

For our final result we obtain

$$\mathrm{Re}(\epsilon'/\epsilon)_{\mathrm{lattice}} = 0.00217(26)(62)(50)\,. \tag{6.99}$$

The third error here is the systematic error associated with isospin breaking and electromagnetic effects, and the first and second errors are the statistical error and the remaining systematic error. This result can be compared to the experimental value

$$\mathrm{Re}(\epsilon'/\epsilon)_{\mathrm{expt.}} = 0.00166(23)\,. \tag{6.100}$$

These values are consistent within the quoted errors.

We believe that ϵ' continues to offer a very important test of the Standard Model with exciting opportunities for the discovery of new physics. For this promise to be realized substantially more accurate Standard Model predictions are needed. Important improvements can be expected from a simple extension of the work presented here, studying a sequence of ensembles with decreasing lattice spacing so that a continuum limit can be evaluated. In addition, we are developing a second, complementary approach to the study of $K \to \pi\pi$ decay which is based on periodic boundary conditions. This avoids the complexity of the G-parity boundary conditions used in the present work but requires that higher energy, excited $\pi\pi$ states be used as the decay final state [94]. More challenging is the problem posed by the inclusion of electromagnetism where new methods [92, 93] are needed to combine the finite-volume methods of Lüscher [6] and Lellouch and Lüscher [36] with the long-range character of electromagnetism.

References

[1] Z. Bai et al., "Standard Model Prediction for Direct CP Violation in K$\to\pi\pi$ Decay," Phys. Rev. Lett., vol. 115, no. 21, p. 212 001, 2015. arXiv: `1505.07863 [hep-lat]`.

[2] T. Blum et al., "$K \to \pi\pi$ $\Delta I = 3/2$ decay amplitude in the continuum limit," Phys. Rev. D, vol. 91, no. 7, p. 074 502, 2015. arXiv: `1502.00263 [hep-lat]`.

[3] T. D. Lee and C.-N. Yang, "Question of Parity Conservation in Weak Interactions," Phys. Rev., vol. 104, pp. 254–258, 1956.

[4] C. S. Wu, E. Ambler, R. W. Hayward, D. D. Hoppes, and R. P. Hudson, "Experimental Test of Parity Conservation in β Decay," Phys. Rev., vol. 105, pp. 1413–1414, 1957.

[5] J. R. Batley et al., "A Precision measurement of direct CP violation in the decay of neutral kaons into two pions," Phys. Lett. B, vol. 544, pp. 97–112, 2002. arXiv: `hep-ex/0208009`.

[6] M. Luscher, "Two particle states on a torus and their relation to the scattering matrix," Nucl. Phys. B, vol. 354, pp. 531–578, 1991.

[7] G. Colangelo, J. Gasser, and H. Leutwyler, "The s-wave scattering lengths," Physics Letters B, vol. 488, no. 3-4, 261–268, 2000.

[8] B. Ananthanarayan, G. Colangelo, J. Gasser, and H. Leutwyler, "Roy equation analysis of pi pi scattering," Phys. Rept., vol. 353, pp. 207–279, 2001. arXiv: `hep-ph/0005297`.

[9] G. Colangelo, J. Gasser, and H. Leutwyler, "$\pi\pi$ scattering," Nucl. Phys. B, vol. 603, pp. 125–179, 2001. arXiv: `hep-ph/0103088`.

[10] R. Garcia-Martin, R. Kaminski, J. R. Pelaez, J. Ruiz de Elvira, and F. J. Yndurain, "The Pion-pion scattering amplitude. IV: Improved analysis with once subtracted Roy-like equations up to 1100 MeV," Phys. Rev. D, vol. 83, p. 074 004, 2011. arXiv: `1102.2183 [hep-ph]`.

[11] R. Garcia-Martin, R. Kaminski, J. R. Pelaez, and J. Ruiz de Elvira, "Precise determination of the f0(600) and f0(980) pole parameters from a dispersive data analysis," Phys. Rev. Lett., vol. 107, p. 072 001, 2011. arXiv: `1107.1635 [hep-ph]`.

[12] S. Roy, "Exact integral equation for pion pion scattering involving only physical region partial waves," Phys. Lett. B, vol. 36, pp. 353–356, 1971.

[13] N. H. Christ, C. Kelly, and D. Zhang, “Lattice simulations with G-parity Boundary Conditions,” Phys. Rev. D, vol. 101, no. 1, p. 014 506, 2020. arXiv: `1908.08640 [hep-lat]`.

[14] D. Zhang, “Kaon to Two Pion decay from Lattice QCD and CP violation,” Ph.D. dissertation, Columbia University, 2015.

[15] T. Blum et al., “Lattice determination of $I = 0$ and 2 $\pi\pi$ scattering phase shifts with a physical pion mass,” Mar. 2021. arXiv: `2103.15131 [hep-lat]`.

[16] R. Abbott et al., “Direct CP violation and the $\Delta I = 1/2$ rule in $K \to \pi\pi$ decay from the standard model,” Phys. Rev. D, vol. 102, no. 5, p. 054 509, 2020. arXiv: `2004.09440 [hep-lat]`.

[17] M. Tanabashi et al., “Review of Particle Physics,” Phys. Rev., vol. D98, no. 3, p. 030 001, 2018 and 2019 update.

[18] P. W. Atkins, M. S. Child, and C. S. G. Phillips, Tables for Group Theory [by] PW Atkins, MS Child and CS University Press, 1970.

[19] R. C. Brower, H. Neff, and K. Orginos, “The Möbius domain wall fermion algorithm,” Comput. Phys. Commun., vol. 220, pp. 1–19, 2017. arXiv: `1206.5214 [hep-lat]`.

[20] T. Blum et al., “Domain wall QCD with physical quark masses,” Phys. Rev. D, vol. 93, no. 7, p. 074 505, 2016. arXiv: `1411.7017 [hep-lat]`.

[21] P. M. Vranas, “Domain wall fermions in vector theories,” NATO Sci. Ser. C, vol. 553, pp. 11–26, 2000. arXiv: `hep-lat/0001006`.

[22] ——, “Gap Domain Wall Fermions,” Phys. Rev. D, vol. 74, p. 034 512, 2006. arXiv: `hep-lat/0606014`.

[23] H. Fukaya, S. Hashimoto, K.-I. Ishikawa, T. Kaneko, H. Matsufuru, T. Onogi, and N. Yamada, “Lattice gauge action suppressing near-zero modes of H(W),” Phys. Rev. D, vol. 74, p. 094 505, 2006. arXiv: `hep-lat/0607020`.

[24] D. Renfrew, T. Blum, N. Christ, R. Mawhinney, and P. Vranas, “Controlling Residual Chiral Symmetry Breaking in Domain Wall Fermion Simulations,” PoS, vol. LATTICE2008, C. Aubin, S. Cohen, C. Dawson, J. Dudek, R. Edwards, B. Joo, H.-W. Lin, K. Orginos, D. Richards, and H. Thacker, Eds., p. 048, 2008. arXiv: `0902.2587 [hep-lat]`.

[25] Y.-C. Chen and T.-W. Chiu, “Exact Pseudofermion Action for Monte Carlo Simulation of Domain-Wall Fermion,” Phys. Lett. B, vol. 738, pp. 55–60, 2014. arXiv: `1403.1683 [hep-lat]`.

[26] ——, “One-Flavor Algorithms for Simulation of Lattice QCD with Domain-Wall Fermion: EOFA versus RHMC,” PoS, vol. IWCSE2013, p. 059, 2014. arXiv: `1412.0819 [hep-lat]`.

[27] J. Foley, K. Jimmy Juge, A. O’Cais, M. Peardon, S. M. Ryan, and J.-I. Skullerud, “Practical all-to-all propagators for lattice QCD,” Comput. Phys. Commun., vol. 172, pp. 145–162, 2005. arXiv: `hep-lat/0505023`.

[28] Q. Liu, “Kaon to two pions decays from lattice qcd: Δi= 1/2 rule and cp violation,” Ph.D. dissertation, Columbia University, 2012.

[29] C. Kelly and T. Wang, “Update on the improved lattice calculation of direct CP-violation in K decays,” PoS, vol. LATTICE2018, p. 277, 2019.

[30] ——, “Update on the improved lattice calculation of direct CP-violation in K decays,” PoS, vol. LATTICE2019, p. 129, 2019. arXiv: `1911.04582 [hep-lat]`.

[31] G. P. Lepage, “The Analysis of Algorithms for Lattice Field Theory,” in Theoretical Advanced Study Institu
Jun. 1989.

[32] M. Luscher and U. Wolff, “How to Calculate the Elastic Scattering Matrix in Two-dimensional Quantum Field Theories by Numerical Simulation,” Nucl. Phys. B, vol. 339, pp. 222–252, 1990.

[33] B. Blossier, M. Della Morte, G. von Hippel, T. Mendes, and R. Sommer, “On the generalized eigenvalue method for energies and matrix elements in lattice field theory,” JHEP, vol. 04, p. 094, 2009. arXiv: `0902.1265 [hep-lat]`.

[34] J. J. Dudek, R. G. Edwards, and C. E. Thomas, “S and D-wave phase shifts in isospin-2 pi pi scattering from lattice QCD,” Phys. Rev. D, vol. 86, p. 034 031, 2012. arXiv: `1203.6041 [hep-ph]`.

[35] N. Irges and F. Knechtli, “Lattice gauge theory approach to spontaneous symmetry breaking from an extra dimension,” Nucl. Phys. B, vol. 775, pp. 283–311, 2007. arXiv: `hep-lat/0609045`.

[36] L. Lellouch and M. Luscher, “Weak transition matrix elements from finite volume correlation functions,” Commun. Math. Phys., vol. 219, pp. 31–44, 2001. arXiv: `hep-lat/0003023`.

[37] K. Rummukainen and S. A. Gottlieb, “Resonance scattering phase shifts on a nonrest frame lattice,” Nucl. Phys. B, vol. 450, pp. 397–436, 1995. arXiv: `hep-lat/9503028`.

[38] N. H. Christ, C. Kim, and T. Yamazaki, “Finite volume corrections to the two-particle decay of states with non-zero momentum,” Phys. Rev. D, vol. 72, p. 114 506, 2005. arXiv: `hep-lat/0507009`.

[39] C. h. Kim, C. T. Sachrajda, and S. R. Sharpe, "Finite-volume effects for two-hadron states in moving frames," Nucl. Phys. B, vol. 727, pp. 218–243, 2005. arXiv: `hep-lat/0507006`.

[40] T. Yamazaki et al., "I = 2 pi pi scattering phase shift with two flavors of O(a) improved dynamical quarks," Phys. Rev. D, vol. 70, p. 074 513, 2004. arXiv: `hep-lat/0402025`.

[41] T. Wang and C. Kelly, "Studies of I=0 and 2 $\pi\pi$ scattering with physical pion mass," PoS, vol. LATTICE2018, p. 276, 2019.

[42] P. F. Bedaque, I. Sato, and A. Walker-Loud, "Finite volume corrections to pi-pi scattering," Phys. Rev. D, vol. 73, p. 074 501, 2006. arXiv: `hep-lat/0601033`.

[43] T. Blum et al., "K to $\pi\pi$ Decay amplitudes from Lattice QCD," Phys. Rev. D, vol. 84, p. 114 503, 2011. arXiv: `1106.2714 [hep-lat]`.

[44] C. W. Bernard, T. Draper, A. Soni, H. D. Politzer, and M. B. Wise, "Application of Chiral Perturbation Theory to K —> 2 pi Decays," Phys. Rev. D, vol. 32, pp. 2343–2347, 1985.

[45] T. Blum et al., "Kaon matrix elements and CP violation from quenched lattice QCD: 1. The three flavor case," Phys. Rev. D, vol. 68, p. 114 506, 2003. arXiv: `hep-lat/0110075`.

[46] C. Lehner and C. Sturm, "Matching factors for Delta S=1 four-quark operators in RI/SMOM schemes," Phys. Rev. D, vol. 84, p. 014 001, 2011. arXiv: `1104.4948 [hep-ph]`.

[47] R. Arthur and P. A. Boyle, "Step Scaling with off-shell renormalisation," Phys. Rev. D, vol. 83, p. 114 511, 2011. arXiv: `1006.0422 [hep-lat]`.

[48] R. Arthur, P. A. Boyle, N. Garron, C. Kelly, and A. T. Lytle, "Opening the Rome-Southampton window for operator mixing matrices," Phys. Rev. D, vol. 85, p. 014 501, 2012. arXiv: `1109.1223 [hep-lat]`.

[49] G. McGlynn, "Advances in Lattice Chromodynamics," Ph.D. dissertation, Columbia University, 2016.

[50] Y. Aoki et al., "Non-perturbative renormalization of quark bilinear operators and B(K) using domain wall fermions," Phys. Rev. D, vol. 78, p. 054 510, 2008. arXiv: `0712.1061 [hep-lat]`.

[51] ——, "Continuum Limit of B_K from 2+1 Flavor Domain Wall QCD," Phys. Rev. D, vol. 84, p. 014 503, 2011. arXiv: `1012.4178 [hep-lat]`.

[52] S. Bertolini, J. O. Eeg, and M. Fabbrichesi, "Studying epsilon-prime / epsilon in the chiral quark model: gamma(5) scheme independence and NLO hadronic matrix elements," Nucl. Phys. B, vol. 449, pp. 197–228, 1995. arXiv: `hep-ph/9409437`.

[53] A. J. Buras and J.-M. Gérard, “$K \to \pi\pi$ and $K - \pi$ Matrix Elements of the Chromomagnetic Operators from Dual QCD,” JHEP, vol. 07, p. 126, 2018. arXiv: `1803.08052 [hep-ph]`.

[54] G. Buchalla, A. J. Buras, and M. E. Lautenbacher, “Weak decays beyond leading logarithms,” Rev. Mod. Phys., vol. 68, pp. 1125–1144, 1996. arXiv: `hep-ph/9512380`.

[55] G. Martinelli, G. C. Rossi, C. T. Sachrajda, S. R. Sharpe, M. Talevi, and M. Testa, “Nonperturbative improvement of lattice QCD at large momenta,” Nucl. Phys. B, vol. 611, pp. 311–337, 2001. arXiv: `hep-lat/0106003`.

[56] M. Tomii and N. H. Christ, “$O(4)$-symmetric position-space renormalization of lattice operators,” Phys. Rev. D, vol. 99, no. 1, p. 014 515, 2019. arXiv: `1811.11238 [hep-lat]`.

[57] A. J. Buras, M. Jamin, M. E. Lautenbacher, and P. H. Weisz, “Two loop anomalous dimension matrix for $\Delta S = 1$ weak nonleptonic decays I: $O(\alpha_s^2)$,” Nucl. Phys. B, vol. 400, pp. 37–74, 1993. arXiv: `hep-ph/9211304`.

[58] P. A. Boyle, N. Garron, R. J. Hudspith, C. Lehner, and A. T. Lytle, “Neutral kaon mixing beyond the Standard Model with $\mathrm{n}_f = 2 + 1$ chiral fermions. Part 2: non perturbative renormalisation of the $\Delta F = 2$ four-quark operators,” JHEP, vol. 10, p. 054, 2017. arXiv: `1708.03552 [hep-lat]`.

[59] R. Arthur et al., “Domain Wall QCD with Near-Physical Pions,” Phys. Rev. D, vol. 87, p. 094 514, 2013. arXiv: `1208.4412 [hep-lat]`.

[60] T. Blum et al., “Lattice determination of the $K \to (\pi\pi)_{I=2}$ Decay Amplitude A_2,” Phys. Rev. D, vol. 86, p. 074 513, 2012. arXiv: `1206.5142 [hep-lat]`.

[61] A. J. Buras, P. Gambino, and U. A. Haisch, “Electroweak penguin contributions to nonleptonic Delta F = 1 decays at NNLO,” Nucl. Phys. B, vol. 570, pp. 117–154, 2000. arXiv: `hep-ph/9911250`.

[62] M. Gorbahn and U. Haisch, “Effective Hamiltonian for non-leptonic $|\Delta F|$= 1 decays at NNLO in QCD,” Nucl. Phys. B, vol. 713, pp. 291–332, 2005. arXiv: `hep-ph/0411071`.

[63] J. Brod and M. Gorbahn, “$_K$ at Next-to-Next-to-Leading Order: The Charm-Top-Quark Contribution,” Phys. Rev. D, vol. 82, p. 094 026, 2010. arXiv: `1007.0684 [hep-ph]`.

[64] M Cerdà-Sevilla, M Gorbahn, S Jäger, and A Kokulu, “Towards NNLO accuracy for ε'/ε,” J. Phys. Conf. Ser., vol. 800, no. 1, p. 012 008, 2017. arXiv: `1611.08276 [hep-ph]`.

[65] M. Cerdà-Sevilla, “NNLO QCD Contributions to ε'/ε,” Acta Phys. Polon. B, vol. 49, M. Jeżabek, Ed., pp. 1087–1096, 2018.

[66] M. Bruno, C. Lehner, and A. Soni, “Towards a nonperturbative calculation of weak Hamiltonian Wilson coefficients,” Phys. Rev. D, vol. 97, no. 7, p. 074 509, 2018. arXiv: `1711.05768 [hep-lat]`.

[67] T. van Ritbergen, J. A. M. Vermaseren, and S. A. Larin, “The Four loop beta function in quantum chromodynamics,” Phys. Lett. B, vol. 400, pp. 379–384, 1997. arXiv: `hep-ph/9701390`.

[68] M. Tanabashi, K. Hagiwara, K. Hikasa, K. Nakamura, Y. Sumino, F. Takahashi, J. Tanaka, K. Agashe, G. Aielli, C. Amsler, M. Antonelli, D. M. Asner, H. Baer, S. Banerjee, R. M. Barnett, T. Basaglia, C. W. Bauer, J. J. Beatty, V. I. Belousov, J. Beringer, S. Bethke, A. Bettini, H. Bichsel, O. Biebel, K. M. Black, E. Blucher, O. Buchmuller, V. Burkert, M. A. Bychkov, R. N. Cahn, M. Carena, A. Ceccucci, A. Cerri, D. Chakraborty, M.-C. Chen, R. S. Chivukula, G. Cowan, O. Dahl, G. D’Ambrosio, T. Damour, D. de Florian, A. de Gouvêa, T. DeGrand, P. de Jong, G. Dissertori, B. A. Dobrescu, M. D’Onofrio, M. Doser, M. Drees, H. K. Dreiner, D. A. Dwyer, P. Eerola, S. Eidelman, J. Ellis, J. Erler, V. V. Ezhela, W. Fetscher, B. D. Fields, R. Firestone, B. Foster, A. Freitas, H. Gallagher, L. Garren, H.-J. Gerber, G. Gerbier, T. Gershon, Y. Gershtein, T. Gherghetta, A. A. Godizov, M. Goodman, C. Grab, A. V. Gritsan, C. Grojean, D. E. Groom, M. Grünewald, A. Gurtu, T. Gutsche, H. E. Haber, C. Hanhart, S. Hashimoto, Y. Hayato, K. G. Hayes, A. Hebecker, S. Heinemeyer, B. Heltsley, J. J. Hernández-Rey, J. Hisano, A. Höcker, J. Holder, A. Holtkamp, T. Hyodo, K. D. Irwin, K. F. Johnson, M. Kado, M. Karliner, U. F. Katz, S. R. Klein, E. Klempt, R. V. Kowalewski, F. Krauss, M. Kreps, B. Krusche, Y. V. Kuyanov, Y. Kwon, O. Lahav, J. Laiho, J. Lesgourgues, A. Liddle, Z. Ligeti, C.-J. Lin, C. Lippmann, T. M. Liss, L. Littenberg, K. S. Lugovsky, S. B. Lugovsky, A. Lusiani, Y. Makida, F. Maltoni, T. Mannel, A. V. Manohar, W. J. Marciano, A. D. Martin, A. Masoni, J. Matthews, U.-G. Meißner, D. Milstead, R. E. Mitchell, K. Mönig, P. Molaro, F. Moortgat, M. Moskovic, H. Murayama, M. Narain, P. Nason, S. Navas, M. Neubert, P. Nevski, Y. Nir, K. A. Olive, S. Pagan Griso, J. Parsons, C. Patrignani, J. A. Peacock, M. Pennington, S. T. Petcov, V. A. Petrov, E. Pianori, A. Piepke, A. Pomarol, A. Quadt, J. Rademacker, G. Raffelt, B. N. Ratcliff, P. Richardson, A. Ringwald, S. Roesler, S. Rolli, A. Romaniouk, L. J. Rosenberg, J. L. Rosner, G. Rybka, R. A. Ryutin, C. T. Sachrajda, Y. Sakai, G. P. Salam, S. Sarkar, F. Sauli, O. Schneider, K. Scholberg, A. J. Schwartz, D. Scott, V. Sharma, S. R. Sharpe, T. Shutt, M. Silari, T. Sjöstrand, P. Skands, T. Skwarnicki, J. G. Smith, G. F. Smoot, S. Spanier, H. Spieler, C. Spiering, A. Stahl, S. L. Stone, T. Sumiyoshi, M. J. Syphers, K. Terashi, J. Terning, U. Thoma, R. S. Thorne, L. Tiator, M. Titov, N. P. Tkachenko, N. A. Törnqvist, D. R. Tovey, G. Valencia, R. Van de Water, N. Varelas, G. Venanzoni, L. Verde, M. G. Vincter, P. Vogel, A. Vogt, S. P. Wakely, W. Walkowiak, C. W. Walter, D. Wands, D. R. Ward, M. O. Wascko, G. Weiglein, D. H. Weinberg, E. J. Weinberg, M. White, L. R. Wiencke, S. Willocq, C. G. Wohl, J. Womersley, C. L. Woody, R. L. Workman, W.-M. Yao, G. P. Zeller, O. V. Zenin, R.-Y. Zhu, S.-L. Zhu, F. Zimmermann, P. A. Zyla, J. Anderson, L. Fuller, V. S. Lugovsky, and P. Schaffner, “Review of particle physics,” Phys. Rev. D, vol. 98, p. 030 001, 3 2018.

[69] J. Bijnens, G. Colangelo, G. Ecker, J. Gasser, and M. E. Sainio, "Pion-pion scattering at low energy," Nucl. Phys. B, vol. 508, pp. 263–310, 1997, [Erratum: Nucl.Phys.B 517, 639–639 (1998)]. arXiv: `hep-ph/9707291`.

[70] A. J. Buras, M. Gorbahn, S. Jäger, and M. Jamin, "Improved anatomy of ε'/ε in the Standard Model," JHEP, vol. 11, p. 202, 2015. arXiv: `1507.06345 [hep-ph]`.

[71] T. Kitahara, U. Nierste, and P. Tremper, "Singularity-free next-to-leading order ΔS = 1 renormalization group evolution and ϵ'_K/ϵ_K in the Standard Model and beyond," JHEP, vol. 12, p. 078, 2016. arXiv: `1607.06727 [hep-ph]`.

[72] A. Schenk, "Absorption and dispersion of pions at finite temperature," Nucl. Phys. B, vol. 363, pp. 97–113, 1991.

[73] M. A. Shifman, A. I. Vainshtein, and V. I. Zakharov, "Light Quarks and the Origin of the Delta I = 1/2 Rule in the Nonleptonic Decays of Strange Particles," Nucl. Phys. B, vol. 120, pp. 316–324, 1977.

[74] F. J. Gilman and M. B. Wise, "Effective Hamiltonian for Delta s = 1 Weak Nonleptonic Decays in the Six Quark Model," Phys. Rev. D, vol. 20, p. 2392, 1979.

[75] M. K. Gaillard and B. W. Lee, "Δ I = 1/2 Rule for Nonleptonic Decays in Asymptotically Free Field Theories," Phys. Rev. Lett., vol. 33, p. 108, 1974.

[76] G. Altarelli and L. Maiani, "Octet Enhancement of Nonleptonic Weak Interactions in Asymptotically Free Gauge Theories," Phys. Lett. B, vol. 52, pp. 351–354, 1974.

[77] F. J. Gilman and M. B. Wise, "The Delta I = 1/2 Rule and Violation of CP in the Six Quark Model," Phys. Lett. B, vol. 83, pp. 83–86, 1979.

[78] P. A. Boyle et al., "Emerging understanding of the $\Delta I = 1/2$ Rule from Lattice QCD," Phys. Rev. Lett., vol. 110, no. 15, p. 152 001, 2013. arXiv: `1212.1474 [hep-lat]`.

[79] T. Blum et al., "The $K \to (\pi\pi)_{I=2}$ Decay Amplitude from Lattice QCD," Phys. Rev. Lett., vol. 108, p. 141 601, 2012. arXiv: `1111.1699 [hep-lat]`.

[80] J. F. Donoghue, E. Golowich, W. A. Ponce, and B. R. Holstein, "Analysis of Delta S=1 Nonleptonic Weak Decays and the Delta I=1/2 Rule," Phys. Rev. D, vol. 21, p. 186, 1980.

[81] W. A. Bardeen, A. J. Buras, and J. M. Gerard, "A Consistent Analysis of the Delta I = 1/2 Rule for K Decays," Phys. Lett. B, vol. 192, pp. 138–144, 1987.

[82] A. Pich and E. de Rafael, "Weak K amplitudes in the chiral and 1/n(c) expansions," Phys. Lett. B, vol. 374, pp. 186–192, 1996. arXiv: `hep-ph/9511465`.

[83] S. Bertolini, M. Fabbrichesi, and J. O. Eeg, “Theory of the CP Violating Parameter ϵ'/ϵ,” Rev. Mod. Phys., vol. 72, pp. 65–93, 2000. arXiv: `hep-ph/9802405`.

[84] A. J. Buras, J.-M. Gérard, and W. A. Bardeen, “Large N Approach to Kaon Decays and Mixing 28 Years Later: $\Delta I = 1/2$ Rule, $\hat{B}_K$ and ΔM_K,” Eur. Phys. J. C, vol. 74, p. 2871, 2014. arXiv: `1401.1385 [hep-ph]`.

[85] A. Donini, P. Hernández, C. Pena, and F. Romero-López, “Dissecting the $\Delta I = 1/2$ rule at large N_c,” Eur. Phys. J. C, vol. 80, no. 7, p. 638, 2020. arXiv: `2003.10293 [hep-lat]`.

[86] A. J. Buras and J. M. Gerard, “Isospin Breaking Contributions to Epsilon-prime / Epsilon,” Phys. Lett. B, vol. 192, pp. 156–162, 1987.

[87] V. Cirigliano, A. Pich, G. Ecker, and H. Neufeld, “Isospin violation in epsilon-prime,” Phys. Rev. Lett., vol. 91, p. 162 001, 2003. arXiv: `hep-ph/0307030`.

[88] V. Cirigliano, H. Gisbert, A. Pich, and A. Rodríguez-Sánchez, “Isospin-violating contributions to ϵ'/ϵ,” JHEP, vol. 02, p. 032, 2020. arXiv: `1911.01359 [hep-ph]`.

[89] V. Cirigliano, G. Ecker, H. Neufeld, A. Pich, and J. Portoles, “Kaon Decays in the Standard Model,” Rev. Mod. Phys., vol. 84, p. 399, 2012. arXiv: `1107.6001 [hep-ph]`.

[90] P. A. Boyle, L. Del Debbio, N. Garron, A. Juttner, A. Soni, J. T. Tsang, and O. Witzel, “SU(3)-breaking ratios for $D_{(s)}$ and $B_{(s)}$ mesons,” Dec. 2018. arXiv: `1812.08791 [hep-lat]`.

[91] C. Lehner, E. Lunghi, and A. Soni, “Emerging lattice approach to the K-Unitarity Triangle,” Phys. Lett. B, vol. 759, pp. 82–90, 2016. arXiv: `1508.01801 [hep-ph]`.

[92] N. Christ and X. Feng, “Including electromagnetism in $K \to \pi\pi$ decay calculations,” EPJ Web Conf., vol. 175, M. Della Morte, P. Fritzsch, E. Gámiz Sánchez, and C. Pena Ruano, Eds., p. 13 016, 2018. arXiv: `1711.09339 [hep-lat]`.

[93] Y. Cai and Z. Davoudi, “QED-corrected Lellouch-Luescher formula for $K \to \pi\pi$ decay,” PoS, vol. LATTICE2018, p. 280, 2018. arXiv: `1812.11015 [hep-lat]`.

[94] D. Hoying, “Pion-pion scattering with physical quark masses,” PoS, vol. LATTICE2018, p. 064, 2019.

[95] J. Bijnens, G. Colangelo, G. Ecker, J. Gasser, and M. E. Sainio, “Elastic pi pi scattering to two loops,” Phys. Lett. B, vol. 374, pp. 210–216, 1996. arXiv: `hep-ph/9511397`.

Appendix A: Quark level momentum distribution

A.1 Pion operator

In Sec. 4.1, Eqs. (4.1)-(4.3) we detail the interpolating operators for the charged and neutral pions. The pion momentum, $\vec{P} = \vec{p}+\vec{q}$ is the sum of the momenta $\vec{p}$ and $\vec{q}$ assigned to the quark and antiquark, respectively. Given a pion momentum, there are multiple ways of distribute momentum between quark and anti-quark component.

As shown in Ref. [13] the allowed quark momenta (for G-parity BCs in 3 directions) are

$$\pm \frac{\pi}{2L}(1,1,1) + \frac{2\pi}{L}\vec{n}\,, \tag{A.1}$$

where $\vec{n}$ is a vector of integers. While any combination of $\vec{p}$ and $\vec{q}$ satisfying this condition result in valid pion interpolating operators, we observed in Ref. [13] that the cubic symmetry breaking manifest in the operator amplitudes between pion states of total momentum related by cubic rotations is dramatically suppressed by averaging over pairs of bilinear operators with the same total momentum but with different assignments of quark momenta. The specific criteria for selecting those momenta are discussed in more detail in that paper; here in Tab. A.1 we list only the two choices for each of the 32 total momenta. The momentum distribution is listed below for all 32 pions we use (in units of $\pi/2L$):

Recall that in addition to the above, we also symmetrize the momentum between the quark and antiquark by averaging the assignments $(\vec{p},\vec{q})$ and $(\vec{q},\vec{p})$. Thus in practice our pion interpolating operators comprise an average over a total of four quark field bilinears.

Pion momentum	quark momentum, choice 1	quark momentum, choice 2
(2, 2, 2)	(1, 1, 1) + (1, 1, 1)	(-1,-1,-1) + (3, 3, 3)
(-2,-2,-2)	(-1,-1,-1) + (-1,-1,-1)	(1, 1, 1) + (-3,-3,-3)
(2, 2,-2)	(1, 1, 1) + (1, 1,-3)	(-1,-1,-1) + (3, 3,-1)
(2,-2, 2)	(1, 1, 1) + (1,-3, 1)	(-1,-1,-1) + (3,-1, 3)
(-2, 2, 2)	(1, 1, 1) + (-3, 1, 1)	(-1,-1,-1) + (-1, 3, 3)
(-2,-2, 2)	(-1,-1,-1) + (-1,-1, 3)	(1, 1, 1) + (-3,-3, 1)
(-2, 2,-2)	(-1,-1,-1) + (-1, 3,-1)	(1, 1, 1) + (-3, 1,-3)
(2,-2,-2)	(-1,-1,-1) + (3,-1,-1)	(1, 1, 1) + (1,-3,-3)
(2, 2, 6)	(1, 1, 1) + (1, 1, 5)	(-1,-1,-1) + (3, 3, 7)
(2, 6, 2)	(1, 1, 1) + (1, 5, 1)	(-1,-1,-1) + (3, 7, 3)
(6, 2, 2)	(1, 1, 1) + (5, 1, 1)	(-1,-1,-1) + (7, 3, 3)
(-2,-2,-6)	(-1,-1,-1) + (-1,-1,-5)	(1, 1, 1) + (-3,-3,-7)
(-2,-6,-2)	(-1,-1,-1) + (-1,-5,-1)	(1, 1, 1) + (-3,-7,-3)
(-6,-2,-2)	(-1,-1,-1) + (-5,-1,-1)	(1, 1, 1) + (-7,-3,-3)
(2, 2,-6)	(1, 1, 1) + (1, 1,-7)	(-1,-1,-1) + (3, 3,-5)
(2,-6, 2)	(1, 1, 1) + (1,-7, 1)	(-1,-1,-1) + (3,-5, 3)
(-6, 2, 2)	(1, 1, 1) + (-7, 1, 1)	(-1,-1,-1) + (-5, 3, 3)
(-2,-2, 6)	(-1,-1,-1) + (-1,-1, 7)	(1, 1, 1) + (-3,-3, 5)
(-2, 6,-2)	(-1,-1,-1) + (-1, 7,-1)	(1, 1, 1) + (-3, 5,-3)
(6,-2,-2)	(-1,-1,-1) + (7,-1,-1)	(1, 1, 1) + (5,-3,-3)
(-2, 2, 6)	(1, 1, 1) + (-3, 1, 5)	(-1,-1,-1) + (-1, 3, 7)
(2, 6,-2)	(1, 1, 1) + (1, 5,-3)	(-1,-1,-1) + (3, 7,-1)
(6,-2, 2)	(1, 1, 1) + (5,-3, 1)	(-1,-1,-1) + (7,-1, 3)
(2,-2,-6)	(-1,-1,-1) + (3,-1,-5)	(1, 1, 1) + (1,-3,-7)
(-2,-6, 2)	(-1,-1,-1) + (-1,-5, 3)	(1, 1, 1) + (-3,-7, 1)
(-6, 2,-2)	(-1,-1,-1) + (-5, 3,-1)	(1, 1, 1) + (-7, 1,-3)
(2,-2, 6)	(1, 1, 1) + (1,-3, 5)	(-1,-1,-1) + (3,-1, 7)
(-2, 6, 2)	(1, 1, 1) + (-3, 5, 1)	(-1,-1,-1) + (-1, 7, 3)
(6, 2,-2)	(1, 1, 1) + (5, 1,-3)	(-1,-1,-1) + (7, 3,-1)
(-2, 2,-6)	(-1,-1,-1) + (-1, 3,-5)	(1, 1, 1) + (-3, 1,-7)
(2,-6,-2)	(-1,-1,-1) + (3,-5,-1)	(1, 1, 1) + (1,-7,-3)
(-6,-2, 2)	(-1,-1,-1) + (-5,-1, 3)	(1, 1, 1) + (-7,-3, 1)

Table A.1: The quark/anti-quark momenta choices for all 32 pion total momenta. For each total momenta, two momentum choices are given to suppress the cubic symmetry given. All momenta are given in units of $\pi/2L$.

Index	quark momentum
1	(1, 1, 1)
2	(-1,-1,-1)
3	(-3, 1, 1)
4	(3,-1,-1)
5	(1,-3, 1)
6	(-1, 3,-1)
7	(1, 1,-3)
8	(-1,-1, 3)

Table A.2: The 8 orientations of quark momentum we average to get the σ operator with zero total momentum. The anti-quark momentum in each case is the reverse of the quark momentum. All momenta are given in units of $\pi/2L$.

A.2 σ operator

In this work we use the σ operator only in the case of zero total momentum, and as a result the momenta assigned to the quark and anti-quark fields must be equal and opposite. We construct an operator that is symmetric under cubic rotations by averaging over 8 orientations of the quark momentum. The list of momenta assigned to the quark operator are given in Tab. A.2.

Appendix B: Chpt prediction for phase shift

In this appendix we present the partial wave amplitude $t^I_{l=0}$ results from the next-to-leading-order (NLO) ChPT. These amplitudes are connected with the scattering phase shift by

$$t^I_{l=0} = \left(\frac{s-4}{s}\right)^{1/2} e^{i\delta^I_{l=0}(s)} \sin[\delta^I_{l=0}(s)] \tag{B.1}$$

$$\begin{aligned}
t^0_0\left(m_\pi, f_\pi, k\right) = {} & \frac{7m_\pi^2}{16\pi f_\pi^2}\left(1+\frac{8}{7}\frac{k^2}{m_\pi^2}\right) + \frac{m_\pi^4}{8\pi f_\pi^4}\left[\left(5b_1 + 12b_2 + 48b_3 + 32b_4 + \frac{83}{24\pi^2}\right)\right. \\
& \left. + \left(8b_2 + 96b_3 + 96b_4 + \frac{269}{36\pi^2}\right)\frac{k^2}{m_\pi^2} + \left(\frac{176}{3}b_3 + \frac{272}{3}b_4 + \frac{311}{54\pi^2}\right)\frac{k^4}{m_\pi^4}\right] \\
& + \frac{m_\pi^4}{256\pi^3 f_\pi^4}\frac{1}{\sqrt{1+\frac{m_\pi^2}{k^2}}}\left(49 + 112\frac{k^2}{m_\pi^2} + 64\frac{k^4}{m_\pi^4}\right)\log\left(\frac{1-\sqrt{1+\frac{m_\pi^2}{k^2}}}{1+\sqrt{1+\frac{m_\pi^2}{k^2}}}\right) \\
& + \frac{m_\pi^4}{1152\pi^3 f_\pi^4}\sqrt{1+\frac{m_\pi^2}{k^2}}\left(27 + 64\frac{k^2}{m_\pi^2} + 112\frac{k^4}{m_\pi^4}\right)\log\left(\frac{\sqrt{1+\frac{m_\pi^2}{k^2}}-1}{\sqrt{1+\frac{m_\pi^2}{k^2}}+1}\right) \\
& - \frac{m_\pi^4}{128\pi^3 f_\pi^4}\left(1-\frac{1}{24}\frac{m_\pi^2}{k^2}\right)\left\{-4[\log(2)]^2 + \left[\log\left(\frac{4k^2}{m_\pi^2}\right)\right]^2 - \left[\log\left(\frac{\sqrt{1+\frac{m_\pi^2}{k^2}}-1}{\sqrt{1+\frac{m_\pi^2}{k^2}}+1}\right)\right]^2\right. \\
& + 4\log\left(\frac{4k^2}{m_\pi^2}\right)\log\left(1+\sqrt{1+\frac{m_\pi^2}{k^2}}\right) + 4\left[\log\left(1+\sqrt{1+\frac{m_\pi^2}{k^2}}\right)\right]^2 \\
& \left. + 2\log\left(\frac{4k^2}{m_\pi^2}\right)\log\left(\frac{\sqrt{1+\frac{m_\pi^2}{k^2}}-1}{\sqrt{1+\frac{m_\pi^2}{k^2}}+1}\right) + 4\log\left(1+\sqrt{1+\frac{m_\pi^2}{k^2}}\right)\log\left(\frac{\sqrt{1+\frac{m_\pi^2}{k^2}}-1}{\sqrt{1+\frac{m_\pi^2}{k^2}}+1}\right)\right\}
\end{aligned} \tag{B.2}$$

$$
\begin{aligned}
t_0^2\left(m_\pi, f_\pi, k\right) = {}& -\frac{m_\pi^2}{8\pi f_\pi^2}\left(1+2\frac{k^2}{m_\pi^2}\right)+\frac{m_\pi^4}{4\pi f_\pi^4}\left[\left(b_1+16b_4+\frac{43}{96\pi^2}\right)\right. \\
& \left.-\left(2b_2-48b_4-\frac{199}{144\pi^2}\right)\frac{k^2}{m_\pi^2}+\left(\frac{16}{3}b_3+\frac{112}{3}b_4+\frac{265}{216\pi^2}\right)\frac{k^4}{m_\pi^4}\right] \\
& +\frac{m_\pi^4}{64\pi^3 f_\pi^4}\frac{1}{\sqrt{1+\frac{m_\pi^2}{k^2}}}\left(1+4\frac{k^2}{m_\pi^2}+4\frac{k^4}{m_\pi^4}\right)\log\left(\frac{1-\sqrt{1+\frac{m_\pi^2}{k^2}}}{1+\sqrt{1+\frac{m_\pi^2}{k^2}}}\right) \\
& +\frac{m_\pi^4}{1152\pi^3 f_\pi^4}\sqrt{1+\frac{m_\pi^2}{k^2}}\left(27+112\frac{k^2}{m_\pi^2}+88\frac{k^4}{m_\pi^4}\right)\log\left(\frac{\sqrt{1+\frac{m_\pi^2}{k^2}}-1}{\sqrt{1+\frac{m_\pi^2}{k^2}}+1}\right) \\
& +\frac{m_\pi^4}{256\pi^3 f_\pi^4}\left(1+\frac{13}{12}\frac{m_\pi^2}{k^2}\right)\left\{-4[\log(2)]^2+\left[\log\left(\frac{4k^2}{m_\pi^2}\right)\right]^2-\left[\log\left(\frac{\sqrt{1+\frac{m_\pi^2}{k^2}}-1}{\sqrt{1+\frac{m_\pi^2}{k^2}}+1}\right)\right]^2\right. \\
& +4\log\left(\frac{4k^2}{m_\pi^2}\right)\log\left(1+\sqrt{1+\frac{m_\pi^2}{k^2}}\right)+4\left[\log\left(1+\sqrt{1+\frac{m_\pi^2}{k^2}}\right)\right]^2 \\
& \left.+2\log\left(\frac{4k^2}{m_\pi^2}\right)\log\left(\frac{\sqrt{1+\frac{m_\pi^2}{k^2}}-1}{\sqrt{1+\frac{m_\pi^2}{k^2}}+1}\right)+4\log\left(1+\sqrt{1+\frac{m_\pi^2}{k^2}}\right)\log\left(\frac{\sqrt{1+\frac{m_\pi^2}{k^2}}-1}{\sqrt{1+\frac{m_\pi^2}{k^2}}+1}\right)\right\}.
\end{aligned}
\tag{B.3}
$$

The parameters $b_1 - b_4$ are linear combinations of low energy constants defined in Ref [95], and we took their values from Ref [9]. In this work, these expressions are used to estimate the unphysical pion mass error. The two pion masses we use are the lattice pion mass $m_\pi^{\text{lat}} = 142.3$ MeV and physical pion mass $m_\pi^{\text{phy}} = 135$ MeV.

Appendix C: Contractions for $\pi\pi$ and σ operators

In this appendix we list the contraction formula for each diagram introduced in Sec. 4.3. The first four diagrams are associated with the product of two $\pi\pi$ interpolating operators, where the four time slices are the time coordinates of the four single-pion interpolating operators, which are $t_{\text{src}} - 4, t_{\text{src}}, t_{\text{snk}}$ and $t_{\text{snk}} + 4$, respectively. The final four expressions correspond to the cases where at least one of the source or sink operators is a σ operator. The quantity P_{t_a,t_b} is the G-parity quark propagator from t_a to t_b while the flavor-spin matrix S_1 is defined as $S_1 = \sigma_3\gamma_5$. These eight amplitudes are obtained from the following contractions:

$$C = \frac{1}{2} Tr\left\{P_{t_1,t_3} S_1 P_{t_3,t_2} S_1 P_{t_2,t_4} S_1 P_{t_4,t_1} S_1\right\} \tag{C.1}$$

$$D = \frac{1}{2}\left[\left(\frac{1}{2} Tr\left\{P_{t_1,t_3} S_1 P_{t_3,t_1} S_1\right\}\right) \cdot \left(\frac{1}{2} Tr\left\{P_{t_2,t_4} S_1 P_{t_4,t_2} S_1\right\}\right) + (t_3 \leftrightarrow t_4)\right] \tag{C.2}$$

$$R = \frac{1}{2}\left[\frac{1}{2} Tr\left\{P_{t_1,t_2} S_1 P_{t_2,t_3} S_1 P_{t_3,t_4} S_1 P_{t_4,t_1} S_1\right\} + (t_3 \leftrightarrow t_4)\right] \tag{C.3}$$

$$V = \left(\frac{1}{2} Tr\left\{P_{t_1,t_2} S_1 P_{t_2,t_1} S_1\right\}\right) \cdot \left(\frac{1}{2} Tr\left\{P_{t_3,t_4} S_1 P_{t_4,t_3} S_1\right\}\right) \tag{C.4}$$

$$C_{\sigma\sigma} = Tr\left\{P_{t_1,t_2} P_{t_2,t_1}\right\} \tag{C.5}$$

$$V_{\sigma\sigma} = \left(Tr\left\{P_{t_1,t_1}\right\}\right) \cdot \left(Tr\left\{P_{t_2,t_2}\right\}\right) \tag{C.6}$$

$$C_{\sigma\pi\pi} = i \cdot Tr\left\{P_{t_1,t_0} P_{t_0,t_2} S_1 P_{t_2,t_1} S_1\right\} \tag{C.7}$$

$$V_{\sigma\pi\pi} = i \cdot Tr\left\{P_{t_0,t_0}\right\} \cdot Tr\left\{P_{t_1,t_2} S_1 P_{t_2,t_1} S_1\right\} \ . \tag{C.8}$$

Appendix D: Wick contractions for the $K \to \pi\pi$ three-point function with the σ operator

In this appendix we provide the expressions for the Wick contraction required to compute the $K \to \pi\pi$ three-point function with the σ operator. The corresponding diagrams for the $\pi\pi(\ldots)$ operators can be found in in Appendix B.1 and B.2 of Ref. [14].

For this appendix we will utilize the notation described in Sec. 3.4 whereby the quark field operators are placed in two-component "flavor" vectors ψ_l and ψ_h for the light and heavy quarks, respectively, and the corresponding propagators are matrices also in this flavor index. In this notation the creation operator for the G-parity even neutral kaon analog has the form,

$$\begin{aligned} O_{\tilde{K}^0} &= \frac{i}{\sqrt{2}}(\bar{d}\gamma^5 s + \bar{s}'\gamma^5 u) \\ &= \frac{i}{\sqrt{2}}\bar{\psi}_l\gamma^5\psi_h\,, \end{aligned} \tag{D.1}$$

where the physical component corresponds to the usual neutral kaon operator (cf. Sec. VI.A of Ref. [13]). The σ creation operator has the form,

$$\begin{aligned} O_\sigma &= \frac{1}{\sqrt{2}}(\bar{u}u + \bar{d}d) \\ &= \frac{1}{\sqrt{2}}\bar{\psi}_l\psi_l\,. \end{aligned} \tag{D.2}$$

For convenience we will treat the meson bilinears as point operators in which both quarks reside on the same lattice site. (In our actual lattice calculation we use more elaborate source and sink operators but those details are not needed to specify how we evaluate the Wick contractions.) The ten effective four-quark operators Q_i for $i \in \{1 \ldots 10\}$ written in the above notation are given in Sec. 3.2.2 of Ref. [14]. While the exact forms are not important for this discussion, we highlight the fact that the operators are written in terms of a common set of matrices,

$$
\begin{aligned}
M^{\mu}_{0,V\pm A} &= F_0\gamma^{\mu}(1\pm\gamma^5)\,,\\
M^{\mu}_{1,V\pm A} &= -F_1\gamma^{\mu}(1\pm\gamma^5)\,,
\end{aligned}
\tag{D.3}
$$

where F_i are diagonal flavor matrices that pick out either the upper (0) or lower (1) element of the vector upon which they act:

$$
F_0 = \begin{pmatrix} 1 & 0 \\ 0 & 0 \end{pmatrix}, \qquad F_1 = \begin{pmatrix} 0 & 0 \\ 0 & 1 \end{pmatrix}. \tag{D.4}
$$

The matrices $M^{\mu}_{i,V\pm A}$ appear inside products of two bilinear operators and the space-time index μ is summed over implicitly. Following the notation of Ref. [14] we will suppress this index.

The Wick contractions of the $K \to \pi\pi$ three-point function with the σ operator,

$$
\mathcal{A}_i = \langle 0|O^{\dagger}_{\sigma}(z)\hat{Q}_i(y)O_{\bar{K}^0}(x)|0\rangle\,, \tag{D.5}
$$

where $\hat{Q}_i$ are the unsubtracted four-quark operators, are divided into three classes by their topology that we label with indices 1, 3 and 4 in homage to the conventional labeling of the $\pi\pi(\ldots)$ contractions. The *type3* and *type4* diagrams are those that contain a quark loop at the location of the four-quark operator, with *type4* corresponding to that subset of those diagrams that are disconnected (i.e. for which the σ operator self-contracts). For the $\pi\pi(\ldots)$ operators the remaining, connected, contractions can be subdivided based on whether the two pion bilinear operators are directly connected by a quark line (*type2*) or not (*type1*); no such distinction exists of course for the σ sink operator. Hence we classify all remaining diagrams as *type1*.

As in Ref. [14] it is convenient to write the ten expressions $\mathcal{A}_i$ in terms of a common basis of, in this case 23, functions $D_{\alpha}(\Gamma_1,\Gamma_2)$ where the subscript indexes the function and $\Gamma_{1,2}$ are spin-flavor matrices.

We will first write down the expressions for the correlation functions $\mathcal{A}_i$ in terms of these functions and will conclude the section with their definition. We list the contributions for each of the three types separately. The *type1* contributions are as follows:

$$\mathcal{A}_1^{\text{type1}} = \frac{1}{2}D_6(M_{0,V-A}, M_{1,V+A}) - \frac{1}{2}D_1(M_{0,V-A}, M_{1,V+A}) \tag{D.6a}$$

$$\mathcal{A}_2^{\text{type1}} = \frac{1}{2}D_{11}(M_{0,V-A}, M_{1,V+A}) - \frac{1}{2}D_8(M_{0,V-A}, M_{1,V+A}) \tag{D.6b}$$

$$\begin{aligned}\mathcal{A}_3^{\text{type1}} = {} & \frac{1}{2}D_6(M_{0,V-A}, M_{1,V+A}) + \frac{1}{2}D_6(M_{0,V-A}, M_{0,V-A}) \\ & - \frac{1}{2}D_1(M_{0,V-A}, M_{1,V+A}) - \frac{1}{2}D_1(M_{0,V-A}, M_{0,V-A})\end{aligned} \tag{D.6c}$$

$$\mathcal{A}_4^{\text{type1}} = D_{11}(M_{0,V-A}, M_{1,V+A}) - \frac{1}{2}D_8(M_{0,V-A}, M_{1,V+A}) - \frac{1}{2}D_{19}(M_{0,V-A}, M_{0,V-A}) \tag{D.6d}$$

$$\mathcal{A}_5^{\text{type1}} = D_6(M_{0,V-A}, M_{1,V-A}) - \frac{1}{2}D_1(M_{0,V-A}, M_{1,V-A}) - \frac{1}{2}D_1(M_{0,V-A}, M_{0,V+A}) \tag{D.6e}$$

$$\mathcal{A}_6^{\text{type1}} = D_{11}(M_{0,V-A}, M_{1,V-A}) - \frac{1}{2}D_8(M_{0,V-A}, M_{1,V-A}) - \frac{1}{2}D_{19}(M_{0,V-A}, M_{0,V+A}) \tag{D.6f}$$

$$\mathcal{A}_7^{\text{type1}} = \frac{1}{4}D_6(M_{0,V-A}, M_{1,V-A}) - \frac{1}{2}D_1(M_{0,V-A}, M_{1,V-A}) + \frac{1}{4}D_1(M_{0,V-A}, M_{0,V+A}) \tag{D.6g}$$

$$\mathcal{A}_8^{\text{type1}} = \frac{1}{4}D_{11}(M_{0,V-A}, M_{1,V-A}) - \frac{1}{2}D_8(M_{0,V-A}, M_{1,V-A}) + \frac{1}{4}D_{19}(M_{0,V-A}, M_{0,V+A}) \tag{D.6h}$$

$$\mathcal{A}_9^{\text{type1}} = \frac{1}{4}D_6(M_{0,V-A}, M_{1,V+A}) - \frac{1}{2}D_1(M_{0,V-A}, M_{1,V+A}) + \frac{1}{4}D_1(M_{0,V-A}, M_{0,V-A}) \tag{D.6i}$$

$$\mathcal{A}_{10}^{\text{type1}} = \frac{1}{4}D_{11}(M_{0,V-A}, M_{1,V+A}) - \frac{1}{2}D_8(M_{0,V-A}, M_{1,V+A}) + \frac{1}{4}D_{19}(M_{0,V-A}, M_{0,V-A})\,, \tag{D.6j}$$

the *type3* contributions are:

$$\mathcal{A}_1^{\text{type3}} = \frac{1}{2}D_2(M_{0,V-A}, M_{1,V+A}) - \frac{1}{2}D_3(M_{0,V-A}, M_{1,V+A}) \tag{D.7a}$$

$$\mathcal{A}_2^{\text{type3}} = \frac{1}{2}D_{10}(M_{0,V-A}, M_{1,V+A}) - \frac{1}{2}D_7(M_{0,V-A}, M_{1,V+A}) \tag{D.7b}$$

$$\begin{aligned}\mathcal{A}_3^{\text{type3}} = {} & \frac{1}{2}D_2(M_{0,V-A}, M_{1,V+A}) + \frac{1}{2}D_2(M_{0,V-A}, M_{0,V-A}) - \frac{1}{2}D_3(M_{0,V-A}, M_{1,V+A}) \\ & - \frac{1}{2}D_3(M_{0,V-A}, M_{0,V-A}) + \frac{1}{2}D_{14}(M_{0,V-A}, M_{0,V-A}) - \frac{1}{2}D_{16}(M_{0,V-A}, M_{0,V-A})\end{aligned} \tag{D.7c}$$

$$\begin{aligned}\mathcal{A}_4^{\text{type3}} = {} & D_{10}(M_{0,V-A}, M_{1,V+A}) - \frac{1}{2}D_7(M_{0,V-A}, M_{1,V+A}) - \frac{1}{2}D_{18}(M_{0,V-A}, M_{0,V-A}) \\ & + \frac{1}{2}D_{21}(M_{0,V-A}, M_{0,V-A}) - \frac{1}{2}D_{23}(M_{0,V-A}, M_{0,V-A})\end{aligned} \tag{D.7d}$$

$$\begin{aligned}\mathcal{A}_5^{\text{type3}} = {} & D_2(M_{0,V-A}, M_{1,V-A}) - \frac{1}{2}D_3(M_{0,V-A}, M_{1,V-A}) - \frac{1}{2}D_3(M_{0,V-A}, M_{0,V+A}) \\ & + \frac{1}{2}D_{14}(M_{0,V-A}, M_{0,V+A}) - \frac{1}{2}D_{16}(M_{0,V-A}, M_{0,V+A})\end{aligned} \tag{D.7e}$$

$$\begin{aligned}\mathcal{A}_6^{\text{type3}} &= D_{10}(M_{0,V-A}, M_{1,V-A}) - \frac{1}{2}D_7(M_{0,V-A}, M_{1,V-A}) - \frac{1}{2}D_{18}(M_{0,V-A}, M_{0,V+A}) \\ &\quad + \frac{1}{2}D_{21}(M_{0,V-A}, M_{0,V+A}) - \frac{1}{2}D_{23}(M_{0,V-A}, M_{0,V+A})\end{aligned} \tag{D.7f}$$

$$\begin{aligned}\mathcal{A}_7^{\text{type3}} &= \frac{1}{4}D_2(M_{0,V-A}, M_{1,V-A}) - \frac{1}{2}D_3(M_{0,V-A}, M_{1,V-A}) + \frac{1}{4}D_3(M_{0,V-A}, M_{0,V+A}) \\ &\quad - \frac{1}{4}D_{14}(M_{0,V-A}, M_{0,V+A}) + \frac{1}{4}D_{16}(M_{0,V-A}, M_{0,V+A})\end{aligned} \tag{D.7g}$$

$$\begin{aligned}\mathcal{A}_8^{\text{type3}} &= \frac{1}{4}D_{10}(M_{0,V-A}, M_{1,V-A}) - \frac{1}{2}D_7(M_{0,V-A}, M_{1,V-A}) + \frac{1}{4}D_{18}(M_{0,V-A}, M_{0,V+A}) \\ &\quad - \frac{1}{4}D_{21}(M_{0,V-A}, M_{0,V+A}) + \frac{1}{4}D_{23}(M_{0,V-A}, M_{0,V+A})\end{aligned} \tag{D.7h}$$

$$\begin{aligned}\mathcal{A}_9^{\text{type3}} &= \frac{1}{4}D_2(M_{0,V-A}, M_{1,V+A}) - \frac{1}{2}D_3(M_{0,V-A}, M_{1,V+A}) + \frac{1}{4}D_3(M_{0,V-A}, M_{0,V-A}) \\ &\quad - \frac{1}{4}D_{14}(M_{0,V-A}, M_{0,V-A}) + \frac{1}{4}D_{16}(M_{0,V-A}, M_{0,V-A})\end{aligned} \tag{D.7i}$$

$$\begin{aligned}\mathcal{A}_{10}^{\text{type3}} &= \frac{1}{4}D_{10}(M_{0,V-A}, M_{1,V+A}) - \frac{1}{2}D_7(M_{0,V-A}, M_{1,V+A}) + \frac{1}{4}D_{18}(M_{0,V-A}, M_{0,V-A}) \\ &\quad - \frac{1}{4}D_{21}(M_{0,V-A}, M_{0,V-A}) + \frac{1}{4}D_{23}(M_{0,V-A}, M_{0,V-A})\,,\end{aligned} \tag{D.7j}$$

and the *type4*:

$$\mathcal{A}_1^{\text{type4}} = -\frac{1}{2}D_5(M_{0,V-A}, M_{1,V+A}) + \frac{1}{2}D_4(M_{0,V-A}, M_{1,V+A}) \tag{D.8a}$$

$$\mathcal{A}_2^{\text{type4}} = -\frac{1}{2}D_{12}(M_{0,V-A}, M_{1,V+A}) + \frac{1}{2}D_9(M_{0,V-A}, M_{1,V+A}) \tag{D.8b}$$

$$\begin{aligned}\mathcal{A}_3^{\text{type4}} &= -\frac{1}{2}D_5(M_{0,V-A}, M_{1,V+A}) - \frac{1}{2}D_5(M_{0,V-A}, M_{0,V-A}) + \frac{1}{2}D_4(M_{0,V-A}, M_{1,V+A}) \\ &\quad + \frac{1}{2}D_4(M_{0,V-A}, M_{0,V-A}) - \frac{1}{2}D_{13}(M_{0,V-A}, M_{0,V-A}) + \frac{1}{2}D_{15}(M_{0,V-A}, M_{0,V-A})\end{aligned} \tag{D.8c}$$

$$\begin{aligned}\mathcal{A}_4^{\text{type4}} &= -D_{12}(M_{0,V-A}, M_{1,V+A}) + \frac{1}{2}D_9(M_{0,V-A}, M_{1,V+A}) + \frac{1}{2}D_{17}(M_{0,V-A}, M_{0,V-A}) \\ &\quad - \frac{1}{2}D_{20}(M_{0,V-A}, M_{0,V-A}) + \frac{1}{2}D_{22}(M_{0,V-A}, M_{0,V-A})\end{aligned} \tag{D.8d}$$

$$\begin{aligned}\mathcal{A}_5^{\text{type4}} &= -D_5(M_{0,V-A}, M_{1,V-A}) + \frac{1}{2}D_4(M_{0,V-A}, M_{1,V-A}) + \frac{1}{2}D_4(M_{0,V-A}, M_{0,V+A}) \\ &\quad - \frac{1}{2}D_{13}(M_{0,V-A}, M_{0,V+A}) + \frac{1}{2}D_{15}(M_{0,V-A}, M_{0,V+A})\end{aligned} \tag{D.8e}$$

$$\begin{aligned}\mathcal{A}_6^{\text{type4}} = &-D_{12}(M_{0,V-A}, M_{1,V-A}) + \frac{1}{2}D_9(M_{0,V-A}, M_{1,V-A}) + \frac{1}{2}D_{17}(M_{0,V-A}, M_{0,V+A}) \\ &- \frac{1}{2}D_{20}(M_{0,V-A}, M_{0,V+A}) + \frac{1}{2}D_{22}(M_{0,V-A}, M_{0,V+A})\end{aligned} \tag{D.8f}$$

$$\begin{aligned}\mathcal{A}_7^{\text{type4}} = &-\frac{1}{4}D_5(M_{0,V-A}, M_{1,V-A}) + \frac{1}{2}D_4(M_{0,V-A}, M_{1,V-A}) - \frac{1}{4}D_4(M_{0,V-A}, M_{0,V+A}) \\ &+ \frac{1}{4}D_{13}(M_{0,V-A}, M_{0,V+A}) - \frac{1}{4}D_{15}(M_{0,V-A}, M_{0,V+A})\end{aligned} \tag{D.8g}$$

$$\begin{aligned}\mathcal{A}_8^{\text{type4}} = &-\frac{1}{4}D_{12}(M_{0,V-A}, M_{1,V-A}) + \frac{1}{2}D_9(M_{0,V-A}, M_{1,V-A}) - \frac{1}{4}D_{17}(M_{0,V-A}, M_{0,V+A}) \\ &+ \frac{1}{4}D_{20}(M_{0,V-A}, M_{0,V+A}) - \frac{1}{4}D_{22}(M_{0,V-A}, M_{0,V+A})\end{aligned} \tag{D.8h}$$

$$\begin{aligned}\mathcal{A}_9^{\text{type4}} = &-\frac{1}{4}D_5(M_{0,V-A}, M_{1,V+A}) + \frac{1}{2}D_4(M_{0,V-A}, M_{1,V+A}) - \frac{1}{4}D_4(M_{0,V-A}, M_{0,V-A}) \\ &+ \frac{1}{4}D_{13}(M_{0,V-A}, M_{0,V-A}) - \frac{1}{4}D_{15}(M_{0,V-A}, M_{0,V-A})\end{aligned} \tag{D.8i}$$

$$\begin{aligned}\mathcal{A}_{10}^{\text{type4}} = &-\frac{1}{4}D_{12}(M_{0,V-A}, M_{1,V+A}) + \frac{1}{2}D_9(M_{0,V-A}, M_{1,V+A}) - \frac{1}{4}D_{17}(M_{0,V-A}, M_{0,V-A}) \\ &+ \frac{1}{4}D_{20}(M_{0,V-A}, M_{0,V-A}) - \frac{1}{4}D_{22}(M_{0,V-A}, M_{0,V-A})\,.\end{aligned} \tag{D.8j}$$

The *type1* contractions are:

$$D_1(\Gamma_1, \Gamma_2) = \text{tr}\left(\Gamma_2 \mathcal{G}^l_{y,x}\gamma^5\mathcal{G}^h_{x,y}\Gamma_1\mathcal{G}^l_{y,z}\mathcal{G}^l_{z,y}\right) \tag{D.9a}$$

$$D_6(\Gamma_1, \Gamma_2) = \text{tr}\left(\mathcal{G}^h_{x,y}\Gamma_1\mathcal{G}^l_{y,x}\gamma^5\right)\text{tr}\left(\mathcal{G}^l_{z,y}\Gamma_2\mathcal{G}^l_{y,z}\right) \tag{D.9b}$$

$$D_8(\Gamma_1, \Gamma_2) = \text{tr}_{sf}\left(\left[\Gamma_1\mathcal{G}^l_{y,z}\mathcal{G}^l_{z,y}\right]_{\alpha\beta}\left[\Gamma_2\mathcal{G}^l_{y,x}\gamma^5\mathcal{G}^h_{x,y}\right]_{\alpha\beta}\right) \tag{D.9c}$$

$$D_{11}(\Gamma_1, \Gamma_2) = \text{tr}_{sf}\left(\mathcal{G}^l_{y,x}\gamma^5\mathcal{G}^h_{x,y}\Gamma_1\right)_{\alpha\beta}\text{tr}_{sf}\left(\Gamma_2\mathcal{G}^l_{y,z}\mathcal{G}^l_{z,y}\right)_{\alpha\beta} \tag{D.9d}$$

$$D_{19}(\Gamma_1, \Gamma_2) = \text{tr}_{sf}\left(\text{tr}_c\left[\mathcal{G}^l_{y,x}\gamma^5\mathcal{G}^h_{x,y}\Gamma_1\right]\text{tr}_c\left[\mathcal{G}^l_{y,z}\mathcal{G}^l_{z,y}\Gamma_2\right]\right)\,, \tag{D.9e}$$

and the *type3* are:

$$D_2(\Gamma_1, \Gamma_2) = \text{tr}\left(\gamma^5\mathcal{G}^h_{x,y}\Gamma_1\mathcal{G}^l_{y,z}\mathcal{G}^l_{z,x}\right)\text{tr}\left(\mathcal{G}^l_{y,y}\Gamma_2\right) \tag{D.10a}$$

$$D_3(\Gamma_1, \Gamma_2) = \text{tr}\left(\mathcal{G}^l_{y,z}\mathcal{G}^l_{z,x}\gamma^5\mathcal{G}^h_{x,y}\Gamma_1\mathcal{G}^l_{y,y}\Gamma_2\right) \tag{D.10b}$$

$$D_7(\Gamma_1, \Gamma_2) = \text{tr}_{sf}\left(\left[\Gamma_2\mathcal{G}^l_{y,z}\mathcal{G}^l_{z,x}\gamma^5\mathcal{G}^h_{x,y}\right]_{\alpha\beta}\left[\Gamma_1\mathcal{G}^l_{y,y}\right]_{\alpha\beta}\right) \tag{D.10c}$$

$$D_{10}(\Gamma_1, \Gamma_2) = \text{tr}_{sf}\left(\Gamma_2\mathcal{G}^l_{y,y}\right)_{\alpha\beta}\text{tr}_{sf}\left(\Gamma_1\mathcal{G}^l_{y,z}\mathcal{G}^l_{z,x}\gamma^5\mathcal{G}^h_{x,y}\right)_{\alpha\beta} \tag{D.10d}$$

$$D_{14}(\Gamma_1,\Gamma_2) = \mathrm{tr}\left(\mathcal{G}^l_{y,z}\mathcal{G}^l_{z,x}\gamma^5\mathcal{G}^h_{x,y}\Gamma_1\right)\mathrm{tr}\left(\mathcal{G}^h_{y,y}\Gamma_2\right) \tag{D.10e}$$

$$D_{16}(\Gamma_1,\Gamma_2) = \mathrm{tr}\left(\mathcal{G}^h_{y,y}\Gamma_1\mathcal{G}^l_{y,z}\mathcal{G}^l_{z,x}\gamma^5\mathcal{G}^h_{x,y}\Gamma_2\right) \tag{D.10f}$$

$$D_{18}(\Gamma_1,\Gamma_2) = \mathrm{tr}_{sf}\left(\mathrm{tr}_c\left[\mathcal{G}^l_{y,y}\right]\mathrm{tr}_c\left[\Gamma_2\mathcal{G}^l_{y,z}\mathcal{G}^l_{z,x}\gamma^5\mathcal{G}^h_{x,y}\Gamma_1\right]\right) \tag{D.10g}$$

$$D_{21}(\Gamma_1,\Gamma_2) = \mathrm{tr}_c\left(\mathrm{tr}_{sf}\left[\mathcal{G}^h_{y,y}\Gamma_2\right]\mathrm{tr}_{sf}\left[\Gamma_1\mathcal{G}^l_{y,z}\mathcal{G}^l_{z,x}\gamma^5\mathcal{G}^h_{x,y}\right]\right) \tag{D.10h}$$

$$D_{23}(\Gamma_1,\Gamma_2) = \mathrm{tr}_{sf}\left(\mathrm{tr}_c\left[\mathcal{G}^h_{y,y}\right]\mathrm{tr}_c\left[\Gamma_1\mathcal{G}^l_{y,z}\mathcal{G}^l_{z,x}\gamma^5\mathcal{G}^h_{x,y}\Gamma_2\right]\right)\,, \tag{D.10i}$$

where $\mathcal{G}^l$ and $\mathcal{G}^h$ are light and strange quark propagators, respectively, and α, β are color indices. We indicate spin and flavor traces as tr_{sf} and color traces as tr_c; traces over all three indices (spin, color and flavor) are denoted as tr without a subscript.

For simplicity, in Eqs. (D.13) given below for the *type4* diagrams we do not include the disconnected σ "bubble",

$$B_\sigma = \mathrm{tr}\left(\mathcal{G}^l_{z,z}\right)\,. \tag{D.11}$$

In computing the expectation values of these diagrams it is also necessary to perform a vacuum subtraction. Thus, the expressions D_i^* given in Eqs. (D.13) can be used to obtain the complete contributions of the corresponding diagrams to the *type4* amplitudes as follows:

$$\langle D_i(\Gamma_1,\Gamma_2)\rangle = \langle D_i^*(\Gamma_1,\Gamma_2)B_\sigma\rangle - \langle D_i^*(\Gamma_1,\Gamma_2)\rangle \times \langle B_\sigma\rangle\,, \tag{D.12}$$

where D^* are defined as:

$$D^*_4(\Gamma_1,\Gamma_2) = \mathrm{tr}\left(\mathcal{G}^l_{y,x}\gamma^5\mathcal{G}^h_{x,y}\Gamma_1\mathcal{G}^l_{y,y}\Gamma_2\right) \tag{D.13a}$$

$$D^*_5(\Gamma_1,\Gamma_2) = \mathrm{tr}\left(\mathcal{G}^h_{x,y}\Gamma_1\mathcal{G}^l_{y,x}\gamma^5\right)\mathrm{tr}\left(\mathcal{G}^l_{y,y}\Gamma_2\right) \tag{D.13b}$$

$$D^*_9(\Gamma_1,\Gamma_2) = \mathrm{tr}_{sf}\left(\left[\Gamma_1\mathcal{G}^l_{y,y}\right]_{\alpha\beta}\left[\Gamma_2\mathcal{G}^l_{y,x}\gamma^5\mathcal{G}^h_{x,y}\right]_{\alpha\beta}\right) \tag{D.13c}$$

$$D^*_{12}(\Gamma_1,\Gamma_2) = \mathrm{tr}_{sf}\left(\mathcal{G}^l_{y,x}\gamma^5\mathcal{G}^h_{x,y}\Gamma_1\right)_{\alpha\beta}\mathrm{tr}_{sf}\left(\mathcal{G}^l_{y,y}\Gamma_2\right)_{\alpha\beta} \tag{D.13d}$$

$$D^*_{13}(\Gamma_1,\Gamma_2) = \mathrm{tr}\left(\gamma^5\mathcal{G}^h_{x,y}\Gamma_1\mathcal{G}^l_{y,x}\right)\mathrm{tr}\left(\Gamma_2\mathcal{G}^h_{y,y}\right) \tag{D.13e}$$

$$D^*_{15}(\Gamma_1,\Gamma_2) = \mathrm{tr}\left(\Gamma_1\mathcal{G}^l_{y,x}\gamma^5\mathcal{G}^h_{x,y}\Gamma_2\mathcal{G}^h_{y,y}\right) \tag{D.13f}$$

$$D^*_{17}(\Gamma_1,\Gamma_2) = \mathrm{tr}_{sf}\left(\mathrm{tr}_c\left[\mathcal{G}^l_{y,y}\right]\mathrm{tr}_c\left[\Gamma_2\mathcal{G}^l_{y,x}\gamma^5\mathcal{G}^h_{x,y}\Gamma_1\right]\right) \tag{D.13g}$$

$$D^*_{20}(\Gamma_1,\Gamma_2) = \mathrm{tr}_c\left(\mathrm{tr}_{sf}\left[\mathcal{G}^l_{y,x}\gamma^5\mathcal{G}^h_{x,y}\Gamma_1\right]\mathrm{tr}_{sf}\left[\mathcal{G}^h_{y,y}\Gamma_2\right]\right) \tag{D.13h}$$

$$D^*_{22}(\Gamma_1,\Gamma_2) = \mathrm{tr}_{sf}\left(\mathrm{tr}_c\left[\mathcal{G}^h_{y,y}\right]\mathrm{tr}_c\left[\Gamma_1\mathcal{G}^l_{y,x}\gamma^5\mathcal{G}^h_{x,y}\Gamma_2\right]\right)\,. \tag{D.13i}$$

Appendix E: Wick contractions for matrix elements required for subtraction of the vacuum and pseudoscalar operator contributions

As described in Sec. 6.3 it is necessary to subtract a pseudoscalar operator $P = \bar{s}\gamma^5 d$ from the unsubtracted weak effective four-quark operators $\hat{Q}_i$ in order to remove a divergent contribution for off-shell terms. The subtraction and the evaluation of the corresponding coeffients, α_i, require the measurement of $\langle O^\dagger_{\pi\pi} P \tilde{O}_{\tilde{K}^0}\rangle$, $\langle P O_{\tilde{K}^0}\rangle$ and $\langle \hat{Q}_i O_{\tilde{K}^0}\rangle$ correlation functions. The vacuum subtraction of the *type4* diagrams also requires evaluating the $\langle \hat{Q}_i O_{\tilde{K}^0}\rangle$ correlation functions. Here and below we use the shorthand $\langle ABC\ldots\rangle$ to denote the n-point Green's functions of the operators A, B, C, and so on, in descending time order.

It is easy to see that the $\mathcal{A}^{\text{vac}}_i = \langle \hat{Q}_i O_{\tilde{K}^0}\rangle$ are directly proportional to the *type4*, disconnected contributions to $\langle O^\dagger_{\pi\pi} \hat{Q}_i O_{\tilde{K}^0}\rangle$ with the $\pi\pi$ "bubble" removed. The results are

$$\mathcal{A}^{\text{vac}}_1 = \frac{1}{\sqrt{2}}\big(C_{23}(M_{0,V-A}, M_{1,V+A}) - C_{26}(M_{1,V+A}, M_{0,V-A})\big) \tag{E.1a}$$

$$\mathcal{A}^{\text{vac}}_2 = \frac{1}{\sqrt{2}}\big(C_{24}(M_{0,V-A}, M_{1,V+A}) - C_{27}(M_{1,V+A}, M_{0,V-A})\big) \tag{E.1b}$$

$$\begin{aligned}\mathcal{A}^{\text{vac}}_3 = \frac{1}{\sqrt{2}}\big(&C_{23}(M_{0,V-A}, M_{1,V+A}) + C_{23}(M_{0,V-A}, M_{0,V-A}) - C_{26}(M_{1,V+A}, M_{0,V-A})\\ &- C_{26}(M_{0,V-A}, M_{0,V-A}) + C_{29}(M_{0,V-A}, M_{0,V-A}) - C_{31}(M_{0,V-A}, M_{0,V-A})\big)\end{aligned} \tag{E.1c}$$

$$\begin{aligned}\mathcal{A}^{\text{vac}}_4 = \frac{1}{\sqrt{2}}\big(&C_{24}(M_{0,V-A}, M_{1,V+A}) + C_{25}(M_{0,V-A}, M_{0,V-A}) - C_{27}(M_{1,V+A}, M_{0,V-A})\\ &- C_{28}(M_{0,V-A}, M_{0,V-A}) + C_{30}(M_{0,V-A}, M_{0,V-A}) - C_{32}(M_{0,V-A}, M_{0,V-A})\big)\end{aligned} \tag{E.1d}$$

$$\begin{aligned}\mathcal{A}^{\text{vac}}_5 = \frac{1}{\sqrt{2}}\big(&C_{23}(M_{0,V-A}, M_{1,V-A}) + C_{23}(M_{0,V-A}, M_{0,V+A}) - C_{26}(M_{1,V-A}, M_{0,V-A})\\ &- C_{26}(M_{0,V+A}, M_{0,V-A}) + C_{29}(M_{0,V-A}, M_{0,V+A}) - C_{31}(M_{0,V-A}, M_{0,V+A})\big)\end{aligned} \tag{E.1e}$$

$$\begin{aligned}\mathcal{A}^{\text{vac}}_6 = \frac{1}{\sqrt{2}}\big(&C_{24}(M_{0,V-A}, M_{1,V-A}) + C_{25}(M_{0,V-A}, M_{0,V+A}) - C_{27}(M_{1,V-A}, M_{0,V-A})\\ &- C_{28}(M_{0,V+A}, M_{0,V-A}) + C_{30}(M_{0,V-A}, M_{0,V+A}) - C_{32}(M_{0,V-A}, M_{0,V+A})\big)\end{aligned} \tag{E.1f}$$

$$\begin{aligned}\mathcal{A}_7^{\text{vac}} = \frac{1}{\sqrt{2}}\bigg(&C_{23}(M_{0,V-A}, M_{1,V-A}) - \frac{1}{2}C_{23}(M_{0,V-A}, M_{0,V+A}) - C_{26}(M_{1,V-A}, M_{0,V-A})\\ &+ \frac{1}{2}C_{26}(M_{0,V+A}, M_{0,V-A}) - \frac{1}{2}C_{29}(M_{0,V-A}, M_{0,V+A}) + \frac{1}{2}C_{31}(M_{0,V-A}, M_{0,V+A})\bigg)\end{aligned} \tag{E.1g}$$

$$\begin{aligned}\mathcal{A}_8^{\text{vac}} = \frac{1}{\sqrt{2}}\bigg(&C_{24}(M_{0,V-A}, M_{1,V-A}) - \frac{1}{2}C_{25}(M_{0,V-A}, M_{0,V+A}) - C_{27}(M_{1,V-A}, M_{0,V-A})\\ &+ \frac{1}{2}C_{28}(M_{0,V+A}, M_{0,V-A}) - \frac{1}{2}C_{30}(M_{0,V-A}, M_{0,V+A}) + \frac{1}{2}C_{32}(M_{0,V-A}, M_{0,V+A})\bigg)\end{aligned} \tag{E.1h}$$

$$\begin{aligned}\mathcal{A}_9^{\text{vac}} = \frac{1}{\sqrt{2}}\bigg(&C_{23}(M_{0,V-A}, M_{1,V+A}) - \frac{1}{2}C_{23}(M_{0,V-A}, M_{0,V-A}) - C_{26}(M_{1,V+A}, M_{0,V-A})\\ &+ \frac{1}{2}C_{26}(M_{0,V-A}, M_{0,V-A}) - \frac{1}{2}C_{29}(M_{0,V-A}, M_{0,V-A}) + \frac{1}{2}C_{31}(M_{0,V-A}, M_{0,V-A})\bigg)\end{aligned} \tag{E.1i}$$

$$\begin{aligned}\mathcal{A}_9^{\text{vac}} = \frac{1}{\sqrt{2}}\bigg(&C_{24}(M_{0,V-A}, M_{1,V+A}) - \frac{1}{2}C_{25}(M_{0,V-A}, M_{0,V-A}) - C_{27}(M_{1,V+A}, M_{0,V-A})\\ &+ \frac{1}{2}C_{28}(M_{0,V-A}, M_{0,V-A}) - \frac{1}{2}C_{30}(M_{0,V-A}, M_{0,V-A}) + \frac{1}{2}C_{32}(M_{0,V-A}, M_{0,V-A})\bigg)\,.\end{aligned} \tag{E.1j}$$

These results can be obtained by isolating the $C_{23} - C_{32}$ *type4* contributions from the expressions in Sec. 3.2.2 of Ref. [14] and multiplying the result by a factor of $1/\sqrt{3}$. Equivalent results can also be obtained from the *type4* contributions given in Eq. (D.13) by multiplying the result by a factor of $\sqrt{2}$. When measured with A2A propagators the results computed in these two bases are not exactly equal due to differing choices of where to employ γ^5-hermiticity, a symmetry that is broken by the stochastic "high-mode" approximation and restored only in the large ensemble-size limit (or the large-hit limit on a single configuration). This gives rise to the small differences observed in Sec. 6.3.2.

In our notation the pseudoscalar operator becomes

$$P = \bar{s}\gamma^5 d = \bar{\psi}_h \gamma^5 F_0 \psi_l\,, \tag{E.2}$$

where F_0 is defined in Eq. (D.4).

The $\langle P O_{\bar{K}^0}\rangle$ and $\langle O^\dagger_{\pi\pi} P O_{\bar{K}^0}\rangle$ correlation functions with the $\pi\pi(\ldots)$ and σ operators can be written in terms of three diagrams:

$$\text{mix3} = \text{tr}\left(\mathcal{G}^l_{z_2,x}\gamma^5\mathcal{G}^h_{x,y}\gamma^5F_0\mathcal{G}^l_{y,z_1}\gamma^5\sigma_3\mathcal{G}^l_{z_1,z_2}\gamma^5\sigma_3\right) \tag{E.3a}$$

$$\text{mix3}_\sigma = \text{tr}\left(\mathcal{G}^l_{z,x}\gamma^5\mathcal{G}^h_{x,y}\gamma^5F_0\mathcal{G}^l_{y,z}\right) \tag{E.3b}$$

$$\text{mix4} = \text{tr}\left(\mathcal{G}^h_{x,y}\gamma^5F_0\mathcal{G}^l_{y,x}\gamma^5\right)\ . \tag{E.3c}$$

where x and y are the locations of the kaon source and the operator insertion, respectively. The σ sink operator is located at z, and the coordinates of the two pion bilinear operators in the $\pi\pi(\ldots)$ operators are z_1 and z_2.

The result for $\mathcal{A}^{\text{vac,P}} = \langle P\mathcal{O}_{\bar{K}^0}\rangle$ is

$$\mathcal{A}^{\text{vac,P}} = -\frac{1}{\sqrt{2}}\ \text{mix4}\,. \tag{E.4}$$

The amplitudes $\mathcal{A}^{\pi\pi(\ldots),P} = \langle\mathcal{O}^\dagger_{\pi\pi}P\mathcal{O}_{\bar{K}^0}\rangle$ for the $\pi\pi(\ldots)$ operators are computed as

$$\mathcal{A}^{\pi\pi(\ldots),P} = -\frac{3}{\sqrt{6}}\left(B\ \text{mix4} + \text{mix3}\right) \tag{E.5}$$

where

$$B = -\frac{1}{2}\text{tr}\left(\mathcal{G}^l_{z_1,z_2}\gamma^5\sigma_3\mathcal{G}^l_{z_2,z_1}\gamma^5\sigma_3\right) \tag{E.6}$$

is the $\pi\pi$ self-contraction “bubble” introduced in Sec. B.2 of Ref. [14]. The corresponding result for the σ sink operator is

$$\mathcal{A}^{\sigma,P} = \frac{1}{2}\left(B_\sigma\ \text{mix4} - \text{mix3}_\sigma\right) \tag{E.7}$$

where B_σ is defined in Eq. (D.11).